Mimma Maggio, B.Sc., M.Sc.

BONE-DERIVED VESICLES AND ASSOCIATED MIRNAS AS A MULTI-TARGETED STRATEGY FOR BONE REGENERATION

Trinity College Dublin, February 2026

A thesis submitted to the University of Dublin in partial fulfilment of the requirements for the degree of

Doctor of Philosophy

Supervisor: Professor David Hoey

Internal Examiner: Professor Mark Ahearne

External Examiner: Professor Johannes Grillari

Declaration

I declare that this thesis has not been submitted as an exercise for a degree at this or any other university and it is entirely my own work. I confirm that the work has been completed in full compliance with relevant university policies, including the Academic Integrity policy, the 37 Trinity Policy on Good Research Practice, and the guidance on AI and GenAI in Teaching, Learning, Assessment and Research.

I agree to deposit this thesis in the University's open access institutional repository or allow the Library to do so on my behalf, subject to Irish Copyright Legislation and Trinity College Library conditions of use and acknowledgement.

I consent to the examiner retaining a copy of the thesis beyond the examining period, should they so wish (EU GDPR May 2018).

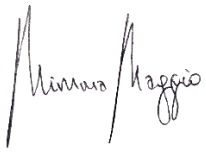

Mimma Maggio

Dublin, February 2026

Summary

Bone is a highly specialised, dynamic tissue that undergoes continuous remodelling to maintain structural integrity, mineral homeostasis, and mechanical function throughout life. This process depends on the precise coordination of bone-forming osteoblasts and bone-resorbing osteoclasts and is tightly regulated by osteocytes, which comprise the majority of bone cells and function as the primary mechanosensors of the skeleton. By sensing mechanical loading generated during daily activity, osteocytes translate physical forces into biochemical signals that direct bone formation and resorption. Disruption of this tightly coupled system, as occurs with ageing, prolonged unloading, or osteoporosis, results in progressive bone loss, microarchitectural deterioration, and increased fracture risk. While mechanical loading through exercise is known to preserve bone mass and reduce fracture risk, the mechanisms through which mechanical cues are communicated between bone cells to coordinate remodelling remain incompletely understood.

Extracellular vehicles (EVs) have emerged as critical mediators of intercellular communication within the bone microenvironment. These nanoscale vesicles transport bioactive cargo, including proteins and nucleic acids, such as microRNAs (miRNAs), enabling coordinated regulation of osteogenesis, angiogenesis, immune signalling, and bone resorption. Increasing evidence indicates that both the release and molecular composition of EVs are sensitive to the physiological state of the parent cell and to external stimuli such as mechanical loading. This positions EVs as a potential mechanistic link between mechanical cues and the multi-target regulation of bone remodelling. Despite this promise, translation of EV-based therapies is currently limited by low production yield, variability in bioactivity, and incomplete understanding of the mechanisms by which EV cargo drives regenerative outcomes.

The overarching aim of this thesis was to exploit mechanical loading to optimise bone-derived EVs and bone tissue-derived matrix vesicles (MVs) as cell-free strategies for tissue regeneration. Specifically, this work sought to define how mechanical cues regulate vesicle-mediated signalling between bone cells, identify vesicle-associated miRNAs that drive regenerative outcomes, and evaluate scalable approaches suitable for translational application.

The first experimental study demonstrated that regulation of osteoclast differentiation by mesenchymal-lineage cells is EV-mediated and highly dependent on both differentiation stage and mechanical environment. Rather than acting as a uniform regulatory population, mesenchymal stromal/stem cells (MSCs), osteoblasts, and osteocytes exhibited distinct paracrine and vesicle-mediated signalling profiles. Osteocytes emerged as the most potent inhibitors of osteoclast differentiation and function, with EVs identified as the dominant mediators of this anti-catabolic regulation. Mechanical stimulation selectively enhanced the inhibitory potency of osteocyte-derived EVs, reinforcing the central role of osteocytes in coordinating bone resorption during mechanoadaptation.

The second study addressed a key translational barrier by evaluating nanovibrational bioreactor technology for scalable production of mechanically activated osteocyte-derived EVs. Although this platform enabled increased EV yield, the specific vibration regimen tested was not sufficient to activate osteocyte mechanotransduction or enhance EV regenerative potency. These findings highlight that effective mechanical conditioning requires precise stimulation parameters and that scalable manufacturing strategies must preserve biological function, not simply increase output.

To overcome the limitations of cell-derived EV production, the third study identified vesicles embedded within mineralised bone matrix as a previously underexplored but highly translational therapeutic source. These MVs were collected in high yield and exhibited robust, multi-target regenerative activity, promoting osteogenesis and angiogenesis while suppressing osteoclastogenesis. Notably, vesicle potency was shaped by physiological context, including age, sex, and exercise, suggesting that bone-derived vesicles encode adaptive information from the skeletal microenvironment and retain regenerative capacity even in aged tissue. This positions tissue-derived vesicles as scalable, biologically informed candidates for cell-free bone regeneration strategies.

The final study established vesicle-associated miRNAs as key molecular effectors of mechanically regulated bone regeneration. Mechanical stimulation selectively altered the miRNA cargo of osteocyte-derived EVs, supporting active, regulated cargo loading rather than passive release. Among these, miR-150-5p emerged as a mechanosensitive regulator capable of simultaneously enhancing osteoblast mineralisation, promoting endothelial network formation, and inhibiting osteoclast differentiation. Delivery of miR-150-5p using

a clinically relevant scaffold further demonstrated its translational potential and capacity to enhance late-stage mineralisation.

In conclusion, this thesis defines a mechanosensitive, vesicle-based signalling framework that integrates mechanical cues with coordinated regulation of osteogenesis, angiogenesis, and bone resorption. By identifying both mechanically activated EVs and tissue-derived MVs, together with functionally relevant miRNA effectors, this work establishes a robust foundation for the development of next-generation, cell-free therapeutics aimed at restoring remodelling balance and enhancing bone regeneration in osteoporotic and mechanically compromised skeletal environments.

Acknowledgements

Time really does fly. It feels like just yesterday that I applied for the PhD, thinking Trinity College was probably out of my league and secretly hoping I wouldn't actually have to leave my life in Turin behind. And yet, within 48 hours, everything changed. Four years later, I can only feel grateful. These years have been full of challenges, a good number of failures (and a good number of tears), a lot of learning, and so much personal and professional growth. Most of all, they've been shaped by incredible people and unforgettable moments that I will always carry with me.

There are so many people I would like to thank for supporting me throughout this journey and for making this Irish chapter of my life so special. First and foremost, thank you to my supervisor, Dr. David Hoey. None of this would have been possible without you. Thank you for constantly challenging me to become the best version of myself and for believing in me even when I struggled to believe in myself. I will truly miss working together, and I sincerely hope our paths will cross again in the future. I am also very grateful to my doctoral committee members, Dr. Conor Buckley and Dr. Mark Ahearne, and my external examiner Dr. Johannes Grillari. Your constructive feedback has been invaluable and has helped me broaden the way I think about my research. To all our collaborators, thank you. Collaboration is what I love most about science: people coming together, combining expertise, and moving forward together. A special thank you to Dr. Lorraine O'Driscoll and Dr. Rawan Almasri, my EVs super-experts. Thank you for your constant support and for teaching me so much. Thank you as well to Dr. Matthew Dalby and Dr. Peter Childs at the University of Glasgow for giving me the opportunity to work with your bioreactor and for being so supportive, even when experiments were not going to plan. Thank you to Dr. Fiona Mary Roche and Dr. Karsten Hokamp for your guidance over the years and for continuously inspiring me with your incredible expertise. Thank you to Dr. Carolin Curtin and Harini Ganesh, at RCSI, for helping me carry out my very last experiment and for encouraging me to step outside my comfort zone to explore scaffold delivery and 3D culture. I am deeply grateful to TBSI for providing the resources, environment, and opportunities that allowed me to grow, learn new techniques, and become a better researcher. Thank you to Dr. Simon Carroll for truly being an ally throughout this journey. Finally, a heartfelt thank you to the Hoey Lab, Luke, Rosario, Matilde, and Linda, for putting up with me bossing you around and

always being so willing to help. Thank you as well to my postdocs, Dr. Cansu Gorgun and Dr. Mathieu Brunet. I am truly, truly grateful for your guidance and support, not only during our time working together, but even after you moved on to new jobs and new countries. That continued encouragement has meant more to me than I can express.

One of the most important things I learned during my PhD is that none of us does this alone, we are truly all in it together. Along the way, I met some of the most incredible people and built friendships that I know will last a lifetime. I genuinely wouldn't have made it without you. First of all, Stéphane, my guardian angel. Thank you for being there from the very beginning, for supporting me and standing by me even when I was ready to quit and go back home. If I am here today, it is also because of you. Morgan, I could write an entire book about how important you have been to me. You have been the best lab partner and friend I could have ever wished for. It's rare to find someone you are so perfectly in sync with, and I feel incredibly lucky that I found that in you. Thank you for the wine nights, the pints after terrible days, the endless laughs, the Thanksgiving dinners and for being such a burst of energy. Dublin simply wouldn't have been the same without you. And my dear Matthia, I don't even know how to fully put into words how much you mean to me. Your support went far beyond friendship. You have always put me first, always shown up for me, and supported me no matter what, in every high and every low. From the countless breaks where you let me vent, to helping me design experiments and think through data, to making my days feel lighter when everything seemed dark, to go out clubbing, you were always there. Thank you for your loyalty, your humour, and your unwavering presence. I could go on for days, but you know. Thank you, Niamh, for being such a wonderful friend. Your kindness and your smile could instantly make even the hardest day better. Thank you for patiently enduring months of me completely butchering your name and never once making me feel awkward about it. Thank you for the weekends in Kerry, for the baking tips, for cooking together at your place, and for all the special time we shared. Tara, from day one, when we were both completely lost trying to figure out the coffee machine, you have been irreplaceable in my life. Thank you for always being ready to help, for all the Luas rides home, and for being such great craic. Jake, my dear desk mate, thank you for always being there and for being such a genuine friend. Looking back, it was definitely worth putting in the effort to understand you! Matilde, even if we didn't get to spend as much time together as we would

have liked, you have been an incredible friend. Thank you for caring for me so deeply, and for all the dinners, dancing, and beautiful moments we shared. Thank you, Angelica and Matteo, for being such thoughtful and wise friends, especially in the beginning when everything felt new and overwhelming. You helped me find my place, feel welcome, and settle into this new chapter with much more confidence. And most of all, thank you for leaving me your apartment. It truly felt like you threw me a lifeline at exactly the right moment. Having that space gave me stability, comfort, and a sense of home when I needed it most. That apartment became the setting of so many memories, and it made my experience in Dublin even more special. I also want to thank Marcin, Tug, Stelios and Alessandro for bringing so much fun and lightness into these years. You were always ready for a laugh, a spontaneous plan, or a much-needed break from the lab, and you made my time in Dublin brighter and far more colourful. Thank you, Colette, for welcoming to Ireland since day one and helping me settle in and truly enjoy my time here. And to all of you, thank you for the dinners, the trips, the distractions, the encouragement, and the constant reminders that there is a whole world beyond experiments and deadlines. Each of you, in your own way, made this journey lighter, happier, and so much more meaningful.

To my friends back in Italy, Eleonora, Serena, Emanuela, Tolo, Angelo, Gabriele, Vera, Ludovico, Erika, Carla, thank you for being my constant, even from afar. No matter the distance, the time apart, or the different lives we were building, your support never wavered. Thank you for the calls, the messages, the visits, and for always making it feel like nothing had changed. Knowing I could always come home to you gave me strength in the hardest moments and reminded me where I started. I carry you with me, wherever I go.

To my family, my aunts, uncles, my grandmothers, and cousins, thank you for your constant love and encouragement throughout these years. Even from a distance, I always felt your support and pride, and that meant more than I can say. Thank you for cheering me on, for celebrating every small milestone, and for reminding me that no matter where I go, I always have a home and a family who believe in me.

To my sister, my other half, there are no words that could truly capture what you mean to me. Thank you for always being there, for your honest advice, and for constantly reminding me that no obstacle is too big and that I am stronger than I think. You have always believed in me, even in moments when I struggled to believe in myself. Thank you especially for

these last month's living together, for staying by my side while I was writing my thesis, and for patiently putting up with my stress, my doubts, and my insecurities, all while going through one of the most stressful periods of your own life. Your presence gave me strength, calm, and perspective when I needed it most. I am endlessly grateful to have you, not just as my sister, but as my safest place and greatest supporter.

To my parents, I truly would not be who I am without you. Everything I have achieved rests on the love, support, and values you have given me. Thank you for being my number one supporter, for always encouraging me to push beyond my limits, and for giving me the support and confidence to pursue every dream I have ever had. From the moment you supported my decision to move to Turin at just 19 years old, to later encouraging me to take the leap and move to Dublin, even when it meant being so far from home, you have always stood behind me. You did everything you could to remove obstacles from my path, to make things easier when they felt overwhelming, and to remind me that I was capable of more than I imagined. Thank you for being such a constant, steady presence in my life, for the calls, the reassurance, the sacrifices, and the unconditional love. Knowing that you are always there for me has given me the courage to take risks and the strength to keep going, even when things felt uncertain. I owe you more than words can ever fully express.

Finally, thank you to my favourite places, and of course my favourite pubs, for being the backdrop to so many memories, laughs, deep chats, celebrations, and much-needed escapes from the lab. And thank you, Dublin, for the opportunities, the friendships, the growth… and yes, even for the rain. Especially the rain. The horizontal rain. The "four seasons in one day" rain. The kind of rain that makes you question every life choice while going home from the lab. You achieved what I once thought was impossible: you taught a Sicilian to go out even when it's raining. Jokes aside, you gave me resilience, independence, and a third home. I arrived uncertain and a little scared (maybe more than a little), I leave stronger, grateful, and with a piece of my heart that will forever belong to you, rainy days and all.

Table of Contents

List of Figures

List of Supplementary Figures

List of Tables

Nomenclature

€	Euro
µg	Microgram
µL	Microlitre
µm	Micrometre
18s	18S Ribosomal RNA
2D	Two-Dimensional
3D	Three-Dimensional
AFF	Atypical Femoral Fractures
ALIX	ALG-2-Interacting Protein X
ALP	Alkaline Phosphatase
AMicon™	Amicon Ultra Centrifugal Filter Units
ANOVA	Analysis of Variance
APC	Allophycocyanin
ASC	Adipose Stem/Stromal Cell
ATCC	American Type Culture Collection
BCA	Bicinchoninic Acid
Bcl-2	B-cell Lymphoma-2
BMD	Bone Mineral Density
BMP	Bone Morphogenetic Protein
BMP-2	Bone Morphogenetic Protein-2
BMSC	Bone Marrow Stromal/Stem Cell
BMU	Basic Multicellular Unit
B-MVs	Bone-Derived Matrix Vesicles
BP	Bisphosphonates
bp	Base Pair
BSA	Bovine Serum Albumin
BSP	Bone Sialoprotein
$CaCl_2$	Calcium Chloride
CD	Cluster of Differentiation
cDNA	Complementary DNA
CKD	Chronic Kidney Disease
CM	Conditioned Medium
CM-F	Fluid Shear Stimulated Conditioned Medium
CM-S	Static Conditioned Medium
CO_2	Carbon Dioxide
Col1	Type 1 Collagen
Coll-nHA	Collagen-Nano-Hydroxyapatite
COX2	Cyclooxygenase-2
CPC	Cetylpyridinium Chloride
CS	Calf Serum
CTSK	Cathepsin K
Cx43	Connexin 43
DAPI	4’,6-Diamidino-2-Phenylindole
DAVID	Database for Annotation, Visualization, and Integrated Discovery

dCS	EV-Depleted Calf Serum
DC-STAMP	Dendritic Cell-Specific Transmembrane Protein
DESeq2	Differential Expression Sequencing 2
dFBS	EV-Depleted Fetal Bovine Serum
diH_2O	Deionised Water
DKK1	Dickkopf-1
DM	EV-Depleted Conditioned Medium
DMEM	Dulbecco's Modified Eagle Medium
DM-F	Fluid Shear Stimulated EV-Depleted Conditioned Medium
DMOG	dimethyloxalylglycine
DMP-1	Dentin Matrix Protein 1
DM-S	Static EV-Depleted Conditioned Medium
DNA	Deoxyribonucleic Acid
dsDNA	Double-Stranded DNA
dSTORM	Direct Stochastic Optical Reconstruction Microscopy
EBM-2	Endothelial Basal Medium-2
ECM	Extracellular Matrix
EDAC	1-Ethyl-3-(3-Dimethylaminopropyl) Carbodiimide Hydrochloride
EGM-2	Endothelial Growth Medium-2
ELISA	Enzyme-Linked Immunosorbent Assay
ERK1/2	Extracellular Signal–Regulated Kinases 1/2
ESCRT	Endosomal Sorting Complex Required for Transport
EV-F	Fluid Shear Stimulated Extracellular Vesicles
EVP2	EV Profiler Kit 2
EVs	Extracellular Vesicles
EV-S	Static Extracellular Vesicles
EX	Exercised Group
FBS	Fetal Bovine Serum
FDR	False Discovery Rate
FITC	Fluorescein Isothiocyanate
FMO	Fluorescence minus one
FSS	Fluid Shear Stress
GFP-HUVECs	Green Fluorescent Protein-Expressing Human Umbilical Vein Endothelial Cells
GMP	Good Manufacturing Practice
GO	Gene Ontology
GRCh38	Genome Reference Consortium Human Build 38
GRCm38	Genome Reference Consortium Mouse Build 38
h	Hour
HCl	Hydrochloric Acid
HFB	Hollow-Fiber Bioreactor
HIF-1α	Hypoxia-Inducible Factor 1-alpha
hMSCs	Human Mesenchymal Stromal/Stem Cells
HRP	Horseradish Peroxidase
Hz	Hertz
IBTS	Irish Blood Transfusion Service
ICC	Immunocytochemistry

IDEAS	Image Data Exploration and Analysis Software
KCl	Potassium Chloride
kDa	Kilodalton
kHz	Kilohertz
K-MVs	Kidney-Derived Matrix Vesicles
kV	Kilovolt
LCS	Lacunar-Canalicular System
lEVs	Large Extracellular Vesicles
L-G	L-Glutamine
LMHFV	Low-Magnitude, High-Frequency Vibration
lncRNA	Long non-coding RNA
MAPK	Mitogen-Activated Protein Kinase
MCP-1	Monocyte Chemoattractant Protein-1
M-CSF	Macrophage Colony-Stimulating Factor
MEM	Minimum Essential Medium
MFI	Median Fluorescence Intensity
$MgCl_2$	Magnesium dichloride
miEAA	miRNA Enrichment Analysis and Annotation Tool
min	Minute
miRBase	MicroRNA Database
miRNA	MicroRNA
miRNA-seq	MicroRNA Sequencing
MISEV	Minimal Information for Studies of Extracellular Vesicles
mL	Millilitre
MLO-Y4	Murine Long Bone Osteocyte-Y4
mM	Millimolar
MMP	Matrix Metallopteinase
mmu-miR	Mus musculus MicroRNA
mRNA	Messenger Ribonucleic Acid
MSC	Mesenchymal Stem/Stromal Cell
MVBs	Multivesicular Bodies
MVs	Matrix Vesicles
MWCO	Molecular Weight Cut-Off
N:P ratio	Nitrogen-to-Phosphate Ratio
Na_2SO_4	Sodium Sulphate
NaCl	Sodium Chloride
NaH_2PO_4	Sodium Dihydrogen Phosphate
$NaHCO_3$	Sodium Bicarbonate
NFATc1	Nuclear Factor of Activated T Cells 1
NF-κB	Nuclear Factor Kappa B
nHA	Nano-Hydroxyapatite
NHS	N-Hydroxysuccinimide
NIH	National Institutes of Health
nm	Nanometre
NO	Nitric Oxide
NPs	Nanoparticles

NTA	Nanoparticle Tracking Analysis
OB	Osteoblast
OCN	Osteocalcin
OCT	Optimal Cutting Temperature Compound
OCY	Osteocyte
OM	Osteogenic Medium
ON	Osteonectin
ONJ	Osteonecrosis of the Jaw
OPG	Osteoprotegerin
OPN	Osteopontin
ORA	Overrepresentation Analysis
Pa	Pascal
PBMCs	Peripheral Blood Mononuclear Cells
PBS	Phosphate-Buffered Saline
PCA	Principal Component Analysis
PCR	Polymerase Chain Reaction
PFA	Paraformaldehyde
PHOSPO1	Phosphoethanolamine/phosphocholine phosphatase 1
Pi	Inorganic Phosphate
piRNA	Piwi-interacting RNA
pNPP	p-nitrophenyl phosphate
PPFC	Parallel Plate Flow Chamber
PPi	Pyrophosphate
PRDM1	PR Domain Zinc Finger Protein 1
PRP	Platelet-Rich Plasma
P-S	Penicillin–Streptomycin
PTH	Parathyroid Hormone
qRT-PCR	Quantitative Real-Time Polymerase Chain Reaction
RANK	Receptor Activator of Nuclear Factor κB
RANKL	Receptor Activator of Nuclear Factor κB Ligand
RIN	RNA Integrity Number
RISC	RNA-induced silencing complex
RNA	Ribonucleic Acid
ROI	Region of Interest
rpm	Revolutions Per Minute
rRNA	Ribosomal RNA
RUNX-2	Runt-Related Transcription Factor 2
s	Seconds
SaOS-2	Sarcoma Osteogenic-2
SCL	Synthetic Cartilage Lymph
SD	Standard Deviation
SEC	Size Exclusion Chromatography
SED	Sedentary Group
SEM	Scanning Electron Microscopy
SERMs	Selective Oestrogen Receptor Modulators
sEVs	Small Extracellular Vesicles

SMAD	Suppressor of Mothers against Decapentaplegic
TEM	Transmission Electron Microscopy
TES	N-Tris(hydroxymethyl)methyl-2-aminoethanesulfonic Acid
TFF	Tangential Flow Filtration
TGF-β	Transforming Growth Factor Beta
TNAP	Tissue-Nonspecific Alkaline Phosphatase
TNF-α	Tumour Necrosis Factor Alpha
TRAF	Tumour Necrosis Factor Receptor-Associated Factor
TRAP	Tartrate-Resistant Acid Phosphatase
TRIzol	Total RNA Isolation Reagent
tRNA	Transfer RNA
TSG101	Tumour Susceptibility Gene 101
VEGF	Vascular Endothelial Growth Factor
VEGF-A	Vascular Endothelial Growth Factor A
Wnt	Wingless-related integration site
YAP	Yes-Associated Protein
α-MEM	Minimum Essential Medium, Alpha Modification

Publications

Journal Articles

Maggio, M., Martins, C. S., Almasri, R., Petrousek, S., Brunet, M.Y., Madden, L.A., Gorgun, C., Ní Néill, T., Roche, F.M., Buckley, C.T., O'Driscoll, L., Hoey, D.A. Extracellular Vesicles-Mediated Crosstalk in Bone: miR-150-5p as a Mechanosensitive Inhibitor of Osteoclastogenesis. (Molecular Therapy, 2026)

Martins, C.S., **Maggio, M.**, Gorgun, C., Brunet, M.Y., Dobricic, M., Almasri, R., O'Brien, F. J., O'Driscoll, L., Hoey, D. A. Mechanical Cues and Lineage Commitment Govern the Angiogenic Potential of Mesenchymal Cell-Derived Extracellular Vesicles. (Advanced Biology, 2026)

Shen, N*., **Maggio, M.*,** Woods, I., Lowry, M., Almasri, R., Eichholz, K.F., Gorgun, C., Stavenschi, E., Hokamp, K., Roche, F. M., O'Driscoll, L., Hoey, D. A. Mechanically activated mature bone cells drive vessel formation via an extracellular vesicle mediated mechanism. (Journal of Tissue Engineering, 2023)

Murphy, B., Martins, C., **Maggio, M.**, Morris, M. A., Hoey, D.A. Nano Sized Gallium Oxide Surface Features for Enhanced Antimicrobial and Osteo-Integrative Responses. (Colloids and Surfaces B, 2023)

Conferences and symposia

Podium Presentations

Maggio, M., Brunet, M.Y., Almasri, R., Gorgun, C., Augusto, J., Barad, Z., Kelly, A., O'Driscoll, L., Hoey, D.A., Matrix Vesicles as novel multi-target therapeutic for bone regeneration. TERMIS-EU 2026, Palma de Mallorca, Spain, 2026.

Maggio, M., Martins, C., Petrousk, S., Gorgun, C., Almasri, R., Madden, L., Brunet, M.Y., Ní Néill, T., Augusto, J., Barad, Z., Kelly, A., Buckley, C.T., O'Driscoll, L., Hoey, D.A., Unveiling the therapeutic potential of bone-derived vesicles and their miRNAs in bone regeneration. 31st Annual Conference of the Section of Bioengineering of the Royal Academy of Medicine in Ireland (BinI 2026). Athlone, Ireland, 2026.

Maggio, M., Brunet, M.Y., Almasri, R., Gorgun, C., O'Driscoll, L., Hoey, D.A., Matrix Vesicles as a multi-targeted therapeutic strategy for bone regeneration. TERMIS-EU 2025, Freiburg, Germany, 2025.

Maggio, M., Martins, C., Almasri, R., Petrousek, S., Gorgun, C., Brunet, M.Y., Madden, L., Ní Néill, T., Buckley, C.T., O'Driscoll, L., Hoey, D.A., Bone cell-derived Extracellular Vesicles as emerging anti-catabolic therapeutics for bone regeneration. TERMIS-EU 2025, Freiburg, Germany, 2025.

Maggio, M., Martins, C., Petrousek, S., Gorgun, C., Almasri, R., Brunet, M.Y., Ní Néill, T., Buckley, C.T., Hokamp, K., Roche, F.M., O'Driscoll, L., Hoey, D.A., Bone-derived vesicles and associated miRNAs: unravelling novel nanotherapeutics for bone regeneration, 30th Annual Conference of the Section of Bioengineering of the Royal Academy of Medicine in Ireland (BinI 2025). Athlone, Ireland, 2025.

Maggio, M., Martins, C., Petrousek, S., Almasri, R., O'Driscoll, L., Hoey, D. A., Bone cell of osteoclastogenesis is mediated by extracellular vesicles that is dependent in the parent cell lineage commitment stage and mechanical environment. 29th Annual Conference of the Section of Bioengineering of the Royal Academy of Medicine in Ireland (BinI 2024). Newcastle, Northen Ireland, 2024.

Maggio, M., Martins, C., Petrousek, S., Hoey, D.A. Bone cell regulation of osteoclastogenesis is dependent on the stage of lineage commitment and mechanical environment. TERMIS EU- 2023, Manchester, United Kingdom, 2023.

Maggio, M., Martins, C., Petrousek, S., Hoey, D.A. Bone cell regulation of osteoclastogenesis is dependent on the stage of lineage commitment and mechanical environment. 28th Annual Conference of the Section of Bioengineering of the Royal Academy of Medicine in Ireland (BinI 2023). Enfield, Ireland, 2023.

Maggio, M., Hoey, D.A. Identification of mechanically regulated miRNAs in osteocytes and secreted extracellular vesicles. 27th Annual Conference of the Section of Bioengineering of the Royal Academy of Medicine in Ireland (BinI 2022). Galway, Ireland, 2022.

Poster Presentations

Maggio, M., Martins, C., Petrousk, S., Gorgun, C., Almasri, R., Madden, L., Brunet, M.Y., Ní Néill, T., Augusto, J., Barad, Z., Kelly, A., Buckley, C.T., O'Driscoll, L., Hoey, D.A., Unveiling the therapeutic potential of bone-derived vesicles and their miRNAs in bone regeneration. Trinity Centre for Biomedical Engineering Research Symposium, Dublin, Ireland 2025.

Maggio, M., Brunet, M.Y., Gorgun, C., Almasri, R., O'Driscoll, L., Hoey, D.A., Bone-derived Matrix Vesicles as multi-targeted therapeutic strategy for bone regeneration. International Society for Extracellular Vesicles (ISEV) 2025 Annual Metting, Vienna, Austria, 2025.

Maggio, M., Martins, C., Almasri, R., Petrousek, S., Brunet, M.Y., Ní Néill, T., Buckley, C.T., O'Driscoll, L., Hoey, D.A. Mesenchymal-derived bone cells regulated osteoclastogenesis via an extracellular vesicle-mediated mechanism. International Society for Extracellular Vesicles (ISEV) 2025 Annual Metting, Vienna, Austria, 2025.

Maggio, M., Martins, C., Almasri, R., Petrousek, S., Brunet, M.Y., Ní Néill, T., Buckley, C.T., O'Driscoll, L., Hoey, D.A. Mesenchymal-derived bone cells regulate osteoclastogenesis via an extracellular vesicle-mediated mechanism that is dependent on the stage of mesenchymal lineage commitment and the mechanical environment. Orthopaedic Research Society (ORS) Annual Meeting, Phoenix, USA, 2025.

Maggio, M., Brunet, M.Y., Almasri, R., Gorgun, C., O'Driscoll, L., Hoey, D.A., Bone-derived Matrix Vesicles inhibit osteoclastogenesis: a new role beyond mineralisation. Orthopaedic Research Society (ORS) Annual Meeting, Phoenix, USA, 2025.

Maggio, M., Martins, C., Petrousek, S., Almasri, R., O'Driscoll, L., Hoey, D.A. Bone cell regulation of osteoclastogenesis is dependent on the stage of lineage commitment and mechanical environment. Inaugural School of Engineering Symposium 2023, Dublin, Ireland, 2023.

Maggio, M., Martins, C., Petrousek, S., Tsiapalis, D., O'Driscoll, L., Hoey, D.A., Bone cell regulation of osteoclastogenesis is dependent on the stage of lineage commitment and mechanical stimulation. Trinity Centre for Biomedical Engineering Research Showcase 2023, Dublin, Ireland, 2023.

Maggio, M., Martins, C., Petrousek, S., Tsiapalis, D., O'Driscoll, L., Hoey, D.A. Impact of Osteogenic lineage cells secretome on regulation of osteoclastogenesis. Trinity Centre for Biomedical Engineering Research Showcase 2022, Dublin, Ireland, 2022.

Rapid-fire Presentations

Maggio, M., Martins, C., Almasri, R., Petrousek, S., Brunet, M.Y., Ní Néill, T., Buckley, C.T., O'Driscoll, L., Hoey, D.A. Extracellular vesicles from mesenchymal-derived bone cells regulate osteoclastogenesis. UK Society for Extracellular Vesicles (UKEV) Forum 2024, Newcastle Upon Tyne, UK, 2024.

Maggio, M., Brunet, M.Y., Gorgun, C., Almasri, R., O'Driscoll, Hoey, D.A. multi-targeted bone regeneration: the role of bone-derived Matrix Vesicles. UK Society for Extracellular Vesicles (UKEV) Forum 2024, Newcastle Upon Tyne, UK, 2024.

Maggio, M., Martins, C., Petrousek, S., Gorgun, C., Almasri, R., Brunet, M.Y., Ní Néill, T., Buckley, C.T., Hokamp, K., Roche, F.M., O'Driscoll, L., Hoey, D.A., Bone-derived vesicles and associated miRNAs: unravelling novel nanotherapeutics for bone regeneration. Trinity Centre for Biomedical Engineering Research Symposium, Dublin, Ireland 2024.

Awards and Distinctions

1. Best-rated abstract of the Extracellular Vesicles session. TERMIS-EU 2025, Freiburg, Germany, 2025.
2. 2nd place poster presentation ORS ISFR SECTION.: International Section for Fracture Repair, Orthopaedic Research Society. Phoenix, USA, 2025.
3. 1st prize for Best Mechanobiology Research, oral presentation for mature research category. 28th Annual Conference of the Section of Bioengineering of the Royal Academy of Medicine in Ireland (BinI 2023). Enfield, Ireland, 2023.
4. Medtronic Best Regenerative Medicine Research, oral presentation for early career researchers. 27th Annual Conference of the Section of Bioengineering of the Royal Academy of Medicine in Ireland (BinI 2022). Galway, Ireland, 2022.
5. Best poster in the Orthopaedics session. Trinity Centre for Biomedical Engineering Research Showcase 2022, Dublin, Ireland, 2022.

Chapter 1. Introduction

1.1 Bone physiology and associated pathologies

Bone is a highly hierarchical, multifunctional tissue with the extraordinary ability to self-renew. In addition to providing mechanical support for load bearing, locomotion and protecting vital organs, bone functions as a major mineral reservoir and forms a specialised niche that supports haematopoiesis and immune cell development [1]. To fulfil these functions, bone exhibits unique structural and material properties, integrating stiffness and strength with elasticity and toughness [2]. Bone physiology is sustained through continuous modelling and remodelling, a tightly regulated process that replaces old and damaged bone with newly formed matrix to preserve skeletal integrity and mineral homeostasis. Remodelling is mediated by the synergistic activity of bone forming osteoblasts and bone resorbing osteoclasts [3]. Osteocytes, the most abundant cells in bone, act as master orchestrators of this process by regulating osteoblast and osteoclast activity via paracrine signalling [4]. Through this dynamic and adaptive system, bone continuously responds to metabolic and mechanical demands throughout life.

Disruption of the tightly regulated balance between bone formation and bone resorption, where osteoclast activity exceeds that of osteoblasts, results in the development of bone pathologies such as osteoporosis. As the most common metabolic bone disorder, osteoporosis is characterised by decreased bone mass, deterioration of bone microarchitecture, and an elevated risk of fracture. Because bone loss occurs gradually and often without symptoms, fractures frequently constitute the first clinical presentation, leading to significant morbidity and mortality. Globally, osteoporosis poses a major public health challenge, affecting approximately 18.3% of the population, with a markedly higher prevalence in women (23.1%) than in men (11.7%), and with further increases projected by 2034 [5]. In Europe alone, the disease is associated with an estimated annual economic burden of €464.29 million, reflecting its considerable societal and healthcare impact [6]. Consequently, there is an urgent need for effective therapeutic interventions. Current pharmacological treatments primarily focus on slowing down osteoclast-mediated bone resorption through antiresorptive agents such as bisphosphonates and RANKL inhibitors.

However, these therapies are frequently associated with adverse effects, including gastrointestinal disturbances, musculoskeletal pain, and, in rare cases, serious complications such as osteonecrosis of the jaw and atypical femoral fractures [7]. Alternative therapeutic strategies have sought to enhance bone formation using osteoanabolic agents, including parathyroid hormone analogues and anti-sclerostin antibodies. Although these treatments have demonstrated improvements in fracture outcomes, their clinical utility is limited by adverse effects, constrained treatment duration, cardiovascular concerns, and an increased risk of fracture following treatment discontinuation [8]. In addition to pharmacological therapies, physical exercise has been shown to be promising in osteoporosis prevention and management. Weight-bearing and resistance exercises promote bone formation through mechanical loading, enhance muscle strength and balance, and reduce fall and fracture risk by improving functional stability in older adults [9]. However, exercise alone is insufficient to reverse established osteoporosis and is most effective when integrated into a combined therapeutic approach. The persistent fracture risk and limitations of existing treatments highlight the need for novel strategies that restore coupling between bone resorption and formation, and that offer improved safety, and sustained fracture protection.

1.2 Mechanical regulation of bone physiology

Mechanical loading is a key regulator of bone health, playing a crucial role in preserving skeletal mass, structural organisation, and mechanical strength. [10]. Throughout life, bone is continuously subjected to physical forces generated by daily activities such as standing, walking, and muscle contraction, which provide essential cues that guide bone adaptation. When mechanical loading is adequate, bone formation is promoted, and structural integrity is preserved. In contrast, reduced mechanical stimulation, such as during ageing, prolonged inactivity, immobilisation, or microgravity exposure, leads to an imbalance in bone remodelling, characterised by increased resorption and progressive bone loss [11].

The ability of bone to respond to mechanical demands relies on the coordinated activity of bone cells within the remodelling unit. Rather than acting on a single cell type, mechanical cues influence multiple components of the bone microenvironment, ensuring that bone formation and resorption remain coupled in both space and time [12]. Among

these cells, osteocytes occupy a central position due to their abundance and strategic location within the mineralised matrix. By integrating mechanical information derived from tissue deformation and fluid movement within bone, osteocytes regulate the behaviour of osteoblasts and osteoclasts through changes in their signalling output [13]. In this manner, mechanical loading serves as a mechanism through which local functional requirements are converted into targeted and appropriate bone remodelling responses. Importantly, mechanoregulation of bone remodelling extends beyond osteocytes alone. Cells of the mesenchymal lineage, including mesenchymal stromal/stem cells and osteoblasts, are also responsive to mechanical cues and contribute to load-induced adaptation. Mechanical stimulation influences osteogenic commitment, matrix production, and the secretion of regulatory factors that modulate osteoclast differentiation and activity [14, 15]. Through these combined actions, mechanical loading promotes an environment that supports bone formation while restraining excessive resorption, thereby preserving skeletal integrity.

Although the influence of mechanical loading on bone mass and architecture is well established, the cellular processes that translate mechanical cues into coordinated remodelling responses remain incompletely understood. In particular, how signals generated by mechanically stimulated bone cells are conveyed within the bone microenvironment to regulate osteoblast and osteoclast activity has not been fully defined. This limitation constrains the development of therapeutic strategies that seek to exploit mechanical regulation while preserving the physiological coupling of bone formation and resorption. Improved insight into the mechanisms of mechanically mediated intercellular communication in bone is therefore required to better understand pathological bone loss and to inform the design of more effective approaches for restoring remodelling balance and maintain a skeletal mass and structure.

1.3 Extracellular vesicles as mediators of bone cell-cell communication

In recent years, extracellular vesicles (EVs) have been recognised as key mediators of intercellular communication within the bone microenvironment. These nanoscale, membrane-bound particles are released by cells into the extracellular space and can deliver bioactive cargo, including lipids, proteins, and nucleic acids such as microRNAs (miRNAs),

to recipient cells, thereby coordinating cellular behaviour. Within bone tissue, EVs produced by mesenchymal stromal/stem cells, osteoblasts, osteocytes, and osteoclasts play important roles in regulating bone remodelling by modulating osteogenic differentiation, angiogenesis, immune signalling, and the coupling of bone formation with resorption [16]. As such, EV-mediated communication represents an additional regulatory mechanism that complements traditional soluble factor- and contact-dependent signalling pathways.

Increasing evidence indicates that EV release and cargo composition are closely linked to the physiological state of the parent cell and are responsive to external stimuli, including mechanical loading. Given the central role of mechanical cues in bone remodelling, EVs have been proposed as downstream mediators through which mechanically stimulated bone cells communicate with neighbouring cells in the bone microenvironment [17]. Mechanical stimulation has been shown to alter both the quantity and molecular content of EVs released by bone cells, leading to changes in their biological activity. Previous work from our group has demonstrated that EVs released by mechanically stimulated osteocytes enhance stem cell recruitment and osteogenic differentiation [18], and that EVs derived from mechanically stimulated osteocytes and osteoblasts promote angiogenic responses [19]. Furthermore, mechanical loading has been shown to modify the miRNA composition of EVs, supporting the concept that EV-associated miRNAs act as key regulatory molecules through which mechanical cues are conveyed to osteoblasts, osteoclasts, and their progenitors [19, 20]. Through these mechanisms, EV-mediated signalling may contribute to the coordinated regulation of anabolic and catabolic processes required for balanced bone remodelling.

Despite the growing interest in EV-based therapies, their clinical translation remains constrained by the limited EV yields obtained using standard cell culture and conventional collection methods. In preclinical studies, effective EVs doses commonly range between 10 and 100 μg per mouse, whereas traditional two-dimensional culture systems typically yield only approximately 0.5-1 μg of EVs per millilitre of conditioned medium [21]. This disparity between the quantities required for therapeutic efficacy and those achievable under standard production conditions represents a significant bottleneck for both preclinical investigation and clinical development. To address this limitation, a range of scalable culture and manufacturing strategies have been explored to increase EV production by expanding

cell numbers and maximising conditioned medium output over shorter timeframes. These approaches include the use of multilayer cell culture systems, hollow-fiber bioreactors, stirred-tank bioreactors, and three-dimensional spheroid cultures, all of which have demonstrated substantial improvements in EV yield compared with conventional monolayer cultures [22]. Collectively, these advances indicate that EVs scalability can be addressed through appropriate culture platform selection and process optimisation, while also highlighting opportunities to explore new bioreactors systems and additional EVs sources, such as tissue derived EVs, capable of supporting robust and scalable production for translational applications.

Taken together, current evidence supports a role for EVs in mechanically regulated intercellular communication in bone. However, further investigation is required to elucidate how bone cells coordinate remodelling, how mechanical stimulation influences EV cargo composition, to define the functional relevance of EV-associated miRNAs in bone cell regulation, and to establish scalable production strategies for mechanically activated EVs. Progress in these areas will be important for the continued development of EV-based approaches for bone regeneration.

1.4 Objective of the thesis

Bone remodelling is a tightly regulated process driven by the coordinated activity of osteoblasts and osteoclasts, and its disruption by trauma, disease, or age-related imbalance can result in critical bone defects and osteoporosis, conditions that remain difficult to treat effectively. Mechanical loading is a key physiological regulator of bone homeostasis, eliciting adaptive responses through mechanically induced signalling within the bone microenvironment. Among the factors released in response to mechanical stimulation, EVs have emerged as important mediators of intercellular communication and carry bioactive cargo with regenerative potential. Increasing evidence indicates that EVs composition can be modulated by conditioning the parent cell, including through mechanical stimulation, and previous work from our laboratory has shown that EVs derived from mechanically stimulated osteocytes enhance mesenchymal stem cell recruitment and angiogenic responses. Despite this promise, the translational application of EVs is limited by variability and low production yield. Therefore, the overarching aim of this thesis is to harness

mechanical loading to optimise EVs derived from different bone-resident cell types and tissue, with the objective of developing scalable, multi-targeted strategies to enhance bone regeneration.

This will be achieved via four specific objectives (**Figure 1.1**):

1. To Investigate how distinct cells of the osteogenic lineage regulate bone resorption through paracrine signalling and EV-mediated communication.
    - To determine how progressive stages of osteogenic lineage commitment influence the regulation of osteoclastogenesis via both soluble secreted factors and EV-mediated signalling.
    - To evaluate how the mechanical environment modulates secretome- and EV-driven regulation of osteoclast differentiation and activity.
2. To establish a scalable strategy for the production of mechanically activated EVs.
    - To validate a novel nanovibrational bioreactor platform to increase EVs yield and regenerative properties.
3. To investigate tissue-derived vesicles as an alternative source of regenerative EVs.
    - To isolate and characterise vesicles derived from bone tissue and assess their regenerative properties in comparison to cell-derived EVs.
4. To elucidate the molecular mechanisms mediating the regenerative effects of bone-derived mechanically activated EVs.
    - To identify, functionally characterise and utilise EV-associated miRNAs mediating the regenerative properties of bone derived EVs.

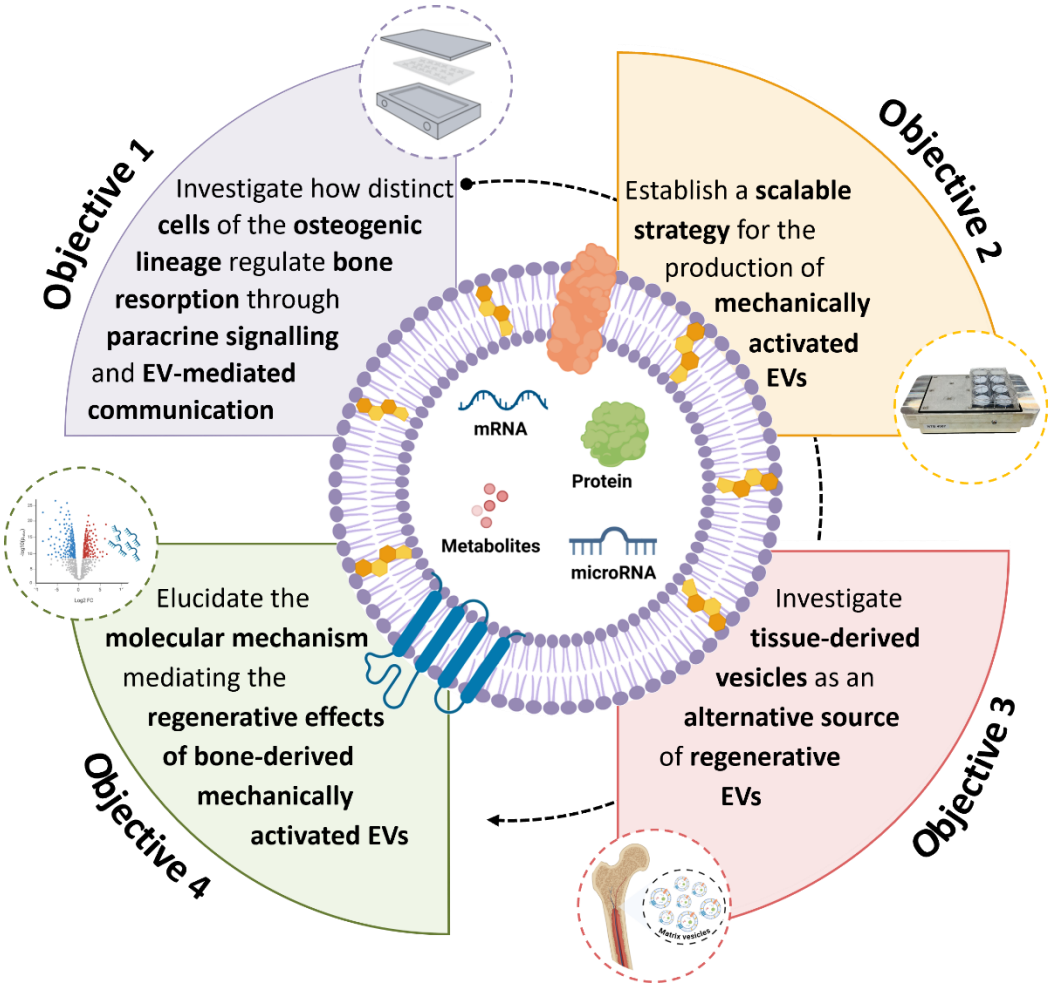

Figure 1.1. Schematic representation of thesis outline. The project begins by investigating how osteogenic lineage cells regulate bone resorption through their secretome and EVs, with particular emphasis on the influence of lineage commitment stage and mechanical environment. The work then advances to the evaluation of a novel strategy for scaling up the production of mechanically activated EVs and explores tissue-derived vesicles as an alternative regenerative EVs source. Finally, the molecular mechanisms underlying the regenerative effects of bone-derived mechanically activated EVs are examined.

Chapter 2. Literature Review

2.1 Bone Physiology

Bone is a highly hierarchical and multifunctional tissue whose complex organisation underpins it diverse physiological roles. Functionally, bone provides mechanical support essential for load bearing and locomotion [1], while also protecting vital organs such as the brain, the heart and the lungs [23]. In parallel, it serves as a major mineral reservoir, storing approximately 99% of the body's calcium and a substantial portion of phosphate, thereby playing a central role in systemic mineral homeostasis [24]. Bone also forms a specialised microenvironment that houses the bone marrow, supporting haematopoiesis and immune cell development [25]. To perform all these functions, bone has a unique structure and mechanics. Structurally, bone is very complex as it must be stiff to accommodate loading and resist deformation but at the same time elastic to deform and absorb energy [2, 26]. To manage these requirements, bone consist in two macroscopic tissues, cortical (compact) and cancellous (trabecular) bone, which are structurally and functionally different [27]. Cortical bone constitutes roughly 80% of the adult human skeleton and forms the dense outer shell of bones, characterised by low porosity (5-10%) and high stiffness, which confers mechanical strength and load-bearing capacity. In contrast, cancellous bone accounts for approximately 20% of skeletal mass and is composed of a highly porous (50-90%), three-dimensional interconnected network of trabecular plates and rods, optimised for energy absorption, load distribution, and metabolic activity (**Figure 2.1**) [28, 29].

At the microscopic scale, cortical bone exhibits a highly organized structure composed of osteons, also referred to as Haversian systems. Each osteon consists of concentric lamellae of mineralized extracellular matrix arranged around a central Haversian canal that houses blood vessels and nerve fibres [30]. Osteocytes, the most abundant bone cells, reside within lacunae between lamellae and form an extensive communication network through canaliculi, enabling mechanotransduction and intercellular signalling [31, 32]. Surrounding the external surface of bone, the periosteum is a thin, specialized membrane composed of an outer fibrous layer and an inner cambium layer. The periosteum plays a critical role in bone protection and repair, acting as a mechanosensory interface for detecting mechanical

loading, a reservoir for bioactive factors, and a niche for osteogenic progenitor cells that contribute to bone formation and regeneration [33].

From a compositional perspective, bone is a bi-phasic material integrating extracellular organic and mineralised inorganic material. The organic component is mostly constituted by type I collagen, which provides flexibility and resilience to bone against stretching, twisting and torsion, along with non-collagenous proteins such as osteocalcin, osteonectin, and various growth factors that regulate mineralisation and cell behaviour. On the other hand, the mineralised inorganic component consists mainly in calcium and phosphate, in the form of hydroxyapatite, and confers bone its compressive strength and rigidity [34-36]. The overall mechanical performance of bone thus depends on the combined and complementary contributions of both phases, with the organic matrix providing toughness and the mineral phase conferring stiffness and load-bearing capacity [37].

At the cellular scale, bone physiology is regulated through the coordinated actions of osteoclasts, osteoblasts, osteocytes, and osteoprogenitor cells. Osteoclasts, which originate from the hematopoietic lineage, mediate bone resorption, whereas osteoblasts, derived from mesenchymal stem/stromal cells, are responsible for the synthesis and mineralization of new bone matrix. A subset of osteoblasts become embedded within the newly formed matrix and differentiate into osteocytes, which function as central regulators of bone remodelling by sensing mechanical stimuli and integrating biochemical signals [38]. Through this tightly controlled cellular interplay, bone is able to dynamically adjust its structure and composition in response to mechanical loading and metabolic requirements, thereby preserving optimal skeletal integrity across the lifespan.

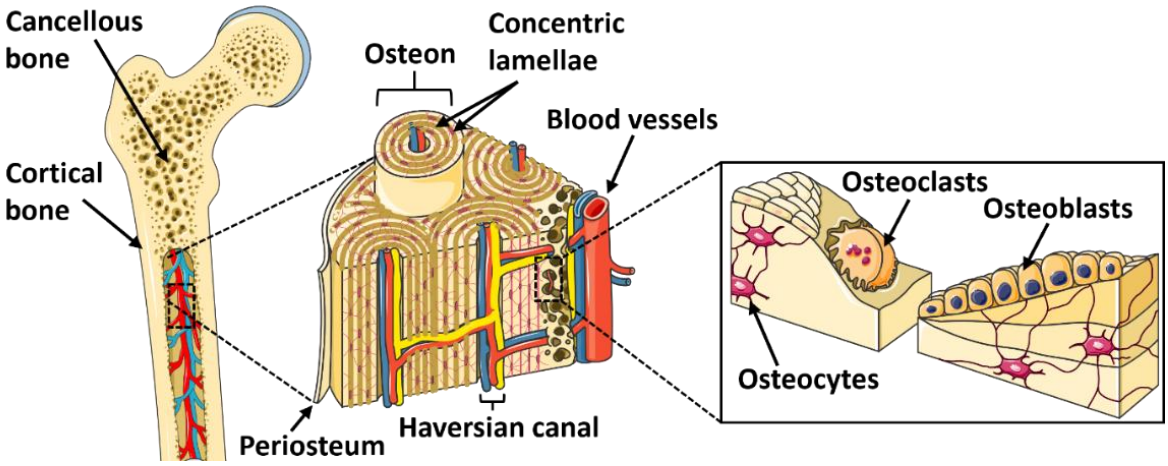

Figure 2.1. Hierarchical structure of bone tissue and associated cells. Schematic illustrating the structural organization of bone, from the structure of a long bone to the microarchitecture of cortical bone. Cancellous (trabecular) bone and cortical (compact) bone are shown, with emphasis on the osteon (Haversian system), including concentric lamellae and the central Haversian canal containing blood vessels and nerves. Osteocytes are shown within lacunae connected by canaliculi, and osteoblasts and osteoclasts are depicted at bone surfaces. This figure was created using Images provided by Servier Medical Art (https://smart.servier.com), licensed under CC BY 4.0 (https://creativecommons.org/licenses/by/4.0/).

2.2 Bone remodelling

Bone remodelling is a lifelong, highly coordinated physiological process that allows the skeleton to maintain structural integrity, adapt to changing mechanical demands, and preserve mineral homeostasis. Far from being a static tissue, bone undergoes continuous renewal through the balanced resorption of old or damage matrix and the formation of new bone. This dynamic turnover is essential for the repair of microcracks generated by daily mechanical loading and for preventing the accumulation of structural fatigue [39]. Remodelling occurs through the tightly coupled action of osteoclasts and osteoblasts within transient anatomical structures known as basic multicellular units (BMUs), which also include osteocytes and supporting stromal and vascular cells [3]. Under physiological conditions, the resorption and formation processes are balanced, resulting in the annual renewal of approximately 5% of cortical bone and 20% of trabecular bone. [40]. The remodelling cycle proceeds through sequential spatially and temporally regulated phases: activation, resorption, reversal and formation and mineralisation. Following activation mononuclear preosteoclasts are recruited to targeted bone surfaces, where they differentiate and fuse into multinucleated osteoclasts, under the control of osteoblast- and

osteocyte-derived factors, most notably receptor activator of nuclear factor-κB ligand (RANKL) and macrophage colony stimulating factor (M-CSF) [41]. During the resorption phase, osteoclasts attach to the mineralised matrix, create a sealed resorption compartment, and degrade both the organic and inorganic compartment of bone through acidification and proteolytic enzyme release [42, 43]. Completion of resorption triggers the reversal phase, during which osteoclasts undergo apoptosis or migrate, and mononuclear reversal cells prepare the eroded surface for new matrix deposition by removing debris and providing signals for osteoblast differentiation and migration [44]. The formation phase is then initiated, with osteoblasts depositing new matrix until the resorbed bone is completely replaced by new (**Figure 2.2**). The final stage of the remodelling cycle is mineralisation, during which the osteoid becomes progressively mineralised. Upon completion of mineralisation, osteoblasts either undergo apoptosis, become quiescent bone-lining cells, or are embedded within the matrix and terminally differentiate into osteocytes [45]. Osteocytes, residing within the bone matrix, play a central regulatory role throughout remodelling by sensing mechanical strain and orchestrating osteoclast and osteoblast activity though the secretion of signalling molecules such as sclerostin, RANKL, and osteoprotegerin (OPG) [4]. Effective bone remodelling therefore depends on the precise communication between bone cells via direct contact, paracrine signalling and growth factors released from the resorbed matrix. Disruption of this tightly regulated coupling leads to imbalances in bone turnover, resulting in bone diseases such as osteoporosis or osteopetrosis and impaired fracture healing [46].

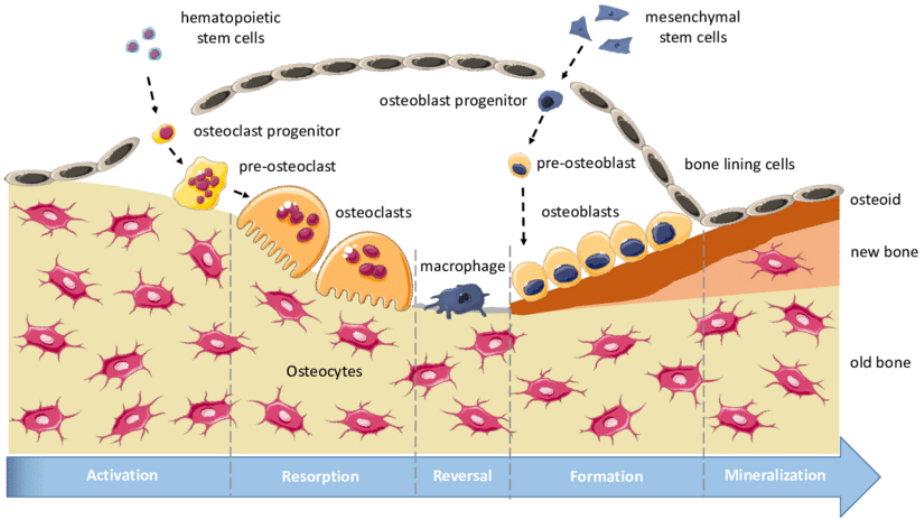

Figure 2.2. The remodelling cycle. The remodelling cycle consists of consecutive phases: activation, resorption, reversal, formation and mineralisation [47].

2.3 Bone cell types

2.3.1 Mesenchymal/Stromal stem cells: osteogenic progenitors

Mesenchymal stem/stromal cells (MSCs) are multipotent stromal cells primarily located in the bone marrow, periosteum, and endosteum, where they function as the principal progenitor population for osteoblasts during bone growth, remodelling and repair [48, 49]. MSCs are characterised by their capacity for self-renewal and multilineage differentiation into osteoblasts, adipocytes, and chondrocytes in response to specific biochemical, mechanical, and environmental cues [50, 51]. Osteogenic commitment of MSCs is regulated by a tightly coordinated network of transcription factors, including runt-related transcription factor (RUNX2) and osterix and signalling pathways such as bone morphogenetic protein (BMP), Wnt/β-catenin, Hedgehog and Notch signalling [52]. BMP signalling promotes osteogenic differentiation by inducing RUNX2 expression [53], while canonical Wnt/β-catenin signalling plays a central role in MSCs fate determination by promoting osteoblast differentiation while suppressing adipogenesis, a balance that is critical for maintaining skeletal integrity, particularly with aging [54]. Mechanical stimuli further influence MSCs lineage commitment by altering cytoskeletal organisation and focal adhesion signalling, thereby coupling mechanical loading to bone formation [55]. Beyond their differentiation potential, MSCs secrete paracrine factors that regulate osteoblast and osteoclast activity, angiogenesis, and immune modulation, thereby contributing to the

regulation of the bone remodelling and regeneration [56-58]. Age-related shifts in MSCs differentiation toward adipogenesis, along with reduced osteogenic potential, have been implicated in osteoporosis and impaired bone regeneration, underscoring the critical role of MSCs in maintaining skeletal health [59].

2.3.2 Osteoblasts: the bone forming cells

Osteoblasts are cuboidal-shaped cells arranged in a single layer along bone surfaces, where they have traditionally been regarded as the primary cell type responsible for the synthesis of the organic components of the bone matrix and its subsequent mineralization [60]. These cells originate from MSCs residing in the stromal compartment of the bone marrow, which provide a renewable pool of osteogenic progenitors for bone growth, modelling, and remodelling [61]. Osteoblast lineage commitment is governed by a tightly regulated transcriptional program involving RUNX2 and osterix and which together drive the differentiation of progenitors into proliferating pre-osteoblasts and subsequently into mature, matrix-producing osteoblasts [62]. RUNX2 regulates the expression of key osteoblast-associated genes, including type I collagen (Col1), alkaline phosphatase (ALP), osteocalcin (OCN), bone sialoprotein (BSP), osteonectin (ON), osteopontin (OPN), vascular endothelial growth factor (VEGF), and RANKL, thereby coordinating both matrix synthesis and osteoblast-osteoclast coupling [63, 64]. Mature osteoblasts are characterized by high biosynthetic activity, reflected by a dense endoplasmic reticulum, and by extensive intercellular contacts with neighbouring osteoblasts, osteocytes, and bone-lining cells, which support coordinated bone formation across active surfaces [65]. Bone formation by osteoblasts occurs through two main phases: deposition of osteoid and matrix mineralization. During osteoid formation, osteoblasts secrete a collagen-rich extracellular matrix composed predominantly of Col1 together with non-collagenous proteins such as OCN, BSP, OPN, proteoglycans, and ALP [66]. Mineralization is subsequently initiated through the release of osteoblast-derived matrix vesicles that concentrate calcium and phosphate ions [67]. ALP plays a critical role by hydrolysing phosphate-containing compounds and increasing local phosphate availability, thereby promoting hydroxyapatite crystal nucleation and growth [68]. The correct proportion of organic matrix to mineral is essential to achieve the appropriate balance between stiffness and flexibility of the skeleton [69]. Osteoblast differentiation and function are further regulated by multiple signalling

pathways, including BMP and canonical Wnt/β-catenin signalling, which promote osteoblastogenesis while suppressing adipogenic differentiation. Canonical Wnt signalling is also closely linked to the anabolic effects of parathyroid hormone (PTH), as PTH receptor activation stabilizes β-catenin and prevents osteoblast and osteocyte apoptosis, whereas inhibition of Wnt signalling by antagonists such as Dickkopf-1 (DKK1) or sclerostin blunts PTH-mediated bone formation [70]. In human bone physiology, osteoblasts participate in two distinct modes of osteogenesis: static and dynamic osteogenesis. Static osteogenesis occurs during skeletal growth and intramembranous ossification, where stationary, pluristratified osteoblasts generate primary trabeculae independently of mechanical loading. These osteoblasts differentiate into osteocytes at the site of origin and are later subject to osteoclast-mediated resorption. In contrast, dynamic osteogenesis is responsible for thickening existing trabeculae and refilling resorption lacunae during bone remodelling in the adult skeleton. In this context, osteoblasts are arranged in an epithelial-like monolayer, polarized in the same direction, and maintain contact with osteocytic dendrites as they migrate from the mineralization front toward the vascular surface, thereby coupling mechanical and metabolic demands to bone formation [71].

Beyond their role in osteogenesis, osteoblasts play a central role in regulating osteoclast differentiation and activity. Immature osteoblasts express high levels of RANKL and support osteoclastogenesis, whereas more mature osteoblasts progressively reduce RANKL expression and secrete increasing amounts of OPG, a soluble decoy receptor that inhibits RANKL-mediated osteoclast formation [72]. Osteoblasts are considered a major source of OPG in cancellous bone, acting in concert with osteocytes to locally modulate the RANKL/OPG ratio and ensure the timely transition from bone resorption to bone formation, thereby protecting newly formed bone from premature resorption [73]. Osteoblasts also regulate osteoclast precursor recruitment through the secretion of chemotactic factors, including OCN , collagen-derived peptides, and monocyte chemoattractant protein-1 (MCP-1), further reinforcing the tight coupling between resorption and formation within the basic multicellular unit [74, 75].

The average lifespan of an active osteoblast is approximately three months [76], after which cells undergo one of three fates. The majority (60-80%) undergo apoptosis [77], a process regulated by Wnt signalling, mechanical stimulation, PTH, sex steroids, and

intracellular survival pathways involving B-cell lymphoma-2 (Bcl-2) family members [78, 79]. Apoptosis plays a key role in controlling the duration and extent of bone formation and is a major determinant of bone mass [80]. A smaller fraction of osteoblasts differentiates into quiescent bone-lining cells that cover inactive bone surfaces, while approximately 5-20% become embedded within the mineralized matrix and undergo the active process of osteocytogenesis [81]. The differentiation of osteoblasts into osteocytes at the end of the remodelling cycle is essential for restoring mechanical competence and maintaining long-term skeletal homeostasis.

2.3.3 Osteoclasts: the bone resorbing cells

Osteoclasts are multinucleated giant cells that originate from the fusion of mononuclear hematopoietic precursors of the monocyte/macrophage lineage and represent the only cell type capable of resorbing mineralised bone matrix [82]. Osteoclastogenesis occurs within the bone marrow and is initiated by the coordinated action of M-CSF and RANKL. M-CSF is essential for the survival and proliferation of early osteoclast precursors and induces expression of the RANK receptor, thereby conferring responsiveness to RANKL [83, 84]. The critical physiological role of M-CSF signalling is underscored by the osteopetrotic phenotype observed in op/op mice, which arises from defective M-CSF expression and impaired osteoclast development [85]. RANKL binding to RANK triggers the recruitment of tumour necrosis factor receptor-associated factor (TRAF) family proteins and the activation of downstream pathways including nuclear factor kappa B (NF-κB) and c-Fos, ultimately inducing nuclear factor of activated T cells c1 (NFATc1) [86]. NFATc1 acts as a master transcriptional regulator of terminal osteoclast differentiation and drives the expression of osteoclast-specific genes such as tartrate-resistant acid phosphatase (TRAP), cathepsin K (CTSK), and fusion-related proteins including dendritic cell-specific transmembrane protein (DC-STAMP) [87, 88]. Osteoclast formation and activity are tightly regulated by OPG, a soluble decoy receptor produced by osteoblast lineage cells and other stromal precursors, which competes with RANK for RANKL and thereby modulates the extent of osteoclastogenesis. The RANKL/OPG ratio is therefore a key determinant of resorption rate in both physiology and disease [89]. *In vivo*, osteoclast differentiation is accompanied by the directed migration of precursors toward the bone surface, a process guided by both physical cues, such as collagenous matrices, and biochemical gradients. Efficient

recruitment and movement of osteoclasts through cellular and extracellular matrix barriers require dynamic cytoskeletal reorganisation and matrix degradation. Recent studies have identified a collagenolytic system involving metalloproteinase (MMP), notably the MMP9/MMP14 axis, that facilitates osteoclast invasion and contributes to both physiological bone resorption and pathological bone loss *in vivo* [90].

Once mature osteoclasts reach the resorptive surface, osteoclast activation requires adhesion to the mineralised matrix through integrin αvβ3, central to osteoclast/bone recognition [91], followed by cell polarisation and the organisation of specialised membrane domains that define the resorptive apparatus. Cytoskeletal remodelling drives the assembly of podosome-based structures into a mature actin ring that forms the sealing zone, thereby isolating the resorption lacuna from the surrounding extracellular environment. Disruption of this structure abolishes effective bone resorption, underscoring its functional necessity [82]. Polarisation is accompanied by development of the ruffled border membrane, which supports targeted delivery of acid and proteolytic enzymes into the sealed compartment. Bone mineral is dissolved by acidification through vacuolar-type proton pumps, while the organic matrix is degraded primarily by lysosomal and matrix-degrading enzymes such as CTSK, TRAP and MMP [92-94]. Degradation products, including collagen fragments and mineral ions, are endocytosed and transcytosed across the cell for release, enabling osteoclasts to maintain stable attachment during active resorption [95]. Following completion of the resorption phase, osteoclasts undergo apoptosis, facilitating their removal from the bone surface and allowing progression to the bone formation stage of the remodelling cycle [96].

2.3.4 Osteocytes: the master orchestrators of bone remodelling

Osteocytes are terminally differentiated osteoblast-lineage cells that become embedded within the mineralized matrix during bone formation and persist as a relatively permanent cellular phenotype. Frost estimated the intrinsic lifespan of osteocytes in humans to be around 25 years [97], highlighting their long-lived contribution to skeletal homeostasis. In the adult skeleton, osteocytes represent >90% of all bone cells and are organized as a stellate cell body housed within lacunae and connected to the surrounding tissue through numerous slender dendritic processes extending within canaliculi, thereby forming the lacunar-canalicular system (LCS) [81]. These processes reach both the cortical compartment

and surfaces adjacent to marrow in trabecular bone, enabling direct physical interaction with other bone cells (osteoblasts, osteoclasts, and bone lining cells) and with stromal elements at the bone-marrow interface. In addition to direct cell-to-cell contacts, osteocytes communicate via paracrine signalling, as the flow of bone extracellular fluid within the LCS facilitates transport of osteocyte-derived soluble mediators to target cells on bone surfaces [98]. Quantitative analyses of the human osteocyte network further emphasize the scale of this communication system: osteocytes form a vast 3D protoplasmic syncytium with tens of trillions of intercellular connections, providing an efficient anatomical substrate for integrating mechanical and metabolic information across the skeleton [99].

Osteocytes are recognized as master regulators of bone remodelling through their ability to coordinate both bone formation and resorption. Regulation of osteoblast activity is largely mediated through control of the Wnt/β-catenin signalling pathway, one of the principal anabolic pathways in bone [100]. Osteocytes can also inhibit bone formation through secretion of Wnt antagonists, most notably sclerostin (encoded by the SOST gene) and DKK1 [101]. Sclerostin is produced almost exclusively by osteocytes, and its functional importance is underscored by genetic studies demonstrating that SOST-deficient mice exhibit markedly increased bone formation, bone mass, and bone strength, whereas sclerostin overexpression suppresses bone formation and reduces skeletal integrity [102]. In parallel, osteocytes exert critical control over bone resorption. Although RANKL is expressed by several cell types, osteocyte-derived RANKL has been shown to be essential for physiological bone remodelling. Conditional deletion of RANKL in osteocytes results in a severe osteopetrotic phenotype characterized by a profound reduction in osteoclast number, demonstrating that osteocytes are a major local source of osteoclastogenic signals in adult bone [103]. Because osteocytes produce both RANKL and its decoy receptor OPG, they are uniquely positioned to dynamically adjust the local RANKL/OPG ratio in response to mechanical, metabolic, and endocrine cues, thereby fine-tuning the timing, rate, and magnitude of bone remodelling.

2.4 The role of mechanical loading in bone physiology

The ability of bone to adapt its mass, architecture, and mechanical competence in response to functional demands is a fundamental biological principle described by Wolff's law, which states that bone structure is continuously optimized to resist habitual mechanical loading [104]. *In vivo*, normal physiological activity causes deformation of the bone matrix, creating a complex mechanical environment where bone cells are exposed to physical forces including matrix strain, fluid shear stress, hydrostatic pressure, and streaming potentials, which arise concurrently during daily activities such as walking, standing, and muscle contraction [105]. Mechanical loading induces site-specific modelling and remodelling, whereby increased strain stimulates bone formation, while reduced mechanical input, such as immobilization, aging, or microgravity, leads to accelerated bone resorption and loss of bone mass and quality [106, 107]. Although whole-bone strains generated during habitual loading are relatively small, typically in the range of 2000-3500 microstrain, these signals are amplified at the cellular level by the ultrastructural features of bone, particularly the LCS, resulting in substantial mechanical stimulation of embedded osteocytes [108, 109].

Dynamic loading drives oscillatory interstitial fluid flow through the LCS, generating fluid shear stresses (FSS) on osteocyte membranes estimated to be in the range of 0.8-3 Pa, which is considered a primary mechanical stimulus for osteocytes *in vivo* [110-112]. Osteocytes are considered the most mechanosensitive cells in bone and play a central role in translating mechanical cues into biochemical signals that govern bone adaptation. They sense FSS through multiple mechanosensory structures, including integrins at focal adhesion complexes [113], which transmit forces to the cytoskeleton, connexin-based gap junctions and hemichannels, particularly connexin 43 (Cx43), which open in response to shear stress [114], primary cilia, which function as flow-sensitive organelles [115, 116], and mechanosensitive ion channels, notably Piezo1, which mediates mechanically induced calcium influx [117]. Activation of these mechanosensors triggers intracellular signalling cascades characterized by rapid calcium influx, cytoskeletal reorganization, anti-apoptotic signals, and activation of downstream pathways such as ERK1/2, and Wnt/β-catenin signalling [118-120]. In addition, the transcriptional co-activators Yes-associated protein (YAP) and transcriptional coactivator with PDZ-binding motif (TAZ) have emerged as central regulators of mechanotransduction downstream of integrin engagement and actomyosin

cytoskeletal tension. Their activity is tightly controlled by the Hippo signalling pathway, in which core kinases such as MST1/2 and LATS1/2 phosphorylate YAP/TAZ, leading to cytoplasmic retention and degradation under low mechanical stimulation. In contrast, mechanical loading, increased substrate stiffness, and fluid shear stress inhibit Hippo pathway activity and promote actin polymerization, resulting in YAP/TAZ dephosphorylation and translocation into the nucleus [121-123]. Once in the nucleus, YAP/TAZ associate primarily with TEAD transcription factors to regulate genes involved in cell survival, proliferation, and differentiation, including CTGF and CYR61. In bone cells, YAP/TAZ signalling has been shown to promote osteogenic differentiation of mesenchymal stem cells and osteoblast-lineage cells, while suppressing adipogenic fate, thereby contributing to lineage commitment under mechanical cues [124, 125]. In osteocytes, emerging evidence indicates that YAP/TAZ respond to fluid shear stress and cytoskeletal strain, integrating signals from focal adhesions and the actin network to modulate mechanoresponsive gene expression [126, 127]. Furthermore, YAP/TAZ interact functionally with other key mechanotransduction pathways, particularly Wnt/β-catenin signalling, through shared regulation of transcriptional programs and modulation of β-catenin activity, indicating coordinated control of gene expression in response to mechanical cues [128-130]. Through these pathways, osteocytes modulate the expression of key regulatory molecules, including RANKL, nitric oxide (NO) , prostaglandins, and Wnt pathway modulators [131, 132], thereby coupling mechanical cues to osteoblast and osteoclast activity.

Within the bone marrow niche, MSCs are predominantly exposed to fluid shear stress under physiological conditions, and mechanical cues have been shown to influence MSCs proliferation and lineage allocation, promoting osteogenic differentiation while suppressing adipogenesis through mechanosensitive pathways, thereby expanding the osteoprogenitor pool and limiting osteoclast recruitment [133-135]. Osteoblasts respond to physiological tensile strain, compression, and fluid shear stress with increased matrix synthesis and mineralization, while simultaneously modulating bone resorption through decreased expression of RANKL and increased OPG, leading to suppression of osteoclastogenesis [136, 137].

Insights into these mechanisms have been derived from *in vivo* loading and unloading models, including axial and bending loading of long bones [138, 139], vibration-based low-

magnitude mechanical stimulation [140], and hind-limb unloading [141], as well as from *in vitro* systems such as parallel plate flow chambers [142], substrate strain devices [143], and 3D perfusion bioreactors [144], which allow controlled interrogation of individual biophysical stimuli despite often requiring supraphysiological strain magnitudes. Collectively, these findings demonstrate that bone remodelling is governed by the integration of physiologically relevant mechanical forces across multiple spatial and temporal scales, with osteocytes serving as central regulators that translate complex mechanical inputs into coordinated anabolic and catabolic responses essential for maintaining skeletal integrity.

2.5 Bone pathologies and current treatment modalities

2.5.1 Osteoporosis: pathophysiology and current treatments

Bone remodelling requires a finely tuned interplay between osteoblast-mediated bone formation and osteoclast-mediated bone resorption. When this equilibrium is chronically shifted toward excessive resorption, with osteoclast activity surpassing osteoblast function, progressive bone loss ensues and culminates in debilitating bone pathologies such as osteoporosis. Osteoporosis is a chronic systemic skeletal disorder characterised by reduced bone mass, diminished bone mineral density, and deterioration of micro-architectural integrity, which collectively increase bone fragility and fracture risk [145]. As bone loss occurs gradually and asymptomatically until a fracture develops, osteoporosis is commonly described as a silent disease. The condition disproportionately affects women and represents a major global public health burden, with an estimated worldwide prevalence of 18.3% in the general population, increasing to 23.1% among women compared with 11.7% among men [5].

Based on the underlying mechanisms affecting bone metabolism, osteoporosis is broadly classified into primary and secondary osteoporosis. Primary osteoporosis is the most prevalent and comprises postmenopausal osteoporosis (type I), driven by oestrogen deficiency and predominantly affecting trabecular bone, and senile osteoporosis (type II), which reflects age-related bone loss involving both cortical and trabecular bone [146-148]. In contrast, secondary osteoporosis develops as a consequence of underlying medical conditions or external influences that interfere with normal bone turnover, including

chronic inflammatory diseases, malignancies, chronic kidney disease, and prolonged immobilisation [149].

Current therapeutic strategies for osteoporosis aim to either suppress excessive bone resorption with antiresorptive agents or enhance bone formation with osteoanabolic therapies. Antiresorptive drugs, including bisphosphonates (BP) and denosumab, reduce osteoclast-mediated bone resorption. BP have been the cornerstone of osteoporosis management owing to their efficacy, availability, and cost effectiveness. They have a high affinity for hydroxyapatite and are preferentially internalised by mature osteoclasts at sites of active bone resorption. Nitrogen-containing BP interfere with key intracellular pathways required for osteoclast function, leading to impaired cytoskeletal organisation, disruption of the ruffled border, and altered vesicular trafficking, ultimately promoting osteoclast apoptosis and resulting in a marked reduction in bone resorptive activity. Optimal duration of treatment remains a subject of debate owing to their prolonged skeletal retention and the rare but serious adverse events associated with long-term use, including osteonecrosis of the jaw (ONJ) and atypical femoral fractures (AFF) [7, 150]. Denosumab is a human monoclonal antibody that inhibits bone resorption by selectively binding to RANKL. Through its high affinity and specificity for RANKL, denosumab suppresses osteoclast differentiation, activity, and survival. Unlike BP, which primarily affect mature resorbing osteoclasts, denosumab inhibits osteoclasts across all stages of development, including precursor and multinucleated cells, thereby achieving more uniform suppression of bone resorption [151, 152].

In contrast, osteoanabolic therapies include PTH analogues and anti-sclerostin antibodies. Intermittent exposure to PTH directly stimulates osteoblasts and osteocytes, promotes MSC differentiation into osteoblasts, enhances osteoblast activity, and prolongs osteoblast lifespan, resulting in increased remodelling-based bone formation, improved bone mineral density (BMD), and reduced fracture risk in high-risk populations [153, 154]. In addition, anti-sclerostin antibodies exert a dual mechanism by strongly stimulating bone formation through activation of the canonical Wnt/β-catenin signalling pathway while concurrently reducing bone resorption, leading to rapid and substantial gains in BMD [155]. Nevertheless, osteoanabolic agents are typically limited by treatment duration recommendations and potential side effects (e.g., hypercalcaemia with PTH analogues and

cardiovascular safety concerns with anti-sclerostin antibodies), and fractures may recur without subsequent antiresorptive consolidation [8, 156].

Beyond pharmacological interventions, physical exercise plays a critical role in osteoporosis prevention and treatment. Weight-bearing, resistance, and impact exercises have been shown to stimulate bone formation, attenuate age-related bone loss, improve muscle strength, enhance balance, and reduce fall risk, thus complementing medical treatment and contributing to fracture prevention. Mechanical loading induces osteogenic responses through osteocyte mechanotransduction and promotes osteoblast differentiation, while also improving postural stability and functional outcomes in older adults [9, 157]. Despite these benefits, exercise alone has limited capacity to reverse established osteoporosis and is best used as part of a multimodal strategy with pharmacological therapies. The limitations of current treatments and the substantial residual fracture risk in many patients underscore the need for the development of novel therapeutic approaches that provide stronger anabolic effects, improved safety profiles, and more durable fracture protection.

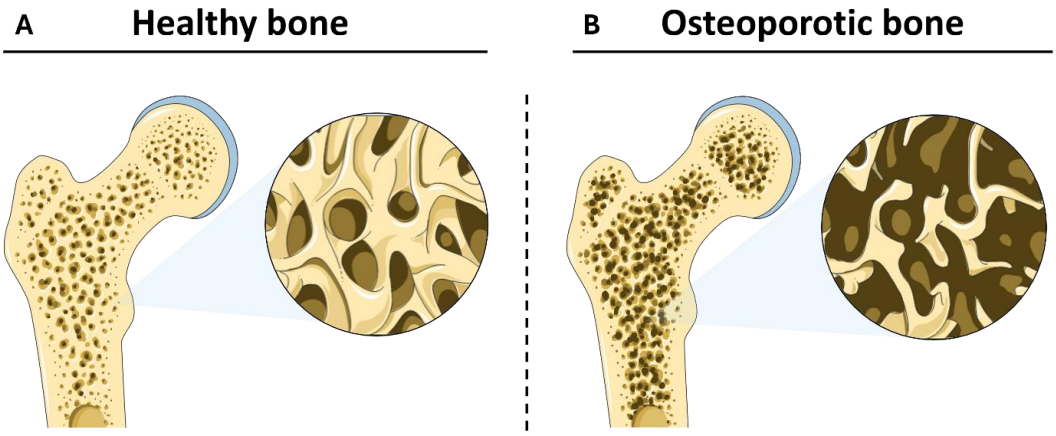

Figure 2.3. Comparison between healthy bone and osteoporotic bone. **(A)** Healthy bone characterised by thick, well-connected trabeculae forming a dense internal network. **(B)** Osteoporotic bone marked by reduced bone mass, thinner trabeculae, increased porosity, and loss of structural connectivity. This figure was created using Images provided by Servier Medical Art (https://smart.servier.com), licensed under CC BY 4.0 (https://creativecommons.org/licenses/by/4.0/).

2.5.2 Osteoporotic fractures

Fragility fractures are the most severe clinical consequence of osteoporosis and arise from low-energy trauma, such as a fall from standing height or less, that would not ordinarily result in fracture in healthy bone. As such, a fragility fracture represents both a sign and a symptom of underlying osteoporosis. These fractures constitute a major global public health problem, with one fragility fracture estimated to occur every 3 seconds worldwide, and are associated with substantial morbidity, mortality, prolonged immobility, and loss of independence in older adults [158, 159].

Fracture healing is a highly regulated regenerative process that proceeds through overlapping phases of inflammation, repair, and remodelling [160]. Following injury, an initial inflammatory response recruits immune cells and progenitor cells to the fracture site and initiates angiogenesis. This is followed by formation of a soft cartilaginous callus that stabilises the fracture, which is subsequently resorbed by osteoclasts replaced by mineralised woven bone during the reparative phase. Finally, the callus undergoes remodelling, during which woven bone is gradually replaced by lamellar bone and the original bone architecture and mechanical strength are restored. Successful fracture healing requires coordinated interactions between osteoclasts, osteoblasts, MSCs, endothelial cells, and the local mechanical environment [161].

In osteoporosis, this finely tuned repair process is fundamentally disrupted. Reduced bone mass, deteriorated microarchitecture, and compromised mechanical stability at the fracture site contribute to delayed healing, increased non-union rates, and inferior mechanical properties of newly formed bone [162, 163]. At the cellular level, osteoporotic bone is characterised by impaired osteogenic differentiation of MSCs, reduced osteoblast number and activity, excessive osteoclast-mediated bone resorption, and diminished angiogenesis, all of which interfere with the normal progression from inflammation to callus formation and remodelling [164-166]. These impairments are further exacerbated by prolonged immobilisation following fracture, which accelerates secondary bone loss and perpetuates a vicious cycle of skeletal deterioration and delayed repair [167]. These challenges highlight that osteoporotic fractures should not be regarded as isolated mechanical injuries, but rather as manifestations of systemic skeletal disease occurring within a biologically compromised healing environment.

Clinical management of fractures and bone defects in osteoporotic patients therefore remains challenging. Although mechanical stabilisation is essential, fixation in osteoporotic bone is limited by low bone density, cortical thinning, and reduced implant anchorage, increasing the risk of loosening, loss of reduction, and mechanical failure [168, 169]. Bone grafting is considered the golden standard for restoring structural integrity and fill bone defects. However, autologous grafting is limited by donor-site morbidity and reduced availability in elderly patients, while allografts and synthetic substitutes typically lack sufficient biological activity to actively stimulate osteogenesis in osteoporotic environments [170]. Pharmacological optimisation of bone metabolism is increasingly recognised as an important adjunct to surgical management. Antiresorptive therapies may help stabilise bone mass and reduce further structural deterioration, whereas osteoanabolic agents can enhance osteoblast activity and bone formation, thereby supporting fracture healing and defect repair [171, 172]. Adjunctive biophysical modalities, including low-intensity pulsed ultrasound, may further augment local biological responses and improve healing outcomes in selected cases. [173]. Emerging therapeutic approaches increasingly focus on correcting the underlying biological deficits characteristic of osteoporotic fractures. These include biologic strategies such as BMPs [174], MSC-based therapies [175], gene therapy targeting osteogenic pathways [176], advanced biomaterial scaffolds designed to provide mechanical support while locally delivering osteoinductive and angiogenic cues [177]. Collectively, these challenges underscore the need for integrated therapeutic strategies that simultaneously address systemic bone loss, local bone defects, and impaired fracture healing.

2.6 Extracellular Vesicles

Extracellular vesicles (EVs) are lipid-bound particles ranging from nanometre to micrometre scale that are released by cells in the extracellular space. They transport a diverse cargo of biomolecules, including lipids, proteins, nucleic acids (DNA, mRNA, miRNA), and metabolites, and play a crucial role in intercellular communication [178]. EVs are broadly classified into subtypes based on their biogenesis and size. Exosomes are a subtype of small EVs with a diameter ranging from 50 to 200 nm. They originate from the endosomal system through the inward budding of endosomal membranes, forming multivesicular bodies (MVBs), and are subsequently released upon MVBs fusion with the plasma membrane.

Microvesicles, or ectosomes, typically range from 50 nm to 1 µm and are formed by outward budding and fission of the plasma membrane [179]. Other subtypes include apoptotic bodies (50 nm - 5 µm), released during programmed cell death and migrasomes, derived from retraction fibres of migrating cells (500 nm - 3 µm) [180, 181] (**Figure 2.4**). However, these classifications have since been superseded by the terms small EVs (sEVs, <200 nm) and large EVs (lEVs, >200 nm) [182]. The composition and quantity of biomolecular cargo contained within EVs are highly dependent on the originating cell type and are frequently shaped by the donor cell's physiological or pathological state, external stimuli that regulate EV production and release, and the molecular pathways governing their biogenesis [183]. In addition, EVs carry membrane proteins, including both transmembrane and membrane associated cargos, which specify or inhibit their interactions with targets cells. Adhesion molecules such as integrins and intercellular adhesion molecules play a pivotal role in EV targeting, uptake and downstream signalling [184, 185]. Other membrane-associated proteins, such as the leukocyte surface antigen CD47, function as "don't eat me" signals that inhibit macrophage phagocytosis, thereby prolonging the circulation time of EVs and enhancing their probability of reaching target cells [186]. Tetraspanins such as CD9, CD63, and CD81 are among the most consistently enriched membrane proteins on small EVs and are widely used as reference markers for EVs characterization. In accordance with the MISEV2023 guidelines established by the International Society for Extracellular Vesicles, these markers should be complemented by cytosolic proteins associated with EVs biogenesis, including ALIX and TSG101, which are linked to the endosomal sorting complex required for transport (ESCRT) pathway. Importantly, MISEV2023 emphasizes that no single marker is sufficient to define EVs and recommends a multiparametric characterization strategy incorporating positive and negative markers to ensure robustness and reproducibility [178].

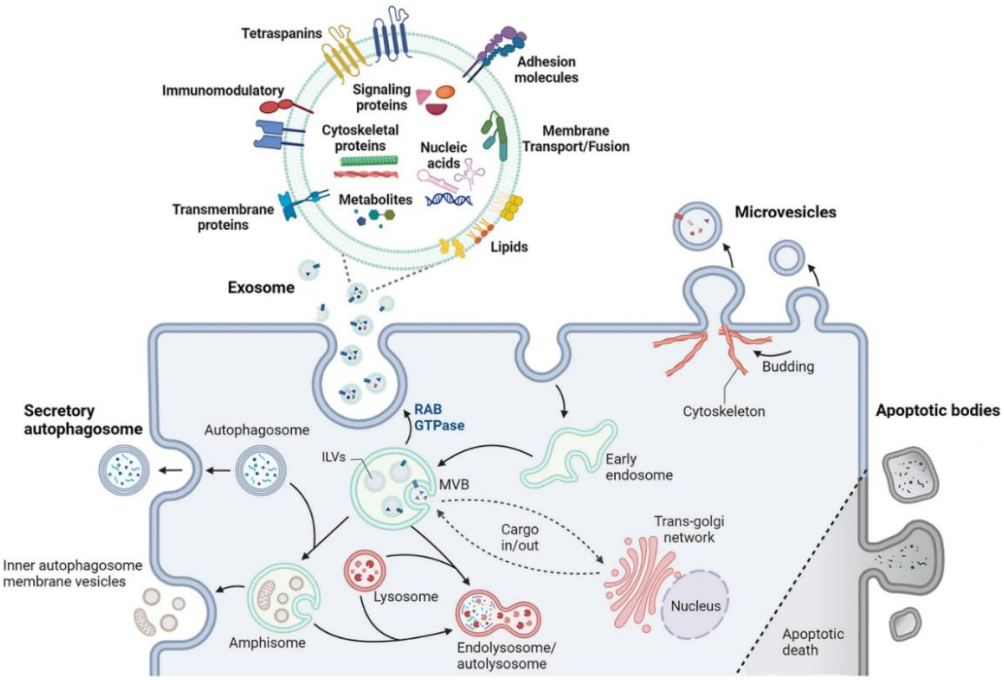

Figure 2.4. EVs classification based on biogenesis. Extracellular vesicles (EVs) are generated via distinct pathways: exosomes form within multivesicular bodies and are released upon fusion with the plasma membrane, while microvesicles bud directly from the cell surface. Additional EVs subtypes include apoptotic bodies, migrasomes. Adapted from [187].

2.6.1 Bone cell-derived EVs and their role in bone remodelling and regeneration

EVs are widely recognised as integral regulators of bone remodelling, repair, and regeneration. Acting as nanoscale conveyors of bioactive cargo, EVs coordinate signalling among osteoblasts, osteocytes, osteoclasts, and MSCs, thereby adding an important regulatory layer to classical soluble and contact-dependent mechanisms of bone homeostasis [16]. This mode of intercellular communication is particularly critical during bone repair and regeneration, where tightly controlled temporal and spatial coordination of inflammation, angiogenesis, osteogenesis, and resorption is required.

Within this framework, MSC-derived EVs have been the most extensively investigated and are increasingly regarded as a promising cell-free alternative to MSC transplantation. A growing body of preclinical evidence demonstrates that MSC-EVs enhance bone healing by stimulating angiogenesis, modulating immune responses, and promoting osteogenic differentiation of resident progenitor cells [188-190]. For example, systemic administration of MSC-derived exosomes has been shown to accelerate fracture healing *in vivo*,

accompanied by increased expression of angiogenic and osteogenic markers [191]. Subsequent studies confirmed that MSC-EVs enhance vascularization and osteogenic marker expression *in vivo*, highlighting the importance of EV-mediated coupling between angiogenesis and bone formation [192].

Beyond MSC-EVs, EVs released by differentiated bone cells contribute directly to coupling signals that regulate the balance between bone formation and resorption. Osteoblast-derived EVs influence the behaviour of neighbouring osteoprogenitors and osteoclasts through tightly regulated stage-specific cargo release during osteogenic differentiation. Seminal *in vitro* studies have shown that exosomes produced by mineralising osteoblasts activate Wnt/β-catenin signalling in recipient stromal cells, leading to enhanced osteogenic gene expression [193]. Consistent with this, proteomic analyses have revealed that the molecular composition of osteoblast-derived EVs is dynamically regulated, supporting the concept that these vesicles mediate stage-specific signalling during bone formation and repair [194]. In addition to their anabolic functions, osteoblast-derived EVs also contribute to osteoblast-osteoclast coupling. Recent *in vivo* studies have provided direct evidence that these vesicles are actively released and taken up within the bone microenvironment, where they modulate both osteoblast activity and osteoclast formation under physiological conditions, reinforcing their role as dynamic regulators of bone remodelling rather than passive by-products of osteoblast function [195]. Consistent with this, *in vitro* studies have shown that osteoblast-derived EVs can differentially influence osteoclastogenesis: while some reports indicate enrichment of RANKL and a capacity to directly promote osteoclast differentiation [196], others describe inhibitory effects on osteoclast formation [197], highlighting a vesicle-based mechanism for coordinating bone resorption and formation.

Osteocyte-derived EVs further expand this regulatory network, reflecting the central role of osteocytes as mechanosensors and orchestrators of bone remodelling. Under normal physiological conditions, osteocytes release EVs into the LCS, providing a mechanism for local cell-cell communication within mineralized bone [198]. Through the transfer of signalling proteins and regulatory molecules that reflect the mechanosensory state of the parent cell, these EVs modulate osteoblast behaviour and bone formation. *In vitro,* EVs released from mechanically stimulated osteocytes have been shown to promote osteogenic differentiation of osteoblasts and MSCs and enhance angiogenic responses [18-20, 198].

Concurrently, osteocyte-derived EVs also participate in the regulation of bone resorption by modulating osteoclast differentiation and activity, thereby integrating mechanical cues with both anabolic and catabolic processes in bone [199].

Finally, EVs released by osteoclasts add another layer of complexity to intercellular communication during bone remodelling. Accumulating evidence indicates that osteoclast-derived EVs can transmit inhibitory signals to osteoblast-lineage cells, effectively linking active bone resorption to suppression of bone formation under certain physiological or pathological conditions [200]. However, osteoclast EVs are functionally heterogeneous, and distinct vesicle populations have also been shown to exert anabolic effects by promoting osteoblast differentiation. These findings emphasise the bidirectional and context-dependent nature of EV-mediated communication between resorptive and formative cells [201].

Collectively, current evidence supports a model in which EVs derived from MSCs, osteoblasts, osteocytes, and osteoclasts form an integrated intercellular communication network that regulates bone homeostasis and regeneration. By transferring regulatory cargo in a highly context-dependent manner, EVs coordinate angiogenesis, immunomodulation, and the coupling of bone formation and resorption. Elucidating the molecular mechanisms underlying EV cargo selection and target specificity will be critical for fully harnessing their therapeutic potential and for the development of next-generation EV-based strategies for bone repair and regeneration.

2.7 Matrix Vesicles

Matrix vesicles (MVs) are a specialised subclass of extracellular vesicles, typically 100-300 nm in diameter, that play a central role in the mineralisation of the organic extracellular matrix (ECM) during skeletal and dental development. They are released by multiple cell types, including hypertrophic chondrocytes, osteoblasts, odontoblasts, and potentially osteocytes [202]. MVs were independently discovered in the late 1960s by H. Clarke Anderson and Ermanno Bonucci through electron microscopy studies of epiphyseal cartilage, where membrane-bound vesicular structures containing early mineral deposits were visualised and associated with sites of initial calcification [203, 204]. These pioneering

studies represent some of the earliest descriptions of EVs and firmly established MVs as key initiators of biomineralisation.

MVs provide a specialised and highly regulated microenvironment optimised for mineral initiation. They are enriched in mineralisation-specific components, including phosphatases, calcium, and inorganic phosphate (P_i), which support the intraluminal crystallisation of calcium phosphate into hydroxyapatite [67]. A defining feature of MVs, distinguishing them from other EVs subtypes, is their strong and selective binding to collagen fibrils, which spatially constrains mineral deposition to appropriate matrix sites [205, 206]. This binding with matrix macromolecules underlies experimental isolation strategies, as MVs are recovered from mineralising tissues following collagenase digestion. However, the lack of unique MV-specific markers and their close embedding within collagen and proteoglycan networks pose significant challenges for their analysis and purification. Current isolation approaches primarily rely on tissue digestion followed by differential ultracentrifugation or discontinuous sucrose density gradient centrifugation. While collagenase-based methods yield vesicle populations with high mineralisation competence, proteolytic damage and purity concerns remain limitations, whereas density gradient approaches often produce more heterogeneous vesicle populations [207].

Mechanistically, the classical two-stage model of MV-mediated mineralisation remains widely accepted. In the initiation stage, MVs bud from specialised microdomains of the plasma membrane of mineralising cells. These vesicles function as enclosed microenvironments that promote the initial nucleation of apatite crystals. Within the MVs lumen, P_i is produced mainly by the enzyme PHOSPHO1, which hydrolyses phosphocholine and phosphoethanolamine produced by phospholipase activity. At the same time, calcium ions accumulate on the phosphatidylserine-rich inner leaflet of the MVs membrane, a process facilitated by annexin family proteins. Together, the local increase in P_i and calcium creates conditions favourable for early crystal formation [208]. In the propagation stage, the growing mineral crystals rupture the MVs membrane and extend into the surrounding collagen matrix. Mineral deposition then continues extracellularly, under ionic conditions tightly regulated by mineralising cells. This includes the hydrolysis of the mineralisation inhibitor pyrophosphate (PP_i) by tissue-nonspecific alkaline phosphatase (TNAP), which further promotes crystal growth within the matrix [209].

In addition to their physicochemical role in mineral initiation, MVs are increasingly recognised as signalling-competent vesicles that participate in cell-cell communication and bone remodelling. Similar to other EV subtypes, MVs carry transmembrane proteins such as CD9, CD63, and CD81 [210], as well as selective protein cargoes including annexins, MMPs, and BMPs that can influence recipient cell behaviour [211, 212]. In addition, accumulating evidence indicates that MVs transport regulatory miRNAs. Notably, MVs collected from the ECM deposited by osteoblasts cultured *in vitro* have been shown to be enriched in miR-125b, which accumulates in the bone matrix and inhibits osteoclastogenesis by downregulating PR domain zinc finger protein 1 (PRDM1) in osteoclast precursors, thereby suppressing bone resorption [213]. In parallel, experimental studies have demonstrated that MVs derived from osteoblast culture promote bone formation and repair *in vivo*. Delivery of MV-enriched fractions embedded into gelatin hydrogels significantly enhanced bone regeneration in a murine femoral defect model by stimulating osteoblastic bone formation, underscoring their therapeutic potential in bone repair and tissue engineering applications [214]. Moreover, MVs isolated from murine bones were shown to enhance bone formation and protect against osteoporosis [215]. Through these mechanisms, MVs contribute to the coupling of bone formation and resorption, extending their functional relevance well beyond mineral nucleation to the active regulation of bone remodelling. These findings align with broader evidence that EV-mediated signalling is an important regulator of bone remodelling and regeneration.

Finally, MV-like calcifying vesicles are not restricted to skeletal tissues but are also detected in soft tissues, linking MV biology to pathological mineralisation. Calcifying vascular smooth muscle cells release MV-like vesicles at sites of medial vascular calcification, where they can nucleate hydroxyapatite and induce calcification in neighbouring cells, suggesting an active, propagative process rather than passive mineral precipitation [216]. Thus, while MVs play essential physiological roles in bone formation, remodelling, and regeneration, dysregulated MV production or cargo composition may contribute to ectopic mineralisation in soft tissues such as the vasculature. Collectively, these features position MVs as multifunctional, mineralisation-competent vesicles with emerging relevance as both therapeutic agents and pathological mediators. Nevertheless,

despite being discovered in the 1960s, their multimodal activity and their classification as a distinct EV subpopulation have not been comprehensively investigated.

2.8 Extracellular Vesicles as therapeutics

EVs have gained considerable attention as cell-free therapeutics for bone regeneration, as they are widely recognized as key mediators of cell-cell signalling capable of delivering coordinated biomolecular cargo that can activate multiple, complementary repair pathways in recipient cells. These vesicles may be used in their native form to exploit their intrinsic regenerative properties or can be bioengineered as targeted drug delivery systems. Among potential sources, MSCs have emerged as the most promising for therapeutic EV production. Notably, transplantation of MSC-derived EVs has been shown to elicit regenerative outcomes comparable to those achieved with MSCs therapy itself, while circumventing many of the limitations associated with cell-based approaches. In this context, EVs exhibit intrinsic regenerative potential with a reduced risk of immunogenicity and tumorigenicity, as well as improved stability and extended shelf life relative to living cells. Consistent with these advantages, MSC-derived EVs have demonstrated therapeutic efficacy across a broad range of disease models, including respiratory [217], hepatic [218], renal [219], neurological [220] , cardiovascular [221], and musculoskeletal diseases [191, 222] .

In parallel, preclinical research in skeletal biology has expanded substantially, with more than forty *in vivo* studies reporting enhanced bone regeneration following EV treatment. These investigations have employed EVs derived from diverse sources, including bone marrow, adipose tissue, umbilical cord and Wharton's jelly, gingiva, synovium, endothelial and perivascular cells, induced pluripotent stem cell derivatives, as well as committed bone-resident cells. Across multiple animal models, such as calvarial critical-size defects, long-bone fractures, distraction osteogenesis, osteonecrosis, ovariectomy-induced osteoporosis, and radiation-associated bone loss, EVs administration has consistently resulted in improved bone volume, mineral density, mechanical strength, and fracture union [223].

Despite this robust preclinical evidence base, translation toward clinical application remains challenging. Key barriers include heterogeneity in EV isolation and purification strategies, inconsistent dosing metrics, limited standardization of cargo characterization,

and insufficient *in vivo* validation of mechanism-of-action, all of which complicate cross-study comparison and regulatory advancement. To address these challenges, Good Manufacturing Practice (GMP)-oriented production frameworks have been developed and experimentally validated, defining scalable and standardized pipelines for clinical-grade MSC-derived EVs that incorporate controlled donor selection, defined culture conditions, reproducible enrichment methods, and quality-controlled release criteria suitable for regulated testing [224]. Early clinical translation in skeletal applications is now emerging, with seven registered clinical trials evaluating the safety of EVs derived from stem cell and platelet sources for inflammatory musculoskeletal disorders, including osteoarthritis, periodontitis, lower back pain, and bone repair. Clinical outcomes reported to date remain limited, with three completed trials, one not yet recruiting, and three of unknown status (**Table 2.1**). Nevertheless, these studies represent an important transition from preclinical proof-of-concept toward regulated human evaluation and underscore the need for rigorous GMP-compliant manufacturing, harmonized reporting standards, and potency-linked mechanistic assays to establish EVs as scalable, reproducible and effective therapeutics for bone regeneration.

Table 2.1. Registered clinical trials (clinicaltrials.gov) related to therapy with extracellular vesicles in the field of musculoskeletal disease treatment.

Clinical trial identifier	Study title	Condition	Intervention	Status
NCT05520125	Treatment of Patients with Bone Tissue Defects Using Mesenchymal Stem Cells Enriched by Extracellular Vesicles	Segmental Fracture-Bone loss	MSCs enriched by EVs	Unknown
NCT05060107	Intra-articular Injection of MSC-derived Exosomes in Knee Osteoarthritis (ExoOA-1)	Osteoarthritis, knee	Exosome sEVs	Unknown
NCT04223622	Effects of ASC Secretome on Human Osteochondral Explants (ASC-OA)	Osteoarthritis	adipose stem cell (ASC) secretome	Completed

NCT04270006	Evaluation of Adipose Derived Stem Cells Exo.in Treatment of Periodontitis	Periodontitis	ASC-exosomes	Unknown
NCT04849429	Intra-discal Injection of Platelet-rich Plasma (PRP) Enriched with Exosomes in Chronic Low Back Pain	Chronic low back pain	PRP with exosomes	Completed
NCT04281901	Efficacy of Platelet- and Extracellular Vesicle-rich Plasma in Chronic Postsurgical Temporal Bone Inflammations	Otitis media chronic	Platelet- and EVs-rich plasma	Completed
NCT04998058	Autogenous Mesenchymal Stem Cell Culture-Derived Signalling Molecules as Enhancers of Bone Formation in Bone Grafting	Bone loss, osteoclastic and alveolar	Bone graft with concentrate ASC-CM	Not yet recruiting

2.9 Optimising the regenerative properties of EVs

Increasing evidence demonstrates that the regenerative efficacy of EVs is strongly influenced by the physiological state and microenvironment of the parent cell at the time of vesicle biogenesis. Beyond cell source and differentiation status, external conditioning cues can modulate EV molecular cargo, and downstream biological activity. Conditioning strategies exploit endogenous EV sorting mechanisms that selectively package proteins and nucleic acids in response to biochemical, biophysical, and environmental stimuli, enabling the generation of EVs with enhanced regenerative potency [17].

Biochemical and environmental preconditioning approaches have been widely explored in the context of bone repair. Hypoxic culture conditions consistently increase the angiogenic and osteogenic capacity of EVs, largely through activation of hypoxia-inducible factor-1α (HIF-1α) signalling and enrichment of pro-angiogenic miRNAs. Hypoxia-preconditioned MSCs-EVs have been shown to enhance fracture healing and vascularisation in multiple preclinical bone defect models, highlighting the critical coupling between angiogenesis and osteogenesis during bone repair. Pharmacological hypoxia mimetics, such as dimethyloxalylglycine (DMOG), similarly stabilise HIF-1α under normoxic conditions and

yield EVs that enhance angiogenesis and promote bone regeneration [225, 226]. In parallel, inflammatory priming using cytokines such as tumour necrosis factor-α (TNF-α) has been shown to enrich EVs cargo with osteoinductive proteins, including WNT3a, enhancing osteoblast proliferation, differentiation, and bone formation [227]. Similarly, Kang *et al.* reported enhanced bone formation following delivery of EVs derived from TNF-α-primed MSCs, an effect associated with increased oncostatin M expression and modulation of osteoimmune signalling [228]. These findings align with the physiological role of inflammatory signalling during early fracture healing and support inflammatory priming as a means of mimicking the post-injury bone microenvironment *in vitro*.

Mechanical and physical conditioning of parent cells represents an additional, highly relevant axis for EVs optimisation for bone regeneration. Bone cells are inherently mechanosensitive, and mechanical stimulation has been shown to regulate EV release and cargo composition. MSCs, osteocytes and osteoblasts subjected to oscillatory fluid shear stress or dynamic flow stimulation secrete EVs enriched in bone regulatory proteins and signalling molecules that enhance MSC recruitment, osteogenic differentiation, and angiogenesis. Such mechanically conditioned EVs recapitulate the mechanoresponsive nature of bone tissue and reinforce the concept that mechanical cues regulate not only cell behaviour but also EV-mediated intercellular communication [18, 19, 198, 229]. Complementary approaches, including scaffold-based culture, surface topography modulation, and magnetic nanoparticle stimulation, have further demonstrated the feasibility of engineering EVs cargo through controlled physical stimulation of the parent cell [230, 231]. Collectively, these conditioning strategies demonstrate that manipulation of the parent-cell environment via biochemical, hypoxic, and mechanical cues can yield EVs populations with enhanced therapeutic potential for bone regeneration.

2.10 Mechanism of action of EV-mediated bone regeneration

EVs play a key role in bone remodelling by delivering regulatory molecular cargo to cells in the bone microenvironment. Their regenerative effects arise from coordinated, context-dependent mechanisms that integrate osteogenesis, osteoclast-osteoblast coupling, angiogenesis, and immune modulation, rather than a single pathway. EVs carry a diverse repertoire of bioactive proteins, mRNAs, miRNAs, lipids, and surface-associated molecules

that collectively shape bone regeneration at multiple levels. EV-associated proteins include osteoinductive growth factors, signalling mediators, and matrix-interacting proteins that activate pathways implicated in bone formation, including Wnt/β-catenin, TGF-β/SMAD, and MAPK, thereby promoting osteoblast differentiation and coordinating osteoclast-osteoblast coupling [232-234]. Transferred mRNAs can be translated within recipient cells, amplifying local production of osteogenic and angiogenic factors [235]. In parallel, EV lipids regulate membrane signalling, and inflammation influencing both bone formation and resorption [236-238]. Finally, EV surface molecules (e.g., integrins, tetraspanins) contribute to cell-specific targeting and uptake, enabling spatially restricted signalling within the bone microenvironment and supporting bone remodelling [239, 240].

Recently, miRNAs have emerged as particularly important molecular effectors of EV-mediated bone regeneration. miRNAs are small non-coding single-stranded RNAs of approximately 19-25 nucleotides that suppress gene expression post-transcriptionally through sequence-specific targeting of mRNAs, resulting in translational repression or mRNA destabilisation. Their biogenesis involves sequential processing from primary transcripts to precursor and mature miRNAs, which are subsequently incorporated into the RNA-induced silencing complex (RISC) to mediate gene silencing [241]. Their ability to regulate numerous genes simultaneously makes miRNAs particularly attractive candidates for EV-based therapies.

Within the osteogenic compartment, EVs derived from osteoblast-lineage cells display dynamic remodelling of miRNA cargo that closely parallels stages of differentiation and matrix mineralisation. EVs released by osteoblasts during active mineralisation have been shown to promote osteogenic differentiation of stromal progenitors. These vesicles are enriched in miRNAs such as miR-667-3p, miR-6769b-5p, miR-7044-5p, miR-7668-3p, and miR-874-3p, which target Axin1, a negative regulator of canonical Wnt/β-catenin signalling [193]. Further insight into bone derived EVs heterogeneity has been gained through direct isolation of vesicles from bone tissue. Distinct MV subpopulations exhibit differential miRNA and protein cargo profiles that reflect specific functional roles. Larger MVs are enriched in early osteogenic miRNAs, including miR-15b-5p, miR-29a-3p, and miR-128-3p, which enhance alkaline phosphatase activity and early differentiation in stromal cells. In contrast, smaller MVs preferentially carry miR-125b alongside mineralisation-associated

proteins, promoting matrix maturation and mineral deposition in osteoblasts. These observations indicate that EVs subtype, cargo composition, and the differentiation state of the parent cell collectively shape osteogenic outcomes [242].

In addition to anabolic signalling, EV-mediated communication can also transmit inhibitory cues that suppress osteogenesis, particularly under ageing, inflammatory, or pathological conditions. EVs isolated from aged bone marrow environments are enriched in the miR-183 cluster, comprising miR-96, miR-182, and miR-183. Delivery of these miRNAs to young bone marrow stromal cells reduces cellular proliferation and osteogenic differentiation, linking age-associated oxidative stress signalling to impaired bone formation [243]. Similarly, disease-altered EVs can negatively impact osteogenesis. In inflammatory bone disorders, circulating EVs enriched in miR-23a and miR-30a suppress RUNX2- and SMAD1/5-dependent transcriptional programmes, resulting in impaired osteoblast differentiation and reduced trabecular bone mass *in vivo* [244].

EV-mediated coupling between bone resorption and formation further highlights the bidirectional nature of vesicle-based signalling in skeletal homeostasis. Osteoclast-derived exosomes enriched in miR-214-3p are selectively internalised by osteoblasts, where they inhibit bone formation. This mechanism provides a direct molecular link between active osteoclastic resorption and suppression of osteoblast function, contributing to coordinated regulation of bone turnover [200].

MSC-derived EVs represent another major regulatory axis in bone regeneration, with osteogenic potency strongly dependent on miRNA cargo composition. These EVs are enriched in osteogenesis-associated miRNAs such as miR-196a, miR-27a, and miR-206, with miR-196a emerging as a dominant mediator of osteogenic signalling. Functional inhibition of miR-196a markedly reduces the osteoinductive capacity of BMSC-derived EVs, providing direct evidence that EV-associated miRNAs are key drivers of their regenerative effects [188]. Complementary studies have shown that exosomal miR-151-5p can be transferred from exogenous BMSCs to endogenous progenitors, promoting osteogenic differentiation and rescuing osteopenia following systemic EVs administration [245]. Broad miRNA profiling further supports this paradigm, with MSCs-derived EVs enriched in miRNAs such as miR-148a-3p, miR-21, and miR-29b-3p, all of which have established roles in bone remodelling and osteogenic differentiation [246]. Beyond bone marrow sources, ASC-

derived EVs have also demonstrated therapeutic potential in skeletal disorders. These vesicles alleviate osteoporotic bone loss through combined delivery of OPG and miRNAs such as miR-21-5p and let-7b-5p, which simultaneously suppress osteoclast differentiation and enhance recruitment and osteogenic differentiation of bone marrow progenitors [247].

Finally, immune-cell-derived EVs provide an additional layer of regulation, linking inflammatory status to bone repair outcomes. Macrophage EVs exert phenotype-dependent effects on osteogenesis. EVs derived from pro-inflammatory M1 macrophages are enriched in miR-155 and suppress osteogenic differentiation by attenuating BMP2, BMP9, and RUNX2 signalling pathways. In contrast, EVs from anti-inflammatory M2 macrophages are enriched in miR-378a and enhance osteogenic gene expression, leading to improved bone regeneration in defect models. These findings underscore the importance of immune-derived EVs in osteoimmunological regulation of bone healing [248].

Together, these findings show that EV-driven bone regeneration depends on coordinated, cargo-specific signalling between multiple cell types, including osteoblast-lineage cells, stromal progenitors, osteoclasts, and immune cells within the bone microenvironment. EV-associated miRNAs act as key regulators in this system, where they can stimulate bone formation, convey inhibitory signals linked to ageing or disease, and balance bone formation with resorption. This understanding provides a clear biological basis for developing EV-based therapies that enhance bone repair by selectively modulating their miRNA cargo.

2.11 High throughput production of EVs

Despite the considerable therapeutic potential of EVs, their clinical translation is hindered by the limited intrinsic secretion capacity of cells and the absence of standardized, scalable manufacturing processes. Consequently, extensive research efforts have focused on developing approaches to increase EV yield while preserving their biological integrity and functionality. These approaches can be broadly classified into three categories: (i) scaling of cell culture platforms, (ii) enhancement of EVs secretion per cell via genetic or environmental modulation, and (iii) generation of EVs mimetics through physical disruption of cellular membranes [249].

The most direct approach to increase EV yield is planar expansion, which involves expanding total culture surface area using multilayer flasks or closed multi-stack vessels (e.g., CellSTACK®, Cell Factory™, HYPERStack®). These platforms maintain 2D culture conditions while allowing more cells to be grown in a smaller incubator space and with less manual handling than using many individual flasks. For this reason, they are widely used in cell therapy manufacturing and are often adopted as an initial scale-up strategy for EV production, particularly during early process development when consistency with existing 2D data is important [250, 251]. However, at larger scales, 2D systems become labour-intensive and can introduce variability, including uneven nutrient and oxygen distribution across layers and inconsistencies in harvest timing. These drawbacks have stimulated growing interest in more controlled, bioreactor-based culture technologies.

3D culture systems further improve scalability by increasing the surface-to-volume ratio available for adherent cells. These systems include microcarrier-based stirred bioreactors, engineered scaffolds, and spheroid cultures, all of which promote high-density cell growth [252]. Multiple studies have reported substantially increased EV yield in 3D systems compared with matched 2D cultures, with additional evidence that EV cargo and bioactivity may be altered under 3D conditions [253]. Among available bioreactor configurations, hollow-fiber (HFB) bioreactors are the most extensively validated for EV production. In these systems, cells are cultured at very high density on semi-permeable capillaries, allowing up to 100-fold more cells than a T-flask. These systems allow prolonged culture without passaging, reduced serum-derived EV contamination, and permit repeated harvesting over several weeks, yielding 10- to 40-fold higher EV output than traditional flask-based cultures [254]. GMP-compliant HFB workflows have also been reported for MSC-EV production, supporting longer collection windows and repeated harvests with extensive characterisation [255]. Other high-density formats include two-chamber membrane-based systems, such as CELLine-type devices, which can increase EV yield while minimizing serum EV contamination and reducing incubator space requirements. [256]. Stirred-tank bioreactors, often combined with microcarriers for adherent cells, offer control over pH, dissolved oxygen, agitation, and feeding/perfusion strategies. These features are attractive for GMP translation and scale because they support automation and process monitoring [257]. Notably, improvements in overall EV yield may derive not only from

culture format but also from integrated downstream processing. For instance, combining 3D MSC culture with tangential flow filtration (TFF) has been shown to increase EV yield by approximately 140-fold compared with conventional 2D culture followed by ultracentrifugation [253].

Beyond culture scale-up, EV production can be enhanced by genetic manipulation of key regulators of EV biogenesis, trafficking, and secretion, targeting both ESCRT-dependent and ESCRT-independent pathways involved in MVBs formation and fusion with the plasma membrane [258-260]. EV secretion is highly responsive to environmental conditions. Factors such as hypoxia, oxidative stress, changes in pH or glucose, and exposure to inflammatory cytokines have all been shown to modulate EV secretion [261-264]. Moreover, physical stimuli including shear stress, elevated temperature, ultrasound, irradiation, and electric fields can further stimulate EV production. However, stress-based strategies may alter EV composition or increase contamination with apoptotic vesicles, underscoring the importance of quality control measures. [265].

To overcome the intrinsic limitations of naturally secreted EVs, EV mimetics have been developed using physical disruption of cell membranes followed by spontaneous reassembly into nanoscale vesicles. Common methods include serial extrusion through nanoscale filters, ultrasonication, nitrogen cavitation, and mechanical homogenization. These approaches produce vesicles that resemble natural EVs in size, morphology, and marker expression, while achieving substantially higher production rates [266].

For clinical application, EV production must ultimately conform to GMP standards, including defined cell sources, reproducible and scalable manufacturing protocols, robust downstream purification, and validated quality control assays. GMP-grade EV manufacturing has been demonstrated for several cell types, with comprehensive characterization of identity, purity, potency, and safety. Nonetheless, major challenges remain, including EV heterogeneity, batch-to-batch variability, sensitivity to culture conditions, and the absence of universally accepted potency assays. Overcoming these obstacles will be essential for the successful clinical deployment of EV-based therapeutics.

2.12 Conclusion

Bone is a highly dynamic and mechanosensitive organ whose structural integrity and functional competence are maintained through tightly regulated, multiscale communication between mesenchymal progenitors, osteoblasts, osteoclasts, and osteocytes. This literature review has demonstrated that bone homeostasis and regeneration extend beyond classical soluble mediators and direct cell-cell interactions, encompassing EVs as a critical and versatile signalling modality. By transferring bioactive cargo, particularly regulatory miRNAs, bone cell-derived EVs coordinate osteogenic differentiation, osteoclast-osteoblast coupling, angiogenesis, and immune modulation, thereby integrating anabolic and catabolic processes within the bone microenvironment. Nevertheless, a more comprehensive understanding of how mesenchymal-lineage cells orchestrate bone remodelling remains necessary. A further theme emerging from the literature is the central role of mechanical cues: mechanical loading not only drives remodelling via osteocyte mechanosignalling but can also be exploited as a controllable stimulus to modulate EV release and cargo composition through parent-cell conditioning, potentially generating vesicles with greater regenerative potency. However, translating these concepts into clinically robust therapies will require overcoming persistent challenges, including EV heterogeneity, limited production yields, and variability introduced by culture conditions and isolation methodologies. Advancing the field will therefore depend on linking mechanistic understanding to manufacturable solutions: clarifying how mechanical cues shape vesicle content and function, identifying scalable sources and production platforms, and elucidating the specific signalling components that confer EV bone-regenerative activity. Collectively, these advances hold promise for the development of reproducible EV-based strategies to enhance bone repair and reduce osteoporotic fracture risk.

Chapter 3. Bone cell-derived extracellular vesicles as emerging anti-catabolic therapeutics for bone regeneration

3.1 Introduction

Bone is a dynamic tissue that has the extraordinary capacity for remodelling and self-renewal to accommodate changes in its biochemical and biophysical environment, maintaining mineral homeostasis and repairing microdamage within the bone matrix. Bone remodelling arises from the coupled action of bone forming osteoblasts and bone resorbing osteoclasts. The balance between osteoblast-driven bone formation and osteoclast-driven bone resorption is tightly controlled, maintaining stable bone mass and mechanical strength under physiological conditions [267]. However, disruption of this balance can result in abnormal remodelling, resulting in bone pathologies such as osteoporosis and osteopetrosis [268, 269]. Osteoporosis arises from an imbalance favouring bone resorption. Driven largely by osteoclasts, this disorder leads to decreased bone mass and mineral density, deterioration of bone microarchitecture and increased bone fragility, resulting in high fracture risk [270]. Osteoclasts are multinucleated bone resorbing cells, and they differentiate from monocyte/macrophage precursors cells upon stimulation with M-CSF and receptor activation of RANKL [271]. While controlled bone resorption is essential for bone remodelling and a healthy skeleton, inhibiting osteoclast activity has been shown to be beneficial in the treatment of osteoporosis [272]. Anti-resorptive treatments, such as bisphosphonates (BP), anti-RANKL antibodies (e.g., denosumab), and selective oestrogen receptor modulators (SERMs), function by either inducing osteoclast apoptosis or inhibiting osteoclast recruitment and activity, thereby reducing bone resorption [273]. Although these therapies are effective in maintaining bone density, they have significant limitations, underscoring the need for alternative treatments that can effectively prevent bone loss. Osteoclast formation and function is tightly controlled by biochemical and specifically biophysical cues within the bone microenvironment, often indirectly by signals sent from other mesenchymal derived cells within bone [60]. Therefore, detailing how bone cells regulate osteoclastogenesis and how this may be influenced by their stage of lineage

commitment and mechanical environment, is crucial for identifying novel therapeutic strategies for bone disorders.

Bone cells, such as bone MSCs, osteoblasts, and osteocytes have been shown to play a pivotal role in regulating bone remodelling and osteoclast formation. MSCs have been found to have a dual effect on osteoclastogenesis depending on the microenvironment. *In vivo* and *in vitro* studies have demonstrated that MSCs regulation of osteoclastogenesis can occur both via direct contact and paracrine signalling [274, 275]. Under physiological conditions, MSCs can promote or suppress osteoclastogenesis via the secretion of a range of pro- and anti-osteoclastogenic cytokines [276, 277]. In addition, paracrine crosstalk between the more differentiated osteoblast and osteoclast has been proven to be essential to maintain bone homeostasis [278, 279]. Osteocytes terminally differentiate from osteoblasts and become entrapped in the newly formed bone matrix and represent the most abundant cell type in bone [280]. Previous studies have identified osteocytes as master orchestrators of bone remodelling via the control of osteoblast and osteoclast activity [13]. Osteocytes control osteoclastogenesis both via cell-cell interaction and signalling through the release of paracrine factors. While many studies have explored the role of mesenchymal derived bone cells in regulating osteoclastogenesis in isolation, findings can be challenging to directly compare given the differences in cell type and environmental conditions utilised. Therefore, more targeted studies are required to systematically explore how bone cells of the mesenchymal lineage regulate osteoclastogenesis.

A potent regulator of bone remodelling is mechanical loading. Unloading or low load environments have been shown to cause an acceleration of bone turnover, where bone resorbing osteoclasts outpace bone-forming osteoblasts, leading to rapid bone loss. The ability of bone to sense and respond to mechanical stimuli is orchestrated by the cells of the osteogenic lineage, the MSCs [281], the osteoblast [282], and particularly the osteocyte [283]. These cells are subjected to a constantly changing mechanical environment that comprises various biophysical stimuli, such as strain, stress, shear, pressure and fluid flow, which they convert into biochemical signals driving cellular responses. As mentioned above, mesenchymal-derived cells regulate osteoclastogenesis mainly via paracrine signalling. Secretion of signalling molecules can change in response to a wide variety of stimuli,

including mechanical stimulation [284]. It is widely accepted that the osteocytes are the primary mechanosensors in bone and regulate bone resorption in response to mechanical loading [285-287]. Interestingly, recent *in vivo* studies have also demonstrated the mechanosensitive nature of both MSCs and osteoblasts, highlighting their contribution to mechanically mediated bone remodelling [282]. Consistent with these findings, *in vitro* studies have demonstrated that mechanical stimulation prompts MSCs to alter their secretome suppressing osteoclast formation thereby contributing to rebalance bone remodelling [284]. Similarly, mechanical loading has been shown to modulate osteoblast and osteocyte secretome, resulting in a mechanically driven osteoclast inhibition [288-291]. These mechanically induced changes in the bone cell regulation of osteoclastogenesis warrant further investigation of the specific mechanically regulated signalling components mediating these effects, as they may represent novel anti-catabolic therapies.

Extracellular Vesicles (EVs) have been widely recognised as important mediators of intercellular communication [292]. EVs are lipid bilayer membrane-bound particles released by cells into the extracellular space both in physiologic and pathologic conditions. Over the last few decades, numerous studies have demonstrated that EVs carry and transfer a cargo of biomolecules including proteins, mRNA, and miRNA to regulate pathways in the target cell [293]. Biophysical cues and biochemical cues have been used to tune EVs cargo and enhance their therapeutic potential [198, 227]. For instance, EVs secreted by bone cells have been shown to have a pivotal role in coordinating bone remodelling and our group has previously demonstrated that EVs secreted by mechanically stimulated bone cells can drive an anabolic response by regulating MSCs recruitment, osteogenesis and vessel formation. However, how cells the role of bone cell secreted EVs in regulating osteoclastogenesis has yet to be fully explored to date.

In this chapter, we investigate how distinct cells of the osteogenic lineage regulate bone resorption through paracrine signalling mechanisms and EV-mediated communication. MSCs, osteoblasts and osteocytes, representing successive stages of osteogenic lineage commitment, were cultured under static or mechanically stimulated conditions to determine how lineage progression and mechanical cues shape their secretory profile. Conditioned media and EVs were collected and EVs were comprehensively characterised. To evaluate the functional impact of both vesicular and non-vesicular signalling outputs,

human CD14⁺ monocytes were cultured under osteoclastogenic conditions and treated with whole conditioned media, collected EVs, or EV-depleted fractions derived from each lineage stage and mechanical environment, followed by quantification of osteoclast differentiation. Based on their superior inhibitory effects on osteoclast differentiation, osteocyte-derived EVs were subsequently examined in greater detail to assess dose-dependent effects and their ability to regulate osteoclast resorptive function using a pit formation assay (**Figure 3.1**). Collectively, this chapter establishes an experimental framework to explore how lineage commitment stage and mechanical environment govern mesenchymal cell-derived regulation of osteoclastogenesis, advancing our understanding of EV-based signalling mechanisms and their translational potential in cell-free anti-catabolic strategies for bone regeneration.

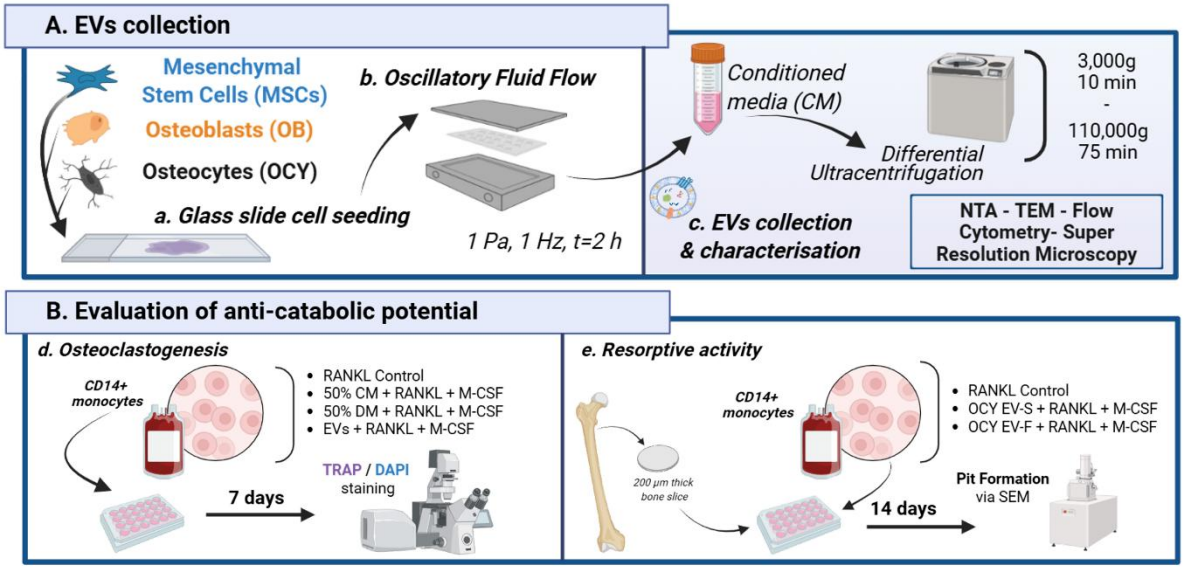

Figure 3.1. **Overview of the experimental workflow used to investigate mechanoregulated paracrine signalling from osteogenic lineage cells and its effect on osteoclastogenesis.** Cells at progressive stages of osteogenic differentiation, MSCs, osteoblasts, and osteocytes, were cultured under static conditions or subjected to oscillatory fluid shear. CM and EVs were subsequently collected and EVs were characterised. Human CD14⁺ monocytes were used to evaluate osteoclast differentiation in response to CM and EVs treatment. Following comparative analysis across lineage stages, osteocyte-derived EVs were selected for further investigation to examine concentration-dependent effects and their capacity to modulate osteoclast resorptive activity.

3.2 Material and Methods

3.2.1 Cell culture

3.2.1.1 Mesenchymal stromal/stem cell culture

Human MSCs were isolated from bone marrow (Lonza) and cultured in Dulbecco's modified eagle medium (DMEM) with GlutaMAX™ (Gibco) supplemented with 10 % Fetal Bovine Serum (FBS) (Gibco) and 1 % Penicillin- Streptomycin (P-S) (Sigma). Cells were cultured at 37 °C and 5 % CO2 and used between passage 3-5 were for all the experiments, as previously described [18, 294].

3.2.1.2 Osteoblast culture and differentiation

MSCs were seeded at 6,500 cells/cm^2 in a 6 well-plate (Sarstedt) and cultured in DMEM GlutaMAX™ (Gibco) supplemented with 10 % FBS and 1 % P-S at 37 °C and 5% CO2. 100 nM dexamethasone, 0.05 nM L-ascorbic acid and 10 mM β-glycerol phosphate were added to the media to induce osteogenic differentiation and were cultured for further 14 days to obtain osteoblasts (OB). Osteoblast differentiation was evaluated by quantification of intracellular alkaline phosphatase (ALP) activity and Alizarin Red staining to assess matrix mineralization. At the endpoint, OB were washed in PBS, then 1 mL/well of 2 mg/ml collagenase type II in PBS (Gibco) was added for 30 min to disrupt the deposited matrix. Collagenase was then removed and 1 mL/well of trypsin (Sigma) was added to lift the OBs for reseeding onto glass slides prior mechanical stimulation (**Figure S1**) [295].

3.2.1.3 Osteocyte culture

As human osteocytes are challenging to obtain in sufficient number and purity, the murine osteocyte-like MLO-Y4 cell line (Kerafast) was chosen for this study [296]. MLO-Y4 cells maintained in MEM Alpha (α-MEM) (Merk) supplemented with 2.5 % FBS (Gibco), 2.5% Calf Serum (CS) (Biosera), 1 % P-S (Sigma), and 1 % L-Glutamine (L-G) (Sigma) as previously described [297] . Cells were cultured at 37 °C and 5 % CO_2 and used for experiments when they had reached 80 % confluency between passages 40-60.

3.2.2 Mechanical stimulation and conditioned media collection

Glass slides (75x38 mm) (Corning) were sterilised in 70 % ethanol for 1 h, allowed to dry, and coated with rat tail collagen type I (0.15 mg/mL) (Corning) for 1 h. Prior to seeding a

wash step was performed with PBS (Sigma). MLO-Y4 cells were seeded with a density of 11,600 cells/cm^2 onto the coated glass slides. MSCs and OB were seeded independently on the coated glass slides at a density of 6,140 cells/cm^2. Different initial seeding densities were deliberately employed to account for variations in cell size between the cell types. Specifically, MSCs and OB are larger than MLO-Y4 cells and therefore require lower seeding densities to achieve comparable surface coverage [298-300]. By adjusting the initial cell numbers accordingly, all cell types attained similar levels of confluency over the same culture period, enabling valid comparisons across experimental conditions. After 24 h culture, cells were treated with serum reduced media overnight. Osteocyte (OCY) media consisted of α-MEM supplemented with 0.5 % FBS, 0.5 % CS, 1 % L-G, 1 % P-S, while the MSCs and OB media consisted of DMEM GlutaMAX™ supplemented with 0.5 % FBS, 1 % P-S. The slides were then placed in a custom-made parallel plate flow chamber (PPFC) bioreactor as previously described [301]. Briefly, the PPFCs were connected to a syringe pump to mechanically stimulate the cells by applying an oscillatory fluid flow included shear stress of 1 Pa at 1 Hz for 2 h. Cells were also cultured statically in the PPFCs for 2 h as a control. Following stimulation, the chambers were disassembled, the slides were washed with PBS and put in custom made slide chambers with 2.5 mL of α-MEM supplemented with 0.5 % EVs-depleted FBS (dFBS), 0.5 % EVs-depleted CS (dCS), 1 % L-G and 1 % P-S for osteocytes and DMEM supplemented with 0.5 % dFBS and 1 % P-S for MSCs and OB. After 24 h of culture, static conditioned media (CM-S) and fluid shear stimulated conditioned media (CM-F) were collected and centrifuged at 3,000 x g for 10 min at 4 °C to remove debris. Supernatant was collected and stored at -80 °C.

3.2.3 Osteoclastogenesis assay following CM treatment

The use of human blood samples for this study was approved by the research ethics committee of Trinity College Dublin and was conducted in accordance with the Declaration of Helsinki. Leukocyte-enriched buffy coats from anonymous healthy donors were obtained with permission from the Irish Blood Transfusion Service (IBTS), St. James's Hospital, Dublin (Researcher code: 0000RES625). Donors provided informed written consent to the IBTS for their blood to be used for research purposes. Peripheral blood mononuclear cells (PBMCs) were isolated from leukocyte-enriched human buffy coats using density gradient centrifugation with LymphoPrep^{TM} solution (Progen). CD14$^+$ monocytes were isolated from

PBMCs by magnetic sorting using MagniSort Human CD14 Positive Selection Kit (Invitrogen) according to the manufacturer's instructions. $CD14^+$ monocytes were seeded at 625,000 cells/cm^2 in 96-well plates in α-MEM containing 10 % FBS, 1 % P-S and 1 % L-G supplemented with 25 ng/mL M-CSF (Myltenyi Biotec) and 50 ng/mL Recombinant Human sRANK Ligand (RANKL) (PeproTech) (+RANKL) to induce osteoclastogenesis for 7 days. Groups cultured in growth media supplemented with 25 ng/mL M-CSF acted as a negative control for osteoclastogenesis (-RANKL). To assess the effect of bone cell secretome on osteoclastogenesis, CM collected from statically or mechanically stimulated cells was supplemented with 9 % FBS and added in a ratio of 1:1 along with growth media in presence of 50 ng/mL RANKL and 25 ng/mL M-CSF. Media and CM were replenished every 3.5 days. At day 7 cells were fixed with 2 % paraformaldehyde (PFA) for 15 min at room temperature, then washed twice with PBS and stained for tartrate-resistant acid phosphatase (TRAP) activity with a leukocyte acid Phosphatase (TRAP) Kit (Sigma) according to the manufacturer's protocols. Finally, cells were incubated with Triton X-100 0.1 % (Sigma) for 10 min, rinsed with PBS and then incubated with DAPI (1:2000) (Sigma) for 10 min. TRAP-positive multinuclear cells containing 3 or more nuclei were counted as osteoclasts. Cells were imaged using an Olympus IX83 inverted microscope with 10x objective and osteoclasts, number of nuclei per osteoclast, and total number of cells were manually counted using the cell counter plugin on Image-J software (version 1.54p, NIH, USA).

3.2.4 Extracellular vesicles collection

EVs were collected from CM via ultracentrifugation using a 70Ti-fixed angle rotor as previously described [19]. Briefly, CM was centrifuged at 2,000 x g for 15 min at 4 °C and then filtered through a 0.45 µm pore filter. Next, CM was ultracentrifuged at 110,000 x g for 75 min at 4 °C. The resulting EVs pellets were washed in PBS and ultracentrifuged again at 110,000 x g for 75 min at 4 °C. Finally, pellets were resuspended in PBS and stored at -80 °C.

3.2.5 Extracellular vesicles characterisation

3.2.5.1 Bicinchoninic acid (BCA) assay

EVs sample of 50 µL was suspended in 50 µL of cell lysis buffer (Invitrogen) and 25X proteinase inhibitor (Roche). EVs lysate was incubated on ice for 30 min, vortexing every 10 min for 10 s. After 30 min, the sample was centrifuged at 13200 rpm at 4 °C for 10 min. The

supernatant was transferred to a new tube and stored at -20 °C until required. EVs lysate was quantified using the Bio-Rad protein assay dye reagent (Bio-Rad). Bovine serum albumin (BSA) standards of 12.5-800 µg/mL were prepared in PBS and used to calculate the protein content of the samples. Lysed EVs was diluted 1:2 in PBS and whole cell lysate were diluted 1:20 in PBS. 10 µL of standards and sample was added to a 96-well plate in duplicate. Bio-Rad dye reagent was diluted 1:5 in deionised water and 200 µL added to each standard and sample. Absorbance was read at 570 nm using a fluoStar optima microplate reader (Serial #: 08-100-241) and protein levels were calculated from the standard curve.

3.2.5.2 Flow Cytometry

EVs surface antigens were exposed to antibodies diluted in 0.22 µm-filtered PBS with 2 % dFBS supplemented with protease inhibitor and phosphatase inhibitor (IFCM buffer). The antibodies used were anti-CD63 conjugated with FITC (1:150) (Biolegend), CD9-PE (1:5000) (Biolegend), CD81-PE-Cy7 (1:150) (Biolegend). The EVs were incubated with the antibodies for 45 min at room temperature in the dark, and washed using a 300kDa filter (Nanosep), resuspended in 50 µL IFCM buffer and acquired within 2 h on the ImageStream X MK II imaging flow cytometer (Amnis/Luminex, Seattle, USA) at 60x magnification and low flow rate. EVs-free IFCM buffer, unstained EVs, single-stained controls and fluorescence minus one (FMO) controls were run in parallel. Fluorescence was within detection linear range in the following channels: FITC was measured in channel 2 (B/YG_480-560 nm), PE in channel 3 (B/YG_560-595 nm), PE-Cy7 in channel 6 (B/YG_ 745- 780 nm) and APC in channel 11 (R/V_642-745 nm). Brightfield in channel 1 and 9 (B/YG_435-480 and R/V_560-595 nm filter, respectively) and side scatter channel (SSC) in channel 12 (R/V_745-780 nm 49 filter). Data analysis performed using IDEAS software v6.2 (Amnis/Luminex, Seattle, USA). EVs were gated as SCC-low vs fluorescence, then as non-detectable brightfield (Fluorescence vs Raw Max Pixel Brightfield channel), gated EVs were confirmed in IDEAS Image Gallery.

3.2.5.3 Nanoparticle tracking analysis

Nanoparticle tracking analysis (NTA) was performed on EVs suspensions using the NTA NS500 system (NanoSight, Amesbury, UK) to determine particle size based on Brownian motion. EVs samples were diluted at 1:50 in PBS and injected into the NTA system, which obtained four 40 s videos of the particles in motion. Videos were then analysed with the NTA software to determine particle size.

3.2.5.4 Transmission electron microscopy

A 20 µL sample of EVs suspension was placed onto parafilm (Sigma-Aldrich). A formvar carbon-coated nickel grid (Ted Pella Inc) was placed on top (coated side facing the droplet) of the EVs suspension droplet. The grid was incubated for 60 min at room temperature**,** washed in 30 µL of PBS (x3 times) on parafilm for 5 min. Absorbent paper was used to remove excess PBS from the washing steps. A droplet of PFA (2 %) was placed on parafilm, and the grid was placed on top and fixed for 10 min. The PBS washing steps were repeated. The grid was then contrasted in 2 % uranyl acetate (BDH), and all images were taken using the JEOL JEM-2100 transmission electron microscope at 120 kV.

3.2.5.5 Super-resolution dSTORM microscopy

Super-resolution fluorescent microscopy analyses of EVs were performed with 100x oil immersion 1.45 NA objective using Nanoimager S Mark II microscope from ONI (Oxford Nanoimaging, Oxford, UK) equipped with 405 nm/150 mW, 488 nm/1 W, 560 nm/500 mW, 640 nm/1 W lasers. Fluorescence excited by 488, 560 and 640 lasers was recorded using band pass filters 498-551 nm, 576 - 620 and 665-705 nm respectively. Fluorescence excited by 488, 560 and 640 lasers was recorded using band pass filters 498-551nm, 576 - 620 and 665-705nm respectively. ONI EV Profiler Kit 2 (EVP2) were used to prepare EVs samples for dSTORM as per manufacturer's instruction. This kit includes panEV stain (membrane dye), tetraspanin antibodies (CD9, CD63, CD81), capture chips, capture reagents and ONI BCubed dSTORM Imaging Buffer used in this study. Three-channel (647, 560 and 488) dSTORM data (1000 frames per channel) were acquired sequentially using AutoEV CODI acquisition software using 180 mW power at the objective for 488 nm laser, 45mW for 560 nm laser and 170mW for 640 nm laser at 40 ms exposure per frame. For panEV stain 3,000 images were acquired. Before each imaging session, beads slide calibration was performed to align fluorescent channels, achieving a channel mapping precision smaller than 10 nm. Single-molecule localization, clustering and positivity counting was performed using default EVP2 app setting within the CODI software provided by ONI (https://alto.codi.bio). Data was exported as report and csv file for further analysis.

3.2.6 Osteoclastogenesis assay following EV treatment

To determine whether EVs released by mesenchymal derived bone cells influence osteoclastogenesis, human blood derived $CD14^+$ monocytes were seeded at 625,000 cells/cm^2 in 96-well plates in α -MEM containing 10 % dFBS, 1 % P-S and 1 % L-G (growth media) supplemented either with 25 ng/mL M-CSF (Myltenyi Biotec) and 50 ng/mL RANKL (PeproTech) (+RANKL) to induce osteoclastogenesis for 7 days or with 25 ng/mL M-CSF alone (-RANKL) as a control. EVs enriched media was prepared by supplementing growth media with 0.5 µg/mL of MSCs, osteoblast and osteocyte derived static EVs (EV-S), and fluid shear stimulated EVs (EV-F) in the presence of M-CSF and RANKL. To assess the effect of secreted soluble factors not packaged within EVs, CM-S and CM-F depleted of EVs (DM-S and DM-F) were supplemented with EVs-depleted FBS and added in a ratio of 1:1 along with growth media in presence of both M-CSF and RANKL. Media and EVs were replenished after 3.5 days. Osteoclast differentiation was assessed by TRAP and DAPI staining as described above. Cells were imaged using Olympus IX83 inverted microscope with 10x objective and osteoclasts, number of nuclei per osteoclast and total number of cells were manually counted using the cell counter plugin on Image-J software (version 1.54p, NIH, USA).

To assess the influence of EVs concentration on osteoclastogenesis, EVs enriched media was prepared by adding 0.5, 1, 2, and 4 µg/mL of both static and fluid shear stimulated osteocyte derived EVs to the growth media. Human blood derived $CD14^+$ were cultured in EVs enriched media in a ratio of 1:1 along with growth media in the presence of M-CSF and RANKL for 7 days as described above. Osteoclast were stained for TRAP and DAPI staining and imaged using Olympus IX83 inverted microscope with 10x objective and quantification was performed using Image-J software (Version 1.54p, NIH, USA).

3.2.7 Osteoclast resorption activity assay

Osteoclast activity was assessed by determining the area of resorption on bovine bone slices. Briefly, bone slices (6 mm diameter, 200-220 µm thickness) were cut from bovine cortical femur with a low-speed water-cooled diamond saw (Beuhler). 24 h before seeding, bone slices were sterilized in 70 % ethanol, dried and incubated in media overnight. Subsequently, $CD14^+$ monocytes were cultured on the sterile bone slices in a 96-well plate at a density of 200,000 cells per bone slice in αMEM supplemented with 10 % dFBS, 1 % P-

S and 1 % L-G, in the presence of M-CSF (25 ng/mL) and RANKL (50 ng/mL) for 14 days. The effect of osteocyte derived EVs on osteoclast resorption activity was assessed by adding EVs enriched media, containing 0.5 µg/mL EV-S and EV-F in a ratio of 1:1 with growth media, in the presence of M-CSF and RANKL. Media and EVs were replenished every 3.5 days. After culture, samples were washed with PBS and 200 µL of deionised water was added for 30 min. Subsequently, samples surface was scraped with a cotton swab to remove cells. Finally, samples were serially dehydrated in an increasing concentration of ethanol and a final drying step in hexamethyldisilazane to remove all water before being imaged by scanning electron microscopy (SEM). After dehydration, samples were left to dry on adhesive double-sided carbon tape attached to 11.7 mm diameter aluminium stubs (Micro to Nano) overnight. Samples were then coated with a 5 nm thick coating of gold/palladium using a sputter coater and imaged in a Zeiss Ultra SEM (Zeiss). Representative images were taken using a secondary electron detector with an accelerating voltage of 10 kV. Images for quantitative analysis were taken using an in-lens detector under identical conditions. Resorption pit area was calculated using Image-J software (Version 1.54p, NIH, USA).

3.2.8 Statistical analysis

All data were analysed using GraphPad Prism 10.2.2. All data were analysed using an ordinary one-way or two-way ANOVA, assuming Gaussian distribution. Statistically significant differences were indicated as *p<0.05, **p<0.01, ***p<0.001, **** p<0.0001.

3.3 Results

3.3.1 Mesenchymal-derived bone cells secrete paracrine factors that regulate osteoclastogenesis in a manner that is dependent on the stage of lineage commitment and the mechanical environment.

To investigate the extent to which cells of the mesenchymal lineage can regulate osteoclastogenesis, osteoclast differentiation in response to conditioned media (CM) collected from stem/stromal cells, osteoblasts, and osteocytes cultured statically (CM-S) or exposed to 2 h oscillatory fluid shear (CM-F) was evaluated. Human blood derived $CD14^+$ monocytes cultured for 7 days in the presence of M-CSF and RANKL resulted in the formation of TRAP-positive multinucleated cells, demonstrating the ability of this cell type to differentiate into mature osteoclasts. Treatment with CM collected from MSCs cultured in static or mechanically stimulated conditions resulted in a significant inhibition of osteoclast formation. Specifically, the secretome from statically cultured MSCs (CM-S) demonstrated a robust near total inhibition of osteoclastogenesis (99 % reduction, $p<0.0001$) when compared to +RANKL controls. Interestingly, the application of fluid shear to the MSCs (CM-F) altered the secretome resulting in a less inhibitory response (35 % reduction compared to +RANKL, $p<0.0001$), (**Figure 3.2 A, B**). Cell nuclei number was also assessed as a proxy for osteoclast maturity and quantification demonstrated that osteoclast maturation was also reduced following treatment with MSCs CM when compared to +RANKL control (**Figure 3.2 A C**). A key step in the formation of osteoclasts is the adherence of the $CD14^+$ monocyte to the surface [302]. It was visually evident (**Figure 3.2 A**) that factors released from statically cultured MSCs reduced the adhesion of monocytes to the culture plate, which was further validated upon quantification (**Figure 3.2 A, D**). This reduction in adhesion was not seen following treatment with CM-F. Taken together, this data indicates that statically cultured MSCs significantly inhibit osteoclastogenesis in part via the secretion of factors that reduces monocyte adhesion, an effect that is diminished following mechanical stimulation.

To assess the effect of mesenchymal lineage commitment on the regulation of osteoclastogenesis, MSCs were differentiated into osteoblasts (OB) for 14 days before CM was collected from both statically and mechanically stimulated cultures [295]. Unlike the parent MSCs, the secretome from statically cultured OB does not contain paracrine factors

that inhibit osteoclastogenesis. However, following mechanical stimulation of the osteoblast, CM treatment results in a significant inhibition of osteoclastogenesis when compared to the static group and RANKL positive control (34 %, $p< 0.01$, and 36 % , $p<0.05$, reduction in osteoclastogenesis respectively) (**Figure 3.2 A, E**). No differences in osteoclast maturity were observed between the + RANKL control and the CM treated groups **(Figure 3.2 A, F**). This inhibitory effect of the mechanically stimulated OB secretome was not due to effects on monocyte adhesion as no difference was identified between treated groups **(Figure 3.2 A, G**). Therefore, the commitment of MSCs to the osteogenic lineage alters the osteoclastogenic properties of the secretome.

Osteocytes represent the terminally differentiated state of the mesenchymal lineage and their role in coordinating osteoclastogenesis is well studied [303]. Both CM collected from osteocytes cultured in static or mechanically stimulated conditions resulted in a significant inhibition of osteoclast formation. The secretome from statically cultured osteocytes elicited a 72 % reduction ($p<0.0001$) in osteoclast formation which was further augmented following mechanical stimulation (99 % reduction, $p<0.0001$) when compared to +RANKL controls (Figure 3.2 A, H). This enhanced anti-catabolic property following mechanical stimulation is consistent with that seen in OB. Similarly, nuclei number quantification identified a decreased number of nuclei upon treatment with CM-S which was further reduced with CM-F, indicating a lower level of osteoclast maturation (**Figure 3.2 A, I**). Interestingly, monocyte adhesion was not affected by treatment with CM collected from static osteocytes. However, treatment with CM collect following osteocyte mechanical stimulation resulted in a significant decrease in monocyte adhesion (**Figure 3.2. A, J**). This data is consistent with the previous identified role of the osteocyte in the regulation of osteoclasts and indicates that mechanically stimulated osteocyte may inhibit osteoclastogenesis in part via the secretion of factors that reduces monocyte adhesion. Taken together these data demonstrate that mesenchymal derived bone cells can regulate osteoclastogenesis and maturation via a paracrine mechanism that is strongly dependent on the stage of lineage commitment and the mechanical environment at each stage of the cell lineage.

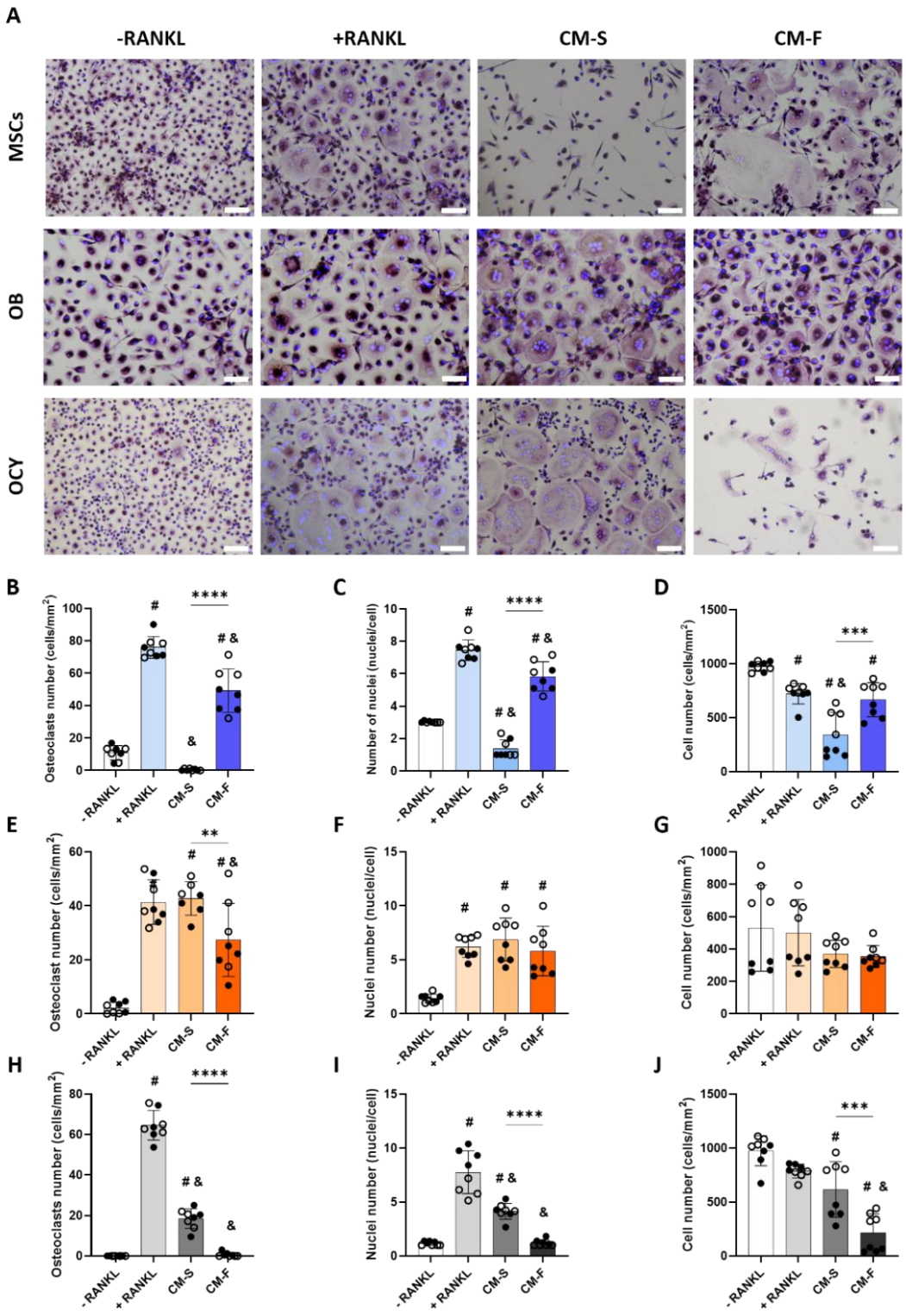

Figure 3.2. Bone cells from the mesenchymal lineage secrete paracrine factors that inhibit osteoclastogenesis in a manner that is dependent on the stage of lineage commitment and mechanical environment. (A) TRAP and DAPI staining of human $CD14^{+}$ monocytes following 7 days treatment with M-CSF (-RANKL); M-CSF and RANKL (+RANKL); M-CSF, RANKL and static MSCs, OB or OCY conditioned media (CM-S); and M-CSF, RANKL and mechanically activated MSCs, OB or OCY conditioned media (CM-F). **(B, E, H)**

Quantification of osteoclast number (identified as $TRAP^+$ cells with ≥3 nuclei), (C, F, I) nuclei number per osteoclast and **(D, G, J)** total cell number for MSCs, OB, and OCY CM groups respectively. Scale bar 100 µm. Values are mean ± SD for 2 different human donors (● = Donor 1, ○ = Donor 2). Statistical analysis performed via ordinary one-way ANOVA, *p<0.05, **p<0.01, ***p<0.001, **** p<0.0001, #p < 0.01 vs -RANKL, & p< 0.0001 vs +RANKL.

3.3.2 Mesenchymal derived bone cells secrete extracellular vesicles that are of similar size but differ in quantity and surface marker expression at each stage of lineage commitment

EVs were collected and characterised from media conditioned by MSCs (MSCs-EVs), osteoblasts (OB-EVs) and osteocytes (OCY-EVs) as per MISEV guidelines [178]. NTA analysis was performed to determine their respective size distribution and concentration. As displayed in **Figure 3.3 A** and **B**, similar size distribution profiles were observed between all EVs groups ranging from 100 to 200 nm with respective average diameters of 163 nm, 160 nm, and 160 nm for MSCs-EVs, OB-EVs, and OCY-EVs. Interestingly, normalising the EVs concentration to the parent cell seeding density, highlighted a significantly greater EVs average yield from osteoblasts (6.99×10^9 NPS/mL/10^6 cells) compared to EVs secreted from MSCs (2.64×10^9 NPS/mL/10^6 cells) or osteocytes (2.23×10^9 NPS/mL/10^6 cells) (**Figure 3.3 C**). The morphology of these vesicles was evaluated by TEM revealing nanosized particles (<200 nm) with a spherical shape (white arrow) for all three groups which is consistent with the NTA analysis (**Figure 3.3 F**). The total protein content in EVs lysates was determined via a BCA assay and exhibited a similar trend in protein level to that seen in the nanoparticle concentration where there is a slight but non-significant increase in protein quantity in the OB-EVs group when compared to the MSCs and OCY-EVs (**Figure 3.3 E**). Finally, the presence of tetraspanin markers (CD9, CD63 and CD81) was assessed by flow cytometry and super resolution microscopy. All three groups were found positive for the three markers with no significant variations as the cells progress through the lineage (**Figure 3.3 D, G**).

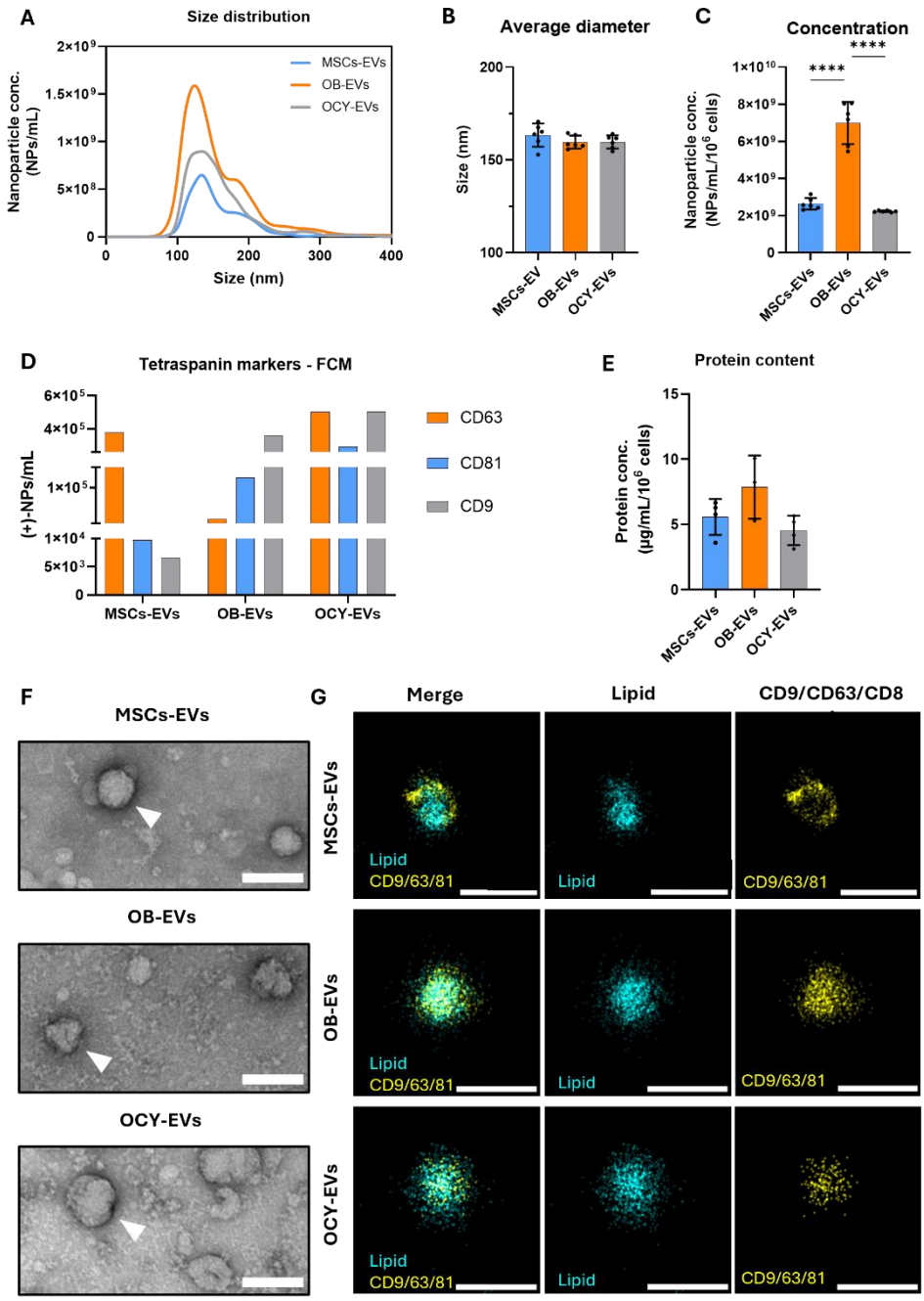

Figure 3.3. Comparative isolation and characterisation of EVs derived from the conditioned media of mesenchymal stem cells (MSCs), osteoblasts (OB) and osteocytes (OCY). Nanoparticle Tracking Analysis (NTA) was performed to determine **(A)** Size Distribution **(B)** Average diameters and **(C)** Nanoparticle Concentrations. **(D)** Detection of tetraspanin markers CD63, CD81 and CD9 via flow cytometry. **(E)** Protein content via the bicinchoninic acid assay. **(F)** TEM observations with scale 100nm (white arrow indicating EVs). **(G)** Super resolution microscopy observations of single nanoparticle with the fluorescence detection of membrane (lipid stain) and trio-tetraspanin markers (CD9/CD63/CD81) with scale bar = 200 nm. Statistical analysis performed via one-way ANOVA with post-hoc Tukey test, p*≤ 0.05, p**≤ 0.005, ***p≤ 0.001, **** p≤0.0001.

3.3.3 Mesenchymal derived bone cells secrete extracellular vesicles that inhibit osteoclast differentiation.

Given the key role that EVs play in coordinating cell-cell communication, we next sought to investigate the role that EVs may play in the above demonstrated paracrine signaling between mesenchymal-derived bone cells and osteoclasts under both static conditions (EV-S) or following mechanical stimulation (EV-F). The EVs dose used was 0.5 μg/mL, equivalent to the average EVs protein concentration found in the CM from each cell type. In addition to collected EVs, the effect of static and mechanically activated CM that was depleted of EVs (DM) was also investigated to assess whether soluble factors within the CM, not packaged within EVs, may influence osteoclast differentiation.

EVs released by statically cultured and mechanically stimulated MSCs significantly inhibited osteoclastogenesis, independent of the mechanical environment. Similarly, CM collected from statically cultured and mechanically stimulated MSCs that was depleted of EVs also demonstrated an inhibition of osteoclastogenesis, indicating that soluble factors not packaged within EVs can also affect this process (**Figure 3.4 A, B**). Furthermore, quantification of osteoclast nuclei showed that osteoclasts differentiated upon treatment with EVs or CM depleted of EVs (DM) displayed decreased number of nuclei per cell (**Figure 3.4 A, C**), which is consistent with what was identified with full conditioned media treatment. In addition, monocyte adhesion was not found to be impaired by EVs or soluble factors contained within the DM independent of mechanical stimulation of the MSCs (**Figure 3.4 A, D**).

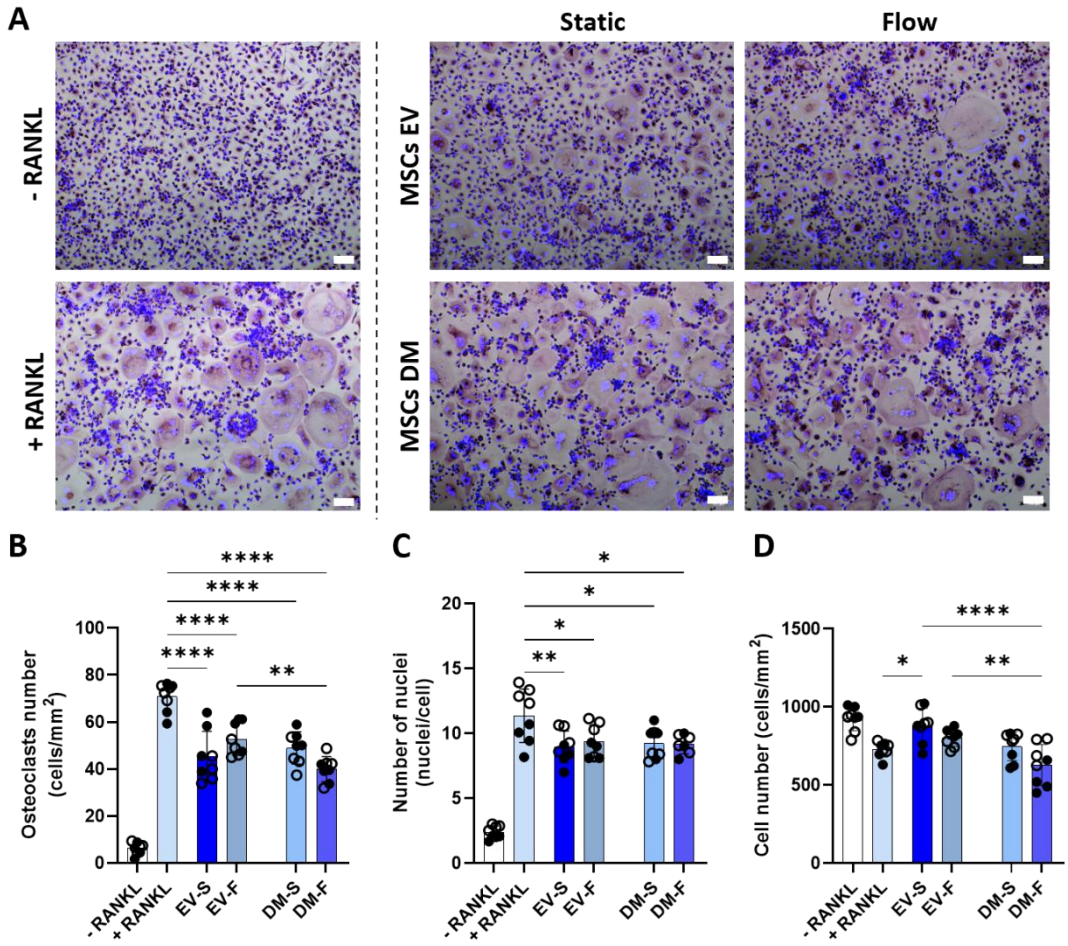

Figure 3.4. MSCs secrete extracellular vesicles that inhibit osteoclastogenesis independent of mechanical stimulation. (A) TRAP and DAPI staining of human monocytes following 7days treatment with M-CSF (-RANKL); M-CSF and RANKL (+RANKL); M-CSF, RANKL and 0.5 µg/mL static MSCs derived EVs (EV-S); M-CSF, RANKL and 0.5 µg/mL mechanically activated MSCs derived EVs (EV-F); M-CSF, RANKL and static EVs depleted MSCs CM (DM-S); and M-CSF, RANKL and mechanically activated EVs depleted MSCs CM (DM-F). **(B)** Quantification of osteoclast number (identified as $TRAP^+$ cells with ≥3 nuclei), **(C)** nuclei number and **(D)** total cell number. Scale bar = 100 µm. Values are mean ± SD for 2 different human donors (● = Donor 1, ○ = Donor 2). Statistical analysis performed via ordinary one-way ANOVA, *p<0.05, **p<0.01, ***p<0.001, **** p<0.0001.

Moving forward along the mesenchymal lineage, EVs secreted by osteoblasts both in static culture and following mechanical stimulation were shown to possess anticatabolic potential. Specifically, osteoblasts cultured in static conditions produced EVs that led to a 25 % decrease in osteoclast differentiation when compared to the RANKL treated control (p<0.0001). However, mechanical stimulation of the osteoblast was shown to increase the anti-catabolic potential of the secreted EVs, resulting in a significantly more pronounced

osteoclast inhibition (37 % reduction, p<0.0001), an effect that is consistent with that seen from the whole secretome (**Figure 3.5 A, B**). Osteoclasts differentiated in the presence of osteoblast derived EVs showed decreased number of nuclei when compared to the +RANKL control, indicating a lower level of maturity (**Figure 3.5 A, C**). Furthermore, monocyte adhesion wasn't impaired upon treatment with both static and mechanically activated EVs (**Figure 3.5 A, D**). Interestingly, treatment with EVs-depleted CM (DM) led to a notable impairment in monocyte adhesion and a subsequent complete inhibition of osteoclastogenesis. This suggests a preferential packaging of factors within osteoblast EVs that may facilitate monocyte adhesion but also inhibit osteoclast maturation, particularly in response to mechanical stimulation.

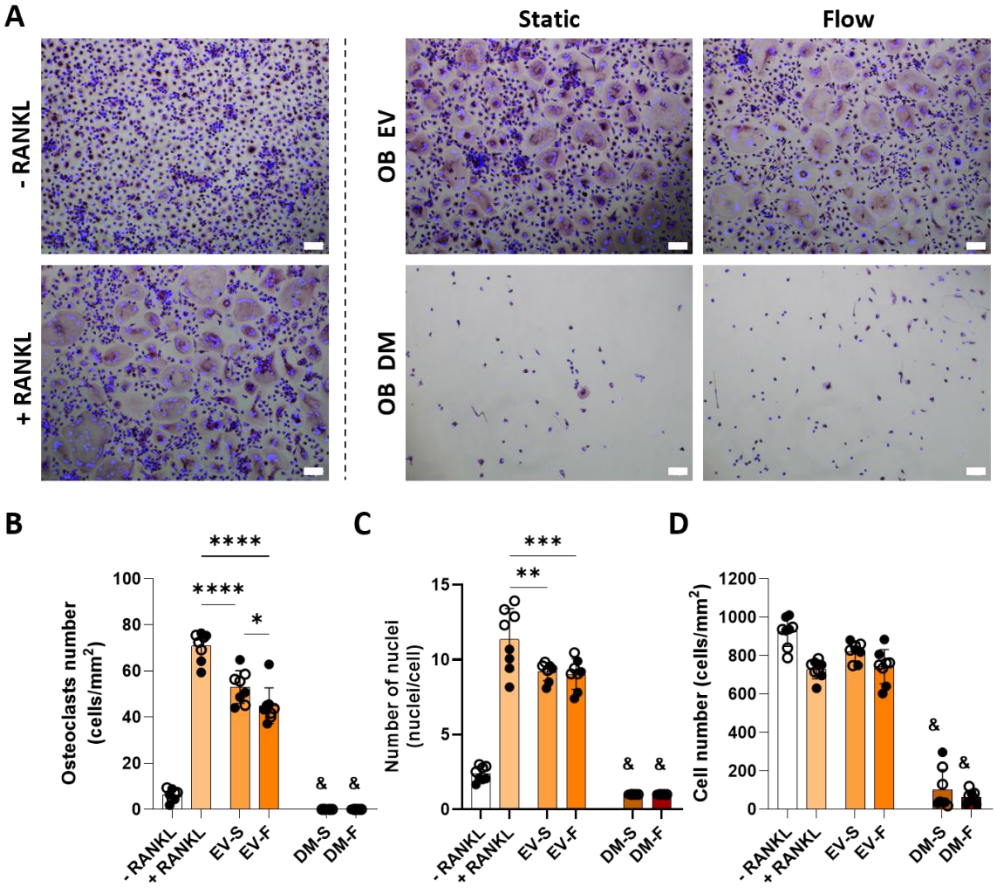

Figure 3.5. Osteoblasts secrete extracellular vesicles that inhibit osteoclastogenesis, where the inhibitory properties of the EVs are augmented following mechanical stimulation of the osteoblast. (A) TRAP and DAPI staining of human monocytes following 7days treatment with M-CSF (-RANKL); M-CSF and RANKL (+RANKL); M-CSF, RANKL and 0.5 µg/mL static osteoblast derived EVs (EV-S); M-CSF, RANKL and 0.5 µg/mL mechanically activated osteoblast derived EVs (EV-F); M-CSF, RANKL and static EVs depleted osteoblast CM (DM-S); and M-CSF, RANKL and mechanically activated EVs depleted osteoblast CM (DM-F). **(B)** Quantification of osteoclast

number (identified as $TRAP^+$ cells with ≥3 nuclei), **(C)** nuclei number and **(D)** total cell number. Scale bar = 100 µm. Values are mean ± SD for 2 different human donors (● = Donor 1, ○ = Donor 2). Statistical analysis performed via ordinary one-way ANOVA, *p<0.05, **p<0.01, ***p<0.001, **** p<0.0001, $^{\&}$ p< 0.0001 vs +RANKL, EV-S and EV-F.

Interestingly, similar to that which was observed when treating human monocytes with osteoblast EVs, both static culture and mechanical stimulation of osteocytes resulted in the production of EVs possessing anti-catabolic properties. Quantification of osteoclast numbers revealed that treatment with EVs derived from statically cultured osteocytes resulted in a 54 % reduction in osteoclast formation (p<0.0001). EVs secreted after mechanical stimulation of osteocytes demonstrated a heightened anti-catabolic effect, resulting in a near complete inhibition of osteoclast formation (91 % reduction, p<0.0001) (**Figure 3.6 A, B**). In line with what was observed with the other two EVs populations, osteoclasts differentiated in the presence of osteocyte-derived EVs demonstrated a reduced number of nuclei compared to the +RANKL control (**Figure 3.6 A, C**). Furthermore, EVs treatment had no impact on the ability of monocytes to adhere. Conversely, CM depleted of EVs (DM) resulted in a substantial impairment of monocyte adhesion, subsequently leading to a lack of osteoclast formation, regardless of mechanical stimulation, in a similar manner to that identified from OB DM. Specifically, the reduction in monocyte adhesion was notably more pronounced when treated with mechanically activated EVs-depleted CM (DM-F) (**Figure 3.6 A, D**). To determine whether the reduction in monocyte adhesion in the DM-S and DM-F conditions was due to cell death or impaired adhesion, flow cytometry-based live/dead staining was performed on cells collected from the supernatants. Quantification of live cells among single-cell populations demonstrated that substantial numbers of viable cells were present in suspension, indicating that cells had not undergone cell death but rather failed to adhere to the culture surface (data not shown). This confirms that the observed reduction in osteoclast formation under DM conditions is attributable to impaired monocyte adhesion rather than loss of cell viability. These findings suggest that role of secreted soluble factors in controlling monocyte adhesion and the presence of a selective packaging mechanisms within the EVs that is dependent on the stage of lineage commitment and mechanical environment. The inhibition of osteoclastogenesis elicited by osteocyte derived EVs aligns with that observed

upon treatment with the full osteocyte secretome, suggesting that osteocytes coordinate osteoclastogenesis via an EVs-mediated mechanism.

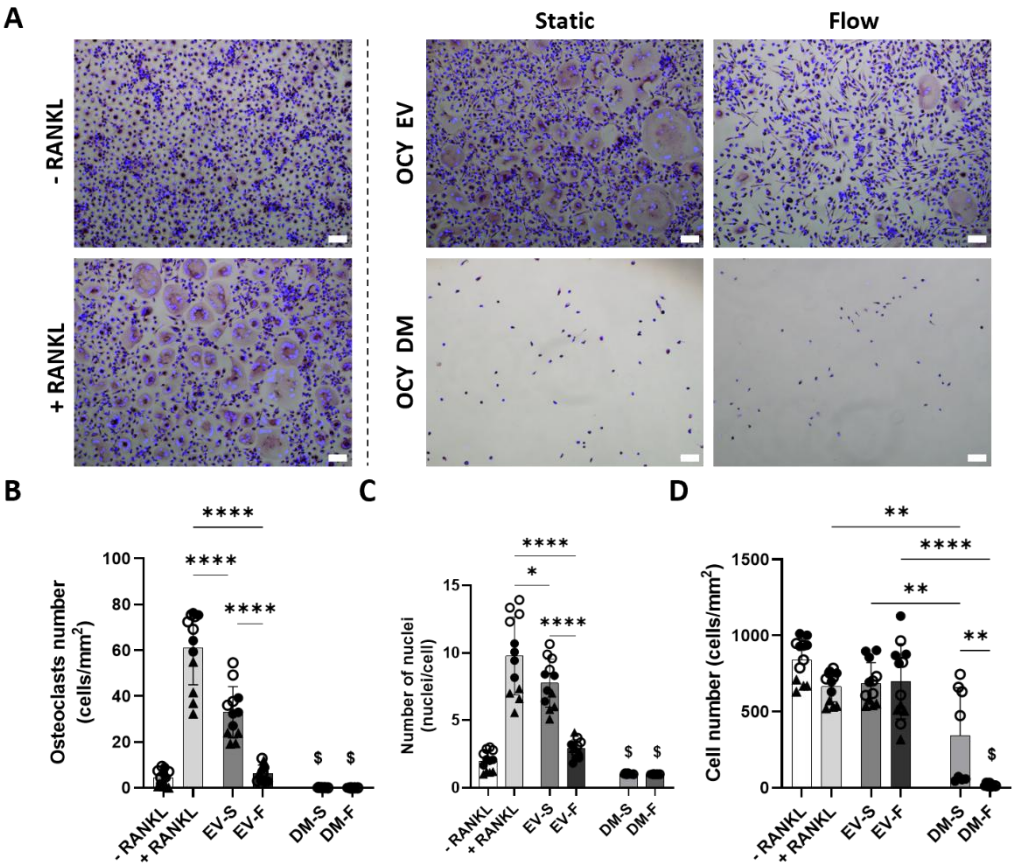

Figure 3.6. Osteocytes secrete extracellular vesicles that inhibit osteoclastogenesis, where the inhibitory properties of EVs are significantly augmented following mechanical stimulation of the osteocyte. (A) TRAP and DAPI staining of human monocytes following 7 days treatment with M-CSF (-RANKL); M-CSF and RANKL (+RANKL); M-CSF, RANKL and 0.5 µg/mL static osteocyte derived EVs (EV-S); M-CSF, RANKL and 0.5 µg/mL mechanically activated osteocyte derived EVs (EV-F); M-CSF, RANKL and static EVs depleted osteocyte CM (DM-S); and M-CSF, RANKL and mechanically activated EVs depleted osteocyte CM (DM-F). **(B)** Quantification of osteoclast number (identified as $TRAP^+$ cells with ≥3 nuclei), **(C)** nuclei number and **(D)** total cell number. Scale bar = 100 µm. Values are mean ± SD for 3 different human donors (● = Donor 1, ○ = Donor 2, ▲ = Donor 3). Statistical analysis performed via ordinary one-way ANOVA, *p<0.05, **p<0.01, ***p<0.001, **** p<0.0001, $ p< 0.0001 vs +RANKL and EV-S.

Taken together, this data demonstrates that mesenchymal derived bone cells can regulate osteoclastogenesis via an EV-mediated paracrine mechanism that is dependent on the stage of lineage commitment and mechanical environment of the EVs parent cell.

3.3.4 The anti-bone resorptive properties of the osteocyte derived EVs are strongly dependent on dosage.

As the osteocyte is known to be the master orchestrator of bone remodelling, the mechanically activated osteocyte derived EVs possessed the most robust anti-catabolic response, coupled with the fact we have previously demonstrated that these EVs possess both osteogenic and angiogenic properties [18, 19, 295], we next sought to explore the impact of osteocyte-EVs dosage on osteoclastogenesis. In this context we treated human monocytes with increasing concentration of both static and mechanically activated osteocyte derived EVs, namely 0.5, 1, 2 and 4 μg/mL in the presence of both RANKL and M-CSF for 7 days. Interestingly, quantification of osteoclasts revealed that only the treatment with the lower dose of EVs resulted in osteoclast inhibition, mirroring that seen in the CM. However, inhibition was more pronounced in the presence of EVs derived from mechanically stimulated osteocytes. Conversely, doses exceeding the corresponding EVs concentration in the CM - specifically, 1, 2, and 4 μg/mL - prompted an opposite response, enhancing osteoclast differentiation regardless of mechanical stimulation (**Figure 3.7 A, B**). In addition, osteoclast nuclei number was upregulated upon treatment with all concentration of EVs, with exception of the lowest EVs dose (0.5 μg/mL), when compared to the +RANKL control group. Mechanical stimulation didn't affect osteoclast nuclei number following treatment with EVs doses exceeding EVs concentration in the CM, while it elicited a significant reduction following treatment with the lowest EVs dose (**Figure 3.7 A, C**). Finally, the total number of cells was not affected by any EVs dose or mechanical stimulation (**Figure 3.7 A, D**). These data demonstrate the presence of an optimal dose to maximise the anti-catabolic potential of osteocyte derived EVs.

After evaluating the anti-osteoclastogenic properties of osteocyte-derived EVs and determining the optimal dose for maximum therapeutic efficacy, we next investigated whether EVs treatment could modulate osteoclast resorptive activity. Treatment with M-CSF and RANKL (+ RANKL control) resulted in resorption of 53 % of the total bone slice area. However, quantification of the osteoclast-resorbed area of bone slices following EVs treatment revealed that EVs derived from both static and mechanically stimulated cultures reduced osteoclast-mediated bone resorption. Notably, EVs secreted in response to osteocyte mechanical stimulation induced a significantly greater reduction in resorbed area

compared to both the +RANKL control (62 % reduction, p<0.001) and their static counterparts (48 % reduction, p<0.05). Taken together these results showcase osteocyte-derived EVs as promising regulators of both osteoclast differentiation and bone resorptive activity (**Figure 3.7 E, F**).

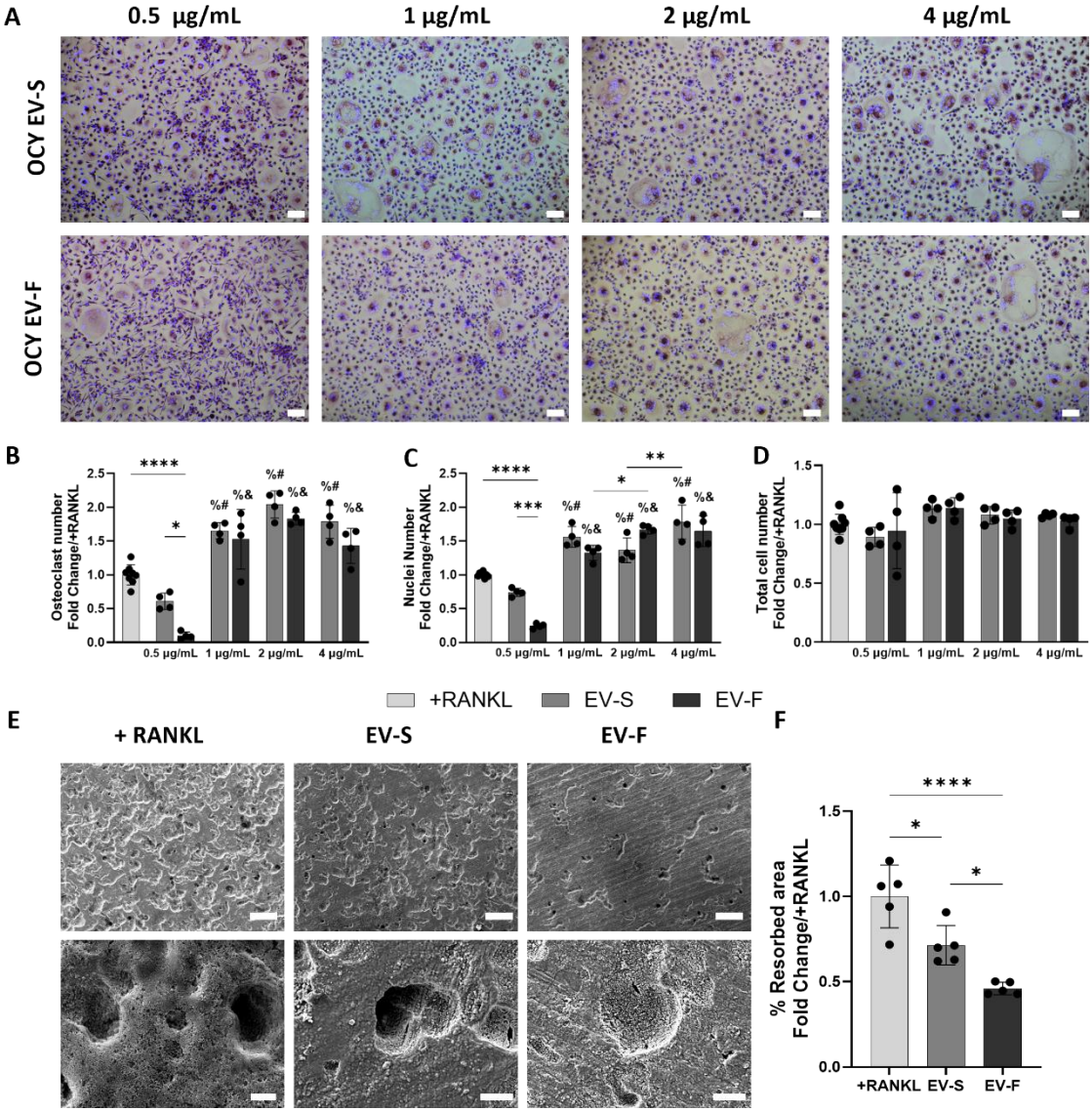

Figure 3.7. Optimal doses of osteocyte derived EVs inhibit osteoclast differentiation and function. (A) TRAP and DAPI staining of human monocytes following 7 days treatment with 0.5, 1, 2 and 4 µg/mL osteocyte-like MLO-Y4 cells derived- static and mechanically activated EVs (Flow) (Scale bar 100 µm). **(B)** Quantification of osteoclast number, (C) nuclei number and (D) total number of cells. (E) SEM images of resorption pits on bovine bone surfaces produced by osteoclasts following 0.5 µg/mL OCY-EVs treatment, Scale bars = 200 µm (top row), 20 µm (bottom row) and **(F)** resorbed area quantification. Values are means ± SD. Statistical analysis performed via ordinary one-way ANOVA, *p<0.05, **p<0.01, ***p<0.001, **** p<0.0001, % p<0.05 vs + RANKL, # p< 0.001 vs 0.5 µg/mL EV-S, & p< 0.0001 vs 0.5 µg/mL EV-F.

3.4 Discussion

Bone is a dynamic tissue that is constantly remodelling via a tightly controlled balance between formation and resorption. This process enables bone to adapt to changing environmental or mechanical cues, adjusting bone mass to maintain an optimal strength to weight ratio. However, when bone resorption exceeds bone formation, it can lead to a net bone loss, microarchitectural deterioration and an increased risk of fracture and/or poor fracture healing. Therefore, this study aimed to characterise how cells from the mesenchymal lineage regulate osteoclastogenesis; how this is influenced by their stage of lineage commitment; and by the dynamic mechanical cues these cells are exposed to physiologically and finally to identify the signalling components mediating this anti-catabolic potential. We demonstrated that the secretome of mesenchymal-derived bone cells inhibited osteoclast differentiation to differing degrees depending on their stage of lineage commitment and on the mechanical environment. Moreover, we have shown that the inhibition of osteoclastogenesis is mediated by EVs released by these bone cells. In addition, we identified the osteocyte as the optimal parent cell for the production of EVs with the most robust anti-catabolic potential and have highlighted the importance of EVs dosage to efficiently regulate both osteoclast differentiation and bone resorptive activity. Taken together, this study provides an important advancement towards the understanding of EV-mediated osteoclastogenesis, paving the way for the development of novel nanotherapeutics to prevent bone loss.

Bone cells secrete paracrine factors that inhibit osteoclastogenesis to differing degrees depending on their stage of lineage commitment. We demonstrated that statically cultured MSCs secrete factors that almost completely inhibit osteoclastogenesis, an effect likely mediated by a strong impairment of monocyte adhesion. Conversely, other studies provided evidence of MSCs supporting osteoclastogenesis [274, 304]. These conflicting *in vitro* findings on the impact of MSCs on osteoclastogenesis may stem from variations in the experimental approaches used. Several studies have investigated the interaction between osteoblasts and osteoclasts. In this context, we differentiated osteoblasts from the human MSCs, and our results demonstrated that statically cultured osteoblasts also did not inhibit or promote osteoclastogenesis [288]. These findings demonstrate a change in cell secretome following differentiation along the mesenchymal lineage from the same donor.

Osteocytes differentiate from osteoblasts and their role in the regulation of osteoclast activity is well established. Our findings demonstrate that osteocyte secretome has a strong inhibitory effect on osteoclastogenesis. This is supported by previous work demonstrating that osteocyte derived conditioned media dramatically inhibited osteoclast activity, suggesting that osteocytes produce osteoclast inhibitor factors [305, 306]. Taken together, these results demonstrate that bone cells are involved in the regulation of osteoclastogenesis via paracrine signalling. In addition, the differing extents of osteoclastogenesis inhibition indicates that bone cell regulation of osteoclastogenesis is strongly dependent on the stage of lineage commitment.

Bone cells inhibit osteoclastogenesis via a mechanically driven paracrine mechanism. Osteocytes' ability to respond to mechanical stimulation and regulate osteoclast activity is well known. However, other cells of the osteogenic lineage are also known to be mechanoresponsive, indicating that they might also play a role in mechanically regulated bone remodelling, but the extent to which they can regulate osteoclastogenesis in less well understood. Recent studies demonstrated that mechanical unloading of MSCs promoted osteoclast differentiation [284], while MSCs subjected to oscillatory flow-induced shear stress inhibited osteoclastogenesis [307]. Similarly, our work demonstrated that MSCs subjected to fluid shear stress elicited an inhibition on osteoclastogenesis when compared to the RANKL treated control, but to a lesser extent when compared to the static counterpart. On the other hand, Liu *et al.* observed that both static and dynamic pressure increased osteoclastogenesis [308]. Differences between the studies may be attributed by differences in mechanical regimen and cell species. Osteoblast have also been shown to be involved in the regulation of osteoclastogenesis, and that mechanical cues play a key role in this process [136, 282, 288]. In this context, we demonstrated that osteoblasts subjected to oscillatory fluid flow produced a secretome that inhibited osteoclast differentiation when compared to the static group, in line with previous reports employing other form of mechanical stimulation [309]. Moreover, our results demonstrate that osteocytes subjected to oscillatory fluid flow strongly inhibit osteoclastogenesis via a mechanically driven paracrine mechanism, showing a more pronounced effect than osteoblasts in suppressing osteoclast formation [290]. This is supported by previous studies showing that osteocytes are mechanosensitive, and they inhibit osteoclastogenesis in response to fluid flow [291,

310]. Taken together we have demonstrated the mechanical cues play a key role in bone cell regulation of osteoclastogenesis. When compared to that observed upon treatment with static cultured bone cell conditioned medium, these findings suggest the impact of mechanical stimulation on osteoclastogenesis may differ depending on the mesenchymal lineage stage.

Bone cells from the mesenchymal lineage can coordinate osteoclastogenesis via the release of EVs, a response that can be enhanced following mechanical stimulation. Previous studies have highlighted the pro-anabolic potential of osteoblasts and osteocyte derived EVs and how the anabolic potential can be enhanced by mechanically stimulating the parent cell [18, 311-313]. However, a limited number of studies have investigated whether these EVs can elicit an anti-catabolic response and furthermore delineated the factors involved. Herein, we demonstrate that EVs secreted by both statically cultured and mechanically stimulated MSCs suppressed osteoclastogenesis, an effect mirrored by MSCs-conditioned media (CM) depleted of EVs. This indicates that MSCs secrete both vesicular and soluble inhibitory cues affecting early and late stages of osteoclast development. Previous studies have reported stem cell-derived EVs can suppress osteoclast differentiation and contribute to the regulation of bone resorption under various conditions, including mechanical stimulation [314, 315]. Our data add to this by showing that MSCs-derived EVs reduce osteoclast multinucleation, a hallmark of maturation, without impairing monocyte adhesion, and that their inhibitory effect is not significantly altered by mechanical stimulation. We were also able to demonstrate that by differentiating MSCs into osteoblasts we obtained EVs with a different anti-catabolic potential. Our findings reveal that OB-derived EVs inhibit osteoclastogenesis to differing degrees depending on the OB mechanical environment. EVs from mechanically stimulated OB led to a more pronounced decrease in both the number and maturity of osteoclasts compared to their static counterparts [197]. Interestingly, EVs-depleted OB-CM impaired monocyte adhesion and completely inhibited osteoclastogenesis. Among all cell types, OCY-EVs showed the strongest inhibitory impact on osteoclastogenesis. In particular, mechanically activated OCY-EVs inhibited osteoclast formation by 91 %, aligning with prior evidence that osteocytes are the central regulators of bone resorption during mechanoadaptation [199, 316]. Interestingly, OCY-EVs displayed dose-sensitive behaviour, with low (0.5 μg/mL) doses

inhibiting osteoclastogenesis and high doses (>1 µg/mL) promoting it. This biphasic effect suggests a threshold-dependent balance between pro- and anti-catabolic factors, possibly due to changes in cargo saturation or uptake dynamics at higher concentrations [317]. Our findings indicate that optimal dosing is crucial for therapeutic use of osteocyte-derived EVs, especially in pathological states like osteoporosis where remodelling balance is disturbed.

One potential limitation of this study is the use of a murine osteocyte cell line to generate OCY-EVs. However, our data demonstrate similar trends in osteoclast formation inhibition and monocyte adhesion following treatments with human OB and murine OCY derived EVs and DM, which differs from the effects observed with human MSCs derived EVs and DM. This suggests that the MLO-Y4 cell line may serve as a reliable model for human osteocyte. In addition, from a therapeutic prospective, previous research has explored the use of plant-derived EVs in human cell treatments, reporting no adverse effects, while supporting human cell proliferation, reducing inflammation and apoptosis [318]. Additionally, reported findings have demonstrated that EVs from human cells can be functionally active and well-tolerated in rodent models [319], suggesting that EVs from different species may represent a safe and viable therapeutic approach for human applications.

3.5 Conclusion

In conclusion, this study demonstrates that MSCs, osteoblasts, and osteocytes secrete EVs with the potential to inhibit osteoclastogenesis, with the extent and underlying mechanisms of regulation shaped by both lineage stage and mechanical environment. Osteocytes, in keeping with their role as master orchestrators of bone remodelling, were found to release EVs with the strongest inhibitory effects on osteoclast differentiation and resorptive function, particularly in response to mechanical stimulation Together with the previously reported osteogenic and angiogenic properties of these vesicles, mechanically activated osteocyte-derived EVs represent a promising novel multi-targeted therapeutic for bone regeneration.

Chapter 4. Investigation of the Nanokick Bioreactor to scale production of mechanically activated cell derived EVs

4.1 Introduction

Bone is a dynamic, metabolically active tissue that continuously remodels throughout life to maintain structural integrity and mineral homeostasis. This remodelling process involves the coordinated actions of bone-resorbing osteoclasts and bone-forming osteoblasts, and dysregulation of this balance contributes to a spectrum of skeletal disorders such as osteoporosis, Paget's disease, and fracture non-union, which together represent a significant clinical burden worldwide [267]. Mechanical loading is a fundamental regulator of bone health, playing a crucial role in the maintenance of bone mass and strength, as demonstrated by the profound bone loss associated with ageing, immobilisation, and microgravity exposure [106, 107]. In contrast, physiological mechanical stimulation promotes bone formation and suppresses excessive bone resorption, thereby preserving skeletal function [320]. At a cellular level, when bone is mechanically loaded, osteocytes sense the physical deformation of the bone matrix and the fluid flow induced shear stress through the LCS network and transduce these mechanical stimuli into secreted biological cues to coordinate the activities of osteoblasts and osteoclasts, thereby controlling bone formation and resorption [321, 322] These observations have led to increasing interest in harnessing mechanical cues as therapeutic tools to prevent or treat bone diseases. Strategies that deliver controlled mechanical stimuli offer the potential to non-invasively coordinate bone cell behaviour and restore remodelling balance, providing a strong rationale for the development of emerging mechanotherapeutic approaches.

In the last decades, several studies have focused on the prevention and treatment of bone diseases such as osteoporosis harnessing the effects of physical exercise. Recent studies demonstrate that low-magnitude, high-frequency vibration (LMHFV) can enhance trabecular bone properties, increase bone formation, and improve overall mechanical strength [323, 324]. However, the effects appear to be strongly dependent on vibration parameters such as frequency and amplitude: while lower frequencies have been shown to stimulate osteogenic signalling and promote bone formation, higher frequencies may inhibit these processes [325, 326]. *In vitro* studies further support that LMHFV can promote

osteoblast proliferation and differentiation, suggesting a direct role in bone remodelling [327]. In addition, animal studies suggest that whole-body vibration can support bone healing after fractures in osteoporotic conditions [328, 329]. The beneficial effects appear to involve both direct stimulation of bone-forming processes and the influence of hormone-related pathways [330]. Moreover, whole body vibration may help regulate the immune response, inducing a more anti-inflammatory environment that supports fracture repair [331]. Similar anti-inflammatory effects have also been observed in healthy individuals, and reduced osteoclast differentiation during vibration *in vitro* [332, 333]. Importantly, whole body vibration has also been applied clinically in humans, where it has shown potential benefits for bone health, fracture healing, and reducing fall risk, particularly in older adults [334-336]. Collectively, current evidence suggests that vibration can positively influence bone health by promoting osteogenesis, but the precise cellular and biomechanical mechanisms remain to be fully elucidated.

EVs have recently been identified as key mediators of osteocyte-driven regulation of bone formation and resorption, functioning as potent vehicles for intercellular communication within the bone microenvironment. Increasing evidence demonstrates that EVs secreted by mechanically stimulated osteocytes promote stem cell recruitment [18], enhance bone formation and vascularization [19], and suppress osteoclastogenesis [199]. Importantly, these findings suggest that mechanical cues can be exploited not only to regulate bone remodelling in situ, but also to prime bone cells to produce EVs with enhanced pro-anabolic and pro-regenerative potential, positioning mechanically activated EVs as promising cell-free therapeutic agents. Collectively, this body of work highlights the broad therapeutic potential of EVs as multi-targeted, biologically active therapeutics for bone diseases. Despite these advantages, clinical translation of EVs-based therapies remains significantly limited by the low EVs yield obtained by standard cell culture and conventional isolation methods. In most *in vivo* studies, effective EVs doses typically range from 10 to 100 µg EVs per mouse [21, 337], however, standard culture systems generally yield only 0.5-1 µg EVs per 1 mL of conditioned medium. The pronounced gap between the therapeutic dose required and the achievable yields represents a major barrier to the advancement of EVs-based therapies in both preclinical and clinical applications. To overcome these limitations, various bioreactor systems have been tested to scale up EVs production, aiming to stimulate

larger amounts of cells to produce larger volumes of conditioned media in short amount of time. Scale up approaches include the use to multilayered cell culture flasks [251], hollow-fiber bioreactor [254, 338], stirred-tank bioreactor [257] and spheroid culture [339, 340].

In this context, the Nanokick bioreactor, designed by the Dalby group in collaboration with Dr. Peter Childs and team at the university of Glasgow, offers a time- and cost-efficient platform for stimulating large numbers of cells [341]. Previous studies have shown that this system applying nanovibration at 1 kHz and 30 nm displacement can enhance MSCs osteogenesis and inhibit osteoclast differentiation [332, 342, 343]. Building on this, this chapter aims to investigate the Nanokick Bioreactor as a method to scale-up production of osteocyte-derived mechanically activated EVs. For the first time, this bioreactor system was harnessed to stimulate osteocytes for 1 day and to assess how nanovibration influences their cellular response and the release of soluble factors with anabolic and anti-catabolic properties. Anabolic properties were characterised by assessing osteogenic potential, determined through osteogenic gene expression and calcium deposition, as well as angiogenic potential, evaluated by tube formation assay. EVs were subsequently isolated from nanovibrated osteocyte cultures and the anti-catabolic properties of CM and EVs were evaluated via osteoclastogenesis assay (**Figure 4.1**).

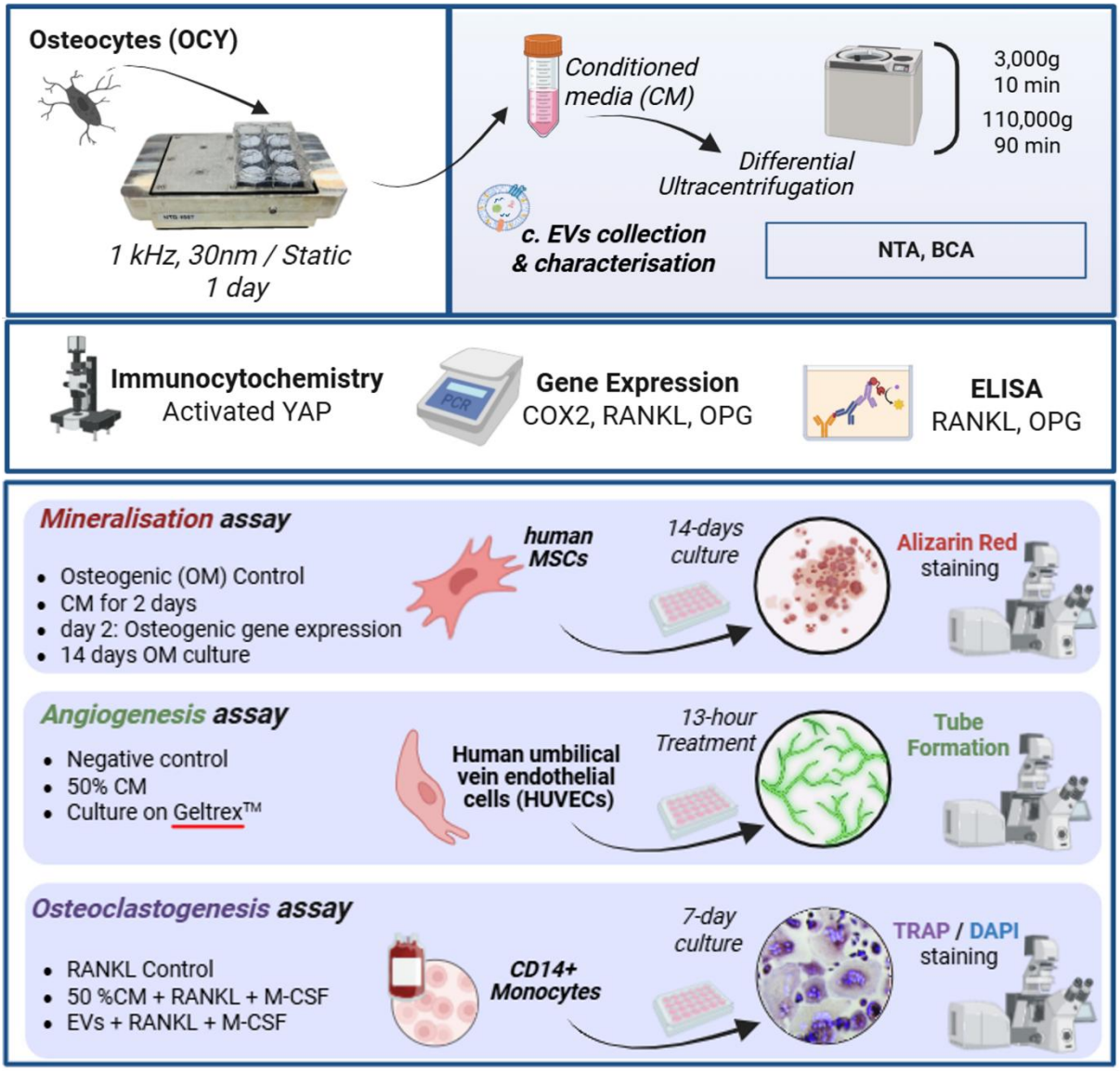

Figure 4.1. Schematic illustrating experiment design. Osteocytes were cultured under static conditions or subjected to 1 day nanovibration using the Nanokick Bioreactor. Cellular response to nanovibration was assessed through immunocytochemistry, gene expression, and cytokine production. The osteogenic, angiogenic and anti-osteoclastogenic potential of static and dynamic CM was subsequently evaluated. Finally, EVs were collected from static and dynamic CM, and their anti-catabolic potential was assessed.

4.2 Materials and methods

4.2.1 Cell culture

Murine osteocyte-like MLO-Y4 cells (Kerafast) were maintained in α-MEM (Merk) supplemented with 2.5 % FBS (Gibco), 2.5 % CS (Biosera), 1% P-S (Sigma) and 1% L-G (Sigma). Tissue culture flasks were coated for 1 h at room temperature with 0.15 mg/mL rat tail collagen type I (Corning), prepared in 0.02 M acetic acid (Sigma), prior to cell seeding. Cells were used for experiments when they had reached 80% confluency between passages 40-60.

4.2.2 Mechanical stimulation

MLO-Y4 were seeded into 6-well plates (Sarstedt) precoated for 1 h at room temperature with 0.15 mg/mL rat tail collagen type I, prepared in 0.02 M acetic acid, at a density of 1.16 x 10^4 cells/cm^2, and cultured in α-MEM supplemented with 2.5 % FBS, 2.5 % CS, 1% P-S and 1% L-G. After 24 h media was removed and replaced with 2.5 mL of fresh medium (serum free media was used when conditioned media was collected for angiogenesis assay). For EVs collection, cells were cultured in T-175 flasks under the same conditions. After 24 h, culture media was replaced with 20 mL EV-depleted fresh medium. Cells were then either maintained under static conditions or subjected to mechanical stimulation using the Nanokick bioreactor NTB 4000 series (Nanokick technologies), with the well plate or flask coupled to the bioreactor plate using a 2 mm tick rubber magnet sheet. Nanovibration was applied at 1 kHz frequency and 30 nm displacement for 1 day. Following stimulation, static and dynamic conditioned medium (CM) were collected, centrifuged at 3000 x g for 10 min at 4 °C and stored at 80 °C. The cells were either fixed for immunocytochemistry or lysed for mRNA extraction.

4.2.3 Immunocytochemistry

For immunocytochemistry (ICC), cells were fixed in 4% (w/v) paraformaldehyde (PFA) for 10 min at room temperature, then stored in PBS at 4 °C until immunostaining. Permeabilization was performed with 0.1% Triton X-100 (Sigma) for 10 min , followed by two PBS washes (Sigma) and blocking with 1% (w/v) bovine serum albumin (BSA) for 1 h. Activated YAP antibody was applied at a 1:100 dilution and incubated for 1 h at room temperature in the

dark, followed by Phalloidin staining (1:40) for 20 min under the same conditions. Finally, nuclei were counterstained with 4',6-diamidino-2-phenylindole (DAPI) (1:1000) for 10 min at room temperature, protected from light. Antibodies used are summarized in **Table 4.1** . Samples were imaged using a Leica SP8 scanning confocal microscope.

Table 4.1. Antibodies for ICC

Antibody	Supplier	Reference	Dilution
Activated YAP 1	Abcam	Ab225440	1:100
AlexaFluor488-Phalloidin	Life Tech	A12379	1:40

4.2.4 Image Analysis

Z-stacks from each image were combined into maximum intensity projections, and channels were overlaid. Background was excluded, and regions of interest (ROIs) were defined using the software (version 1.54p, NIH, USA) thresholding tool. Fluorescence intensity was then measured and background corrected.

4.2.5 Gene expression

Relative gene expression was assessed using quantitative real-time polymerase chain reaction (qRT-PCR). Total RNA was extracted by adding 1 mL TRIzol reagent (Sigma) to each well, and miRNA was isolated according to the manufacturer's protocol. RNA concentration was measured using a NanoDrop spectrophotometer (Thermo Fisher Scientific), and RNA purity was evaluated based on the 260/280 and 260/230 absorbance ratios. A total of 500 ng RNA from each sample was reverse transcribed into complementary DNA (cDNA) using the High-Capacity cDNA Reverse Transcription Kit (Applied Biosystems), following the manufacturer's instructions. The concentration of the resulting cDNA was determined using the Qubit™ ssDNA Assay Kit (Thermo Fisher Scientific). Quantitative PCR (qPCR) reactions were prepared using TaqMan Master Mix (Applied Biosystems) with 10 ng cDNA per reaction. The target genes analysed were *Cox2*, *Rankl*, and *Opg,* with *18s* used as housekeeping control. Amplification was performed on the 7500 Fast Real-Time PCR System (Life Technologies). Relative mRNA expression levels were calculated using the $2^{-\Delta\Delta Ct}$ method, normalized to *18s* expression, and expressed as fold change relative to the Static control group. Primer sequences are listed in **Table 4.2**.

Table 4.2. Murine TaqMan primes for qRT-PCR

Gene	Supplier	Catalogue Number	Assay ID
18s	Applied Biosystems	4331182	Mm03928990_g1
Cox2	Applied Biosystems	4331182	Mm00478374_m1
Rankl	Applied Biosystems	4331182	Mm00441906_m1
Opg	Applied Biosystems	4331182	Mm00435454_m1

4.2.6 Cytokine production

The concentrations of RANKL (Peprotech) and OPG (R&D Systems) in the collected CM were quantified by enzyme-linked immunosorbent assay (ELISA). Prior to the assay, CM was concentrated 2.5-fold using 10 kDa molecular weight cut-off (MWCO) Amicon™ Ultra-15 centrifugal filter units (Millipore). High-binding 96-well plates (Greiner Bio-One) were coated with 100 µL of capture antibody per well and incubated overnight at 4 °C. Following incubation, the capture antibody was removed, and non-specific binding sites were blocked with 1% (w/v) BSA in PBS for 1 h at room temperature. After blocking, plates were washed in tween-PBS solution, dried, and 100 µL of concentrated CM from each sample were loaded into wells in triplicate. A standard curve of serially diluted recombinant cytokine standard was loaded onto plates in triplicate. Blank wells containing assay diluents were included in each plate for background subtraction. Samples were incubated overnight at 4 °C. Following incubation, plates were washed and dried before the addition of 100 µL of biotinylated detection antibody per well and incubated for 2 h at room temperature with shaking (150 rpm). After washing, 100 µL of horseradish-peroxidase (HRP) conjugated to avidin (for RANKL) or streptavidin (for OPG) was added and incubated for 30 min in the dark with shaking (150 rpm). Plates were washed and dried again, and 100 µL of substrate solution was added according to the manufacturer's instructions. The enzyme-mediated colour reaction was protected from light during development. For OPG detection, the reaction was stopped with 2 N H_2SO_4, whereas the RANKL ELISA did not require a stop solution. Absorbance was measured at 405 nm (RANKL) and 450 nm (OPG) using a plate reader. Cytokine concentrations were determined from the standard curves, corrected for the concentration factor, using GraphPad Prism 10.5 software.

4.2.7 Osteogenesis assay

hMSCs were isolated from bone marrow and maintained in DMEM with GlutaMAX™ (Gibco) supplemented with 10 % FBS and 1 % P-S Cells were used for experiments when they had reached 80% confluency between passages 3-5. hMSCs were plated at a density of 6,500 cells/cm^2 for 4 days DMEM with GlutaMAX™ supplemented with 10 % FBS and 1 % P-S. Cells were then incubated for 48 h in static or dynamic CM and either lysed for gene expression or cultured for additional 14 days in supplemented osteogenic medium (growth media supplemented with 100 nM Dexamethasone, 10 mM βGlycerol Phosphate, 0.05 mM Ascorbic Acid). Expression of osteogenic genes and mineralisation were then assessed.

4.2.7.1 Osteogenic genes expression

Following 48 h incubation in static or dynamic CM, the expression of osteogenic genes was evaluated. Total RNA was extracted from samples using TRIzol reagent (Sigma) according to the manufacturer's protocol. RNA concentration was quantified with a NanoDrop spectrophotometer (Thermo Fisher Scientific), and purity was assessed using the 260/280 and 260/230 absorbance ratios. From each sample, 500 ng of RNA was reverse transcribed into cDNA using the High-Capacity cDNA Reverse Transcription Kit (Applied Biosystems), following the manufacturer's instructions. The concentration of the resulting cDNA was measured with the Qubit™ ssDNA Assay Kit (Thermo Fisher Scientific). qPCR was carried out using SYBR Select Master Mix (Applied Biosystems) with 10 ng of cDNA per reaction. The target genes analysed were *RUNX2*, *ALP*, *BMP2*, and *OCN*, with *18S* rRNA used as the housekeeping control (**Table 4.3**). Plates were read on the 7500 Fast Real-Time PCR System (Life Technologies).

Table 4.3. Forward and reverse SYBR Green primer sequences for qRT-PCR

Gene	Supplier	Catalogue number	Forward/Reverse sequence
RUNX2	Invitrogen	10629012	F: 5'- AAGCTTGATGACTCTAAACC
			R: 5'- TCTGTAATCTGACTCTGTCC
ALP	Invitrogen	10629012	F: 5'- TCTTCACATTTGGTGGATAC
			R: 5'- ATGGAGACATTCTCTCGTTC
BMP-2	Invitrogen	10629012	F: 5'- TCCACCATGAAGAATCTTTG
			R: 5'- TAATTCGGTGATGGAAACTG

OCN	Invitrogen	10629012	F: 5'- TTCTTTCCTCTTCCCCTTG R: 5'- CCTCTTCTGGAGTTTATTTGG
18S	Sigma	-	F: 5'-ATCGGGGATTGCAATTATTC R: 5'-CTCACTAAACCATCCAATCG

4.2.7.2 Mineral deposition

After 14 days of culture in osteogenic medium, calcium deposition was evaluated by Alizarin Red staining. Cells were fixed in 4% (w/v) paraformaldehyde (PFA) for 15 min at room temperature, rinsed with PBS and subsequently with deionized water (diH_2O), and then incubated with 1% Alizarin Red solution (Sigma) for 20 min at room temperature in the dark. Following incubation, the staining solution was removed, and wells were rinsed thoroughly with diH_2O until the background appeared clear. Wells were then air-dried and imaged under phase-contrast microscopy using an Olympus IX83 microscope equipped with a 4× objective. Quantification of calcium deposition was performed by destaining with 10% cetylpyridinium chloride (CPC) solution, and absorbance was measured at 540 nm.

4.2.8 Angiogenesis assay

Green Fluorescent Protein-expressing human umbilical vein endothelial cells (GFP-HUVECs) were maintained in Endothelial Basal Medium (EBM-2) supplemented with the EGM-2 BulletKit (Lonza). Cells were thawed at passage 8 and cultured in T-75 flasks (Sarstedt) pre-coated with 0.15 mg/mL rat tail collagen type I (Corning), prepared in 0.02 M acetic acid (Sigma). For angiogenesis assays, 48-well plates were coated with 100 µL/well of reduced growth factor basement membrane matrix Geltrex (Thermo Fisher Scientific) and incubated for 45 min at 37 °C to allow polymerization. GFP-HUVECs were seeded at a density of 25,000 cells/cm² onto the coated wells in a 1:1 ratio of serum free static or dynamic CM and serum-free HUVEC medium (growth medium lacking FBS and VEGF-A supplements) and incubated for 12 h at 37 °C, 5% CO_2 to enable tube formation. A negative control (-VEGF) consisting of a 1:1 combination of serum free MLO-Y4 growth medium (α-MEM supplemented with 1% L-G and 1% P-S) and serum free HUVEC medium was included in the experimental setup. Following incubation, cells were imaged at 488 nm using an Olympus IX83 microscope equipped with a 4x objective. Tube formation was analysed using the Angiogenesis Analyzer

plugin in ImageJ (version 1.54p, NIH, USA) and quantified by the number of junctions, number of segments, and total segment length, normalized to the negative control.

4.2.9 Osteoclastogenesis assay

The use of human blood samples for this study was approved by the research ethics committee of Trinity College Dublin and was conducted in accordance with the Declaration of Helsinki. Leukocyte-enriched buffy coats from anonymous healthy donors were obtained with permission from the IBTS, St. James's Hospital, Dublin (Researcher code: 0000RES625). Donors provided informed written consent to the IBTS for their blood to be used for research purposes. PBMCs were isolated from leukocyte-enriched human buffy coats using density gradient centrifugation with LymphoPrepTM solution (Progen). $CD14^+$ monocytes were isolated from PBMCs by magnetic sorting using MagniSort Human CD14 Positive Selection Kit (Invitrogen) according to the manufacturer's instructions. $CD14^+$ monocytes were seeded at 625,000 cells/cm^2 in 96-well plates in α -MEM containing 10 % FBS, 1 % P-S and 1 % L-G supplemented with 25 ng/mL M-CSF (Myltenyi Biotec) and 50 ng/mL Recombinant Human sRANK Ligand (RANKL) (PeproTech) (+RANKL) to induce osteoclastogenesis for 7 days. Groups cultured in growth media supplemented with 25 ng/mL M-CSF acted as a negative control for osteoclastogenesis (-RANKL). Static and dynamic was supplemented with 5 % FBS and added in a ratio of 1:1 along with growth media in presence of 50 ng/mL RANKL and 25 ng/mL M-CSF. Media and CM were replenished every 3.5 days. At day 7 cells were fixed with 2 % PFA for 15 min at room temperature, then washed twice with PBS and stained for tartrate-resistant acid phosphatase (TRAP) activity with a leukocyte acid Phosphatase (TRAP) Kit (Sigma) according to the manufacturer's protocols. Finally, cells were incubated with Triton X-100 0.1 % (Sigma) for 10 min, rinsed with PBS and then incubated with DAPI (1:1000) (Sigma) for 10 min. TRAP-positive multinuclear cells containing 3 or more nuclei were counted as osteoclasts. Cells were imaged using an Olympus IX83 inverted microscope with 10x objective and osteoclasts, number of nuclei per osteoclast, and total number of cells were manually counted using the cell counter plugin on Image-J software (version 1.54p, NIH, USA).

4.2.10 EVs collection and characterisation

EVs were collected from CM via ultracentrifugation using a TH660 swinging rotor. Static and dynamic CM were centrifuged at 2,000 g for 15 min at 4 °C and then filtered through a 0.45 µm pore filter. Next, CM were ultracentrifuged at 110,000 x g for 90 min at 4 °C. The resulting EVs pellets were washed in PBS and ultracentrifuged again at 110,000 x g for 90 min at 4 °C. Finally, EVs pellets were resuspended in PBS and stored at -80 °C. Protein content was assessed by BCA assay. 20 µL of EVs sample was suspended in 20 µL cell lysis buffer (Invitrogen) and 25X proteinase inhibitor (Roche). EVs lysate was incubated on ice for 30 min, vortexing every 10 min for 10 s. After 30 min, the sample was centrifuged at 13200 rpm at 4 °C for 10 min. The supernatant was transferred to a new tube and diluted 1:1 with PBS. EVs lysate protein content was quantified using Pierce™ BCA Protein Assay Kit (Thermo Fisher Scientific). BSA standards of 6.15-2000 µg/mL were prepared in PBS and used to calculate the protein content of the samples. 10 µL of standards and sample was added to a 96-well plate in triplicate. BCA reagent B was diluted 1:50 in BCA reagent A and 200 µL added to each standard and sample. Absorbance was read at 562 nm using a plate reader and protein levels were calculated from the standard curve. Nanoparticle size distribution, average diameter and concentration were assessed by NTA. EVs samples were diluted at 1:200 in PBS and injected into the NanoSight NS300 system (Malvern Technologies), which obtained five 60 s recordings of the particles in motion. Videos were then analysed with the NTA 3.4 software (camera level 14) to determine particle size and concentration.

4.2.11 Osteoclastogenesis assay following EV treatment

Human blood derived $CD14^+$ monocytes were seeded at 625,000 cells/cm^2 in 96 well plates in in α-MEM containing 10 % dFBS, 1 % P-S and 1 % L-G (growth media) supplemented either with 25 ng/mL M-CSF (Myltenyi Biotec) and 50 ng/mL RANKL (PeproTech) (+RANKL) to induce osteoclastogenesis for 7 days or with 25 ng/mL M-CSF alone (-RANKL) as a control. EVs enriched media was prepared by supplementing growth media with 0.25, 1 and 2 µg/mL of static or dynamic osteocyte-derived EVs in the presence of M-CSF and RANKL. Media and EVs were replenished after 3.5 days. Osteoclast differentiation was assessed by TRAP and DAPI staining as described above. Cells were imaged using Olympus IX83 inverted microscope with 10x objective and osteoclasts, number of nuclei per osteoclast and total

number of cells were manually counted using the cell counter plugin on Image-J software (version 1.54p, NIH, USA).

4.2.12 Statistical analysis

All data were analysed using GraphPad Prism 10.5. Data were analysed using unpaired t-test ordinary one-way ANOVA, assuming Gaussian distribution. Statistically significant differences were indicated as *p<0.05, **p<0.01, ***p<0.001, **** p<0.0001.

4.3 Results

4.3.1 Nanovibration of osteocytes does not elicit a mechanically driven cellular response

We first investigated the impact of nanovibration on osteocytes. Stimulation was applied for 1 day (24 h) using the Nanokick bioreactor under fixed parameters of 1 kHz frequency and 30 nm displacement. The response to mechanical stimulation was first assessed by YAP staining. Quantification of nuclear YAP fluorescence intensity after 1 day nanovibration revealed no significant difference between static and dynamic group, suggesting that this mechanical stimulus did not induce YAP dephosphorylation and nuclear translocation (**Figure 4.2 A,B**) a typical marker of mechanotransduction. To further evaluate whether nanovibration modulated osteocyte activity at the transcriptional level, the expression of mechanosensitive genes was analysed. No significant differences were observed in *Cox2* (**Figure 4.2 C**) *Rankl* (**Figure 4.2 D)** and *Opg* (**Figure 4.2 E**) expression, and the *Rankl/Opg* ratio (**Figure 4.2 F**) remained unchanged following stimulation. Cytokine production was then analysed to assess potential changes in osteocyte. ELISA analysis showed no significant differences in RANKL (**Figure 4.2 G**) or OPG (**Figure 4.2 H**) production, and the RANKL/OPG ratio in the CM was unaffected by stimulation (**Figure 4.2 I**). Collectively, these findings indicate that 1 day of nanovibration is insufficient to elicit a mechanically driven osteocyte response.

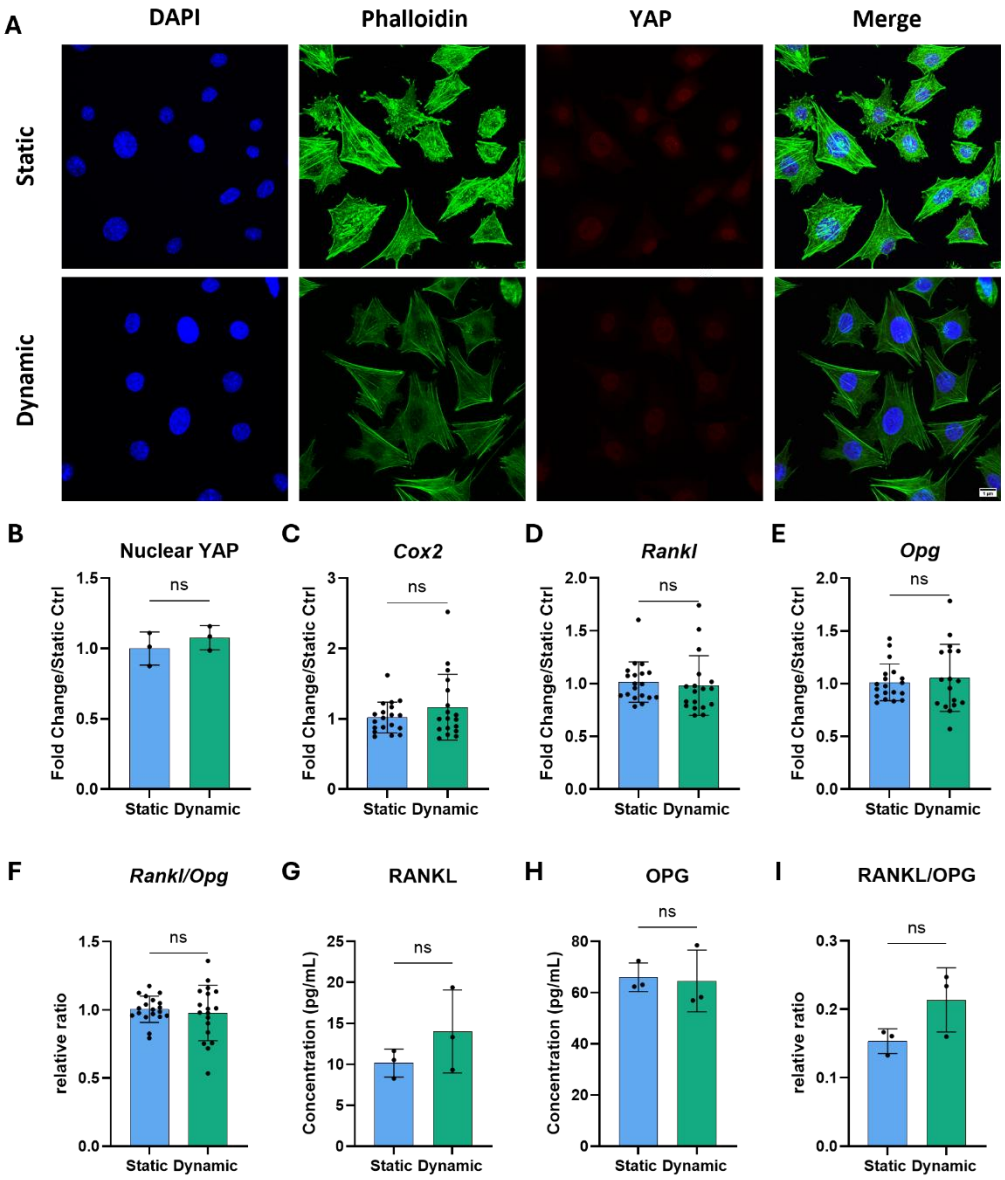

Figure 4.2. Nanovibrational stimulation of osteocytes does not elicit a mechanically driven cell response. **(A)** Nuclear YAP ICC staining (scale bar = 1 µm) and (B) quantification following osteocytes stimulation. Gene expression analysis of **(C)** *Cox2*, **(D)** *Rankl*, **(E)** *Opg* and **(F)** *Rankl/Opg* in response to osteocyte nanovibration. ELISA analysis of **(G)** RANKL, **(H)** OPG and **(I)** RANKL/OPG production in the CM following nanovibration. Statistical analysis was performed via unpaired t-test with Welch's correction.

4.3.2 Nanovibration of osteocyte does not enhance the osteogenic potential of their secretome

Given the established role of osteocytes in coordinating bone formation in response to mechanical cues, we next investigated whether nanovibration could enhance the anabolic properties of the osteocyte secretome. We first investigated the effect of osteocytes CM on hMSCs osteogenic gene expression. No significant differences were observed in *RUNX2*,

ALP, *BMP2* or *OCN* expression following 2 days pre-treatment with CM collected from osteocytes cultured under static or nanovibrated conditions, indicating that osteocyte secretome did not affect osteogenic lineage commitment regardless to the mechanical environment (**Figure 4.3 A**). Next, the impact of static and dynamic osteocyte secretome on long-term osteogenic differentiation of hMSCs was assessed via a 14-day mineralisation assay. Both static and dynamic osteocyte secretome significantly promoted hMSCs mineralisation after 14 days culture, with a 1.3-fold increase ($p<0.01$) for static CM and a 1.33-fold increase ($p<0.001$) for dynamic CM when compared to standard osteogenic controls. However, no difference was observed between static and dynamic groups, suggesting that nanovibration of osteocytes does not enhance the osteogenic potential of their secretome (**Figure 4.3 B, C**).

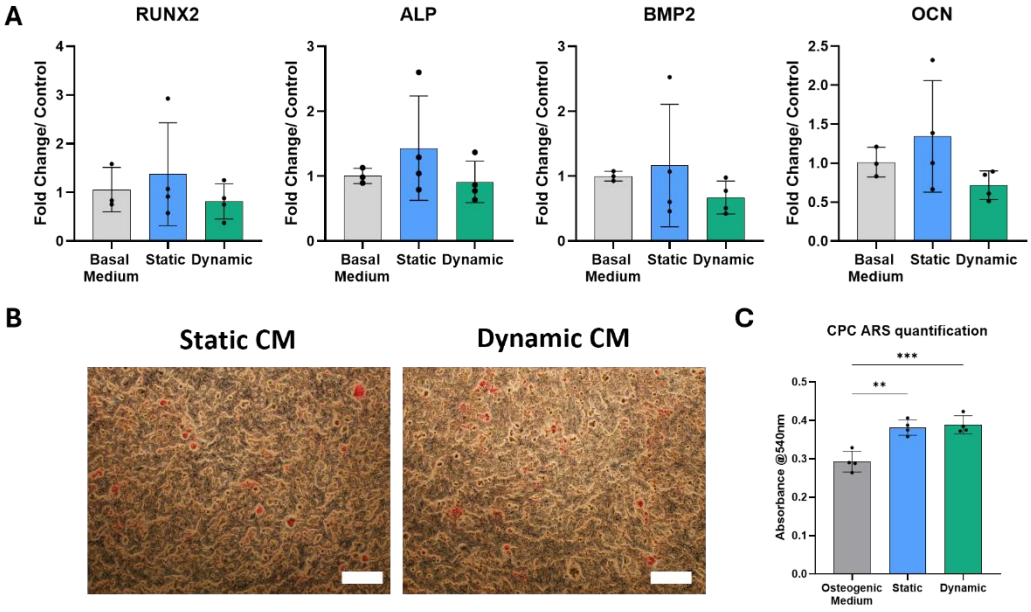

Figure 4.3. Nanovibrational stimulations of osteocytes does not alter the osteogenic potential of their secretome. (A) Gene expression osteogenesis related genes RUNX2, ALP, BMP2 and OCN following MSCs treatment for 48h with CM collected from osteocyte cultured in static condition or subjected to nanovibrational bioreactor. **(B)** Alizarin red staining following MSCs culture in osteogenic media for additional 14 days and **(C)** semi-quantification via CPC destaining. scale bar = 500 µm. Statistical analysis performed via ordinary one-way ANOVA, *p<0.05, **p<0.01, ***p<0.001, **** p<0.0001.

4.3.3 Nanovibration of osteocyte does not result in a secretome with angiogenic properties

Blood vessels play a crucial role in bone development and remodelling, providing resident cells with oxygen and essential growth factors [344]. The bone vasculature is primarily established trough angiogenesis, a process in which new vessels sprout from pre-existing ones. Therefore, we investigated whether subjecting osteocytes to nanovibration for 1 day would induce the secretion of paracrine factors capable of promoting angiogenesis. CM collected from osteocyte cultured under static or dynamic conditions did not enhance tube formation (**Figure 4.4 A**), with no significant differences between the two conditions in number of junctions (**Figure 4.4 B**) , number of segments (**Figure 4.4 C**) or total segments length (**Figure 4.4 D**) compared to negative control (-VEGF). Taken together these results suggest that this nanovibration regimen was not sufficient to stimulate an angiogenic response.

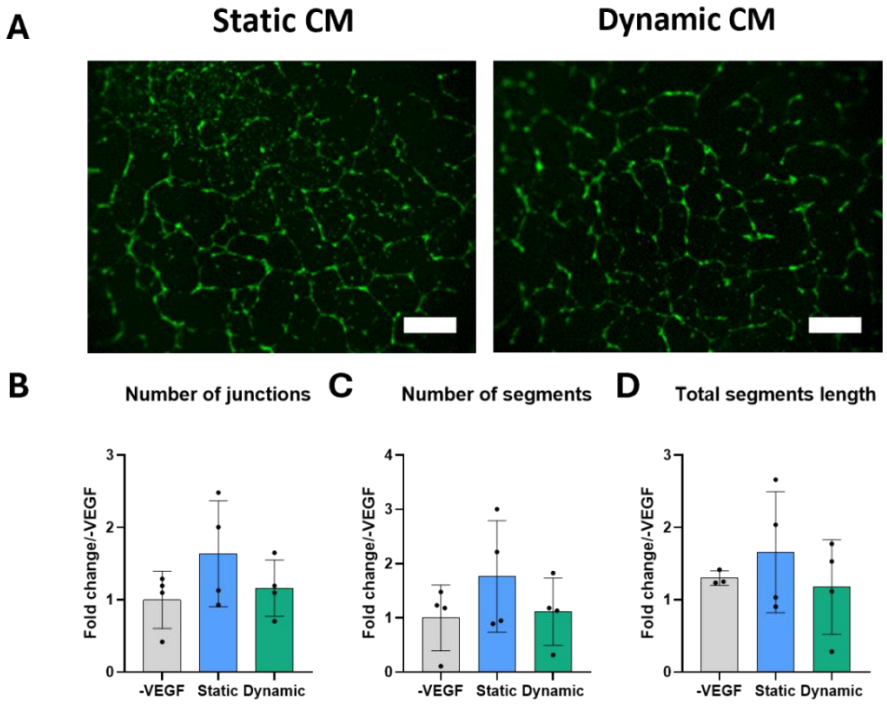

Figure 4.4. Osteocytes subjected to nanovibration do not produce a pro-angiogenic secretome. (A) Representative images of endothelial cell tube formation following a 13 h treatment with serum free osteocyte static and dynamic condition media. **(B, C, D)** Quantification of blood vessel formation assessed via average number of junction, segments and total segments length, respectively. scale bar = 500 µm. Statistical analysis performed via ordinary one-way ANOVA.

4.3.4 Osteocytes subjected to nanovibration secrete paracrine factors that do not possess anti-catabolic properties

Balance between bone formation and bone resorption is essential to maintain skeletal integrity. Disruption of this tight balance can result in bone disorders such as osteoporosis or osteopetrosis. In this context, we sought to determine how nanovibration modulates the osteocyte secretome with respect to its anti-catabolic potential. Osteoclast differentiation was assessed by culturing human $CD14^+$ monocytes for 7 days in presence of M-CSF and RANKL, supplemented with 50% osteocyte CM from either static or dynamic cultures (**Figure 4.5 A**). Quantification of the number of osteoclasts revealed no differences between the treatment groups (**Figure 4.5 B**). Similarly, analysis of the number of nuclei, used as a proxy for osteoclast maturation, showed no changes (**Figure 4.5 C**), and the total number of adhered cells remained comparable across conditions (**Figure 4.5 D**). Together, these findings indicate that under these experimental conditions, the osteocyte secretome does not exhibit anti-catabolic activity, and nanovibration is not sufficient to inhibit osteoclast differentiation.

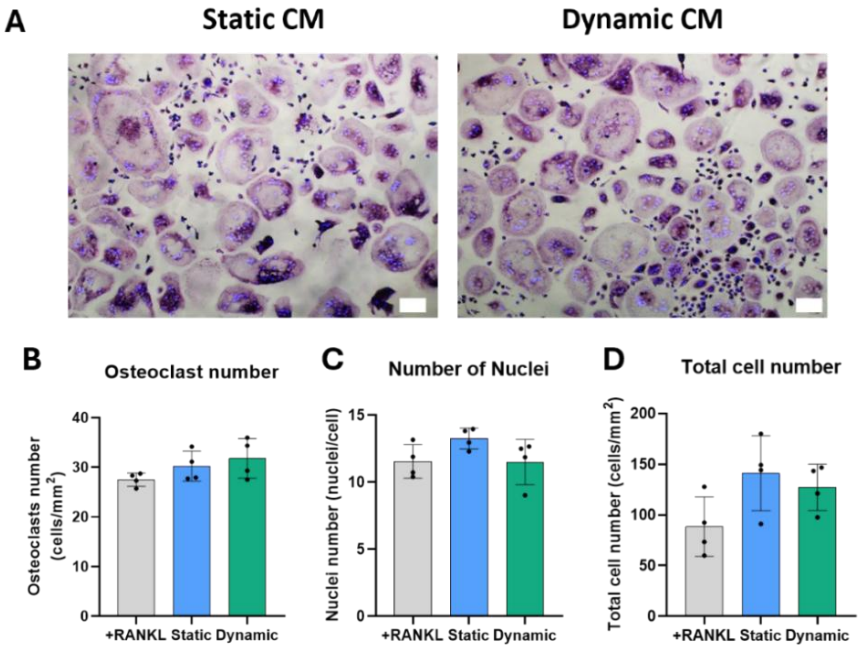

Figure 4.5. Nanovibration stimulation of osteocytes does not elicit the production of a secretome with anti-catabolic properties. (A) Representative images of TRAP and DAPI staining of human $CD14^+$ monocytes following 7 days treatment with static and dynamic osteocyte condition media in presence of M-CSF and RANKL. **(B)** Quantification of osteoclast number (identified as $TRAP^+$ cells with ≥ 3 nuclei), **(C)** number of nuclei and **(D)** total cell number. scale bar = 100 µm. Statistical analysis performed via ordinary one-way ANOVA.

4.3.5 Osteocytes secrete extracellular vesicles with comparable yield following nanovibration

In bone, EVs have emerged as key regulators of remodelling, mediating the coupling between osteoblasts, osteoclasts and osteocytes, as demonstrate by prior work in our group and by the findings discussed in the preceding chapter (Chapter 3) [18, 19]. To assess whether nanovibration influences osteocytes EVs secretion, EVs were collected from CM from osteocyte cultured under static or nanovibrated conditions using ultracentrifugation. NTA analysis was performed to determine size distribution and nanoparticle concentration. EVs collected from both conditions displayed similar size distribution profiles, predominantly ranging from 100 to 200 nm (**Figure 4.6 A**). Analysis of average particle diameter revealed that EVs from nanovibrated osteocytes ere slightly smaller (145 nm) compared to those from static cultures (157 nm, $p < 0.05$) (**Figure 4.6 B**). Nanoparticle concentration was comparable between the two vesicles populations (**Figure 4.6 C**) and similarly, total protein content, quantified by BCA assay, showed no differences (**Figure 4.6 D**). Collectively, these results suggest that osteocyte secrete EVs with comparable yield under static and nanovibrated conditions, with only minor differences in vesicle size.

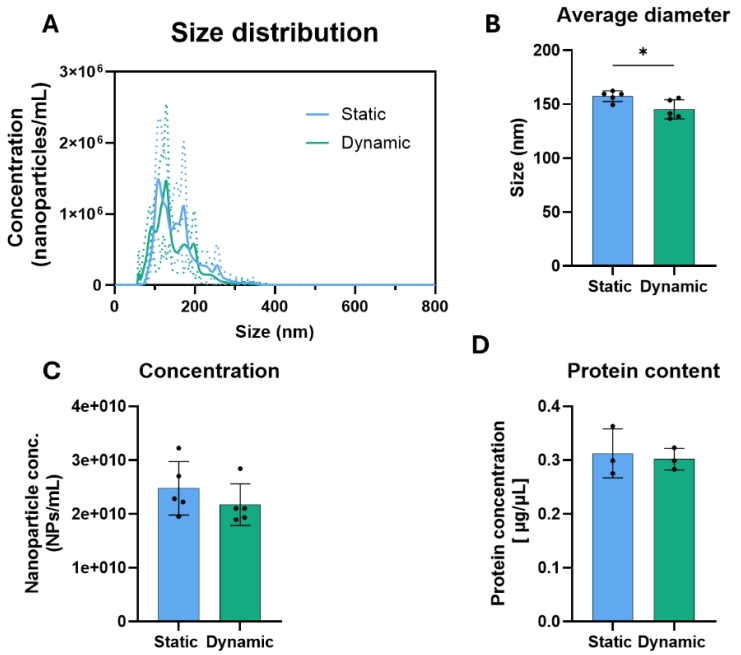

Figure 4.6. Static and nanovibrated osteocyte-derived EVs characterisation. Evaluation of EVs **(A)** Size distribution, **(B)** Average diameter, **(C)** Nanoparticle concentration, **(D)** Protein content. Statistical analysis performed via unpaired t-test, *p<0.05.

4.3.6 Nanovibration of osteocytes does not improve the anti-catabolic potential of secreted EVs

Given the role of osteocyte-derived EVs in inhibiting osteoclastogenesis when subjected to fluid flow [199, 345], we next sought to investigate whether vesicles secreted in response to nanovibration would exhibit anti-catabolic potential. Treatment with EVs at a dose equivalent to that contained in the CM resulted in a reduction in osteoclast number, independent of the mechanical environment. Specifically, EVs derived from static osteocyte culture reduced osteoclast number by 26% ($p< 0.0001$), while those from nanovibrated culture elicited a 23 % reduction ($p<0.001$) (**Figure 4.7 A, B**). Similarly, analysis of nuclei number showed a reduction in multinucleation, with no significant difference between static and nanovibrated condition (**Figure 4.7 C**). Total number of cells, however, showed no significant differences in adhesion compared to +RANKL control, suggesting that EVs did not affect monocyte adhesion (**Figure 4.7 D**). Collectively, these results demonstrate that osteocyte derived EVs inhibit osteoclast differentiation, but this effect is not enhanced by nanovibration.

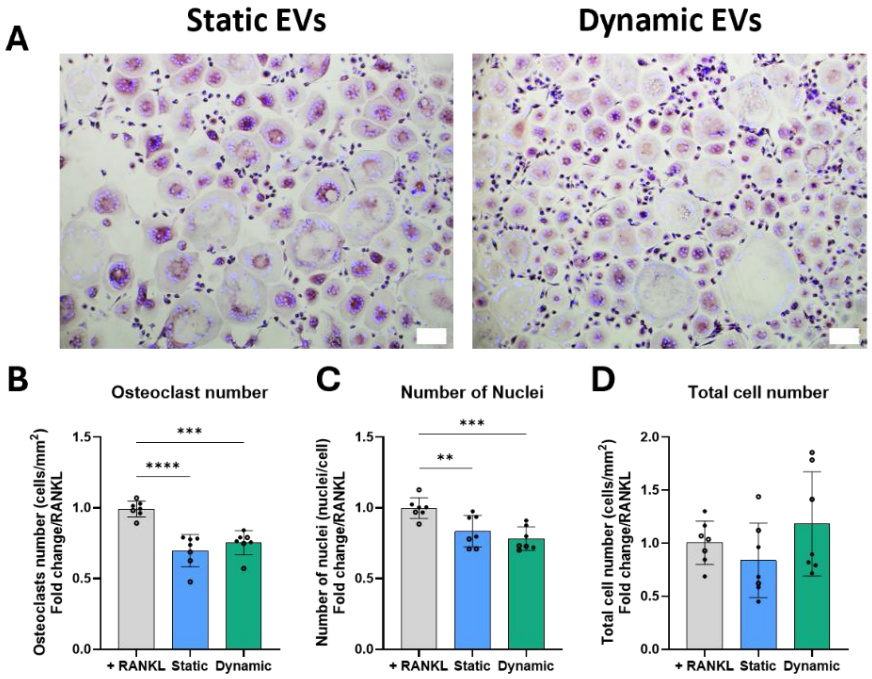

Figure 4.7. Osteocytes secrete extracellular vesicles that inhibit osteoclastogenesis independent of nanovibration. **(A)** Representative images of TRAP and DAPI staining of human $CD14^+$ monocytes following 7 days treatment with extracellular vesicles collected from static and dynamic osteocyte condition media, in presence of M-CSF and RANKL. **(B)** Quantification of osteoclast number (identified as $TRAP^+$ cells with ≥ 3

nuclei), **(C)** number of nuclei and (D) total cell number. scale bar = 100 µm. Statistical analysis performed via ordinary one-way ANOVA, *p<0.05, **p<0.01, ***p<0.001, **** p<0.0001.

4.3.7 Osteocytes-derived EVs anti-catabolic properties are dependent on dosage

Given the comparable anti-catabolic potency of EVs from static and nanovibrated cultures, we next evaluated the impact of EVs dosage on osteoclast differentiation. EVs were added to monocytes cultures in presence of the osteoclastogenic factor RANKL, at concentration of 0.5, 1 and 2 µg/mL to assess the impact of increasing EVs doses on osteoclastogenesis. Notably, only the lowest dose (0.5 µg/mL) significantly reduced osteoclast number, whereas higher doses, exceeding the EVs concentration in the CM, failed to inhibit differentiation. No differences were observed between static and nanovibrated osteocyte-derived EVs at any dose (**Figure 4.8 A, B**). Similarly, quantification of nuclei number revealed no reduction in multinucleation at higher doses (**Figure 4.8 C**), and total cell number remained constant across all groups (**Figure 4.8 D**). These findings highlight the existence of an optimal EVs dose to elicit an osteoclastogenic effect, although none of the tested doses was sufficient to induce a mechanically driven effect.

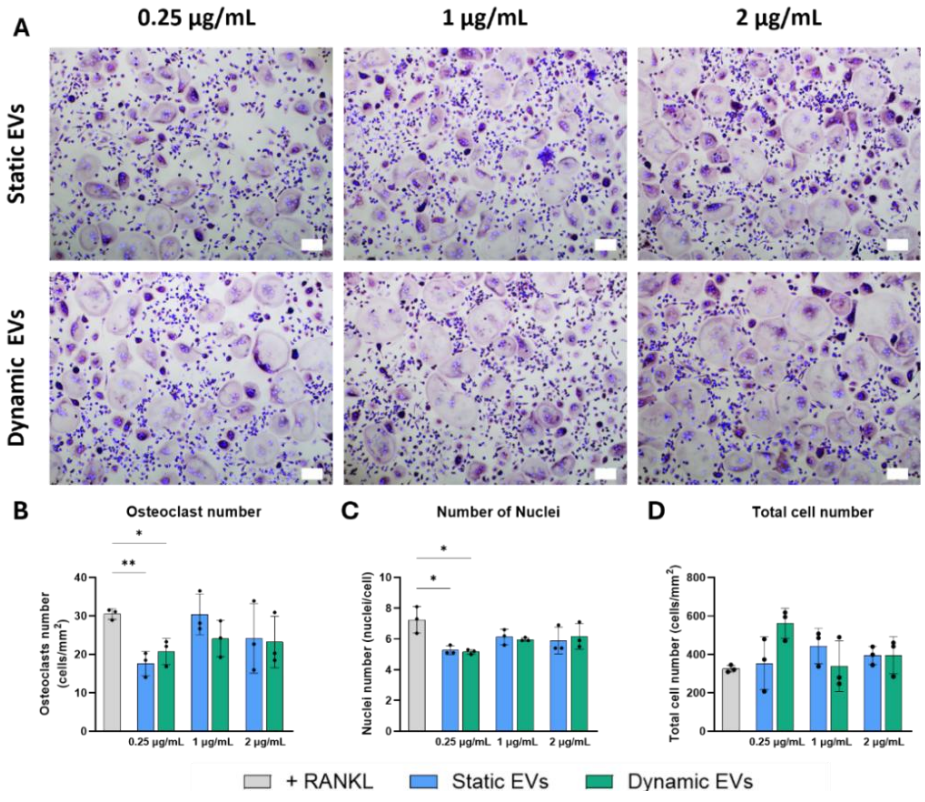

Figure 4.8. Low doses of osteocyte derived EVs demonstrate superior anti-catabolic potential. (A) Representative images of TRAP and DAPI staining of human $CD14^+$ monocytes following 7 days treatment with 0.25, 1 and 2 μg/mL of extracellular vesicles collected from static and dynamic osteocyte condition media, in presence of M-CSF and RANKL. **(B)** Quantification of osteoclast number (identified as $TRAP^+$ cells with ≥ 3 nuclei), **(C)** number of nuclei and **(D)** total cell number. scale bar = 100 μm. Statistical analysis performed via ordinary one-way ANOVA, *p<0.05, **p<0.01, ***p<0.001, **** p<0.0001.

4.4 Discussion

Osteocytes are the master regulators of bone remodelling, orchestrating osteoblast-mediated bone formation and osteoclast-mediated bone resorption in a mechanically regulated manner to maintain bone homeostasis. EVs have recently emerged as pivotal mediators of osteocyte signalling, with multiple lines of evidence demonstrating mechanical stimulation can modulate their cargo, enhancing their regenerative potential. Despite the fact that EVs represent promising therapeutics for bone regeneration, their translation potential is limited by low collection yield, representing a significant barrier to clinical application. In this chapter we investigate the Nanokick bioreactor as a platform to scale-up the production of mechanically activated osteocyte-derived EVs. Osteocytes were subjected to vertical nanovibration at 1 kHz frequency, 30 nm displacement for 1 day and resulting cellular response, pro-regenerative potential of the osteocyte secretome, and anti-catabolic properties of the secreted EVs were assessed. We demonstrate that nanovibration of osteocyte does not elicit a mechanically driven cellular response. Moreover, osteocyte secretome did not exhibit pro-regenerative potential, and the secreted EVs did not elicit an anti-catabolic response. Overall, while the Nanokick system provides a time- and cost-efficient platform for EVs production, nanovibration at 1 kHz and 30 nm of osteocytes is insufficient to elicit a mechanically activated regenerative response.

Exposure of osteocytes to nanovibration did not induce cellular response at either the transcriptional or protein level. While previous investigations have investigated osteocyte stimulation using low magnitude, high frequence vibrations in the 20-90 Hz range, we examined whether osteocytes would respond to a nanovibration regimen of 1 kHz with a 30 nm displacement for 1 day. Our findings demonstrate that 1 kHz nanovibration does not mechanically activate osteocytes, as evidenced by the absence of YAP nuclear translocation, unchanged expression of *Cox2*, *Rankl*, and *Opg*, and the absence of downstream cytokine production. Notably, extending the duration of stimulation to 3 days (data not shown) similarly failed to elicit any measurable osteocyte response, suggesting that duration alone is insufficient to drive mechanotransduction under these conditions. In comparison, Wu *et al.* examined the effects of 10-90 Hz vibration applied for 1 h and demonstrated osteocyte response to low magnitude high frequency vibration is frequency-dependent, demonstrating decreased *Cox2* expression as the frequency increases [325]. Conversely,

another independent study using a similar vibration regimen reported the opposite trend, showing increased *Cox2* expression at the higher frequency [346]. Together, these findings emphasizes that cellular responses to vibrational stimulation are highly dependent on the precise combination of frequency, amplitude, and duration, as well as the physiological context of the target cells. Overall, our observations suggest that osteocytes may require either alternative vibration regimens, particularly different frequencies or magnitudes, to achieve mechanical activation.

Osteocytes subjected to 1 kHz nanovibration do not produce a pro-regenerative secretome. CM secreted by osteocytes subjected to nanovibration did not enhance MSCs mineralisation or elicited endothelial tube formation. In addition to lacking anabolic potential, CM from these cultures did not inhibit osteoclast differentiation. Vibration has been widely investigated as a pro-osteogenic stimulus [347], with most studies focusing on the long-term application of 1 kHz nanovibration to MSCs over 14-28 days [342, 348-351]. In addition, direct application of 1 Hz nanovibration for 7 days in MSC-osteoclast precursor co-cultures has been shown to inhibit osteoclast formation [332]. However, relatively few studies have explored how nanovibration influences the ability of osteocytes to coordinate osteoblasts and osteoclasts activity. Evidence suggests that osteocytes respond differently depending on the vibration regimen. High frequency low magnitude stimulation has been reported to promote osteogenesis at lower frequencies but exert suppressive effects at higher ones [325, 352]. The effects on osteoclastogenesis remain more controversial. One study reported that high-frequency vibration of osteocytes (60 Hz, 0.3 g, 1 h) did not reduce overall osteoclast differentiation compared to static conditions, but it inhibited the formation of large osteoclasts and showed decreased resorption activity [346]. In contrast, another study demonstrated that while vibration itself did not directly affect osteoclastogenesis, preconditioning osteocytes with vibration (48.3 Hz, 0.5 g, 1 min) enhanced osteoclast formation in co-culture, driven by increased RANKL expression in osteocytes [353]. Collectively, our data can suggest 1 kHz frequency, 30 nm displacement nanovibration for 1 day may not lie within the stimulatory window required to induce a mechanically driven regenerative response.

EVs secreted by nanovibrated osteocytes did not display enhanced anti-catabolic potential. Although comparison between the Nanokick bioreactor and the PFC bioreactor

used in Chapter 3 demonstrated a clear improvement in production efficiency with comparable CM yields but substantially reduced hands-on time (~5 h vs ~32 h) and overall processing time (4 days vs 8 days), this increased scalability, and practicality did not translate into functional enhancement of EV bioactivity. When $CD14^+$ monocytes were treated with a dose of osteocyte-derived EVs equivalent to that present in the conditioned medium, osteoclastogenesis was inhibited regardless of the mechanical environment. Thus, nanovibration did not lead to the secretion of EVs with greater anti-catabolic activity. Interestingly, this contrasts with the response observed following treatment with the whole osteocyte secretome, where no inhibition of osteoclastogenesis was detected under either static or nanovibrated conditions. These differences may be explained by the contribution of soluble factors within the secretome, which could have counteracted the inhibitory activity of EVs. Notably, these soluble factors appeared to exert comparable effects under both conditions. These findings align with the lack of osteocyte response at both transcriptional and protein level following nanovibration. Furthermore, treatment with higher doses of osteocyte-derived EVs did not inhibit osteoclastogenesis, under either static or nanovibrated conditions, consistent with our previous findings indicating the presence of an optimal dose to maximise osteocyte-derived EVs anti-catabolic potential. Although previous studies have demonstrated that mechanical stimulation can enhance the anti-catabolic potential of osteocyte-derived EVs [199, 345], we demonstrate that 1 kHz frequency, 30 nm displacement vibration for 1 day does not drive osteocyte mechanical activation and does not result in the secretion of EVs with enhanced anti-catabolic potential. Therefore, despite the improved scalability of EVs production achieved with this bioreactor compared to our standard system, the lack of osteocyte responsiveness and the absence of functionally enhanced EVs preclude its suitability as a high-throughput platform for the generation of mechanically activated osteocyte-derived EVs.

4.5 Conclusion

In summary, this study aimed to develop an approach for scaling up the production of mechanically activated osteocyte-derived EVs to address the scalability limitations of our standard bioreactor system. To achieve this, we assessed the osteocyte response to 1 kHz frequency, 30 nm displacement nanovibration over 1 day, examined the regenerative potential of the osteocyte secretome following stimulation, and evaluated the anti-catabolic activity of the secreted EVs. Our findings demonstrate that this nanovibration regimen was insufficient to elicit a mechanically driven regenerative response, thereby limiting the suitability of this system for large-scale production of mechanically activated osteocyte-derived EVs.

Chapter 5. Bone-Derived Matrix Vesicles as a Multi-targeted Therapeutic Strategy for Tissue Regeneration

5.1 Introduction

Bone fractures constitute a substantial and increasing global health burden, accounting for millions of hospitalizations annually and generating significant long-term disability and healthcare expenditure. This burden is amplified by demographic shifts toward aging populations and the rising prevalence of comorbidities such as osteoporosis and diabetes, all of which compromise skeletal repair. While most fractures heal through endogenous regenerative mechanisms, approximately 10% develop delayed healing or progress to non-union, conditions associated with chronic pain, functional impairment, and the need for repeated surgical interventions. [354, 355]. Fracture repair is a highly dynamic and multistage biological process that requires the precise temporal coordination of inflammation, immune regulation, angiogenesis, osteogenesis, and matrix remodelling. Disruption of any one of these interdependent processes can derail healing, particularly in large defects [356]. This complexity has driven growing interest in multimodal therapeutic approaches capable of modulating several aspects of the repair process simultaneously.

Cell-based regenerative therapies have emerged as a promising approach to enhance fracture healing in challenging clinical scenarios. In particular, MSC-based therapies have attracted considerable attention due to their capacity to influence immune responses, promote vascularization, and support osteogenic processes in parallel. Preclinical and early clinical studies have demonstrated improved healing outcomes following MSC-based interventions in delayed unions, non-unions, and critical-sized bone defects, highlighting their potential as multitargeted biological therapies [357]. Importantly, accumulating evidence has refined the mechanistic understanding of how transplanted cells contribute to regeneration. Rather than functioning primarily through long-term engraftment or direct differentiation into bone-forming cells, MSCs appear to exert their therapeutic effects predominantly via paracrine mechanisms, secreting a diverse array of bioactive mediators that reshape the local fracture microenvironment and activate endogenous repair programs [358]. This shift from a cell replacement paradigm toward a cell-instructive model, guiding

endogenous cells via bioactive cues such as EVs, has important implications for the development of next-generation regenerative strategies.

In this context, attention has increasingly turned toward EVs as central mediators of MSC-derived paracrine signalling. EVs encapsulate proteins, lipids, and nucleic acids reflective of their parent cells and can coordinate immune modulation, angiogenesis, and osteogenic signalling, key biological processes required for effective fracture repair [359]. As a cell-free therapeutic modality, EVs offer several advantages over live cell transplantation, including reduced immunogenicity, elimination of risks associated with uncontrolled proliferation or ectopic engraftment, improved stability during storage and handling, and enhanced feasibility for standardized, scalable, off-the-shelf manufacturing [360]. Despite their therapeutic promise, EV-based strategies for bone repair are limited by several practical and biological challenges. Most current approaches rely on EVs isolated from conditioned media, yielding vesicle populations that are freely secreted into the extracellular space but may not fully represent the diversity of EVs present within native tissues. By contrast, tissue-derived EVs offer enhanced physiological relevance and improved yields by capturing vesicles produced and retained within their endogenous extracellular environment. This distinction is particularly important given evidence that EV-mediated signalling is predominantly short-range, with vesicles acting mainly within the pericellular or local tissue niche [361], highlighting the importance of context-specific EV populations. In bone, where cellular activity is tightly integrated with the extracellular matrix, this spatial restriction suggests the existence of EV subpopulations that are locally retained rather than freely diffusible. As a result, standard EV preparations that do not account for tissue-resident vesicles may overlook populations with specialised roles in local mineralisation and cell-matrix communication. Moreover, challenges associated with EV production, including limited yields and difficulties in achieving scalable manufacturing, further constrain their translational potential. Together, these considerations motivate focused investigation of bone-derived EV subtypes that are intrinsically adapted to the extracellular matrix and may exert distinct biological functions relevant to skeletal physiology and regeneration.

Matrix vesicles (MVs) are a specialised class of EVs released into the extracellular space and embedded within the extracellular matrix, where they act as sites of nucleation for apatite crystals playing a central role in physiological calcification. Interest in these vesicles

dates to the late 1960s, when electron microscopy studies first described membrane-bound, electron-dense “calcifying globules” in epiphyseal cartilage and linked them to the earliest sites of mineral deposition. Early biochemical analyses showed that these vesicles contain specialized lipids, alkaline phosphatase, and calcium-binding components that promote the deposition of hydroxyapatite [362, 363]. Subsequent work on mineralization mechanisms demonstrated that non-collagenous proteins and other extracellular matrix components regulate crystal nucleation, growth, and mineral maturation, providing essential biochemical context for how MVs initiate mineralization [364, 365]. These findings established that mineralisation is not a passive chemical event but a tightly regulated, vesicle-mediated process initiated by MVs. Although originally described in bone and cartilage, MVs have also been identified in other tissues in physiological conditions, such as in bladder [366], and liver [367], or in pathological contexts such as vascular calcification [368]. Besides their role in mineralisation, MVs have also been shown to have a role in cell-cell communication as they can carry morphogenetic proteins, metalloproteases, and miRNAs [369]. However, despite their early discovery, compared with the extensive work on EVs, relatively few studies have systematically isolated MVs from mineralised or soft tissues and characterised their molecular cargo or investigated their physiological function, particularly in relation to regenerative potential.

Recent evidence indicates that MVs are naturally retained within decellularized extracellular matrix scaffolds [366] and are also likely to be present in auto- and allografts, the current gold standard for bone repair. Their persistence in these materials suggests that MVs may contribute to the biological activity associated with ECM-derived grafts. Coupled with their distinctive biochemical features and their capacity to carry regulatory proteins, lipids, and nucleic acids, this raises the intriguing possibility that MVs could support regenerative processes when delivered within a biomaterial context. This possibility has gained conceptual interest, yet their translational relevance within tissue-engineering strategies, particularly in combination with clinically applicable scaffolds and MSCs, has not been investigated to date. As a result, the extent to which MVs might be harnessed for therapeutic purposes remains uncertain.

In parallel, accumulating evidence indicates that the composition and function of bone cell-derived EVs are shaped by age-dependent changes in skeletal structure and cell

behaviour that differ substantially between males and females. Skeletal ageing follows sex-specific trajectories, reflecting differences in bone geometry, remodelling dynamics, and cellular responsiveness established earlier in life. In males, ageing is commonly associated with continued periosteal expansion and relative preservation of bone size, whereas females exhibit more limited periosteal growth, leading to distinct age-related changes in cortical thickness, bone geometry, and mechanical competence [370]. Consequently, male and female bones experience ageing-related mechanical and biological cues within different architectural contexts. At the cellular level, ageing alters osteogenic cell populations in both sexes, but these changes are increasingly recognised as sexually dimorphic. MSCs from aged donors show reduced proliferation, altered differentiation, and changes in paracrine signalling, with age-associated declines in colony formation and osteogenic potential being more pronounced in MSCs derived from female donors compared with males [371]. Such sex-specific alterations in cell behaviour provide a plausible basis for age-related changes in EV bioactivity. Accordingly, circulating EVs from elderly donors exhibit reduced osteo-inductive potential relative to those from young individuals [372]. Mechanical loading remains a key regulator of bone throughout ageing, yet skeletal responses to mechanical cues differ between sexes and change with age. Male and female bones experience distinct strain distributions under equivalent loads, with these differences becoming more pronounced with ageing due to sex-specific changes in bone geometry and material properties rather than differences in loading per se [373]. At the cellular level, ageing impairs the ability of bone cells to sense and respond to mechanical strain in a sex-dependent manner. Cortical long-bone osteoblasts from aged males and females both were shown to exhibit reduced proliferative responses to mechanical strain compared with young cells, but the mechanisms underlying this decline differ between sexes, indicating that ageing disrupts mechanosensitivity through distinct cellular pathways in males and females [374, 375]. These observations raise the possibility that MVs may be dynamically shaped by physiological factors like sex, age and exercise, although the extent to which these variables alter MVs function remains to be fully elucidated.

Taken together, these considerations highlight the need for a systematic and comparative evaluation of MVs across tissue sources, physiological conditions, and translational scenarios. In this chapter, we therefore investigate the protein signature, miRNA cargo and

functional characteristics of MVs derived from murine long bones and kidneys, examine how physiological factors such as age and exercise modulate the bioactivity of bone-derived MVs, and assess whether their incorporation into biomaterials can enhance human osteogenesis. By integrating compositional insights, functional assays, and biomaterial-based approaches, this work seeks to develop a comprehensive understanding of the biological and regenerative properties of MVs and to evaluate whether they could serve as a more scalable alternative to cultured cell-derived EVs within cell-free strategies for bone repair.

5.2 Materials and methods

5.2.1 Matrix Vesicles collection

Matrix vesicles were isolated from C57BL/6J mice of different ages and conditions: 5-month-old males, 3-month-old males and females, and 18-month-old sedentary or exercised males and females. The exercised group began treadmill training at 3 months of age, consisting of three sessions per week (30 min/session: 5 min at 6 m/min, 5 min at 10 m/min, and 20 min at 14 m/min, 0° incline). Following euthanasia, femurs, tibiae, and kidneys were collected. Bone marrow was removed, and tissues were minced into small fragments. Samples were sequentially washed with 70% ethanol, iodine solution, and finally with cold synthetic cartilage lymph (SCL) containing 2 mM $CaCl_2$, 1.42 mM NaH_2PO_4, 1.83 mM $NaHCO_3$, 12.7 mM KCl, 0.57 mM $MgCl_2$, 100 mM NaCl, 0.47 mM Na_2SO_4, 5.55 mM D-glucose, 63.5 mM sucrose, 15.5 mM 2-[(2-hydroxy-1,1-bis(hydroxymethyl)ethyl) amino]-ethanesulfonic acid (TES), pH 7.4. Tissues were digested with collagenase type I from *Clostridium histolyticum* (200 U of collagenase/ g of tissue in SCL supplemented with 1 mM $CaCl_2$) at 37 °C for 3 h under shaking (150 rpm). Digests were filtered through a 70 µm nylon filter and tissue debris were discarded. The filtrate was centrifuged at 600 x g for 15 min at 4 °C and the pellet was discarded. The resulting supernatant was centrifuged at 20,000 x g for 20 min at 4 °C and the supernatant was further ultracentrifuged using a TH660 swinging rotor at 110,000 x g for 90 min at 4 °C. Next, MVs pellets were washed in SCL and ultracentrifuged again at 110,000 x g for 90 min at 4 °C. Finally, MVs pellets were resuspended in SCL and stored at -80 °C.

5.2.2 Osteoblast- and osteocyte-derived EVs collection

Murine osteoblast MC3T3-E1 cells (ATCC) were cultured in α-MEM (Merck) supplemented with 10% FBS (Gibco), 1% P-S (Sigma), and 1% L-G (Sigma). Murine osteocyte MLO-Y4 cells (Kerafast) were maintained in α-MEM supplemented with 2.5% FBS, 2.5% CS (Biosera), 1% P-S, and 1% L-G. For serum-free conditions, osteoblast cells were cultured in α-MEM containing 1% P-S and 1% L-G, while osteocyte cells were cultured in α-MEM supplemented with 0.5% dFBS, 0.5% dCS, 1% P-S, and 1% L-G. Tissue culture flasks for osteocyte cells were pre-coated with 0.15 mg/mL rat tail collagen type I (Corning) in 0.02 M acetic acid (Sigma) for 1 h at room temperature before seeding. Cells were seeded into T-175 flasks at a density

of 1.16 × 10^4 cells/cm^2. After 24 h, cultures were washed twice with PBS and replenished with 15 mL of serum-free medium. CM was collected after an additional 24 h and centrifuged at 3,000 × g for 10 min at 4 °C to remove cells and debris. EVs were isolated from CM by differential ultracentrifugation using a 70Ti fixed-angle rotor. Briefly, CM was centrifuged at 2,000 × g for 15 min at 4 °C, filtered through a 0.45 µm pore filter, and ultracentrifuged at 110,000 × g for 75 min at 4 °C. The EVs pellet was washed once with PBS, followed by a second ultracentrifugation step at 110,000 × g for 75 min at 4 °C. Final EVs pellets were resuspended in PBS and stored at -80 °C.

5.2.3 Matrix Vesicles Characterisation

5.2.3.1 Nanoparticle tracking analysis

Nanoparticle size analysis was performed on MVs with the NanoSight NS300 system (Malvern Technologies) to determine particle size based on Brownian motion. MVs samples were diluted at 1:250 in SCL and injected into the NTA system. For each sample, five 60 s readings were recorded (camera level 14), and particle size and concentration were subsequently analysed using the NTA 3.4 software.

5.2.3.2 BCA assay

10 µL of MVs or EVs were suspended in 10 µL cell lysis buffer (Invitrogen) and 25X proteinase inhibitor (Roche). Samples were incubated on ice for 30 min with brief vortexing (10 s) every 10 min. Following incubation, lysates were centrifuged at 13,200 rpm for 10 min at 4 °C. The resulting supernatant was transferred to a new tube and diluted 1:1 with PBS. Protein concentration was determined using the Pierce™ BCA Protein Assay Kit (Thermo Fisher Scientific). BSA standards ranging from 6.15 to 2000 µg/mL were prepared in PBS to generate a standard curve. For the assay, 10 µL of standards and samples were loaded in triplicate into a 96-well plate. Working BCA reagent was prepared by diluting reagent B (1:50) in reagent A, and 200 µL was added to each well. Absorbance was measured at 562 nm using a microplate reader, and protein concentrations were calculated from the standard curve.

5.2.3.3 Alkaline Phosphatase (ALP) activity

Surface enrichment of ALP on MVs was quantified using the SIGMAFAST™ pNPP kit (Sigma). A standard curve was generated in 96-well plates using serial dilutions of p-nitrophenyl

phosphate (pNPP) with 10 µL of 43 µM ALP enzyme (Sigma). For the assay, MVs samples were diluted 1:250 -1:500 in dH_2O to a final volume of 80 µL per well. Subsequently, 50 µL of 5 mM pNPP was added to each well. Samples were incubated for 1 h at room temperature in the dark, and absorbance was measured at 405 nm using a plate reader. ALP activity was calculated as the amount of pNPP generated by samples, divided by sample volume and reaction time, and expressed relative to the total number of nanoparticles and grams of digested tissue digested.

5.2.3.4 Transmission electron microscopy (TEM)

A 20 µL droplet of MVs derived from 5-month-old mice was placed onto Parafilm (Sigma). A formvar carbon-coated nickel grid (Ted Pella Inc.) was positioned on the droplet with the coated side facing the suspension and incubated for 1 h at room temperature. Grids were then washed three times on 30 µL PBS droplets (5 min each) placed on Parafilm, with excess liquid removed using absorbent paper. For fixation, grids were placed on a 2% PFA droplet for 10 min, followed by the same PBS washing steps. Samples were contrasted with 2% uranyl acetate (BDH) before imaging. Transmission electron micrographs were acquired using a JEOL JEM-2100 microscope operated at 120 kV.

5.2.3.5 Super-resolution dSTORM Microscopy

Super-resolution imaging of MVs derived from 5-month-old mice was performed using a Nanoimager S Mark II microscope (ONI, Oxford Nanoimaging, Oxford, UK) equipped with a 100× oil immersion objective (NA 1.45) and four lasers (405 nm/150 mW, 488 nm/1 W, 560 nm/500 mW, 640 nm/1 W). Fluorescence excited by the 488, 560, and 640 nm lasers was collected using band-pass filters of 498–551 nm, 576–620 nm, and 665–705 nm, respectively. MVs samples were prepared for dSTORM imaging using the ONI EV Profiler Kit 2 (EVP2), following the manufacturer's protocol. The kit includes a panEV membrane dye, tetraspanin antibodies (CD9, CD63, CD81), capture chips and reagents, and the ONI BCubed dSTORM Imaging Buffer, all of which were used in this study. Sequential three-channel dSTORM datasets (647, 560, and 488 nm) were acquired using the AutoEV CODI acquisition software. A total of 1000 frames per channel were collected at 40 ms exposure per frame, with laser powers set to 180 mW (488 nm), 45 mW (560 nm), and 170 mW (640 nm). For panEV staining, 3000 images were recorded. Prior to each imaging session, channel alignment was calibrated using bead slides, achieving mapping precision below 10 nm.

Single-molecule localization, clustering, and positivity analyses were performed using the default EVP2 app settings within the CODI software (https://alto.codi.bio). Data outputs were exported as both reports and CSV files for further analysis.

5.2.3.6 Multiplex Surface Marker Analysis

MACSPlex analysis of MVs and EVs was performed using the MACSPlex EV Kit IO, mouse (Miltenyi Biotec), which detects 37 surface epitopes and includes two isotype controls. Samples containing 5 µg of protein were diluted in MACSPlex buffer to a final volume of 120 µL and incubated overnight with 15 µL of MACSPlex EV Capture Beads in 1.5 mL tubes at room temperature on a tube rotator (12 rpm), protected from light. Following incubation, 500 µL of MACSPlex buffer was added to each tube and samples were centrifuged at 300 × g for 5 min at room temperature. After removing 500 µL of supernatant, 5 µL each of the MACSPlex Detection Reagents CD9, CD63, and CD81 were added. Tubes were incubated for 1 h at room temperature on a rotator (12 rpm), protected from light. Next, 500 µL of MACSPlex buffer was added, followed by centrifugation at 3,000 × g for 5 min. Supernatants (500 µL) were discarded, and 500 µL of fresh buffer was added to each tube for an additional 15 min incubation under the same conditions. Samples were centrifuged again at 3,000 × g for 5 min, and 450 µL of supernatant was removed, leaving 200 µL. The pellet was resuspended and transferred to FALCON™ 5 mL polystyrene round-bottom tubes (Corning). After the final step, a flow cytometry-based quantification method was employed using the Aurora spectral flow cytometer (Cytek Biosciences, USA). Samples were then set to enter the fluidics system at a controlled and low flow rate (10 µL/min) with a set volume of 25 µL (analysis performed with 2 technical replicates per sample). The SpectroFlo® software (Cytek®, USA) was used to acquire all raw data and the FlowJo softwarev10.8.1. (TreeStar, USA) was used for all post-acquisition analysis. Median fluorescence intensity (MFI) for all 39 capture beads was background corrected by subtracting MFI values of non-vesicle buffer that was treated exactly like the vesicles groups. Hierarchical clustered heatmap was generated using ClustVIs [376] and functional annotation and enrichment analysis of the identified proteins was performed using the STRING database [377]. Enriched gene ontology (GO) terms were visualised through bubble plots generated in R Studio (version 2025.05.1, Build 513) using the ggplot2 package.

5.2.4 Osteogenesis Assay

Human osteoblast-like SaOS-2 cells (Cytion) were maintained in DMEM GlutaMAX™ supplemented with 10% FBS and 1% P-S. Cells between passages 12-20 were used once they reached 80% confluency. For osteogenesis assay, cells were seeded into 24-well plates (Corning) pre-coated with 0.15 mg/mL rat tail collagen type I (prepared in 0.02 M acetic acid) at a density of 10,000 cells/cm² and cultured in DMEM GlutaMAX™ supplemented with 10% dFBS and 1% P-S. After 3.5 days, the culture medium was replaced with 500 µL of osteogenic medium (growth medium supplemented with 100 nM dexamethasone, 10 mM β-glycerophosphate, and 0.05 mM ascorbic acid). For experiments with MVs derived from 5-month-old mice, osteogenic medium was supplemented with 0.25, 0.5, 1.5, or 2.5 µg/mL bone- or kidney-derived MVs. For experiments with MVs derived from 3- or 18-month-old mice, osteogenic medium was supplemented with 1.5 µg/mL bone-derived MVs. Positive control received osteogenic medium alone, while negative controls were maintained in growth medium. Osteogenic medium was replenished after 3.5 days of culture. After 7 days in osteogenic medium, calcium deposition was assessed by Alizarin Red staining. Cells were fixed with 4% (w/v) PFA for 15 min at room temperature, rinsed with PBS followed by diH_2O, and incubated with 1% Alizarin Red solution for 20 min at room temperature in the dark. Excess stain was removed by repeated washing with diH_2O until the background appeared clear. Wells were air-dried and imaged under phase-contrast microscopy using an Olympus IX83 microscope equipped with a 4x objective. Quantification of calcium deposition was performed by destaining with 10% CPC solution, and absorbance was measured at 540 nm. Absorbance values were normalised to positive control.

5.2.5 Angiogenesis assay

GFP-HUVECs were maintained in EBM-2 supplemented with the EGM-2 BulletKit (Lonza). Cells were thawed at passage 8 and cultured in T-75 flasks (Sarstedt) pre-coated with 0.15 mg/mL rat tail collagen type I (Corning), prepared in 0.02 M acetic acid. For angiogenesis assays, 96-well plates were coated with 25 µL well of reduced growth factor basement membrane matrix Geltrex (Thermo Fisher Scientific) and incubated for 45 min at 37 °C to allow polymerization. Cells were then seeded at a density of 10,000 cells/well in EBM-2 supplemented with 1% P-S. For experiments with MVs derived from 5-month-old mice, cultures were supplemented with 0.25, 0.5, 1.5, or 2.5 µg/mL bone- or kidney-derived MVs.

For experiments using MVs derived from 3- or 18-month-old mice, 1.5 µg/mL bone-derived MVs were added. Positive controls received growth medium, whereas negative controls received EBM-2 alone. Cells were incubated for 10 h at 37 °C, 5% CO_2 to allow tube formation. Following incubation, cells were imaged at 488 nm using an Olympus IX83 microscope equipped with a 4x objective. Tube formation was analysed using the Angiogenesis Analyzer plugin in ImageJ (version 1.54p, NIH, USA) and quantified by the number of nodes, number of junctions, number of segments, and total segment length, normalized to the negative control.

5.2.6 Osteoclastogenesis assay

The use of human blood samples for this study was approved by the research ethics committee of Trinity College Dublin and was conducted in accordance with the Declaration of Helsinki. Leukocyte-enriched buffy coats from anonymous healthy donors were obtained with permission from the IBTS, St. James's Hospital, Dublin (Researcher code: 0000RES625). Donors provided informed written consent to the IBTS for their blood to be used for research purposes. PBMCs were isolated from leukocyte-enriched human buffy coats using density gradient centrifugation with LymphoPrepTM solution (Progen). $CD14^+$ monocytes were isolated from PBMCs by magnetic sorting using MagniSort Human CD14 Positive Selection Kit (Invitrogen) according to the manufacturer's instructions. $CD14^+$ monocytes were seeded at 625,000 cells/cm^2 in 96-well plates in α -MEM containing 10 % dFBS, 1 % P-S and 1 % L-G supplemented with 25 ng/mL M-CSF (Myltenyi Biotec) and 50 ng/mL Recombinant Human sRANK Ligand (RANKL) (PeproTech) (+RANKL) to induce osteoclastogenesis for 7 days. Negative control (-RANKL) was maintained in growth medium containing only M-CSF (25 ng/mL). For experiments with MVs derived from 5-month-old mice, +RANKL cultures were further supplemented with 0.25, 0.5, 1.5, or 2.5 µg/mL bone- or kidney-derived MVs. For experiments with MVs derived from 3- or 18-month-old mice, 1.5 µg/mL bone-derived MVs were added. Media and MVs were replenished after 3.5 days. After 7 days culture, cells were fixed with 2 % PFA for 15 min at room temperature, then washed twice with PBS and stained for TRAP activity with a leukocyte acid Phosphatase (TRAP) Kit (Sigma) according to the manufacturer's protocols. Finally, cells were incubated with Triton X-100 0.1 % (Sigma) for 10 min, rinsed with PBS and then incubated with DAPI (1:1000) (Sigma) for 10 min. TRAP-positive multinuclear cells containing 3 or more nuclei

were classified as osteoclasts. Cells were imaged using an Olympus IX83 inverted microscope with 10x objective. Osteoclasts, nuclei per osteoclast, and total cell counts were quantified manually using the Cell Counter plugin in ImageJ (version 1.54p, NIH, USA) and normalised to +RANKL control.

5.2.7 miRNA sequencing

5.2.7.1 Total RNA extraction

Total RNA was extracted from EV samples using the miRNeasy Mini Kit (Qiagen) according to the manufacturer's instructions. EVs were lysed in 1 mL QIAzol reagent by mixing on a vortex for 10 s. Lysis buffer was spiked with 1 µL of 1:250 diluted miRCURY spike-in mix (Qiagen). Phase separation was achieved by adding 200 µL chloroform, followed by centrifugation. RNA was precipitated with ethanol in the presence of 50 µg/mL glycogen to enhance the RNA yield. Washing steps were performed automatically on a QIAcube instrument (Qiagen). RNA was eluted in 30 µL nuclease-free water. RNA concentration and integrity were not analysed due to the very low RNA yield. Purified total RNA samples were stored at -80 °C until further processing.

5.2.7.2 Small RNA sequencing

Small RNA libraries were prepared from 8.5 µl total RNA using the RealSeq® Small RNA Library Preparation Kit (RealSeq Biosciences) following the protocol described by Khamina *et al.* [378] Adapter-ligated and reverse-transcribed libraries were quantified by qPCR to determine the optimal number of PCR amplification cycles. Amplification was performed using barcoded Illumina reverse primers in combination with the Illumina forward primer. Library quality was assessed using DNA Fragment Analyzer reagents (Agilent). Equimolar pooling of individual libraries was performed prior to sequencing on a NextSeq 2000 instrument (Illumina) with 100 bp single-end reads. Sequencing data were processed using the miND® analysis pipeline reported by Diendorfer *et al.* [379]. Briefly, reads were demultiplexed, and quality was assessed using the tools FastQC and MultiQC. Adapter trimming and quality filtering were performed with the tool Cutadapt, retaining reads ≥17 nt in length. Reads were mapped to the mouse genome (GRCm39, Ensembl) using Bowtie v1.2.2 allowing up to two mismatches, followed by mapping to miRBase v22.1 (https://www.mirbase.org/) allowing one mismatch, via miRDeep2 v2.0.1.2. Statistical

analyses were performed in R v3.6 using the R packages pheatmap v1.0.12, pcaMethods v1.78, and genefilter v1.68. Differential expression analysis was conducted using R package edgeR v3.28, employing quasi-likelihood negative binomial generalized log-linear models. To enhance false discovery rate (FDR) control, the independent filtering approach of DESeq2 was adapted for edgeR to remove low-abundance miRNAs prior to testing.

5.2.7.3 Bioinformatic data analysis

PCA analysis and heatmaps were generated with ClustVis [376] using ln-transformed and univariate scaled RPM values. Volcano plot was generated in R using the ggplot2. miRNA expression data were retrieved from the miRNA Tissue Atlas (2025 release; https://web.ccb.uni-saarland.de/mirnatissueatlas_2025/). Expression profiles from the indicated mouse tissues were extracted, and the top 12 upregulated and top 12 downregulated miRNAs were selected for subsequent analysis. Target genes of bone enriched microRNAs were identified using miRNAtap (Maciej Pajak 2017), which allows to combine the results of 5 different miRNA-mRNA interaction databases: DIANA [380], Miranda [381], PicTar [382], TargetScan [383], and miRDB [384]. By providing the miRBase ID of individual miRNAs, a predictions table containing the ranks for each target gene as well as the aggregated rank product was estimated. The number of target genes was filtered by specifying a minimum number of 3 databases where the target gene must be found. microRNA~mRNA target interactions were visualized as chord diagrams using the R package chorddiag v0.1.3.

5.2.8 Manufacture of B-MVs delivery platform

5.2.8.1 B-MVs loaded collagen-nHA scaffolds

Collagen-nano-hydroxyapatite (Coll-nHA) scaffold were fabricated following the technique described by Cunniffe *et al*. [385]. Briefly, a collagen slurry was prepared by blending Type-I microfibrillar bovine collagen (Integra Life Sciences, Inc) with 0.5 M acetic acid. nHA particles were synthesized as previously reported [386] and added to the collagen slurry during the blending process to achieve a 1:1 ratio nHA to collagen ratio. Following blending, the slurry was degassed using a vacuum pump to remove entrapped air bubbles and subsequently freeze-dried at -40◦C under 200 Torr vacuum to produce the final scaffold material. Cylindrical samples (6 mm diameter, 4 mm height) were produced using a biopsy

punch and hydrated in PBS prior to crosslinking. Scaffolds were crosslinked for 2 h at room temperature in a solution containing 1-ethyl-3-(3-dimethylaminopropyl) carbodiimide hydrochloride (EDAC) and N-hydroxysuccinimide (NHS) prepared in dH_2O, using 6 mmol EDAC per gram of collagen and a 5:2 EDAC: NHS molar ratio, calculated based on collagen content only. Excess unreacted EDAC/NHS was removed by three sequential PBS washes. For B-MV loading, B-MVs derived from 5 months-old male mice were used and the effective scaffold volume was first calculated by correcting the geometric volume for scaffold porosity. This adjusted volume was then used to determine the total quantity B-MVs required to achieve a final concentration of 1.5 µg/mL. The calculated amount of B-MVs for each scaffold was subsequently suspended in 40 µL of 0.15 mg/mL Type-I collagen solution, which was then soak-loaded into the Coll-nHA scaffolds (20 µL per side) for 15 min at 37 °C. Control scaffolds were soak loaded with 40 µL of collagen solution.

5.2.9 Therapeutic efficacy of B-MVs in hMSCs on Coll-nHA scaffold

5.2.9.1 hMSCs culture and osteogenic differentiation

hMSCs were isolated from bone marrow and cultured in DMEM with GlutaMAX™ (Gibco), supplemented with 10% FBS and 1% P/S. Cells at passage 3 were used once they reached approximately 80% confluency. For seeding, 2×10^5 hMSCs were suspended in 40 µL of medium and distributed evenly onto both sides of each scaffold (20 µL per side), followed by a 15 min incubation at 37 °C to allow cell attachment. After 24 h, the growth medium was replaced with osteogenic medium, composed of growth medium supplemented with 100 nM Dexamethasone, 10 mM β-Glycerol Phosphate, 0.05 mM Ascorbic Acid. Cells were then cultured on the scaffolds for 21 days in osteogenic medium, with medium changes twice weekly.

5.2.9.2 Analysis of hMSCs metabolic activity

Cell metabolic activity during osteogenic differentiation was assessed using the Alamar Blue assay following the manufacturer's protocol (Invitrogen). At days 0, 7, 14, and 21, culture medium was removed, and scaffolds were rinsed with PBS. Alamar Blue reagent was diluted 1:10 in fresh osteogenic medium, and 500 µL of the working solution was added to each scaffold. Samples were incubated for 4 h at 37 °C, protected from light, after which

fluorescence was measured using excitation and emission wavelengths of 530 nm and 590 nm, respectively.

5.2.9.3 Analysis of B-MVs effect on osteogenic gene expression

After 7 days of culture in osteogenic medium, osteogenic gene expression was evaluated. The medium was removed from each scaffold, followed by a PBS rinse, and 1 mL of TRIzol reagent (Sigma) was added. Samples were then stored at -80 °C for 48 h before total RNA extraction using the manufacturer's protocol. RNA concentration was measured using a NanoDrop spectrophotometer (Thermo Fisher Scientific), and purity was assessed from the 260/280 and 260/230 ratios. RNA was reverse-transcribed into cDNA using the High-Capacity cDNA Reverse Transcription Kit (Applied Biosystems), and cDNA concentration was determined with the Qubit™ ssDNA Assay Kit (Thermo Fisher Scientific). Quantitative PCR (qPCR) was performed using SYBR Select Master Mix (Applied Biosystems) with 10 ng of cDNA per reaction. The genes analysed included *RUNX-2*, *BMP-2*, *ALP*, *OCN*, and *VEGF-A*, with *18S* serving as the housekeeping control (**Table 5.1**). Reactions were run on a QuantStudio™ 5 PCR System (Applied Biosystems). The relative mRNA amounts of each sample were calculated using the $2^{-\Delta\Delta Ct}$ method with reference to 18S housekeeping gene and expressed as fold change normalised to the control group.

Table 5.1. Forward and reverse SYBR Green primer sequences for qRT-PCR

Gene	Supplier	Catalogue number	Forward/Reverse sequence
RUNX-2	Invitrogen	10629012	F: 5'- AAGCTTGATGACTCTAAACC R: 5'- TCTGTAATCTGACTCTGTCC
BMP-2	Invitrogen	10629012	F: 5'- TCCACCATGAAGAATCTTTG R: 5'- TAATTCGGTGATGGAAACTG
ALP	Invitrogen	10629012	F: 5'- TCTTCACATTTGGTGGATAC R: 5'- ATGGAGACATTCTCTCGTTC
OCN	Invitrogen	10629012	F: 5'- TTCTTTCCTCTTCCCCTTG R: 5'- CCTCTTCTGGAGTTTATTTGG
VEGF-A	Invitrogen	10629012	F: 5'- AGGGCAGAATCATCACGAAGT R: 5'- AGGGTCTCGATTGGATGGCA
18S	Sigma	-	F: 5'-ATCGGGGATTGCAATTATTC R: 5'-CTCACTAAACCATCCAATCG

5.2.9.4 DNA assay

DNA content was quantified using the Quant-iT™ PicoGreen® dsDNA Assay Kit (Invitrogen) following the manufacturer's protocol. On day 21, culture medium was removed, and scaffolds were rinsed with PBS. Each scaffold was lysed in 1 mL of lysis buffer containing 0.2% (v/v) Triton X-100 (Sigma) and 10 mM Tris (pH 8) (Thermo Fisher Scientific) prepared in ultrapure diH_2O. Complete cell lysis was achieved through three freeze-thaw cycles between -80 °C and room temperature. For the assay, DNA standards were prepared according to the manufacturer's instructions, and 100 µL of either standard or sample lysate was transferred to a black 96-well plate. A 1:200 PicoGreen working solution was then added at 100 µL per well, and fluorescence was measured at 485 nm excitation and 538 nm emission.

5.2.9.5 ALP assay

Intracellular ALP activity was quantified using the SIGMAFAST™ pNPP kit (Sigma) after 21 days of culture. A standard curve was generated in a round bottom clear 96-well plate using serial dilutions of pNPP together with 10 µL of 43 µM ALP enzyme (Sigma). For sample measurements, the cell lysates prepared for DNA quantification were also used for ALP analysis. Lysates were diluted 1:1 in dH_2O to a final volume of 80 µL per well, after which 50 µL of 5 mM pNPP solution was added. Samples were incubated for 1 h at room temperature in the dark, and absorbance was recorded at 405 nm. ALP activity was calculated from the amount of pNPP generated, divided by sample volume and incubation time, and finally normalised to DNA content.

5.2.9.6 Calcium assay

Calcium deposition on the 3D Coll-nHA scaffolds was quantified using the LiquiColor® Calcium kit (StanBio 0150) following the manufacturer's instructions. After 21 days of culture, medium was first aspirated from each scaffold, which was then rinsed twice with PBS. Scaffolds were transferred to individual Eppendorf tubes containing 1 mL of 0.5 M HCl and incubated overnight at 4 °C under rotation to ensure complete decalcification and calcium ion extraction. After incubation, the working reagent was prepared by mixing the Total Calcium Colour Reagent and Total Calcium Base Reagent in a 1:1 ratio, and a standard curve was generated using serial dilutions of the 100 µg/mL calcium standard in 0.5 M HCl. For the assay, 10 µL of each sample, diluted 1:6 in 0.5 M HCl, or standard was pipetted into

a clear 96-well plate, followed by 200 µL of the working reagent. Absorbance was measured at 595 nm. Calcium content of pristine scaffolds (cell-free) was subtracted from the samples' values.

5.2.9.7 Histological evaluation

At day 21 of culture, scaffolds were washed twice in PBS and fixed in 4% PFA for 1 h at room temperature. Following fixation, constructs were rinsed twice in PBS, embedded in optimal cutting temperature (OCT) compound, and frozen at -80 °C for at least 24 h prior to sectioning. Sections of 7 µm thickness were obtained using a cryostat (Leica CM3050 S) and mounted onto SuperFrost™ microscope slides (Fisher Scientific), then stored at -80 °C until staining. Picrosirius Red and Alizarin Red staining were performed to assess collagen and mineral deposition, respectively. Imaging was carried out using an Aperio AT2 slide scanner (Leica).

5.2.10 Statistical analysis

All data were analysed using GraphPad Prism 10.5. Data were analysed using unpaired or Welch's t test, Ordinary or Brown- Forsythe and Welch One-way ANOVA and Ordinary Two-way ANOVA, assuming Gaussian distribution. Statistically significant differences were indicated as *p<0.05, **p<0.01, ***p<0.001, **** p<0.0001.

5.3 Results

5.3.1 Matrix Vesicles can be collected with high yield from adult murine mineralised and non-mineralised tissues

MVs were collected from both long bones and kidneys from 5-month-old male mice. Following collagenase digestion of the tissues, MVs were collected via ultracentrifugation and characterised in accordance with the MISEV guidelines [178] (**Figure 5.1 A**). NTA analysis was performed to determine MVs size distribution and concentration. Bone and kidney-derived MVs exhibited comparable size distribution profiles, ranging from 150 to 200 nm, with average diameters of 165 nm and 180 nm, respectively, a size range consistent with that seen in cell derived EVs (**Figure 5.1 B, C)**. Notably, kidneys-derived MVs displayed a significant higher nanoparticle number per gram of digested tissue (7.35 x 10^9 NPs/g tissue) compared to bone-derived MVs (4.87 10^9 NPs/g tissue, ($p<0.0001$) (**Figure 5.1 D**). However, no significant differences were observed in terms of protein content between the two MVs populations (**Figure 5.1 E**). In terms of their intrinsic activity, both MVs populations were found to harbour functional ALP, with bone-derived MVs displaying significantly higher ALP activity ($p<0.0001$), potentially indicating pro-mineralising potential (**Figure 5.1 F).** TEM revealed that both MVs population possessed nanosized and spherical morphology (**Figure 5.1 G**). Finally, the presence of the traditional tetraspanins markers was assessed via super resolution microscopy. Both bone and kidneys derived MVs were found to express CD9, CD63, and CD81 (**Figure 5.1 H**). The presence of the tetraspanins markers provides further evidence that the isolated vesicles conform to the defining features of EVs, reinforcing the reliability of the isolation protocol. Collectively, these results demonstrate that MVs were successfully isolated in high quantity from adult murine tissues, overcoming the challenge of isolating vesicles from highly mineralised tissues.

A

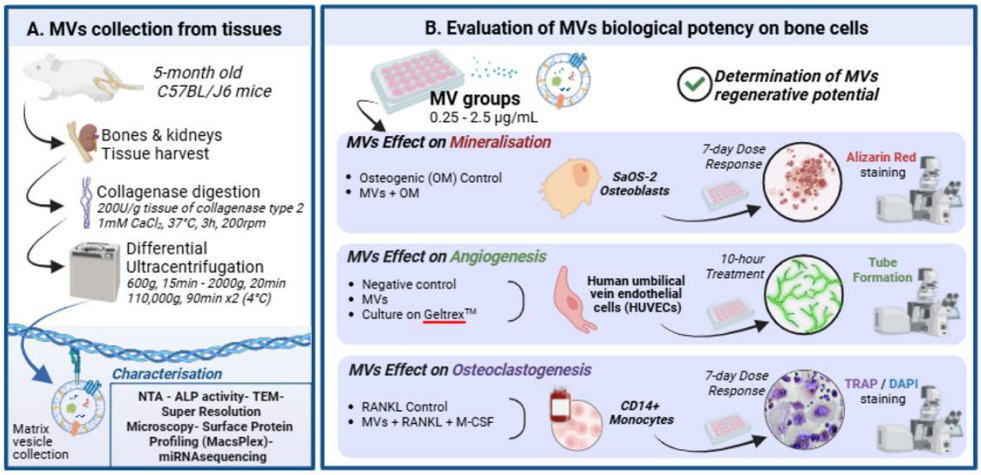
A. MVs collection from tissues
5-month old C57BL/J6 mice
Bones & kidneys Tissue harvest
Collagenase digestion
200U/g tissue of collagenase type 2
1mM CaCl2, 37°C, 3h, 200rpm
Differential Ultracentrifugation
600g, 15min - 2000g, 20min
110,000g, 90min x2 (4°C)
Characterisation
Matrix vesicle collection
NTA - ALP activity- TEM- Super Resolution Microscopy- Surface Protein Profiling (MacsPlex)- miRNAsequencing
B. Evaluation of MVs biological potency on bone cells
MV groups
0.25 - 2.5 µg/mL
Determination of MVs regenerative potential
MVs Effect on Mineralisation
Osteogenic (OM) Control
MVs + OM
SaOS-2 Osteoblasts
7-day Dose Response
Alizarin Red staining
MVs Effect on Angiogenesis
Negative control
MVs
Culture on Geltrex™
Human umbilical vein endothelial cells (HUVECs)
10-hour Treatment
Tube Formation
MVs Effect on Osteoclastogenesis
RANKL Control
MVs + RANKL + M-CSF
CD14+ Monocytes
7-day Dose Response
TRAP / DAPI staining

B

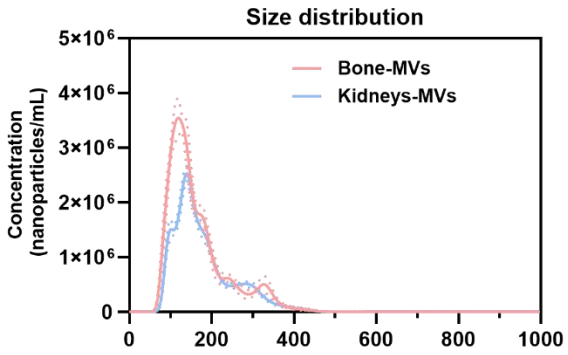
Size distribution
Bone-MVs
Kidneys-MVs
Concentration (nanoparticles/mL)
5×10^6
4×10^6
3×10^6
2×10^6
1×10^6
0
0
200
400
600
800
1000

C

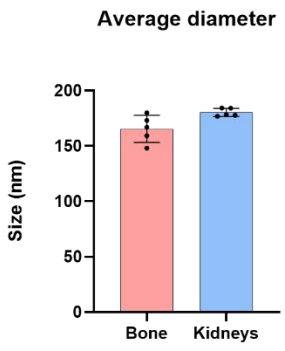
Average diameter
Size (nm)
200
150
100
50
0
Bone
Kidneys

D

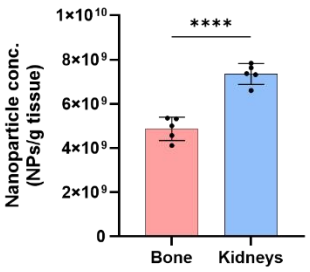
Concentration
Nanoparticle conc. (NPs/g tissue)
1×10^10
8×10^9
6×10^9
4×10^9
2×10^9
0
****
Bone
Kidneys

E

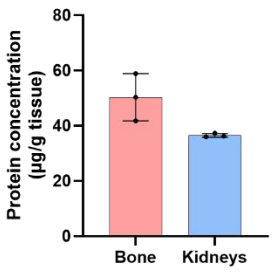
Protein content
Protein concentration (µg/g tissue)
80
60
40
20
0
Bone
Kidneys

F

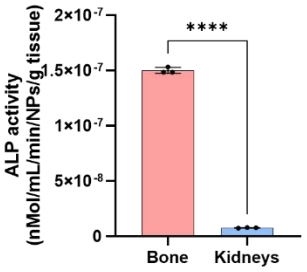
ALP activity
ALP activity (nMol/mL/min/NPs/g tissue)
2×10^-7
1.5×10^-7
1×10^-7
5×10^-8
0
****
Bone
Kidneys

G

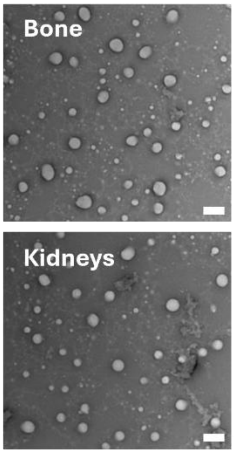
Bone
Kidneys

H

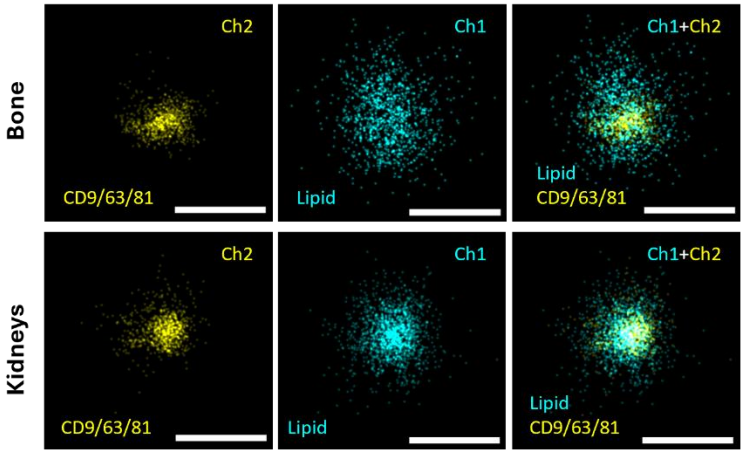
Bone
Kidneys
Ch2
CD9/63/81
Ch1
Lipid
Ch1+Ch2
Lipid
CD9/63/81

Figure 5.1. Isolation and characterisation of MVs derived from murine long bones and kidneys. (A) Schematic of experimental workflow for Matrix Vesicle collection from 5 months old male mice and assessment of their regenerative potential. Nanoparticle Tracking Analysis (NTA) was performed to determine **(B)** Size distribution, **(C)** Average diameter and (D) Nanoparticle concentration. **(E)** Protein content via bicinchoninic acid assay. **(F)** ALP activity. (G) TEM observations with scale bar = 500 nm **(H)** Super resolution microscopy observation pf the single nanoparticle with the fluorescence detection of membrane (lipid stain) and trio-tetraspanins markers (CD9/CD63/CD81), scale bar = 200 nm. Statistical analysis performed via unpaired or Welch's t test. *p<0.05, **p<0.01, ***p<0.001, **** p<0.0001.

5.3.2 Matrix Vesicles possess pro-mineralising potential

Matrix vesicles are well established as key mediators of extracellular matrix mineralisation, acting as sites of primary mineral nucleation with innate osteo-inductive properties [203, 214, 215, 387, 388]. To further validate this property and to determine whether this was tissue dependent, we investigated whether MVs derived from murine long bones and kidneys can promote mineralisation *in vitro* over a 7-day culture period. Human osteoblast-like cells were treated with increasing concentrations of bone- (B-MVs) and kidneys-derived MVs (K-MVs) (0.25, 0.5, 1.5 and 2.5 µg/mL) in the presence of osteogenic supplements and mineralisation was assessed after 7 days (**Figure 5.2 A**). Treatment with the lowest MVs dose (0.25 µg/mL) did not elicit an increase in mineralisation compared to the osteogenic medium control (OM), regardless of the MVs tissue source. Interestingly, treatment with 0.5, 1.5 and 2.5 µg/mL of B-MVs resulted in a significant increase in mineralisation relative to both the osteogenic medium control and the lowest dose ($p<0.05$), corresponding to 1.6-, 1.9-, and 1.7-fold increases in mineral deposition over 7 days (**Figure 5.2 B**). Similarly, treatment with the higher doses of K-MVs led to significant increase in mineralisation compared to the osteogenic medium control, eliciting 1.6-, 1.8- and 2-fold increase, respectively ($p<0.05$). While the 0.5 µg/mL and 1.5 µg/mL doses of K-MVs did not differ significantly from the lowest dose (0.25 µg/mL), the highest concentration (2.5 µg/mL) produced a marked increase ($p<0.001$) (**Figure 5.2 C**). Overall, these findings indicate that both bone- and kidney-derived MVs populations effectively promote mineralisation in a dose-dependent manner, regardless of their tissue origin.

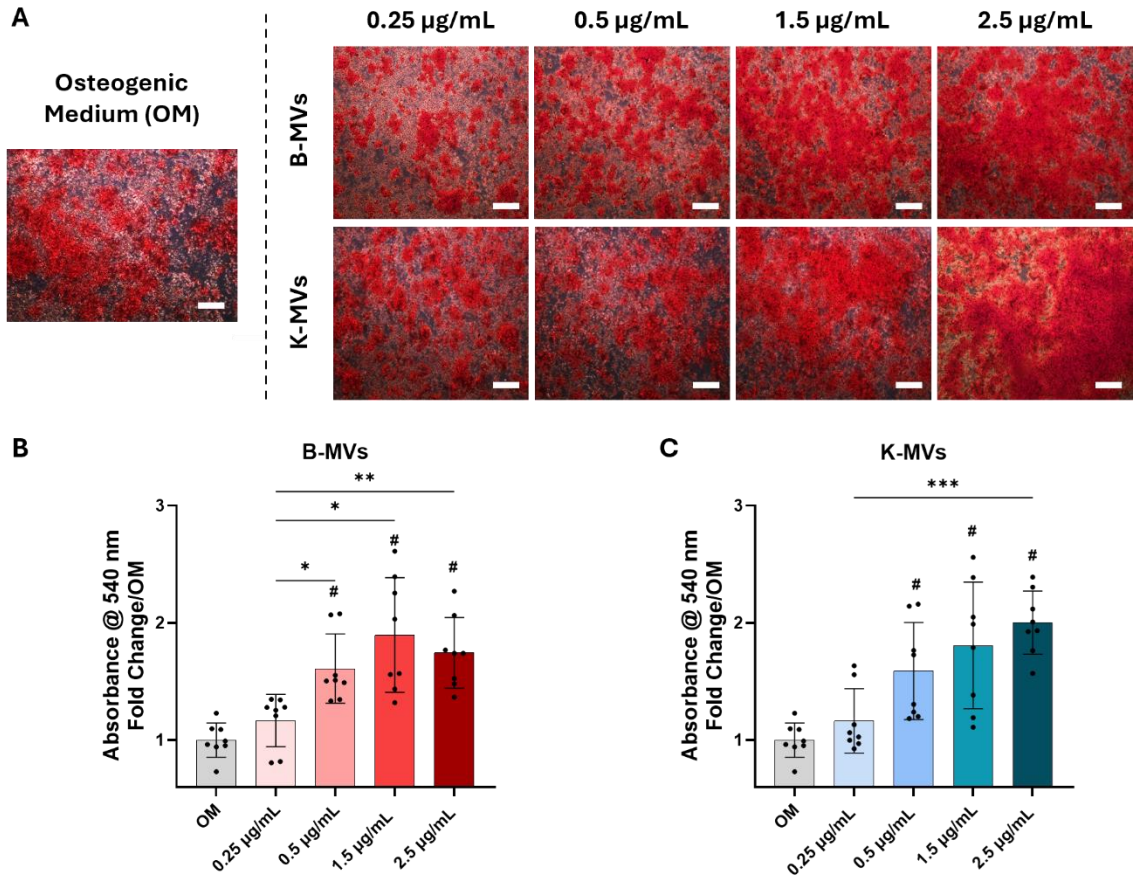

Figure 5.2. MVs promote mineralisation in a dose dependent manner. (A) Representative images of Alizarin red staining following treatment with 0.25, 0.5, 1.5 and 2.5 µg/mL of bone- and kidneys-derived MVs. **(B, C)** Alizarin red semi-quantification via CPC destaining for B-MVs and K-MVs, respectively. Scale bar = 500 µm. Values are mean ± SD. Statistical analysis performed via Brown- Forsythe and Welch One-way ANOVA, *p<0.05, **p<0.01, ***p<0.001, **** p<0.0001, # p < 0.05 vs OM.

5.3.3 Matrix Vesicles possess angiogenic potential in a manner that is source tissue specific

Bone is a highly vascularised tissue, with its vasculature playing a crucial role in bone development, regeneration and remodelling [389, 390]. Blood vessels are vital to supply oxygen, nutrients, hormones and growth factors to bone cells, as well as for removing waste substances. MVs are traditionally known for their role in mineralisation, but their potential involvement in blood vessel formation has not been fully explored to date. Therefore, we next investigated whether B-MVs and K-MVs possess angiogenic properties beyond their osteogenic properties. We first assessed the effect of increasing concentrations of B-MVs (0.25, 0.5, 1.5, and 2.5 µg/mL) on endothelial tube formation (**Figure 5.3 A**). Across all

concentrations tested, B-MVs treatment significantly enhanced tube formation compared to the negative control. Specifically, B-MVs treatment elicited a significant increase in number of nodes across all the concentrations, with 3.9-, 3.2-, 3.0-, and 3.3-fold ($p<0.05$) increases, respectively (**Figure 5.3 B**). A similar pattern was observed for the number of junctions, with all concentrations eliciting significant increases compared to the negative control (**Figure 5.3 C**). Importantly, these effects were comparable across doses, with no significant differences observed between them. Further analysis revealed that treatment with 0.25, 1.5, and 2.5 µg/mL B-MVs significantly increased both the number of segments and the total segment length relative to the negative control (**Figure 5.3 D, E**). In contrast, treatment with 0.25, 0.5 and 2.5 µg/mL K-MVs did not elicit any significant changes in number of nodes or junctions. A significant effect was observed only following treatment with 1.5 µg/mL K-MVs, which induced an increase in the number of nodes (2.7-fold, $p<0.05$) and junctions (2.6-fold, $p<0.05$) compared to the negative control (**Figure 5.3 F, G**). Additionally, no significant differences were observed in the number of segments or total segment length across any of the K-MVs concentration tested (**Figure 5.3 H, I**). Taken together, these findings demonstrate that bone-derived MVs possess pro-angiogenic properties in addition to their pro-mineralising properties, underscoring their overall anabolic potential. Furthermore, bone-derived MVs demonstrated superior pro-angiogenic potential when compared to kidneys-derived MVs, emphasising that the angiogenic potential of MVs is influenced by their tissue of origin.

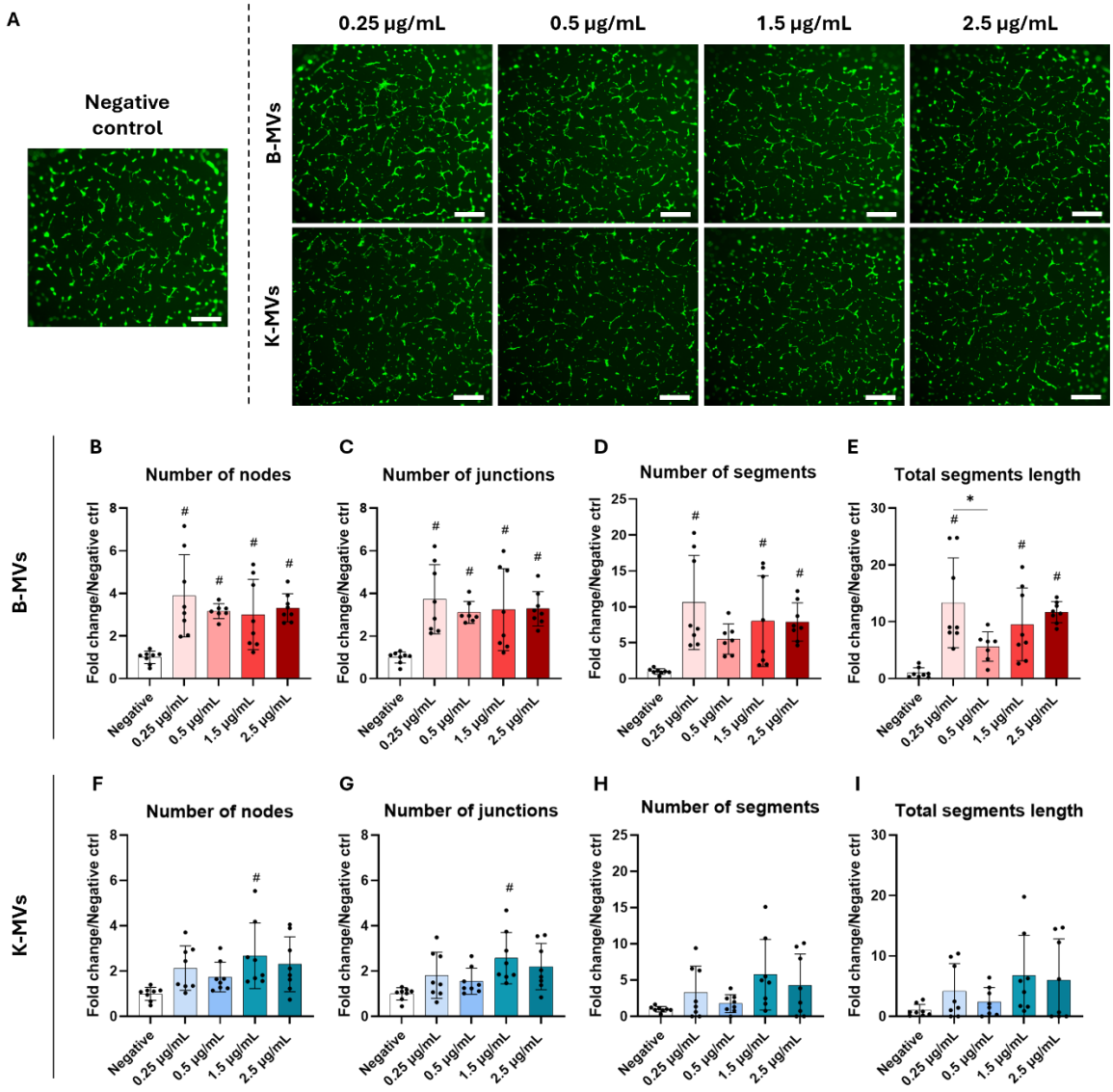

Figure 5.3. Bone-derived MVs promoted angiogenesis demonstrating superior angiogenic potential than kidneys-derived MVs. (A) Representative fluorescent images of tube formation at 10h following treatment with 0.25, 0.5, 1.5 and 2.5 µg/mL of bone- and kidneys-derived MVs. Quantification of (B, F) number of nodes, (C, G) number of junctions, (D, H) number of segments and (E, I) total segment length, each normalised to negative control, for bone B-MVs and K-MVs. Scale bar = 500 µm. Values are mean ± SD. Statistical analysis performed via Ordinary One-way ANOVA, *p<0.05, **p<0.01, ***p<0.001, **** p<0.0001.

5.3.4 Matrix Vesicles demonstrate anti-catabolic potential

Bone remodelling is crucial to maintaining skeletal integrity and relies on a tightly regulated balance between bone formation and bone resorption. Excessive osteoclast-driven bone resorption disrupts this balance, leading to osteoporosis. Although controlled bone resorption is essential for bone remodelling, osteoclast activity has been targeted by anti-

resorptive osteoporosis treatments. In this context, we next investigated whether B-MVs and K-MVs also exert anti-osteoclastogenic effects in addition to their anabolic properties. Such dual effect would endow MVs with multi-targeted therapeutic potential, simultaneously enhancing bone and vessel formation and inhibiting bone resorption. To evaluate MVs anti-catabolic properties, $CD14^+$ monocytes were treated with 0.25, 0.5, 1.5 and 2.5 μg/mL of B-MVs or K-MVs in the presence of the osteoclast inducing factors M-CSF and RANKL and osteoclastogenesis was assessed (**Figure 5.4 A**). B-MVs inhibited osteoclast formation in a dose-dependent manner. Low doses (0.25 and 0.5 μg/mL) elicited modest but significant reductions in osteoclast formation, resulting in 0.8-fold ($p<0.05$) and 0.82-fold ($p<0.05$) decreases relative to the +RANKL control. At 1.5 μg/mL, BMVs induced a more pronounced inhibition of osteoclastogenesis (0.65-fold vs +RANKL, $p < 0.0001$), significantly greater than that observed at the lower doses. The highest concentration (2.5 μg/mL) elicited maximal inhibition, reducing osteoclast formation to 0.3-fold relative to the +RANKL control ($p < 0.0001$) and exceeding the anti-catabolic effect of all other doses ($p < 0.0001$) (**Figure 5.4 B**). Assessment of osteoclast number of nuclei as a proxy of osteoclast maturation indicated that osteoclast maturity remained largely unaffected at 0.25, 0.5 and 1.5 μg/mL B-MVs. However, the 2.5 μg/mL dose elicited a 0.5-fold reduction in number of nuclei ($p<0.0001$ vs +RANKL), producing less multinucleated osteoclasts compared to all lower doses (**Figure 5.4 C**). Total cell counts remained similar across treatments and controls, with the 1.5 and 2.5 μg/mL doses showing comparable cell numbers that were significantly higher than the lower doses (**Figure 5.4 D**), indicating that MVs do not impair monocyte adhesion. Treatment with K-MVs produced a modest but significant reduction in osteoclast numbers relative to the +RANKL control, corresponding to 0.84-, 0.8-, 0.76-, and 0.7-fold ($p < 0.05$) inhibition at 0.25, 0.5, 1.5, and 2.5 μg/mL, respectively. Overall, osteoclastogenesis was similarly inhibited across all doses, with a statistically significant difference observed only between the lowest (0.25 μg/mL) and highest (2.5 μg/mL) concentrations (**Figure 5.4 E**). Multinucleation remained unaffected by treatment with 0.25, 0.5 and 1.5 μg/mL K-MVs, whereas the higher doses slightly reduced nuclei number compared to the +RANKL control ($p=0.043$), albeit no significant differences in nuclei number was observed between any of the doses (**Figure 5.4 F**). Similarly, total cell number was consistent across all doses (**Figure 5.4 G**). Collectively, these findings demonstrate that B-MVs possess dose-dependent anti-catabolic activity superior to K-MVs and, together with

their anabolic effects, hold promising multi-targeted therapeutic potential for bone regeneration.

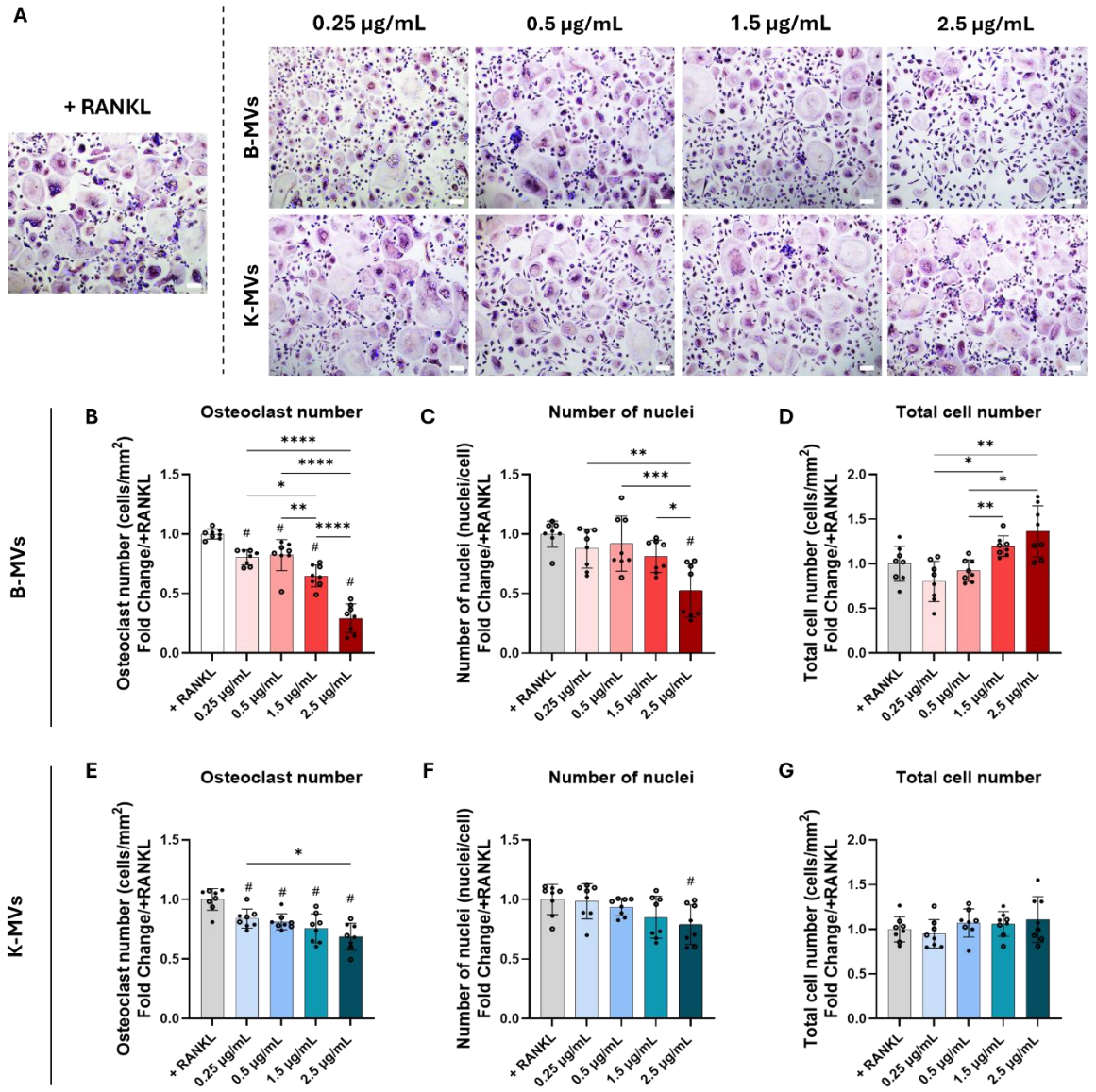

Figure 5.4. MVs inhibit osteoclastogenesis in a dose-dependent manner. (A) Representative images of TRAP and DAPI staining following treatment with 0.25, 0.5, 1.5 and 2.5 µg/mL of bone-derived MVs (B-MVs) and kidneys-derived MVs (K-MVs). Quantification of (B, F) Osteoclast number, (C, G) number of nuclei per osteoclast, (D, H) Total number of cells, each normalised to + RANKL control, B-MVs and K-MVs. Scale bar = 100 µm. Statistical analysis performed via Ordinary One-way ANOVA or Brown- Forsythe and Welch One-way ANOVA, *p<0.05, **p<0.01, ***p<0.001, **** p<0.0001., # p < 0.05 vs +RANKL. Values are mean ± SD for 2 different human donors (● = Donor 1, ○ = Donor 2).

5.3.5 Tissue-derived MVs and bone cell-derived EVs have a unique protein signature

After demonstrating the regenerative properties of bone derived MVs, we next performed an advanced characterisation of B-MV and K-MVs surface protein expression and compared this to EVs derived from murine osteoblasts (OB-EVs) and osteocytes (OCY-EVs) using the MACSPlex protein array. This bead-based flow cytometry analysis allowed for the antibody-based detection of a set of proteins of interest using 37 different surface epitopes and two isotype controls (**Figure S2 A**). Post acquisition, each population of beads corresponding to a single protein was then individually gated (**Figure S2 B**). For each group characterised, the background corrected MFI was then used to compare the relative abundance of each detected protein (**Figure S2 C**). Combined analysis of the MACSPlex phenotyping data revealed distinct marker enrichment profiles for each group, with varying degrees of enrichment across the investigated markers. Interestingly, B-MVs showed enrichment for 14 of the 37 investigated markers, K-MVs for 22, OB-EVs for 19 and OCY-EVs for 21 (**Figure 5.5 A**). Investigating their common features, 8 biomarkers were found to be enriched across all vesicles population as displayed in the Venn diagram. The protein-protein interaction (PPI) analysis demonstrated that all 8 proteins were functionally liked with a p-value of 2.22×10^{-16} (**Figure 5.5 B**). Functional enrichment analysis of the shared markers indicated association with biological process involved in cell adhesion (**Figure S3**).

Hierarchical clustering of the MACSPlex phenotyping data, following row variance scaling, revealed clear separation of the four vesicle populations based on their surface marker enrichment. The column dendrogram shows that OB-EVs and OCY-EVs cluster closely together, forming one branch, while B-MVs and K-MVs grouped into a separate branch. This pattern reflects a higher similarity in surface marker composition between cell-derived vesicles (OB-EVs and OCY-EVs) compared to tissue-derived vesicles (B-MVs and K-MVs). Row clustering further identified four distinct protein clusters that discriminate between vesicles populations, each exhibiting a unique protein signature (**Figure 5.5 C**). The first cluster, comprising MHC II, CD11b, CD45, CD24 and CD66a was predominantly expressed in B-MVs. PPI analysis confirmed significant functional associations between these proteins ($p=7.99 \times 10^{-4}$) (**Figure 5.5 D**). Gene ontology enrichment revealed their involvement in immune system associated process such as “Negative regulation of T cell mediated cytotoxicity” ,

“Leukocyte cell-cell adhesion”, “Regulation of T cell mediated immunity” , “Regulation of leukocyte mediated cytotoxicity”, and “T cell proliferation” (**Figure 5.5 E**). Interestingly, tissue expression enrichment further indicated significant association within marrow cells, femur and (**Figure 5.5 F**). A second protein cluster, including CD20, CD3, CD146, CD41, CD31, Prominin-1, CD49b and CD326 showed higher expression in K-MVs. PPI analysis demonstrated strong functional association with a p value of $5.7x10^{-10}$ (**Figure 5.5 G**). GO analysis highlighted significant enrichment in biological processes such as “Cell-cell adhesion”, “Cell-matrix adhesion”, “Kidney epithelium development” (**Figure 5.5 H**). Tissue expression enrichment analysis indicated predominant expression in several cell types and tissues, including liver cancer stem cells, endothelial progenitor cells, blood, and respiratory epithelium. (**Figure 5.5 I**). Among the cell-derived EVs, OB-EVs were characterized by a CD63/CD81/CD9-enriched cluster associated with immune regulation, membrane fusion processes, and expression in immune-related tissues such as macrophages, blood, and lymphoid tissue (**Figure S4 A-C**). In contrast, OCY-EVs displayed a separate protein cluster enriched for adhesion, angiogenesis, and developmental signalling pathways, with tissue associations linked to mesenchymal, myogenic, and embryonic lineages (**Figure S4 D-F**). Taken together, these results demonstrate clear origin-dependent vesicle marker profiles, enabling discrimination between bone- and kidney-derived MVs as well as between tissue-derived and cell-derived vesicles. This emphasizes pronounced vesicle heterogeneity and supports the concept that surface marker composition is determined by tissue and cellular origin, with potential relevance to regenerative outcomes.

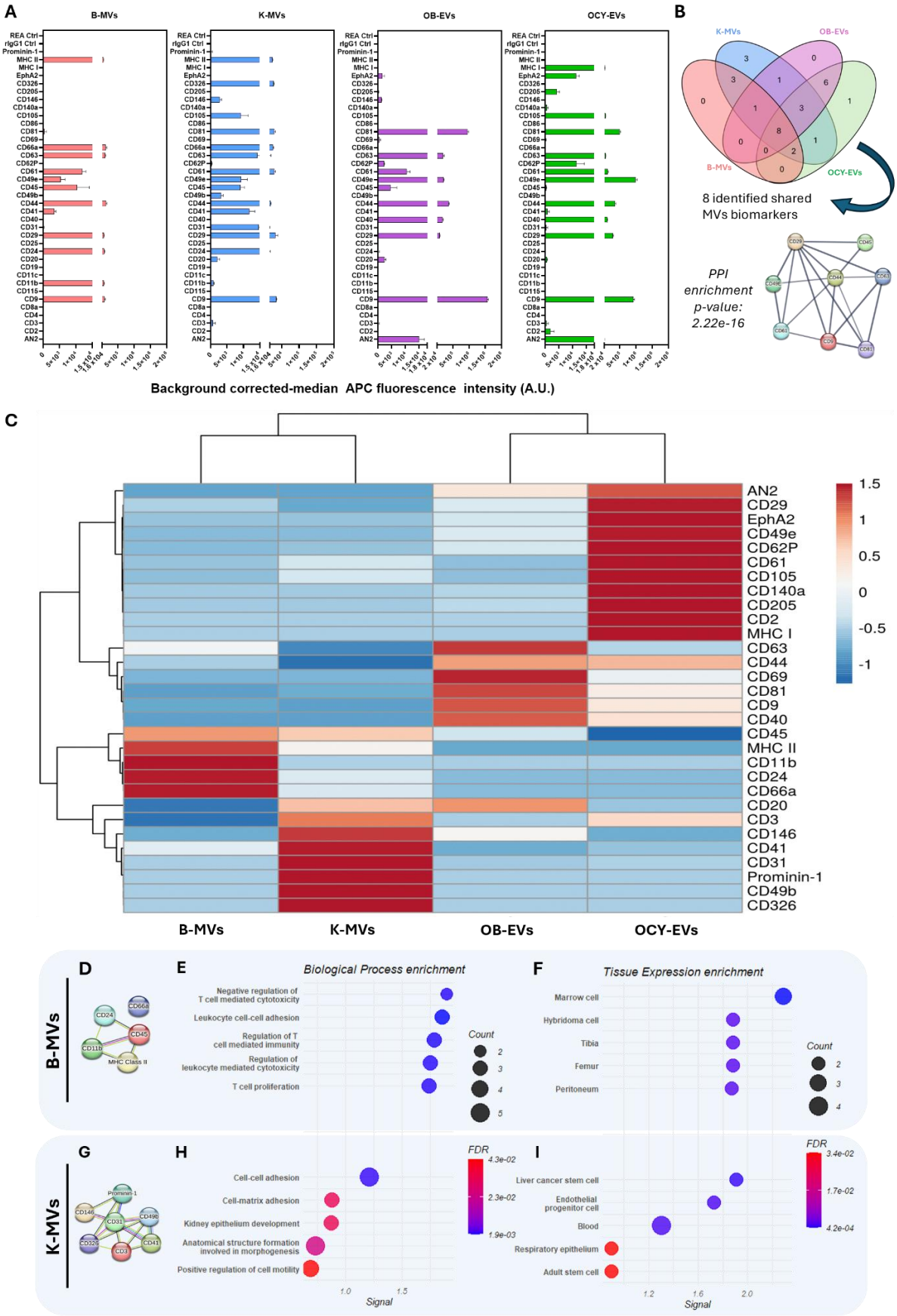
A
B-MVs
K-MVs
OB-EVs
OCY-EVs
Background corrected-median APC fluorescence intensity (A.U.)
B
K-MVs
OB-EVs
B-MVs
OCY-EVs
8 identified shared MVs biomarkers
PPI enrichment p-value: 2.22e-16
C
AN2
CD29
EphA2
CD49e
CD62P
CD61
CD105
CD140a
CD205
CD2
MHC I
CD63
CD44
CD69
CD81
CD9
CD40
CD45
MHC II
CD11b
CD24
CD66a
CD20
CD3
CD146
CD41
CD31
Prominin-1
CD49b
CD326
B-MVs
K-MVs
OB-EVs
OCY-EVs
D
B-MVs
E
Biological Process enrichment
Negative regulation of T cell mediated cytotoxicity
Leukocyte cell-cell adhesion
Regulation of T cell mediated immunity
Regulation of leukocyte mediated cytotoxicity
T cell proliferation
Count
F
Tissue Expression enrichment
Marrow cell
Hybridoma cell
Tibia
Femur
Peritoneum
Count
G
K-MVs
H
Cell-cell adhesion
Cell-matrix adhesion
Kidney epithelium development
Anatomical structure formation involved in morphogenesis
Positive regulation of cell motility
FDR
Signal
I
Liver cancer stem cell
Endothelial progenitor cell
Blood
Respiratory epithelium
Adult stem cell
FDR
Signal

Figure 5.5. Exploring bone derived vesicles specific biomarker signature. (A) Surface marker profiles of bone- and kidneys-derived MVs and OB- and OCY-derived EVs. Background corrected APC median signal intensities after incubation of MVs or EVs with 39 capture antibody bead populations followed by staining with a cocktail of anti-CD9-, anti-CD63- and anti-CD81-APC antibodies. **(B)** Venn diagram showing the overlap of the surface markers profiled in the 4 vesicles populations and STRING network analysis displaying protein-protein interaction. **(C)** Annotated heatmap displaying the hierarchical clustering of MACSPlex profiles for all groups**. (D, G)** PPI analysis displaying protein-protein interaction for B-MVs and K-MVs respectively. **(E, H)** Biological process enrichment and **(F, I)** Tissue Expression enrichment of markers highly expressed in B-MVs and K-MVs.

5.3.6 Tissue-derived MVs possess a unique miRNA cargo

Comprehensive small RNA sequencing was performed to further characterise MV cargo. As shown in **Figure 5.6 A**, both vesicle populations contained a heterogeneous mixture of small RNA biotypes, with ribosomal RNA (rRNA) representing the predominant fraction. miRNAs were detected in both vesicle populations. However, the relative proportion of miRNAs was higher in K-MVs compared with B-MVs, indicating differential enrichment of regulatory small RNAs depending on tissue origin. Additional RNA classes, including tRNA, piRNA, lncRNA, and other small non-coding RNAs, were present in smaller proportions, with broadly similar distributions between groups. To further assess miRNA diversity and overlap between samples, detected miRNAs were analysed across biological replicates (**Figure 5.6 B**). Intersection analysis identified a shared core set of miRNAs present in both B-MVs and K-MVs, alongside distinct subsets unique to each vesicle population. Notably, K-MVs exhibited a higher number of detected miRNAs per sample and a greater proportion of unique miRNAs not observed in B-MVs. Global miRNA expression patterns were next examined using principal component analysis (PCA) (**Figure 5.6 C**). Clear separation between B-MVs and K-MVs was observed along the first principal component, which accounted for 44.1% of total variance, while the second principal component explained an additional 21.2%. Importantly, biological replicates clustered tightly within their respective groups, indicating high reproducibility and underscoring that miRNA expression profiles are strongly influenced by vesicle tissue origin. Consistent with these findings, unsupervised hierarchical clustering of differentially expressed miRNAs further distinguished B-MVs from K-MVs (**Figure 5.6 D**). Samples segregated according to MV source, with distinct clusters of miRNAs exhibiting coordinated upregulation or downregulation between the two groups. This clustering pattern highlights the presence of tissue-specific miRNA expression

signatures and suggests systematic differences in miRNA packaging within bone- versus kidney-derived vesicles. Differential expression analysis was subsequently performed to identify miRNAs significantly altered between B-MVs and K-MVs. The volcano plot identified a subset of miRNAs significantly differentially expressed between B-MVs and K-MVs. Both upregulated and downregulated miRNAs were observed, with a distribution of effect sizes spanning moderate to high $\log_2$ fold changes. The presence of numerous significantly altered miRNAs indicates substantial remodelling of vesicular miRNA cargo according to tissue source (**Figure 5.6 E**). To highlight the most prominent changes, the top 12 downregulated and top 12 upregulated miRNAs in B-MVs relative to K-MVs were selected (**Figure 5.6 F**). Downregulated miRNAs included mmu-miR-30b-5p, mmu-miR-187-3p, and mmu-miR-10b-3p, while upregulated miRNAs included mmu-miR-149-5p, mmu-miR-6946-5p, mmu-miR-3473b, mmu-miR-2137 and mmu-miR-150-5p. These miRNAs represent potential candidates involved in tissue-specific signalling pathways and may contribute to the distinct biological functions of bone- and kidney-derived MVs. Finally, Integration of top 12 upregulated and top 12 downregulated miRNAs across multiple tissue contexts demonstrated structured, tissue-dependent expression patterns (**Figure 5.6 G**). Importantly, the miRNAs classified as upregulated in the differential expression analysis correspond to those enriched in B-MVs, whereas the downregulated miRNAs represent those relatively enriched in K-MVs. Hierarchical clustering revealed a clear separation between bone-associated and kidney-associated expression profiles. The upregulated (bone-enriched) miRNAs displayed coordinated higher expression across bone-related tissues, including osteoblasts, bone tissue, bone marrow, and macrophage-associated cells. In contrast, the downregulated (kidney-enriched) miRNAs showed increased expression within kidney-derived tissues such as epithelium, glomeruli, and arteriole. This reciprocal distribution reinforces the conclusion that the identified miRNA signature reflects tissue-specific regulatory programs. Enrichment of the upregulated miRNAs within bone-associated tissues confirms that this signature is characteristic of B-MVs, whereas the downregulated miRNAs define a kidney-associated profile representative of K-MVs. Overall, these results demonstrate that MVs derived from bone and kidney exhibit distinct miRNA expression profiles. The observed differences in miRNA abundance and diversity suggest that MV cargo is selectively regulated in a tissue-dependent manner, supporting a role for miRNAs in mediating organ-specific intercellular communication.

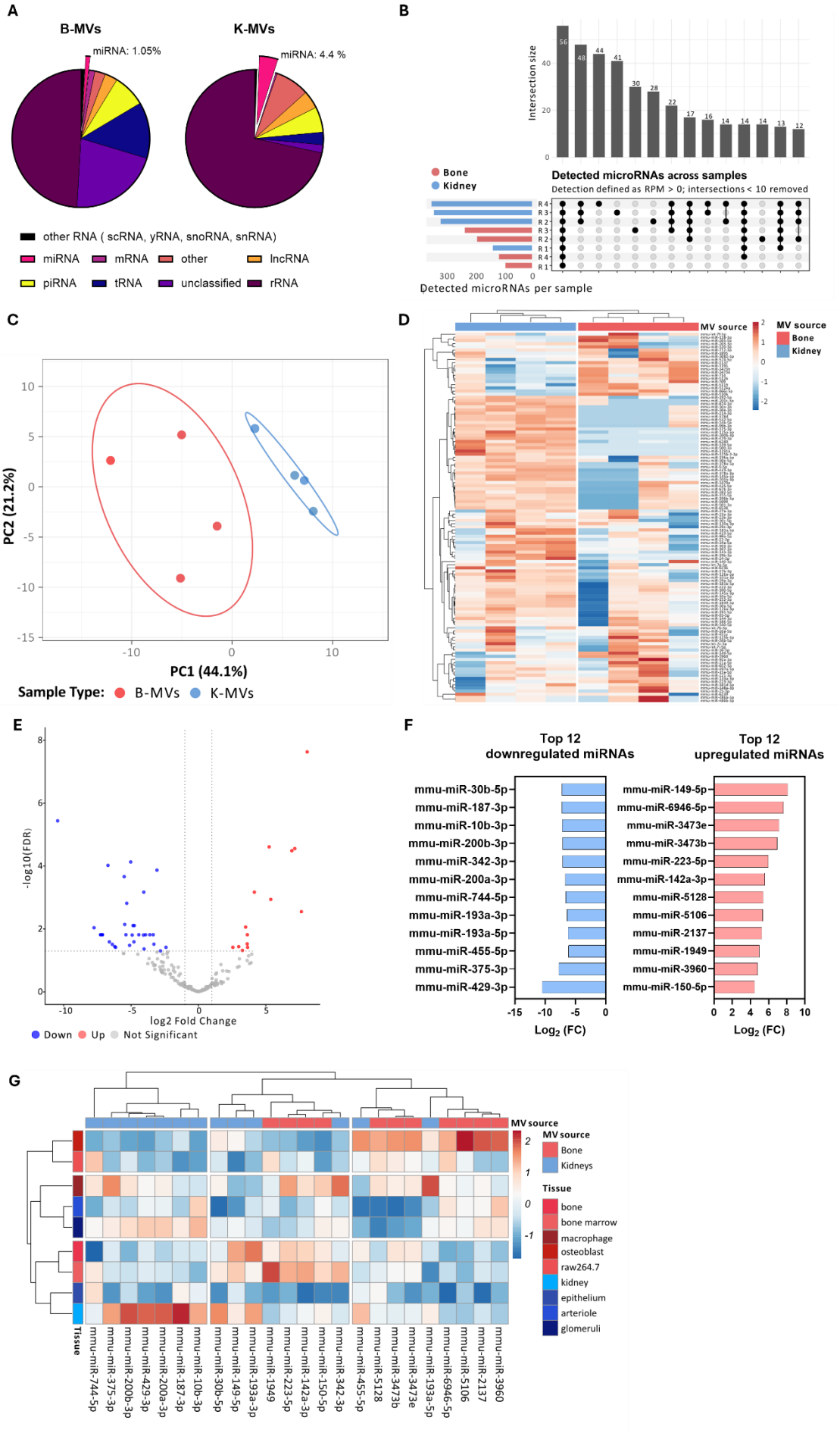
A
B-MVs
K-MVs
miRNA: 1.05%
miRNA: 4.4 %
other RNA (scRNA, yRNA, snoRNA, snRNA)
miRNA
mRNA
other
lncRNA
piRNA
tRNA
unclassified
rRNA
B
Intersection size
Bone
Kidney
Detected microRNAs across samples
Detection defined as RPM > 0; intersections < 10 removed
Detected microRNAs per sample
C
PC2 (21.2%)
PC1 (44.1%)
Sample Type: B-MVs K-MVs
D
MV source
Bone
Kidney
E
-log10(FDR)
log2 Fold Change
Down
Up
Not Significant
F
Top 12 downregulated miRNAs
Top 12 upregulated miRNAs
mmu-miR-30b-5p
mmu-miR-187-3p
mmu-miR-10b-3p
mmu-miR-200b-3p
mmu-miR-342-3p
mmu-miR-200a-3p
mmu-miR-744-5p
mmu-miR-193a-3p
mmu-miR-193a-5p
mmu-miR-455-5p
mmu-miR-375-3p
mmu-miR-429-3p
mmu-miR-149-5p
mmu-miR-6946-5p
mmu-miR-3473e
mmu-miR-3473b
mmu-miR-223-5p
mmu-miR-142a-3p
mmu-miR-5128
mmu-miR-5106
mmu-miR-2137
mmu-miR-1949
mmu-miR-3960
mmu-miR-150-5p
Log2 (FC)
G
MV source
Bone
Kidneys
Tissue
bone
bone marrow
macrophage
osteoblast
raw264.7
kidney
epithelium
arteriole
glomeruli
Tissue

Figure 5.6. MVs possess unique miRNA cargo depending on the tissue source. (A) Small RNA profile in B-MVs and K-MVs. **(B)** Upset plot summarizing the overlap of differentially expressed miRNAs across comparisons, R1-R4 denote MV samples obtained from independent isolations. **(C)** PCA plot and **(D)** Heatmap of differentially expressed miRNAs. **(E)** Volcano plot illustrates differentially expressed miRNAs between B-MVs and K-MVs. Statistical significance was defined as a false discovery rate (FDR) < 0.5. **(F)** Graphical distribution according to their fold change (FC) of the differentially expressed miRNA. **(G)** Heatmap of the top 12 upregulated and top 12 downregulated differentially expressed miRNAs across the indicated murine tissues.

To further define the functional relevance of B-MV miRNA cargo, the most abundant miRNAs were characterised and subjected to target prediction and enrichment analysis. As shown in **Figure 5.7 A**, the miRNA profile within B-MVs was dominated by a limited subset of highly expressed miRNAs, indicating selective enrichment rather than uniform distribution. Among these, mmu-miR-2137 was the most abundantly expressed miRNA. Target prediction analysis demonstrated variability in the number of genes associated with individual miRNAs (**Figure 5.7 B**), suggesting differences in their potential regulatory scope. To enhance confidence and reduce false-positive associations, predicted targets were integrated across five independent databases, and only genes identified by at least three were retained for downstream analysis. Although this stringent threshold improves the robustness of enrichment results, it may disadvantage less well characterised miRNAs. For mmu-miR-2137, limited concordance among prediction platforms meant that its targets did not meet the inclusion criterion. Consequently, despite being the most abundant miRNA in B-MVs, mmu-miR-2137 was not represented in the GO enrichment analysis. Importantly, this exclusion reflects limited cross-database agreement rather than an absence of biological targets, underscoring current gaps in prediction resources for this miRNA. GO biological process enrichment analysis of high-confidence miRNA targets identified several pathways directly relevant to bone regeneration (**Figure 5.7 C**). Significantly enriched categories included angiogenesis and endothelial cell differentiation, processes essential for vascular invasion and the coupling of vascularisation with bone formation during repair. Enrichment of terms such as positive regulation of cell population proliferation, positive regulation of cell differentiation, and negative regulation of cell differentiation highlights regulatory mechanisms governing osteoblast lineage commitment and osteoclast precursor progression during bone remodelling. Additionally, enrichment of chromatin remodelling and protein glycosylation suggests potential regulation of transcriptional, epigenetic, and

post-translational processes necessary for osteogenic and osteoclastogenic differentiation, including modulation of receptor stability and cellular activation in bone cells [391-395]. The insulin receptor signalling pathway was also significantly enriched. Insulin signalling is a key regulator of bone remodelling, promoting osteoblast-mediated bone formation and influencing osteoclast-driven resorption [396, 397], supporting a link between the identified miRNA targets and bone remodelling processes. To further examine the functional architecture of the enriched target genes, network analysis was performed using selected pathways representative of key processes in bone regeneration (**Figure 5.7 D**). Angiogenesis, insulin receptor signalling, and chromatin remodelling were chosen for visualisation due to their relevance to angiogenesis, osteogenesis, and osteoclastogenesis, and their significant enrichment in the GO analysis. Interaction mapping revealed dense connectivity between dominant miRNAs and genes within the selected pathways. Collectively, these analyses demonstrate that B-MVs harbour a structured and functionally coherent miRNA repertoire with predicted regulatory influence over gene networks central to transcriptional control, angiogenesis, and bone cell differentiation. By simultaneously targeting gene networks governing vascularisation, osteogenic commitment, and epigenetic regulation, B-MVs may function as integrated signalling units capable of synchronising multiple cellular processes required for effective bone repair. This systems-level regulatory potential positions B-MV miRNAs as key contributors to bone regeneration and highlights their relevance as both mechanistic drivers and potential therapeutic targets in skeletal repair strategies.

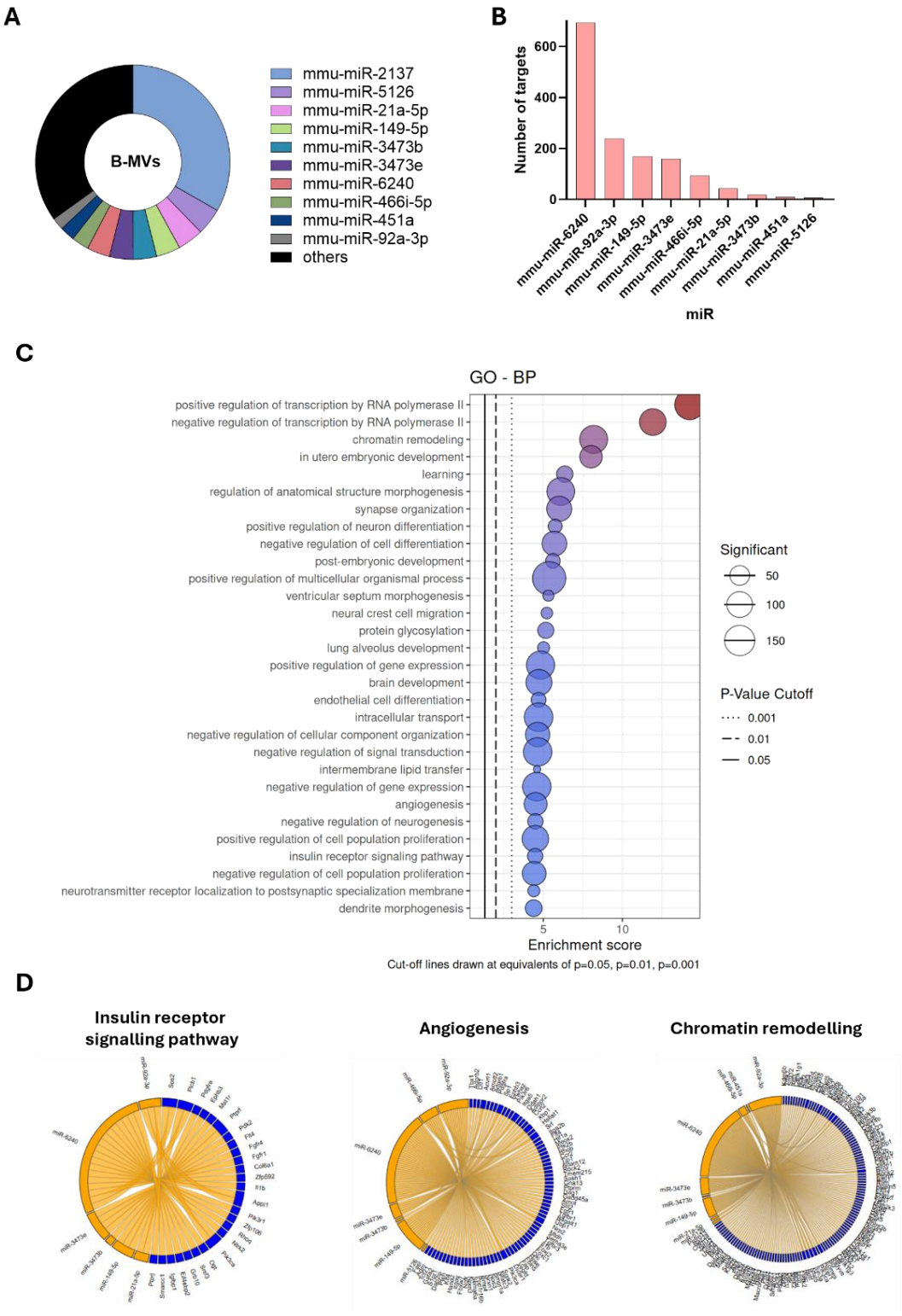

Figure 5.7. Exploring bone derived MVs miRNA cargo. (A) Distribution of miRNAs in B-MVs, pie chart depicts the total miRNA pool and highlight the 10 most abundant miRNAs. **(B)** Top 10 miRNAs target prediction. **(C)** Top 30 significantly enriched GO biological processes associated with top 10 most enriched miRNA target genes in B-MVs. **(D)** Chord diagram showing the involvement of miRNAs in B-MVs in GO of interest.

5.3.7 Age, sex and exercise modulate the size, and yield of bone-derived MVs

Bone has the extraordinary capacity to regenerate and remodel throughout life. However, this regenerative potential progressively declines with age, leading to reduced bone mass, impaired remodelling efficiency and increased fracture risk. Physical activity is widely recognised as one of the most effective non-pharmacological strategies to counteract age-related skeletal deterioration. In this context, our previous studies demonstrated that mechanical loading of bone cells *in vitro* promotes the release of mechanically activated bone cell derived EVs with enhanced regenerative potential [18, 19, 295, 345]. Moreover, we have identified tissue-derived MVs as a promising and scalable alternative to cell-derived EVs, exhibiting broad and multi-targeted regenerative properties. Building on these findings, we hypothesised that exercised-induced mechanical stimulation in aged mice could potentially enhance the regenerative properties of bone tissue-derived MVs, thereby mitigating the detrimental effects of aging on bone tissue function and repair capacity. To assess whether long-term exercise influences the production and characteristics of B-MVs, male and female C57BL/6 mice were subjected to a long-term, controlled treadmill-running regimen. Animals assigned to the exercise (EX) group began training at 3 months of age and continued until 18 months of age, whereas age-matched controls remained sedentary (SED). The exercise protocol consisted of three sessions per week on a motorized treadmill (0° incline), each lasting 30 min and including incremental speed stages: 5 min at 6 m/min, 5 min at 10 m/min, and 20 min at 14 m/min. Following completion of the exercise regimen, MVs were isolated from the bones of the aged sedentary and exercised animals, as well as from 3 months old male and female sedentary controls, using collagenase digestion and differential ultracentrifugation. MVs size and concentration were determined by NTA, ALP activity was quantified, and their bioactivity was evaluated by osteogenesis, angiogenesis, and osteoclastogenesis assays (**Figure 5.8 A**). NTA size distribution profiles revealed that MVs size and yield were influenced by age, sex, and exercise (**Figure 5.8 B, C**). In females, MVs from young mice exhibited smaller average diameter ($p<0.0001$) and a higher nanoparticles concentration ($p<0.05$) compared to the aged counterpart. This age-related shift towards larger vesicles and higher yield was not observed in males. In addition, aged females produced MVs of larger diameter than the age-matched males ($p<0.001$) (**Figure 5.8 D, E**). The effect of age and sex on nanoparticle yield was further supported by protein

cargo quantification, which confirmed sex- and age-dependent variation in MV **Figure 5.8 F**). MVs isolated from young mice of both sexes displayed higher ALP activity, potentially suggestive of their mineralising potential, though changes were only significant in females ($p=0.154$ for 3-months old vs 18-months old female) (**Figure 5.8 G**). Exercise had a selective impact on MV characteristics, primarily in female mice. MVs size was not significantly altered by exercise in either sex. However, MVs from female exercised mice displayed larger diameters than their male counterpart ($p<0.05$, SED female vs SED male; $p<0.0001$ EX female vs EX male) (**Figure 5.8 H**). In contrast, MVs yield significantly increased in exercised females ($p<0.05$), while remaining unchanged in males. Moreover, exercised female mice yielded a higher number of nanoparticles than the male counterpart ($p<0.001$) (**Figure 5.8 I**). Interestingly, protein content did not mirror nanoparticles yield in females, showing a slight but significant decrease following exercise ($p<0.05$), while no changes were observed in males (**Figure 5.8 J**). Finally, MVs ALP activity significantly decreased after exercise ($p<0.0001$), likely reflecting dilution effects due to higher nanoparticle concentration, whereas no significant change was observed in males (**Figure 5.8 K**). Overall, these findings demonstrate that MVs were successfully collected from both young and aged murine bones, and that their size and yield are modulated by age, sex and exercise.

A

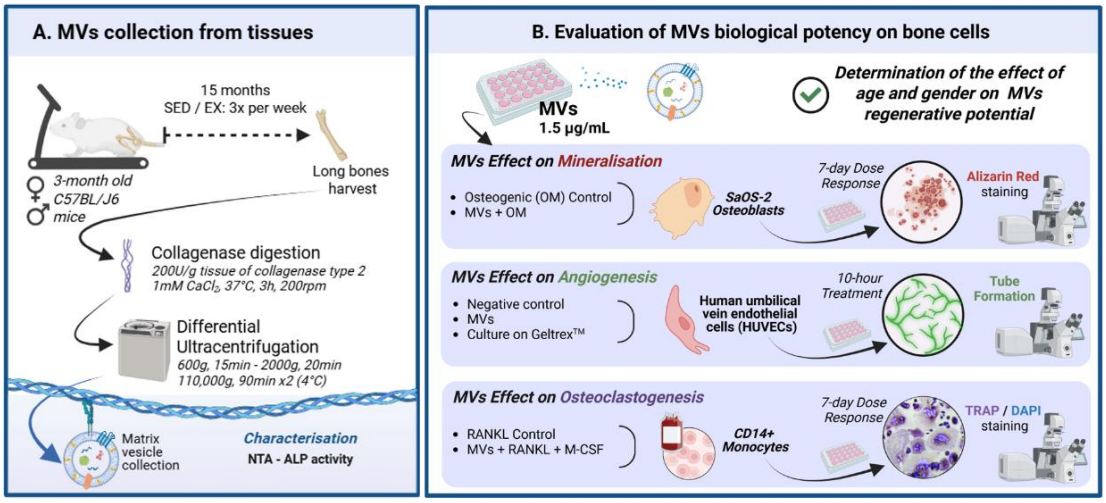

B

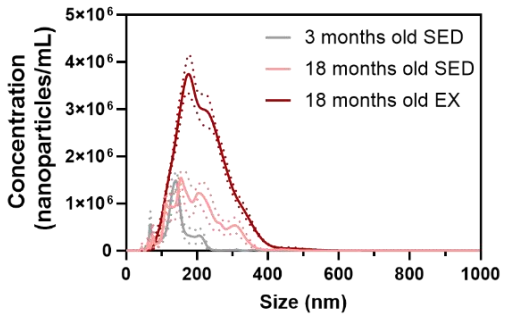

C

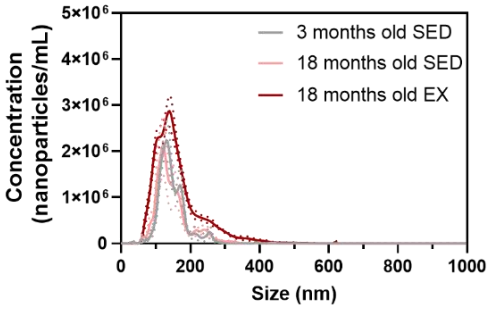

Effect of age

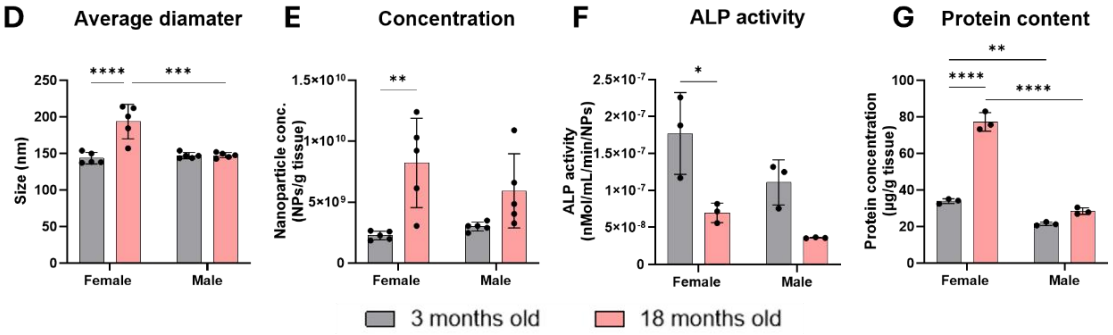

Effect of exercise

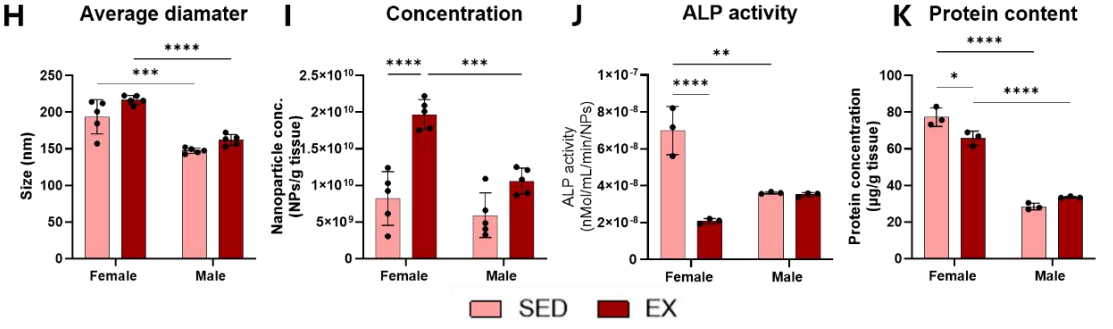

Figure 5.8. **Isolation and characterisation of MVs derived from female and male young sedentary and aged sedentary and exercised mice. (A).** Schematic of experimental workflow for MVs isolation and assessment of their regenerative potential. NTA was performed to determine **(B, C)** Size distribution, **(D, H)** Average diameter, and **(E, I)** Nanoparticle concentration. **(F, J)** Protein content via BCA assay. **(G, K)** ALP activity. Data are grouped to show the effect of age and exercise. Each dot represents an MV sample from the same isolation, not an individual mouse. Statistical analysis performed via Ordinary two-way ANOVA. *p<0.05, **p<0.01, ***p<0.001, **** p<0.0001.

5.3.8 Exercise enhances B-MVs mineralising potential in a sex-dependent manner

To explore whether sex, aging and long-term exercise influence the mineralising properties of B-MVs, human osteoblasts were cultured for 7 days in osteogenic media supplemented at the beginning of culture with 1.5 µg/mL B-MV from young and aged animals in sedentary or exercised conditions. Mineral deposition was assessed by Alizarin red staining and quantification. After 7 days, B-MVs from both young and aged animals significantly enhanced mineralisation compared with the osteogenic medium control ($p<0.0001$), irrespective of sex. Specifically, MVs derived from young and aged female mice induced a 2.45- and 2.38-fold increase in mineral deposition, respectively, while those from young and aged male mice produced a 2.25- and 2-fold increase (**Figure 5.9A, B**). These findings indicate that aging does not affect the intrinsic pro-mineralising potential of B-MVs in either females or males. The influence of exercise revealed a clear sex-dependent response. In aged females, B-MVs from exercised mice produced a 2.1-fold increase in mineralisation relative to the osteogenic medium control ($p<0.0001$). However, this effect was not significantly different from that observed in sedentary aged females. In contrast, exercise markedly enhanced the mineralising potential of B-Vs derived from aged males, with a significant increase compared to sedentary counterparts ($p < 0.0001$), resulting in a 2.96-fold increase in mineralisation over 7 days ($p < 0.0001$) (**Figure 5.9 A, C**). Moreover, B-MVs from exercised aged males exhibited significantly greater mineralising activity than those from age-matched females ($p < 0.0001$). Overall, these findings demonstrate that the pronounced osteogenic potential of B-MVs is not affected by age in either females or males, however exercise can enhance this osteogenic potential specifically in males, indicating a sex-dependent sensitivity to mechanical activation that may underlie differential regenerative responses to physical activity during aging.

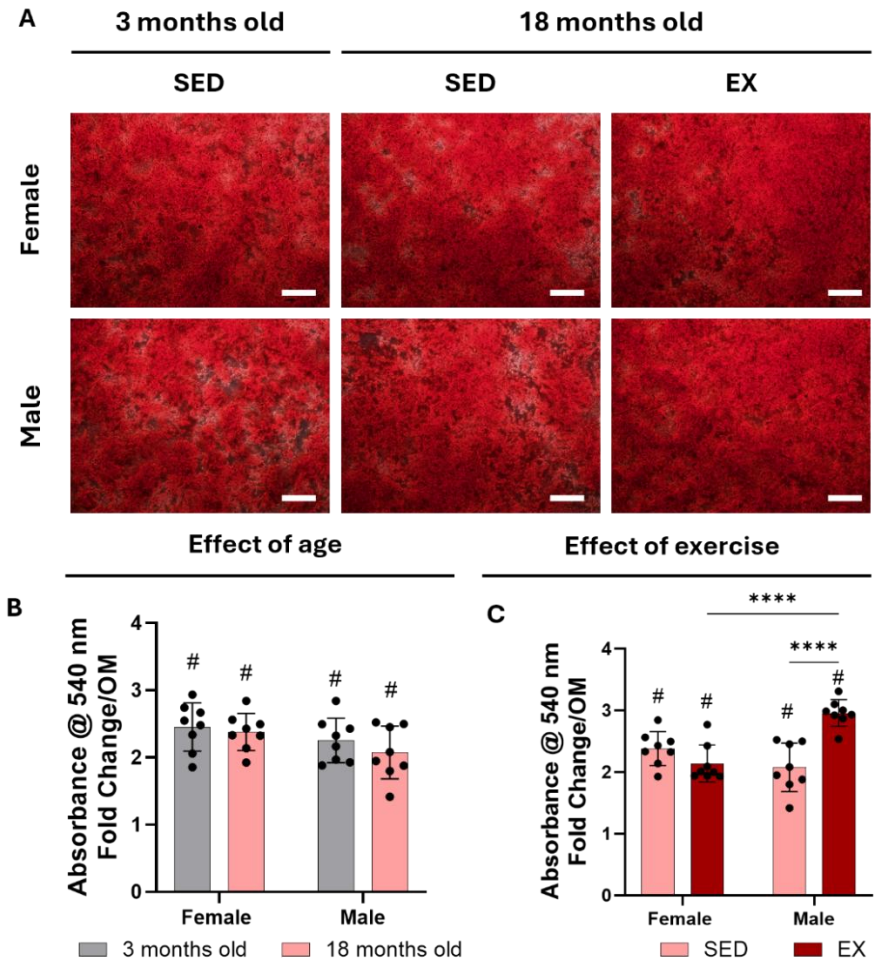

Figure 5.9. B-MVs from young and aged mice promote mineralisation, with exercise enhancing male-derived MVs mineralising potential. **(A)** Representative images of Alizarin red staining following treatment with 1.5 µg/mL of bone-derived MVs. **(B, C)** Alizarin red semi-quantification via cetylpyridium chloride (CPC) destaining for long bone-derived MVs from 3 months old sedentary, 18 months old sedentary and exercised mice, respectively. Scale bar = 500 µm Data are grouped to show the effect of age and exercise. Values are mean ± SD. Statistical analysis performed via Ordinary two-way ANOVA. *p<0.05, **p<0.01, ***p<0.001, **** p<0.0001, # p<0.05 vs OM.

5.3.9 Exercise enhances B-MVs angiogenic potential in a sex-dependent manner

Given the close coupling between osteogenesis and angiogenesis during bone formation and repair [398], we next investigated how age, sex and exercise affect the angiogenic properties of B-MVs. Angiogenic activity was assessed using HUVEC tube formation assays following treatment with 1.5 µg/mL B-MVs isolated from the respective experimental groups (**Figure 5.10 A).** Overall, B-MVs robustly promoted endothelial network formation, with age exerting only a modest influence. B-MVs derived from both young and aged female

mice significantly increased the number of nodes compared with the negative control, showing 1.8- and 1.6-fold increases, respectively ($p < 0.001$). A similar response was observed in males, where B-MVs from young and aged mice induced 1.6- and 1.4-fold increases in node formation ($p < 0.05$) (**Figure 5.10 B**). Comparable age-independent patterns were observed for the number of junctions and segments. In female-derived B-MV treatments, junction and segment numbers increased by 1.7- and 2.1-fold for young mice, and by 1.5- and 1.8-fold for aged mice, respectively ($p < 0.05$). B-MVs from young male mice similarly enhanced junction and segment formation by 1.5- and 1.8-fold ($p < 0.05$). In contrast, B-MVs from aged male mice did not significantly increase junction or segment number relative to the negative control, although no significant differences were detected when compared with the young male group (**Figure 5.10 C, D**). A sex-specific age effect emerged when total segment length was considered**.** B-MVs from female mice significantly increased total segment length irrespective of age, resulting in 2.2- and 1.8-fold increases for young and aged groups, respectively ($p < 0.05$). B-MVs from young male mice also enhanced total segment length by 1.9-fold ($p < 0.05$). However, B-MVs derived from aged male mice showed a significant reduction in total segment length compared with young males ($p < 0.05$) and did not differ from the negative control (**Figure 5.10 E**). We next assessed whether exercise could further promote angiogenesis. In females, B-MVs from exercised mice did not significantly differ from age-matched sedentary controls across any angiogenic parameter. Nevertheless, compared with the negative control, these B-MVs significantly increased node (1.7-fold), junction (1.6-fold), and segment (2.1-fold) formation, as well as total segment length (2-fold) ($p < 0.05$). In contrast, exercise had a pronounced effect in males. B-MVs derived from exercised male mice significantly enhanced node (1.9-fold), junction (1.9-fold), and segment (2.5-fold) formation, as well as total segment length (2.4-fold), compared with the negative control ($p < 0.05$). Importantly, exercise significantly improved all angiogenic parameters relative to age-matched sedentary males ($p < 0.001$), effectively rescuing the age-associated reduction in total segment length (**Figure 5.10 F-I**). Taken together, these findings indicate that the angiogenic capacity of B-MVs is largely preserved with age, whereas exercise selectively enhances this function in a sex-dependent manner. In parallel with the effects observed on osteogenesis, these findings underscore exercise as a potent modulator of B-MVs anabolic activity.

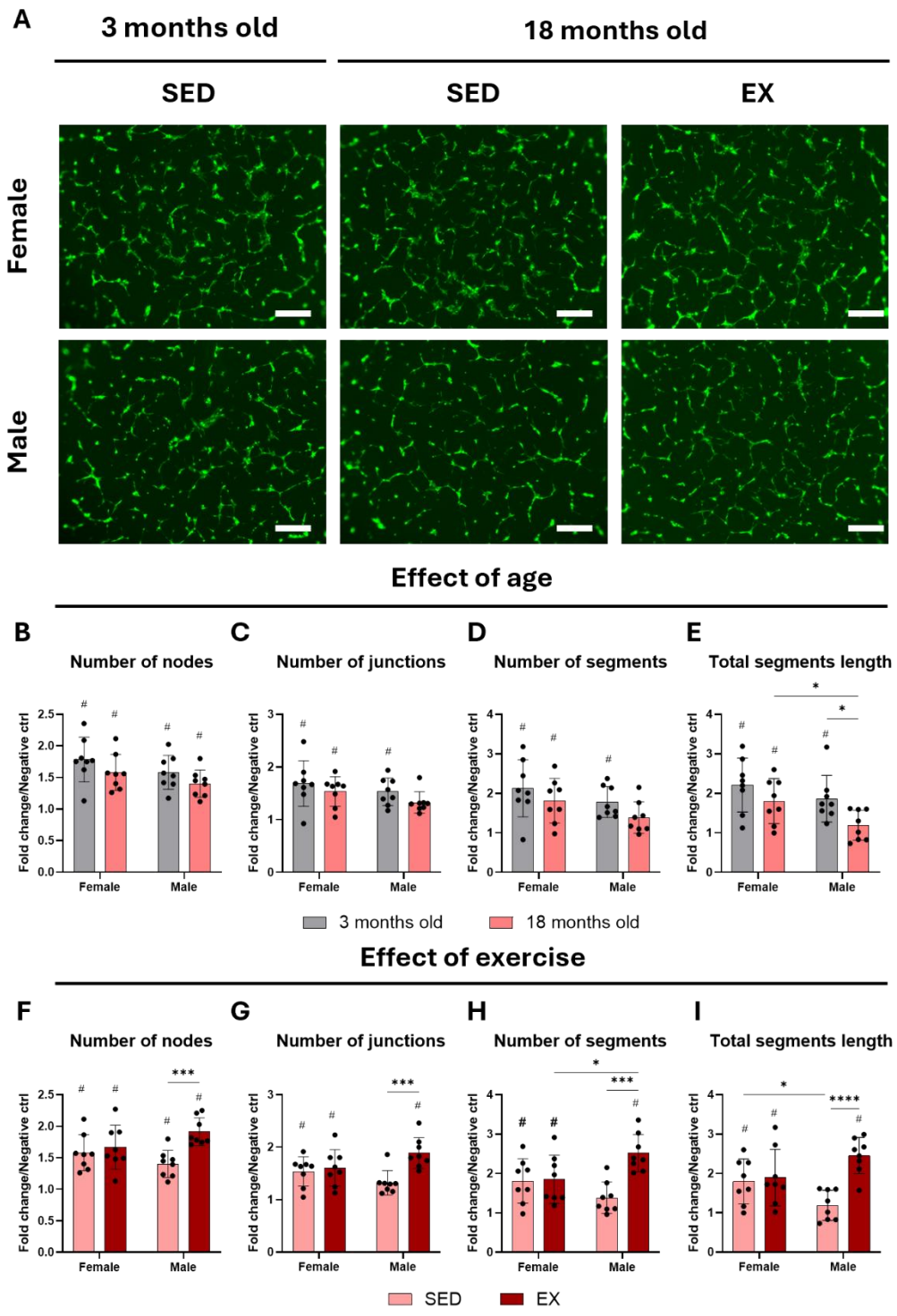

Figure 5.10. B-MVs elicit tube formation in a manner that is dependent on age, gender and exercise. (A) Representative fluorescent images of tube formation at 10h following treatment with 1.5 µg/mL of bone-derived MVs. Quantification of **(B, F)** number of nodes, **(C, G)** number of junctions, **(D, H)** number of segments and **(E, I)** total segment length, each normalised to negative control, for long bone-derived MVs from 3 months old sedentary, 18 months old sedentary and exercised mice, respectively. Scale bar = 500 µm. Data are grouped to show the effect of age and exercise. Values are mean ± SD. Statistical analysis performed via Ordinary two-way ANOVA. *p<0.05, **p<0.01, ***p<0.001, **** p<0.0001, # p<0.05 vs negative control.

5.3.10 Age and exercise influence B-MVs anti-catabolic properties in a sex dependent manner

Having established the effects of age, sex, and exercise on the osteogenic and angiogenic properties of B-MVs, we next investigated whether these factors also influence their anti-osteoclastogenic potential. $CD14^+$ monocytes were cultured for 7 days with RANKL and M-CSF in the presence of 1.5 µg/mL B-MVs derived from the respective experimental groups (**Figure 5.11 A**). Overall, B-MVs exerted a strong inhibitory effect on osteoclastogenesis, which was further amplified with aging**.** B-MVs from young female and male mice significantly reduced osteoclast formation compared with the +RANKL control, resulting in 0.6- ($p<0.01$) and 0.5-fold ($p<0.0001$) reductions, respectively, with no sex-dependent differences. This inhibitory effect was markedly stronger when B-MVs were derived from aged animals. Specifically, B-MVs from aged females reduced osteoclastogenesis by 0.1-fold ($p < 0.0001$), while B-MVs from aged males almost completely abolished osteoclast formation compared to both the +RANKL control and young counterparts ($p < 0.0001$) (**Figure 5.11 B**). Assessment of osteoclast maturity revealed a similar pattern. Osteoclasts differentiated in the presence of B-MVs from young female and male mice showed a 0.5-fold reduction in multinucleation relative to the +RANKL control ($p < 0.0001$). This effect was further enhanced with age, with B-MVs from aged females and males reducing multinucleation by 0.2- and 0.07-fold, respectively, compared with both the +RANKL control and young groups ($p < 0.0001$) (**Figure 5.11 C**). Analysis of total cell numbers indicated that B-MVs from female mice did not significantly affect monocyte adhesion, regardless of age. Similarly, B-MVs from young male mice had no impact on adhesion. In contrast, B-MVs derived from aged male mice significantly reduced monocyte adhesion, resulting in a 0.3-fold decrease compared to the +RANKL control ($p < 0.0001$) (**Figure 5.11 D**). This suggests that the pronounced inhibition of osteoclastogenesis observed in aged male-derived B-MVs may be partially mediated by impaired monocyte adhesion. We next examined whether exercise modulates these anti-osteoclastogenic effects. In females, B-MVs from exercised aged mice significantly inhibited osteoclastogenesis compared with the +RANKL control (0.07-fold) and relative to exercised males ($p<0.0001$). However, no significant differences were observed when compared with age-matched sedentary females. In contrast, exercise exerted a distinct modulatory effect in males. B-MVs from exercised aged male mice partially reversed the near-complete inhibition of osteoclastogenesis induced by sedentary

aged males ($p < 0.0001$), while still maintaining a substantial reduction relative to the +RANKL control (0.2-fold, $p < 0.0001$) (**Figure 5.11 E**). Consistent with these findings, multinucleation was not significantly altered between osteoclasts treated with B-MVs from sedentary and exercised aged females, although exercised female-derived B-MVs reduced multinucleation relative to the +RANKL control (0.2-fold, $p < 0.0001$). Conversely, B-MVs from exercised aged male mice promoted greater multinucleation compared with sedentary males ($p < 0.0001$) yet still induced a 0.4-fold reduction relative to the +RANKL control ($p < 0.0001$) (**Figure 5.11 F**). Finally, monocyte adhesion was unaffected by B-MVs from exercised female mice. Notably, B-MVs from exercised aged male mice restored the adhesion deficit observed in their sedentary counterparts ($p < 0.01$) (**Figure 5.11 G**), indicating that exercise can partially normalise early osteoclast precursor behaviour in males. Collectively, these findings demonstrate that aging markedly enhances the anti-catabolic properties of B-MVs in both sexes. However, exercise exerts a sex-specific modulatory effect, particularly in males, where it attenuates the strong age-associated inhibition of osteoclastogenesis while restoring monocyte adhesion.

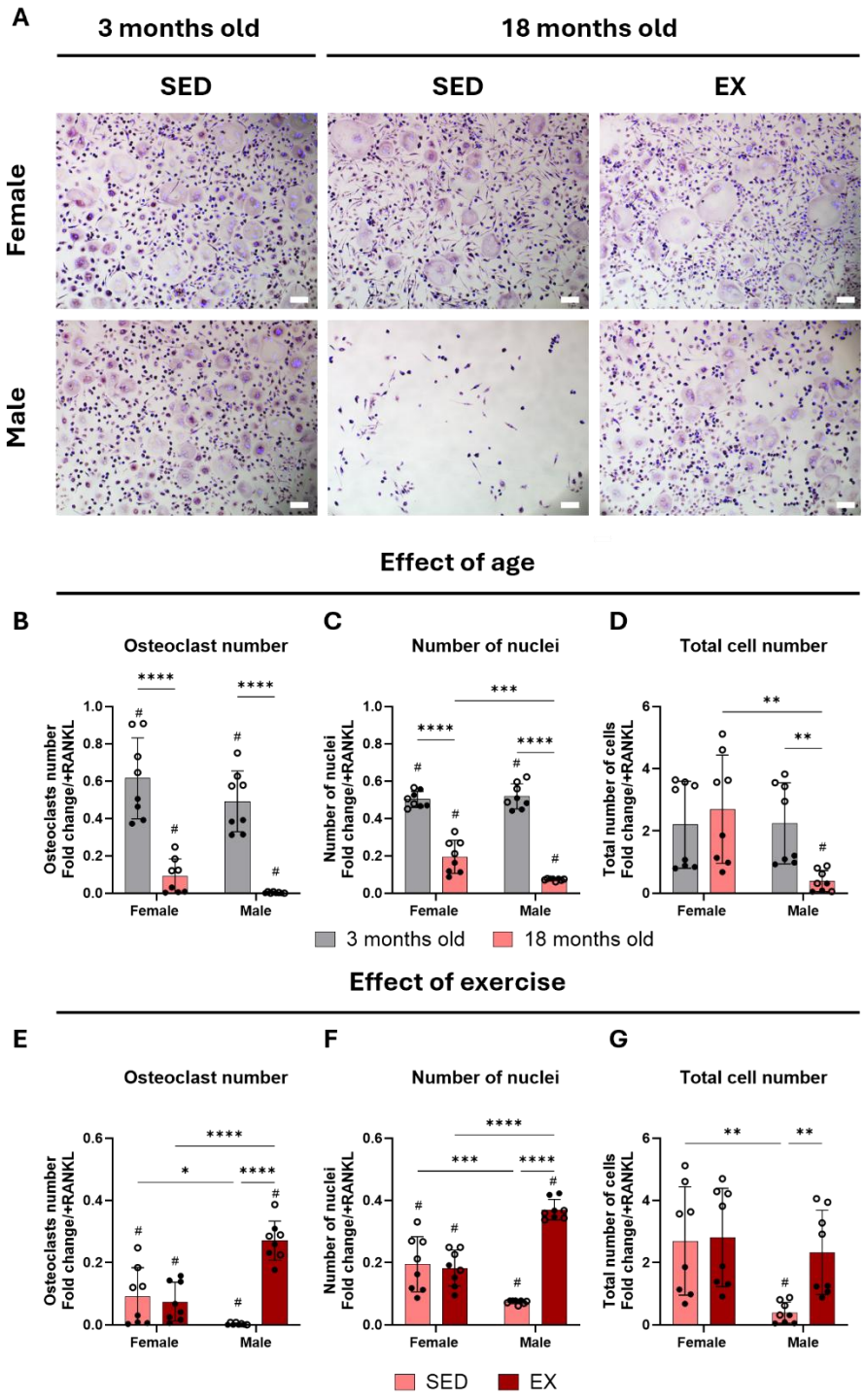

Figure 5.11. Bone-derived MVs inhibit osteoclastogenesis to differing degrees depending on age, sex and exercise. **(A)** Representative images of TRAP and DAPI staining following treatment 1.5 µg/mL of long bone-derived MVs. Quantification of **(B, F)** Osteoclast number, **(C, G)** number of nuclei, (D, H) Total number of cells, each normalised to + RANKL control, for B-MVs from 3 months old sedentary, 18 months old sedentary and exercised mice, respectively. Scale bar = 100 µm. Data are grouped to show the effect of age and exercise. Statistical analysis performed via Ordinary two-way ANOVA. *p<0.05, **p<0.01, ***p<0.001, **** p<0.0001, # p<0.05 vs + RANKL. Values are mean ± SD for 2 different human donors (● = Donor 1, ○ = Donor 2).

5.3.11 Scaffold-mediated delivery of B-MVs enhances hMSC osteogenesis

Following the identification of the multi-targeted regenerative properties of B-MVs and the elucidation of their underlying mechanisms, we next explored their translational potential by integrating them into a clinically relevant collagen-nHA scaffold and assessing human MSC osteogenic differentiation (**Figure 5.12 A**), given the established clinical use of collagen-nHA composites as osteoconductive bone graft substitutes. [399-401]. Metabolic activity of hMSCs cultured on Coll-nHA scaffolds, increased progressively over time, as assessed by Alamar Blue assay, indicating sustained cell viability and metabolic function throughout the culture period. No significant differences in metabolic activity were observed between MVs free scaffolds (control) and scaffolds containing B-MVs at corresponding time points (**Figure 5.12 B**). Analysis of osteogenic and pro-regenerative genes expression at day 7, revealed that B-MVs significantly upregulated key osteogenic markers compared to control. Specifically, expression of BMP-2 (2.6-fold), *ALP* (2.4-fold), *OCN* (1.9-fold) and *VEGF-A* (1.8-fold) ($p<0.05$) was significantly increase by B-MVs compared to control, while *RUNX-2* expression showed an increasing but not significant trend (1.6-fold, $p=0.08$) (**Figure 5.12 C-G**). At end point, total DNA content was comparable between groups (**Figure 5.12 H**), indicating similar cell numbers on control and B-MVs functionalised scaffolds. Interestingly, end point ALP activity normalised to DNA was shown to be significantly higher in the B-MVs group, consistent with the earlier upregulation of ALP gene expression observed at day 7 (**Figure 5.12 I**). In contrast, no significant differences were observed in calcium content after 21 days culture (**Figure 5.12 J**). Histological evaluation at day 21 supported these findings. Picrosirius Red and Alizarin Red staining revealed overall comparable collagen and mineralised matrix deposition between control and B-MVs functionalised scaffolds, although qualitatively the B-MVs-functionalised scaffolds appeared to display slightly more intense Alizarin Red staining (**Figure 5.12 K**). Collectively, these results demonstrate that scaffold-mediated delivery of B-MVs enhances early osteogenic gene expression and ALP activity but does not increase bulk matrix deposition or mineralization at later stages of culture. This pattern suggests that B-MVs primarily act to prime and modulate the osteogenic program of hMSCs rather than driving pronounced late-stage mineralization within the time frame examined.

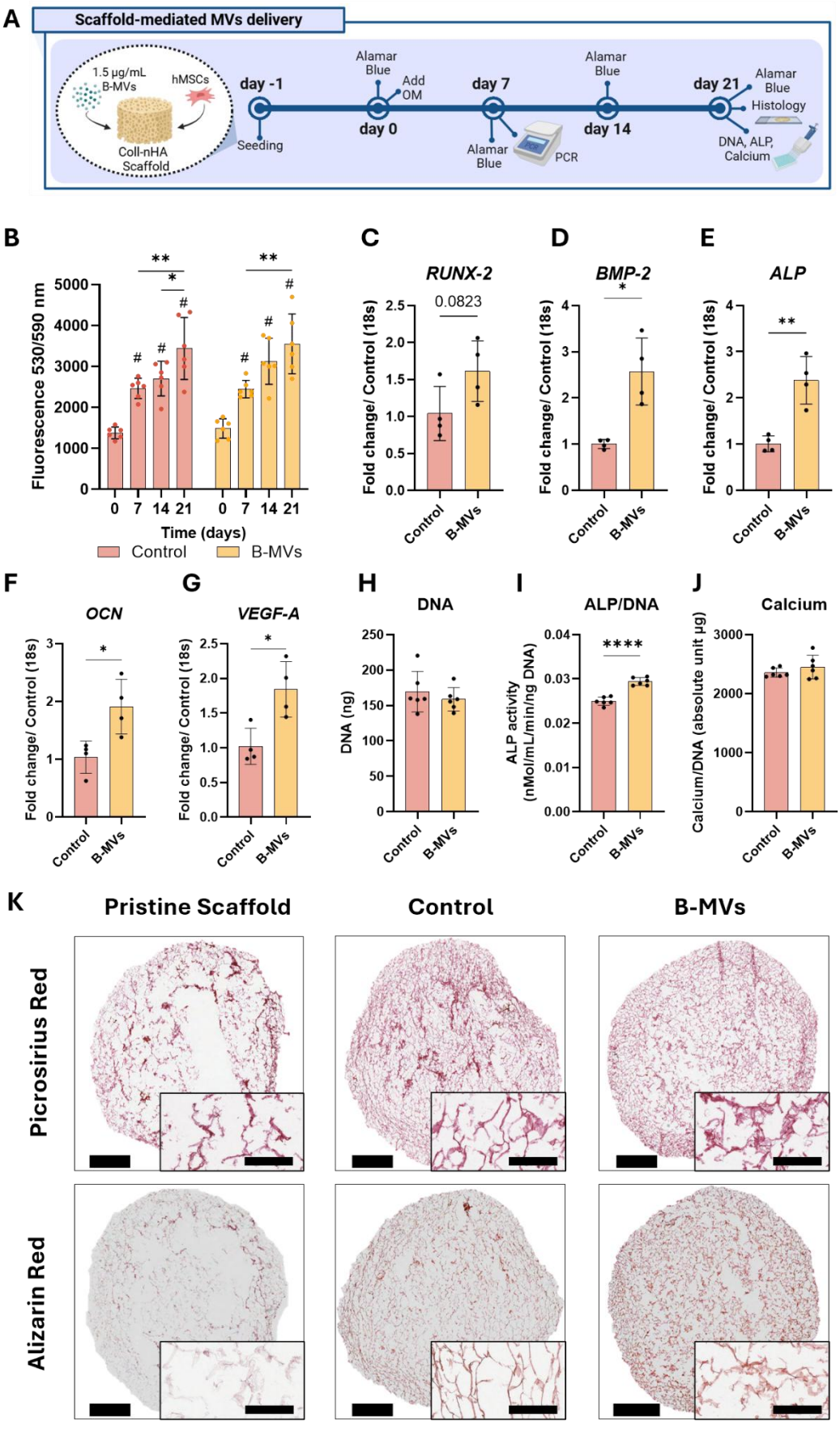
A
Scaffold-mediated MVs delivery
1.5 µg/mL B-MVs
hMSCs
Coll-nHA Scaffold
day -1
Seeding
Alamar Blue
Add OM
day 0
day 7
Alamar Blue
PCR
Alamar Blue
day 14
day 21
Alamar Blue
Histology
DNA, ALP, Calcium
B
Fluorescence 530/590 nm
Time (days)
Control
B-MVs
C
RUNX-2
0.0823
Fold change/ Control (18s)
D
BMP-2
E
ALP
F
OCN
G
VEGF-A
H
DNA
DNA (ng)
I
ALP/DNA
ALP activity (nMol/mL/min/ng DNA)
J
Calcium
Calcium/DNA (absolute unit µg)
K
Pristine Scaffold
Control
B-MVs
Picrosirius Red
Alizarin Red

Figure 5.12. Coll-nHA scaffold mediated delivery of B-MVs supports hMSCs osteogenic differentiation. (A) Schematic representation of the experimental design: Coll-nHA scaffolds were functionalised with B-MVs derived from sedentary 5-month-old male mice and seeded with human hMSCs cultured within the scaffolds in osteogenic medium (OM) for 21 days. (B) Metabolic activity assessed by Alamar Blue assay over the culture period (n=6). (C-G) Gene expression analysis of osteogenic and pro-regenerative markers at day 7, including *RUNX-2* (C), *BMP-2* (D), *ALP* (E), *OCN* (F), and *VEGF-A* (G) (n=4). (H) Total DNA content at day 21 (n=6). (I) Intracellular ALP activity normalized to DNA at day 21 (n=6). (J) Calcium content normalized to DNA at day 21 (n=6). (K) Representative histological images at day 21 with Picrosirius Red showing collagen deposition and Alizarin Red showing mineralization (n=4). Scale bar = 1 mm (200 µm-insert). For all analyses, n indicates the number of independent scaffolds, with each data point representing one scaffold. Statistical analysis was performed using ordinary two-way ANOVA for Alamar Blue data (#p < 0.05 vs. day 0) and unpaired or Welch's t-tests where appropriate, *p<0.05, **p<0.01, ***p<0.001, **** p<0.0001. Data are presented as mean ± SD.

5.4 Discussion

Bone regeneration is a highly coordinated process that depends on the integration of osteogenesis, angiogenesis, and tightly regulated bone resorption, and disruption of any one of these processes can compromise effective repair [398, 402]. While EVs derived from bone cells have emerged as promising cell-free therapeutics, their clinical translation remains limited by challenges related to scalability and manufacturing. MVs, in contrast, are naturally embedded within mineralised extracellular matrix, have been shown to persist within decellularised ECM scaffolds [366], and are likely to be present and biologically active in bone grafts, which remain the clinical gold standard for bone repair. Despite being first described more than five decades ago as initiators of mineralisation, MVs have remained underexplored as regenerative therapeutics. Therefore, this study aimed to systematically evaluate MVs as a scalable, cell-free, and multi-targeted strategy for bone repair. We first established a robust approach for isolating MVs from mineralised tissues and subsequently demonstrated that MVs exhibit a multi-targeted regenerative profile by simultaneously promoting osteogenesis and angiogenesis while suppressing osteoclastogenesis, with these effects varying according to tissue source. Extensive molecular characterisation further revealed that MVs possess distinct surface protein and miRNA signatures associated with their tissue of origin. In addition, we showed that physiological factors, including sex, age, and long-term exercise, dynamically modulate MVs regenerative potency. Finally, we assessed the translational relevance of MVs using a clinically established biomaterial, demonstrating that scaffold-mediated delivery of bone-derived MVs supports early osteogenic differentiation of hMSCs. Collectively, we demonstrate that B-MVs are biologically active vesicles possessing multi-targeted regenerative properties that can be shaped by physiological context and can be harnessed within biomaterial-based strategies.

Bone-derived MVs possess multi-targeted regenerative properties that extend beyond the classical view of MVs as passive initiators of mineralisation and, importantly, can be isolated in substantially higher quantities than EVs derived from *in vitro* cultured bone cells. From a regenerative medicine standpoint, this high vesicle yield constitutes a significant practical advantage, given that vesicle-based therapeutic strategies are often constrained by limited scalability and low production efficiency. In this context, we demonstrated that MVs isolated from bone and kidneys strongly promoted mineral deposition in a dose-dependent

manner, consistent with extensive literature identifying B-MVs as central regulators of early apatite nucleation and mineral propagation through their enrichment in mineralisation-associated enzymes and lipids [203, 214, 215, 403]. Importantly, vesicle-mediated mineralisation is not exclusive to skeletal tissue. A substantial body of work on pathological calcification, including vascular calcification associated with chronic kidney disease (CKD)[404] and kidney stones [405], demonstrates that vesicles released by cells in mineral-prone environments can act as nucleation sites for calcium-phosphate deposition, closely resembling the mechanisms of physiological mineralisation seen in bone. However, effective bone regeneration requires more than mineral deposition alone. In this context, B-MVs were shown to possess strong pro-angiogenic properties, aligning with a growing body of EV literature demonstrating that bone cell-derived vesicles can promote endothelial proliferation, migration and tube formation [19, 192, 406]. These findings support the concept of osteogenesis-angiogenesis coupling, which is now recognised as a key determinant of successful bone regeneration *in vivo* [398, 407]. In addition to their anabolic effects, B-MVs exhibited potent anti-osteoclastogenic activity, consistent with reports demonstrating that vesicles embedded within tissue engineered extracellular matrix can suppress osteoclast differentiation and function, providing a mechanistic link between matrix-associated vesicles and regulation of bone resorption [213]. Furthermore, the superior angiogenic and anti-osteoclastogenic activity of B-MVs compared with K-MVs highlights the tissue-specific biological functions retained by matrix-associated vesicles [408]. Collectively, these observations suggest that vesicles embedded within bone matrix convey regulatory cues aligned with the physiological demands of skeletal tissue, including its strong dependence on vascularisation and continuous remodelling. Importantly, we further demonstrated that B-MVs can be delivered using a clinically relevant biomaterial, enhancing early osteogenic and pro-angiogenic responses. This observation is consistent with previous studies demonstrating that vesicle-functionalised scaffolds support bone regeneration by enabling localised delivery of bioactive cues [312, 409-411]. Collectively, these results demonstrate that B-MVs possess multi-targeted regenerative properties, supporting their potential as therapeutics not only in systemic bone disorders but also in localised bone repair strategies, where spatially controlled vesicle delivery may provide distinct therapeutic advantages.

B-MVs exhibited a distinct protein and miRNA cargo signature that clearly differentiated them from both K-MVs and from bone cell-derived EVs. Hierarchical clustering of vesicle surface protein profiles revealed clear segregation between tissue-derived MVs and cell-derived EVs, with four discrete protein sets identified and one set uniquely enriched in B-MVs. The panel of 37 epitopes assessed by the MACSPlex assay was sufficient to capture this heterogeneity and to define a distinct biomarker signature for B-MVs, distinguishing them from K-MVs and bone cell-derived EVs. Notably, adhesion- and ECM-associated surface markers were enriched across both bone- and kidney-derived MVs, distinguishing tissue-derived MVs from bone cell-derived EVs generated *in vitro*. This shared adhesion signature likely reflects the matrix-associated origin of these vesicles, which are retained within and interact extensively with the extracellular matrix of their native tissues. This observation is consistent with growing evidence that EV heterogeneity is strongly influenced by tissue context and microenvironment, and that vesicles retained withing the ECM carry specialised surface features reflective of local tissue physiology [366, 408, 412]. Beyond this shared tissue-derived signature, B-MVs were further distinguished by a unique enrichment of immune-associated surface markers. Downstream bioinformatic analyses provided insight into the functional relevance of this profile, with protein-protein interaction network analysis revealing strong functional interconnectivity within the B-MV-associated protein set, and gene ontology analyses highlighting biological processes linked to immune regulation. This molecular profile provides a plausible basis for the pronounced anti-osteoclastogenic activity observed for B-MVs. Bone remodelling is tightly regulated by immune-skeletal interactions, and immune cell-derived cues within the bone microenvironment are known to strongly influence osteoclast differentiation and activity. The presence of immune-associated surface markers on B-MVs may suggests that these vesicles directly engage with osteoclast precursors or modulate local immune signalling to suppress excessive resorption [413, 414]. A limitation of this approach is that, although the MACSPlex assay enables the assessment of an extensive panel of selected surface proteins, it remains a targeted analysis and therefore constrains the strength of the conclusions in the absence of comprehensive proteomic profiling. Overall, we demonstrated that MVs possess tissue-specific surface protein profiles that differentiate them from cell-derived extracellular vesicles and are consistent with their biological functions.

Building upon the origin-specific enrichment of surface proteins, small RNA sequencing data further reinforce the concept that B-MVs are molecularly specialised vesicles whose cargo reflects their regenerative phenotype. Principal component and hierarchical clustering analyses demonstrated clear segregation between B-MVs and K-MVs, indicating that miRNA composition is strongly determined by tissue source. This pattern supports an origin-imprinted sorting mechanism rather than passive encapsulation of cytoplasmic content [415, 416]. Notably, the miRNA profile enriched in B-MVs is functionally coherent, with predicted targets clustering in biological processes central to skeletal regeneration. These include angiogenesis, endothelial differentiation, regulation of cell proliferation and differentiation, chromatin remodelling, and insulin receptor signalling. Together, these pathways provide a plausible mechanistic framework explaining the multi-targeted regenerative effects of B-MVs. However, despite MVs possess clearly distinct miRNA signatures upon tissue of origin both B-MVs and K-MVs exhibited comparable pro-osteogenic activity. This finding suggests that osteogenic output is not strictly dependent on the overall complexity of the miRNA cargo. Instead, it is likely that a limited subset of shared or functionally overlapping miRNAs is sufficient to drive mineralisation, consistent with evidence that key osteogenic pathways can be regulated by a relatively small number of dominant miRNA regulators [417, 418] . In parallel, this raises the possibility that vesicle-associated factors beyond miRNAs contribute to this effect, including structural and membrane-associated components that support mineral nucleation [67]. Taken together, these observations point to a model in which osteogenesis is governed by a core set of conserved vesicle-associated cues, while tissue-specific miRNA signatures refine additional regenerative outputs. The enrichment of angiogenic regulatory pathways is particularly compelling given the established coupling between vascularisation and osteogenesis during bone repair [419, 420]. The presence of miRNA targets involved in endothelial differentiation and angiogenic signalling offers a plausible molecular basis for the enhanced pro-angiogenic activity observed in B-MVs. These vesicles may influence endothelial activation and vascular morphogenesis in a manner that promotes coordinated osteogenic coupling. Similarly, enrichment of pathways regulating cell proliferation, differentiation, and insulin receptor signalling aligns with mechanisms central to osteoblast biology. Insulin receptor signalling in osteoblasts promotes bone formation and integrates skeletal and metabolic regulation [397, 421], thereby complementing the intrinsic mineral nucleation

capacity of matrix vesicles and potentially amplifying osteogenic output. The directionality of individual miRNAs further supports this interpretation. For example, miR-30b, a recognised negative regulator of osteogenic differentiation [422, 423], was relatively depleted in B-MVs, suggesting selective exclusion of anti-osteogenic signals. Concurrent enrichment of pathways associated with transcriptional regulation and chromatin remodelling is especially relevant to osteoclastogenesis. Osteoclast differentiation from monocyte precursors is fundamentally governed by transcriptional activation, requiring induction of NFATc1, c-Fos, and other lineage-defining transcription factors [424, 425]. This process is accompanied by extensive chromatin reorganisation that enables expression of osteoclast-specific genes involved in precursor fusion and resorptive machinery. Accordingly, chromatin-remodelling complexes serve as critical regulators of osteoclast lineage commitment and progression [391, 392, 426]. Enrichment of protein glycosylation pathways also holds mechanistic importance. Glycosylation influences receptor stability, trafficking, and surface expression, including key mediators of osteoclast differentiation such as RANK and integrins [394, 427, 428]. Thus, miRNA-driven modulation of glycosylation processes could disrupt receptor functionality or membrane organisation necessary for osteoclast maturation and resorptive activity. Collectively, these findings indicate that the miRNA cargo of B-MVs reflects the molecular identity of their tissue of origin. This origin-imprinted signature aligns closely with their demonstrated multi-targeted regenerative properties, as the enriched miRNAs converge on pathways governing angiogenesis, osteoblast differentiation and osteoclast regulation. Such coordinated targeting suggests that B-MVs function as biologically instructive vesicles, capable of synchronising vascularisation, bone formation, and controlled remodelling.

While the MV isolation strategy was designed to recover vesicles associated with digested tissue, it does not enable definitive discrimination between bona fide MVs and other EV populations present within the tissue microenvironment. These may include EVs contained in interstitial fluid, loosely associated with the ECM, or retained within the matrix and released during enzymatic digestion. Accordingly, the vesicle preparations recovered here should be interpreted as tissue-derived populations enriched for MV-like characteristics rather than a pure MV fraction. This consideration is particularly relevant for the kidney-derived population, as, unlike bone, the kidney is not a classical mineralising tissue in which

matrix vesicles are well-defined mediators of physiological mineral deposition [67]. Nevertheless, several observations support an MV-like identity of the vesicles isolated in this study including their ALP activity, pro-mineralising capacity, nanoscale morphology, EV marker expression, and tissue-specific protein and miRNA signatures. Consistent with current understanding of EV biology, vesicles isolated from tissues following enzymatic digestion are likely to represent heterogeneous populations, and distinguishing between EV subtypes cannot rely on a single defining marker but instead requires combined functional, molecular, and biophysical characterisation [178]. Future refinement of this approach could incorporate complementary purification strategies, such as combining size- and density-based fractionation with fraction-specific functional assessment, to better resolve distinct vesicle subpopulations and associate regenerative activity with defined fractions.

B-MVs anabolic properties were maintained with ageing and were selectively enhanced by long-term exercise in a sex-dependent manner. Bone ageing is traditionally associated with impaired regenerative capacity, reduced mechanosensitivity, and a progressive uncoupling of bone formation and resorption [429, 430]. In contrast, we demonstrate that B-MVs isolated from aged bone maintain the ability to promote mineralisation and angiogenesis while exhibiting an enhanced anti-osteoclastogenic effect. This observation differs from reports describing an age-related decline in the osteo-inductive potential of circulating extracellular vesicles [372], but aligns with evidence from Smith *et al*., who showed that human MSCs cultured with conditioned media derived from decellularised bone matrix from young and aged donors underwent comparable osteogenic differentiation [431]. The influence of donor age on the osteo-inductive capacity of bone-derived graft materials has been widely investigated yet remains controversial. Traianades *et al.* reported that properly processed demineralised bone from donors up to at least 85 years of age retains clinical efficacy as a grafting material [432], a conclusion further supported by clinical studies demonstrating no association between donor age and bone graft-related complications [433]. Conversely, earlier reports suggested that the osteo-inductive capacity of human demineralised bone matrix declines with age [434, 435], raising concerns regarding the use of older donor bone. Taken together, these findings, alongside evidence that MVs are preserved within decellularised extracellular matrix scaffolds [366], suggest that MVs may contribute to the preserved regenerative capacity of bone-derived

graft materials from aged donors. In contrast to anabolic outputs, ageing was associated with a pronounced enhancement of the anti-osteoclastogenic effects of B-MVs. Notably, B-MVs from aged males profoundly impaired monocyte adhesion, resulting in a near complete osteoclastogenesis inhibition. Given that age-related bone loss is driven in part by increased osteoclast activity and dysregulated remodelling balance [436-438], these findings raise the possibility that the ageing bone matrix accumulates vesicle-associated regulatory cues that act to restrain excessive resorption. In addition, our finding demonstrated that long-term exercise further modulated MVs bioactivity in a sex-dependent manner. In aged males, exercise significantly enhanced the osteogenic and angiogenic potential of B-MVs, whereas female-derived B-MVs showed no enhancement in these anabolic outputs. Conversely, although B-MVs from exercised aged males retained anti-catabolic activity, exercise attenuated the near-complete osteoclast inhibition observed with B-MVs from sedentary aged males. This partial attenuation may reflect a rebalancing of remodelling dynamics, whereby mechanical loading restores coupling between bone formation and resorption rather than acting solely through suppression of osteoclastogenesis [157, 320]. This sex-specific response is consistent with extensive evidence demonstrating differential skeletal mechanoadaptation between males and females, with male long bones often showing greater sensitivity to moderate treadmill-based mechanical loading [373, 439]. Collectively, these findings demonstrate that the multi-targeted regenerative properties of B-MVs are dynamically modulated by age, sex, and mechanical loading, positioning them as biologically responsive regulators of bone remodelling and reinforcing their relevance as physiologically relevant platforms for regenerative strategies.

5.5 Conclusion

In summary, this chapter aimed to investigate bone-derived MVs as a multi-targeted therapeutic strategy for bone regeneration. To achieve this, we developed a robust and scalable method for isolating MVs from highly mineralised tissues and performed comprehensive molecular and functional characterisation. Additionally, we demonstrated that B-MVs exert multi-targeted regenerative effects by simultaneously enhancing osteogenesis and angiogenesis while inhibiting osteoclastogenesis. Importantly, we showed that these regenerative properties are resilient to ageing yet remain biologically responsive and can be selectively enhanced by exercise in a sex-specific manner, highlighting mechanical loading as a key regulator of MVs bioactivity. Furthermore, we established that MVs possess a distinct, tissue-specific protein and miRNA signature that differentiates them from cell-derived extracellular vesicles and provides a plausible molecular basis for their functional effects. Finally, we demonstrated that delivery of B-MVs using a clinically relevant scaffold primes osteogenic differentiation of hMSCs, providing proof-of-concept for their translational application. Together, these findings position MVs as novel, scalable, multi-targeted and mechanosensitive cell-free nanotherapeutics for bone regeneration.

Chapter 6. Mechanosensitive miR-150-5p is packaged within osteocyte-derived EVs and possesses both anabolic and anti-catabolic regenerative properties

6.1 Introduction

Bone regeneration is a dynamic, tightly regulated and multi-cellular process that enables bone to adapt to mechanical demands, repair damage, and maintain structural integrity throughout life [440, 441]. Successful bone healing relies on and the precise temporal and spatial coupling of osteogenesis, angiogenesis, and osteoclast-mediated bone resorption [420, 442]. Mechanical loading is a crucial regulator of these processes, with physiological strains promoting bone formation and unloading leading to bone loss [443, 444]. At the centre of this mechanoregulation are osteocytes, terminally differentiated mesenchymal-lineage cells embedded within the mineralised matrix, which act as the primary mechanosensors in bone. Through their extensive lacuna-canalicular network, osteocytes integrate mechanical cues and coordinate the activity of osteoblasts, osteoclasts, and endothelial cells to regulate bone remodelling and regeneration [81, 445]. Traditionally, osteocyte-mediated communication has been attributed to soluble signalling molecules such as prostaglandins, nitric oxide, sclerostin, and growth factors [321, 446]. However, these classical pathways alone cannot fully account for the complexity and specificity of osteocyte signalling, particularly in response to mechanical stimulation.

In recent years, extracellular vesicles (EVs) have emerged as potent mediators of intercellular communication. EVs are nanosized, lipid bilayer-enclosed particles released by all cell types, capable of transferring biologically active cargo, including proteins, lipids, mRNAs, and miRNAs, to recipient cells, thereby modulating their phenotype and function [178]. EVs and their miRNA cargo have been increasingly recognised as regulators of osteogenic and regenerative processes in bone, making them attractive targets for understanding bone biology and developing therapeutic strategies [18, 19, 411, 447]. miRNAs are small, endogenous, non-coding RNAs of approximately 22 nucleotides that regulate gene expression at the post-transcriptional level through sequence-specific interactions with target mRNAs, leading to translational repression or mRNA degradation [448]. miRNAs can target multiple genes simultaneously, often within shared signalling

pathways, allowing them to exert broad and coordinated effects across interconnected biological processes. In bone, miRNAs have been shown to regulate osteoblast differentiation, extracellular matrix production, mineralisation, angiogenesis, and osteoclast differentiation and activity. Dysregulation of miRNA expression has been associated with impaired fracture healing, osteoporosis, and other skeletal pathologies, underscoring their importance in maintaining bone integrity and regenerative capacity [417, 449].

miRNAs can be selectively packaged into EVs, protecting them from enzymatic degradation and enabling their stable transfer to target cells in the microenvironment. A growing body of evidence has shown that the miRNA content of EVs is not a passive reflection of the parent cell transcriptome, but it is actively and selectively sorted in a stimulus-dependent manner [415, 416, 450]. In this context, it has been showed that mechanical loading can alter both intracellular miRNA expression and EV miRNA cargo [451]. Mechanically regulated EV-associated miRNAs are therefore uniquely positioned to translate mechanical cues sensed by osteocytes into coordinated biochemical signals that influence multiple cell types involved in bone regeneration [20]. Through EV-mediated delivery, these miRNAs have the potential to regulate osteogenesis, angiogenesis, and osteoclast activity. Despite growing interest in EV-mediated mechanosignalling, the identity of mechanically regulated miRNAs within osteocyte-derived EVs and their functional relevance to multi-cellular bone regenerative processes remains poorly explored to date.

In this chapter, we investigate whether mechanical stimulation alters the miRNA cargo of EVs released by osteocytes and whether these mechanically regulated miRNAs are associated with biological pathways relevant to bone regeneration. Using miRNA sequencing, we profiled EV-associated miRNAs released by osteocytes under static and mechanically stimulated conditions. Based on differential expression and functional enrichment analyses, we identify miR-150-5p as a candidate mechanically regulated EV-associated miRNA with predicted targets enriched in pathways linked to bone regeneration. In addition, we sought to investigate whether miR-150-5p could regulate osteoblast-mediated mineralisation, angiogenesis, and osteoclast differentiation. Finally, to explore the translational relevance of this miRNA, we investigate whether miR-150-5p can be delivered using a clinically relevant collagen-nanohydroxyapatite scaffold and whether

scaffold-mediated delivery enhances osteogenic differentiation of human MSCs (**Figure 6.1**). Collectively, this chapter aims to identify and harness the specific miRNA components mediating the pro-regenerative effect of mechanically activated EVs.

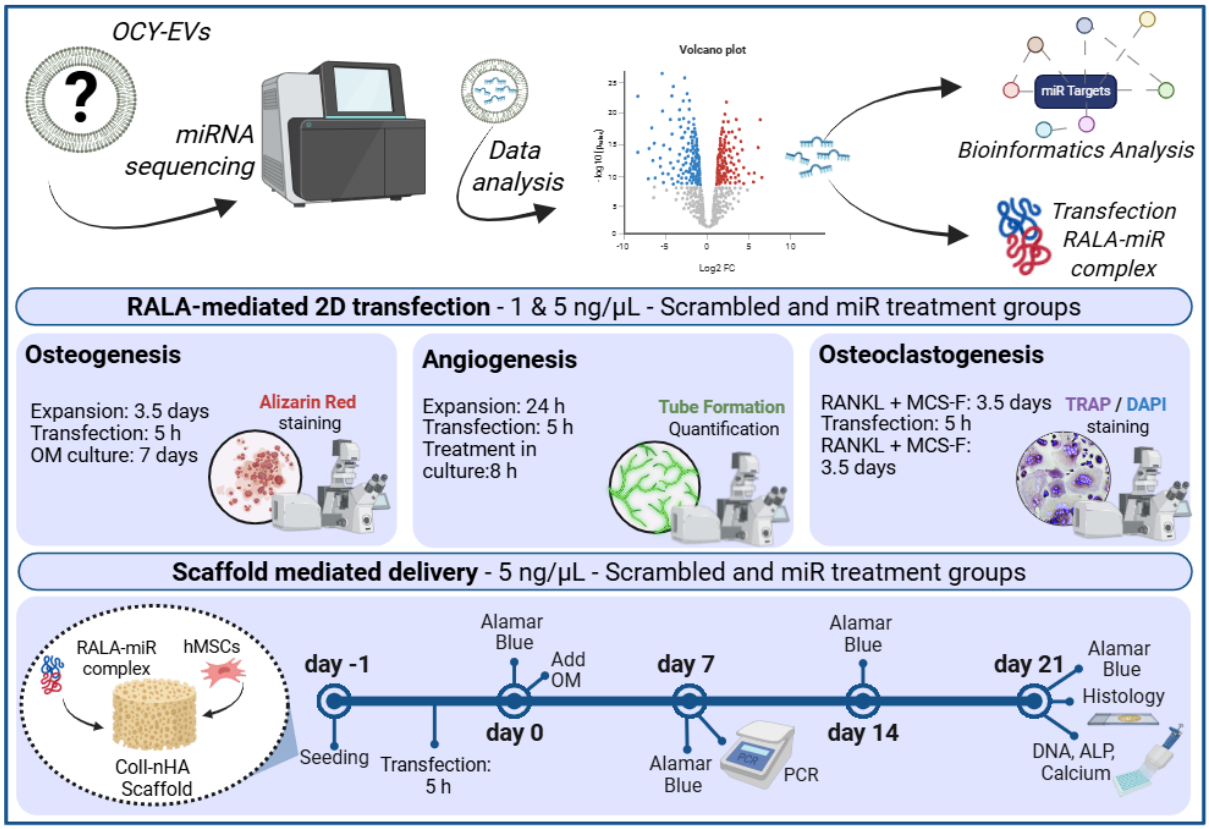

Figure 6.1. Schematic illustrating the experimental workflow used to identify and functionally validate mechanically regulated EV-associated miRNAs. Osteocyte-derived extracellular vesicles (OCY-EVs) were isolated and subjected to miRNA sequencing, followed by differential expression and bioinformatic analyses to identify candidate mechanosensitive miRNAs and their predicted target pathways. miR-150-5p was selected for functional analysis and delivered via RALA-mediated transfection to assess its effects on osteogenesis, angiogenesis, and osteoclastogenesis in 2D culture at two concentrations (1 and 5 ng/µL). Finally, translational relevance was evaluated by functionalising a collagen-nanohydroxyapatite (Coll-nHA) scaffold with miR-150-5p, enabling scaffold-mediated delivery to hMSCs and assessment of metabolic activity, gene expression, and matrix mineralisation over a 21-day osteogenic culture period.

6.2 Materials and methods

6.2.1 Osteocyte mechanical stimulation

Murine osteocyte-like MLO-Y4 cells (Kerafast) were maintained in α-MEM (Merk) supplemented with 2.5 % FBS (Gibco), 2.5 % CS (Biosera), 1% P-S (Sigma) and 1% L-G (Sigma). Tissue culture flasks were coated for 1 h at room temperature with 0.15 mg/mL rat tail collagen type I (Corning), prepared in 0.02 M acetic acid (Sigma), prior to cell seeding. Cells were used for experiments when they had reached 80% confluency between passages 40-60. MLO-Y4 were seeded into collagen-coated 6-well plates with a density of 60,000 cells/well. After 24 h, cultures were washed with PBS and 1.83 mL of serum free α-MEM was added to each well. Mechanical stimulation was applied using an orbital shaker (100 rpm). Following 24 h stimulation CM was collected from static or mechanically stimulated osteocytes and centrifuged at 3,000 x g for 10 min at 4 °C.

6.2.2 Extracellular Vesicles collection

EVs were collected from CM via ultracentrifugation using a 70Ti-fixed angle rotor. Briefly, CM was centrifuged at 2,000 x g for 15 min at 4 °C and then filtered through a 0.45 µm pore filter. Next, CM was ultracentrifuged at 110,000 x g for 75 min at 4 °C. The resulting EVs pellets were washed in PBS and ultracentrifuged again at 110,000 x g for 75 min at 4 °C. Finally, EVs pellets were resuspended in PBS and stored at -80 °C.

6.2.3 miRNA library construction and high throughput sequencing

Total RNA was extracted using Trizol reagent (Invitrogen, CA, USA) following the manufacturer's protocol. The total RNA quality and quantity was analysed with Bioanalyzer 2100 (Agilent, CA, USA) with RIN number >7.0. Approximately 1 µg of total RNA was used to prepare small RNA library according to protocol of TruSeq Small RNA Sample Prep Kits (Illumina, San Diego, USA). Single-end sequencing 50 bp was performed on an Illumina Hiseq 2500 at the LC Sciences (Hangzhou, China) following the vendor's recommended protocol.

6.2.4 Bioinformatic analysis of miRNA-sequencing data

Raw reads were analysed with the ACGT101-miR program (LC Sciences, Houston, Texas, USA) to remove adapter sequences, low quality reads, common RNA families (rRNA, tRNA,

snRNA, snoRNA) and repeats. Subsequently, unique sequences with length between 18–26 nucleotides were mapped to mouse precursors in miRBase 22.0 by BLAST search to identify known mouse miRNAs [452]. Length variations at both 3' and 5' ends and one mismatch inside the sequence were accepted in the alignment. Data quality was assessed using FastQC. miRNAs in static and mechanically stimulated samples were profiled in three biological replicates. Differential expression analysis between conditions was conducted using DESeq2. miRNAs with read counts >25 in two or more replicates in at least one of the treatment groups were included in the analysis. The threshold for significance was set to p-adjusted value <= 0.05 (Benjamini-Hochberg method) and fold change >= 2. Gene ontology enrichment analysis of the miRNAs detected in the EVs was carried out using the miRNA enrichment analysis and annotation tool, miEAA, (https://ccb-compute2.cs.uni-saarland.de/mieaa2/). miRNA gene targets were predicted from TargetScan (version 8.0, http://www.targetscan.org/). Functional annotation and enrichment analysis of the selected genes were performed using the Database for Annotation, Visualization, and Integrated Discovery (DAVID) [453], focusing on GO Biological Process (GO BP) terms. The threshold for significance was set to p-value ≤ 0.05 (EASE score) and Enriched GO BP terms were visualized through a bubble plot generated in R Studio (version 2025.05.1, Build 513) using the ggplot2 package.

6.2.5 miRNA-vector complex formation

miRNA complexes were formed though electrostatic interaction of RALA (GenScript) [454] at an N:P ratio of 10 [455] for miRNA mimic hsa-miR-150-5p and Mimic Negative Control #1 (Scrambled control) (Horizon Discovery) at concentrations of 1 ng/µL and 5 ng/µL in OptiMEM (Gibco).

6.2.6 Osteogenesis assay

Human osteoblast-like SaOS-2 cells (Cytion) were maintained in DMEM GlutaMAX™ supplemented with 10% FBS and 1% P-S. Cells between passages 12-20 were used once they reached 80% confluency. For osteogenesis assay, cells were seeded into 24-well plates (Corning) pre-coated with 0.15 mg/mL rat tail collagen type I (prepared in 0.02 M acetic acid) at a density of 10,000 cells/cm² and cultured in DMEM GlutaMAX™ supplemented with 10% FBS and 1% P-S. After 3.5 days, 200 µL miR-RALA complex were added to the cells

following PBS wash and incubated for 5 h at 37 °C. Positive and negative controls were incubated with OptiMEM alone under the same conditions. At the end of the incubation, complexes where removed, and cells were cultured in growth medium for additional 24 h. Next, medium was replaced with 500 µL of osteogenic medium (growth medium supplemented with 100 nM dexamethasone, 10 mM β-glycerophosphate, and 0.05 mM ascorbic acid). Osteogenic medium was replenished after 3.5 days of culture. After 7 days in osteogenic medium, calcium deposition was assessed by Alizarin Red staining. Cells were fixed with 4% (w/v) PFA for 15 min at room temperature, rinsed with PBS followed by diH_2O, and incubated with 1% Alizarin Red solution for 20 min at room temperature in the dark. Excess stain was removed by repeated washing with diH_2O until the background appeared clear. Wells were air-dried and imaged under phase-contrast microscopy using an Olympus IX83 microscope equipped with a 4x objective. Quantification of calcium deposition was performed by destaining with 10% CPC solution, and absorbance was measured at 540 nm. Absorbance values were normalised to positive control.

6.2.7 Angiogenesis assay

GFP-HUVECs were maintained in EBM-2 supplemented with the EGM-2 BulletKit (Lonza). Cells were thawed at passage 8 and cultured in T-75 flasks (Sarstedt) pre-coated with 0.15 mg/mL rat tail collagen type I (Corning), prepared in 0.02 M acetic acid. Cells were seeded in collagen coated 48-well plates at a density of 30,000 cells/well in growth media. After 24 h culture, cells were washed with PBS, 100 µL miR-RALA complex were added to the cells and incubated for 5 h at 37 °C. Negative control was incubated with OptiMEM alone under the same conditions. At the end of the incubation, complexes where removed, and cells were cultured in growth medium for additional 24 h. Next, 96-well plates were coated with 25 µL well of reduced growth factor basement membrane matrix Geltrex (Thermo Fisher Scientific) and incubated for 45 min at 37 °C to allow polymerization. Transfected cells were then reseeded at a density of 10,000 cells/well in EBM-2 supplemented with 1% P-S and incubated for 8 h at 37 °C, 5% CO_2 to allow tube formation. Following incubation, cells were imaged at 488 nm using an Olympus IX83 microscope equipped with a 4x objective. Tube formation was analysed using the Angiogenesis Analyzer plugin in ImageJ (version 1.54p, NIH, USA) and quantified by the number of nodes, number of junctions, number of segments, and total segment length, normalized to the negative control.

6.2.8 Osteoclastogenesis Assay

The use of human blood samples for this study was approved by the research ethics committee of Trinity College Dublin and was conducted in accordance with the Declaration of Helsinki. Leukocyte-enriched buffy coats from anonymous healthy donors were obtained with permission from the IBTS, St. James's Hospital, Dublin (Researcher code: 0000RES625). Donors provided informed written consent to the IBTS for their blood to be used for research purposes. PBMCs were isolated from leukocyte-enriched human buffy coats using density gradient centrifugation with LymphoPrepTM solution (Progen). $CD14^+$ monocytes were isolated from PBMCs by magnetic sorting using MagniSort Human CD14 Positive Selection Kit (Invitrogen) according to the manufacturer's instructions. Cells were seeded 625,000 cells/cm^2 in 96-well plates in α-MEM containing 10 % FBS, 1 % P-S and 1 % L-G supplemented with 25 ng/mL M-CSF (Myltenyi Biotec) and 50 ng/mL RANKL (PeproTech). After 3.5 days of culture, cells were washed with PBS, and 100 µL of miR-RALA complexes were added. The +RANKL control received Opti-MEM (Gibco) alone. All cultures were incubated for 5 h at 37 °C. After incubation complexes were removed and fresh growth medium supplemented with M-CSF and RANKL was added. On day 7, cells were fixed with 2 % PFA for 15 min at room temperature, then washed twice with PBS and stained for TRAP activity with a leukocyte acid Phosphatase (TRAP) Kit (Sigma) according to the manufacturer's protocols. Finally, cells were incubated with Triton X-100 0.1 % (Sigma) for 10 min, rinsed with PBS and then incubated with DAPI (1:1000) (Sigma) for 10 min. TRAP-positive multinuclear cells containing 3 or more nuclei were classified as osteoclasts. Cells were imaged using an Olympus IX83 inverted microscope with 10x objective. Osteoclasts, nuclei per osteoclast, and total cell counts were quantified manually using the Cell Counter plugin in ImageJ (version 1.54p, NIH, USA) and normalised to +RANKL control.

6.2.9 Manufacture of miRNA delivery platform

6.2.9.1 miR-150-5p functionalised scaffold fabrication

Collagen-nHA (Coll-nHa) scaffolds were fabricated following the technique developed by Cunniffe *et al*. [385, 456]. Briefly, a collagen slurry was prepared by blending Type-I microfibrillar bovine collagen (Integra Life Sciences, Inc) with 0.5 M acetic acid. nHA particles were synthesized as previously reported [386] and added to the collagen slurry during the blending process to achieve a 1:1 ratio nHA to collagen ratio. Following blending,

the slurry was degassed using a vacuum pump to remove entrapped air bubbles and subsequently freeze-dried at -40◦C under 200 Torr vacuum to produce the final scaffold material. Cylindrical samples (6 mm diameter, 4 mm height) were produced using a biopsy punch and hydrated in PBS prior to crosslinking. Scaffolds were crosslinked for 2 h at room temperature in a solution containing EDAC and NHS prepared in dH_2O, using 6 mmol EDAC per gram of collagen and a 5:2 EDAC:NHS molar ratio, calculated based on collagen content only. Excess unreacted EDAC/NHS was removed by three sequential PBS washes. For miRNA loading, the effective scaffold volume was first calculated by correcting the geometric volume for scaffold porosity. This adjusted volume was then used to determine the total quantity of miR/RALA complexes required to achieve a final concentration of 5 ng/µL. The calculated amount of complexes for each scaffold was subsequently suspended in 40 µL of OptiMEM, which was then soak-loaded into the Coll-nHA scaffolds (20 µL per side) for 15 min at 37 °C. Non transfected control scaffolds were incubated with OptiMEM alone.

6.2.10 Therapeutic efficacy of miR-150-5p delivery on Coll-nHA scaffolds

6.2.10.1 hMSCs culture and osteogenic differentiation

hMSCs were isolated from bone marrow and cultured in DMEM with GlutaMAX™ (Gibco), supplemented with 10% FBS and 1% P/S. Cells at passage 3 were used once they reached approximately 80% confluency. For seeding, 2×10^5 hMSCs were suspended in 40 µL of OptiMEM and distributed evenly onto both sides of each scaffold (20 µL per side), followed by a 15-min incubation at 37 °C to allow cell attachment. Scaffolds were incubated for 5 h at 37 °C. After incubation complexes were removed and fresh growth medium was added. After 24 h, the growth medium was replaced with osteogenic medium. Cells were then cultured on the scaffolds for 21 days in osteogenic medium, with medium changes twice weekly.

6.2.10.2 Analysis of hMSCs metabolic activity

Cell metabolic activity during osteogenic differentiation was assessed using the Alamar Blue assay following the manufacturer's protocol (Invitrogen). At days 0, 7, 14, and 21, culture medium was removed, and scaffolds were rinsed with PBS. Alamar Blue reagent was diluted 1:10 in fresh osteogenic medium, and 500 µL of the working solution was added to each scaffold. Samples were incubated for 4 h at 37 °C, protected from light, after which

fluorescence was measured using excitation and emission wavelengths of 530 nm and 590 nm, respectively.

6.2.10.3 Analysis of miR-150-5p transfection on osteogenic gene expression

After 7 days of culture in osteogenic medium, osteogenic gene expression was evaluated. The medium was removed from each scaffold, followed by a PBS rinse, and 1 mL of TRIzol reagent (Sigma) was added. Samples were then stored at -80 °C for 48 h before total RNA extraction using the manufacturer's protocol. RNA concentration was measured using a NanoDrop spectrophotometer (Thermo Fisher Scientific), and purity was assessed from the 260/280 and 260/230 ratios. RNA was reverse-transcribed into cDNA using the High-Capacity cDNA Reverse Transcription Kit (Applied Biosystems), and cDNA concentration was determined with the Qubit™ ssDNA Assay Kit (Thermo Fisher Scientific). Quantitative PCR (qPCR) was performed using SYBR Select Master Mix (Applied Biosystems) with 10 ng of cDNA per reaction. The genes analysed included *RUNX-2*, *BMP-2, ALP*, *OCN*, and *VEGF-A*, with *18S* serving as the housekeeping control (**Table 6.1**). Reactions were run on a QuantStudio™ 5 PCR System (Applied Biosystems). The relative mRNA amounts of each sample were calculated using the $2^{-\Delta\Delta Ct}$ method with reference to *18S* housekeeping gene and expressed as fold change normalised to the NT control group.

Table 6.1. Forward and reverse SYBR Green primer sequences for qRT-PCR

Gene	Supplier	Catalogue number	Forward/Reverse sequence
RUNX-2	Invitrogen	10629012	F: 5'- AAGCTTGATGACTCTAAACC R: 5'- TCTGTAATCTGACTCTGTCC
BMP-2	Invitrogen	10629012	F: 5'- TCCACCATGAAGAATCTTTG R: 5'- TAATTCGGTGATGGAAACTG
ALP	Invitrogen	10629012	F: 5'- TCTTCACATTTGGTGGATAC R: 5'- ATGGAGACATTCTCTCGTTC
OCN	Invitrogen	10629012	F: 5'- TTCTTTCCTCTTCCCCTTG R: 5'- CCTCTTCTGGAGTTTATTTGG
VEGF-A	Invitrogen	10629012	F: 5'- AGGGCAGAATCATCACGAAGT R: 5'- AGGGTCTCGATTGGATGGCA
18S	Sigma	-	F: 5'-ATCGGGGATTGCAATTATTC R: 5'-CTCACTAAACCATCCAATCG

6.2.10.4 DNA assay

DNA content was quantified using the Quant-iT™ PicoGreen® dsDNA Assay Kit (Invitrogen) following the manufacturer's protocol. On day 21, culture medium was removed, and scaffolds were rinsed with PBS. Each scaffold was lysed in 1 mL of lysis buffer containing 0.2% (v/v) Triton X-100 (Sigma) and 10 mM Tris (pH 8) (Thermo Fisher Scientific) prepared in ultrapure diH_2O. Complete cell lysis was achieved through three freeze-thaw cycles between -80 °C and room temperature. For the assay, DNA standards were prepared according to the manufacturer's instructions, and 100 µL of either standard or sample lysate was transferred to a black 96-well plate. A 1:200 PicoGreen working solution was then added at 100 µL per well, and fluorescence was measured at 485 nm excitation and 538 nm emission.

6.2.10.5 ALP assay

Intracellular ALP activity was quantified using the SIGMAFAST™ pNPP kit (Sigma). A standard curve was generated in a round bottom clear 96-well plate using serial dilutions of pNPP together with 10 µL of 43 µM ALP enzyme (Sigma). For sample measurements, the cell lysates prepared for DNA quantification were also used for ALP analysis. Lysates were diluted 1:1 in dH_2O to a final volume of 80 µL per well, after which 50 µL of 5 mM pNPP solution was added. Samples were incubated for 1 h at room temperature in the dark, and absorbance was recorded at 405 nm. ALP activity was calculated from the amount of pNPP generated, divided by sample volume and incubation time, and finally normalised to DNA content.

6.2.10.6 Calcium assay

Calcium deposition in on the 3D Coll-nHA scaffolds was quantified using the LiquiColor® Calcium kit (StanBio 0150) following the manufacturer's instructions. Culture medium was first aspirated from each scaffold, which was then rinsed twice with PBS. Scaffolds were transferred to individual Eppendorf tubes containing 1 mL of 0.5 M HCl and incubated overnight at 4 °C under rotation to ensure complete decalcification and calcium ion extraction. After incubation, the working reagent was prepared by mixing the Total Calcium Colour Reagent and Total Calcium Base Reagent in a 1:1 ratio, and a standard curve was generated using serial dilutions of the 100 µg/mL calcium standard in 0.5 M HCl. For the assay, 10 µL of each sample, diluted 1:6 in 0.5 M HCl, or standard was pipetted into a clear

96-well plate, followed by 200 µL of the working reagent. Absorbance was measured at 595 nm. Calcium content of pristine scaffolds (cell-free) was subtracted from the samples' values.

6.2.10.7 Histological evaluation

Scaffolds were washed twice in PBS and fixed in 4% PFA for 1 h at room temperature. Following fixation, constructs were rinsed twice in PBS, embedded in optimal cutting temperature (OCT) compound, and frozen at -80 °C for at least 24 h prior to sectioning. Sections of 7 µm thickness were obtained using a cryostat (Leica CM3050 S) and mounted onto SuperFrost™ microscope slides (Fisher Scientific), then stored at -80 °C until staining. Picrosirius Red and Alizarin Red staining were performed to assess collagen and mineral deposition, respectively. Imaging was carried out using an Aperio AT2 slide scanner (Leica).

6.2.11 Statistical analysis

All data were analysed using GraphPad Prism 10.5. Data were analysed using ordinary two-way ANOVA or t-test when appropriate. Statistically significant differences were indicated as *$p<0.05$, **$p<0.01$, ***$p<0.001$, **** $p<0.0001$.

6.3 Results

6.3.1 Osteocytes release extracellular vesicles that contain miRNAs associated with bone regeneration that are increased following mechanical stimulation

As extracellular vesicles have been shown to mediate communication via the packaging and delivery of miRNAs [457], many of which are known regulators of bone regeneration [458], we sought to profile the miRNA cargo within mechanically activated EVs in order to investigate their potential mechanism of action. miRNAs within EVs released from statically cultured and mechanically activated osteocytes were profiled in three replicates using high throughput sequencing (miRNA-seq). A total of 550 known (mature) murine miRNAs were detected in EVs collected from both groups. Of these, 428 (78%) were classified as lowly expressed and removed from the analysis. The remaining 122 miRNAs showed a strong expression signal and were used in downstream analysis. Functional overrepresentation analysis (ORA) was performed on this set of miRNAs using miEAA, a web-based application. Over-representation analysis found a significant enrichment of miRNAs associated with gene ontology categories such as blood vessel remodelling, cell proliferation, positive regulation of angiogenesis and ossification (**Figure 6.2 A**). Differential expression analysis using DESeq2 revealed two distinct miRNAs that were significantly upregulated in mechanically activated EVs when compared to EVs derived from statically cultured osteocytes (mmu-miR-150-5p (log2 fold change = 2.3; p-adjusted value = 0.01) and mmu-miR-2137 (log2 fold change = 2.3; p-adjusted value = 0.02) (**Figure 6.2 B**). Building on findings from the previous chapter, which demonstrated enrichment of miR-150-5p and miR-2137 in bone-derived MVs, miR-150-5p was prioritised for further analysis based on existing evidence supporting its involvement in biological processes relevant to bone regeneration [459, 460]. Target Scan analysis identified 356 genes that are potential targets of this mechanically regulated miRNA. Functional enrichment analysis of these genes revealed 112 significantly enriched Gene Ontology (GO) terms. Notably, GO enrichment indicated associations with processes involved in bone regeneration, including “positive regulation of angiogenesis” (GO:0045766) [344], “canonical Wnt signalling pathway” (GO:0060070) [461] and,” positive regulation of nitric oxide biosynthetic process” (GO:0045429) [462]. Additionally, several GO terms were directly related to osteoclast

differentiation and function, such as “osteoclast differentiation”, “regulation of glycolytic process” [463], “cell-cell adhesion” [464], “regulation of cell-matrix adhesion” [465], “cellular response to retinoic acid” [466], and “response to estradiol” [467] (**Figure 6.2 C).** Together, these data identify miR-150-5p as a mechanically regulated EV-associated miRNA with predicted targets enriched in pathways relevant to bone regeneration.

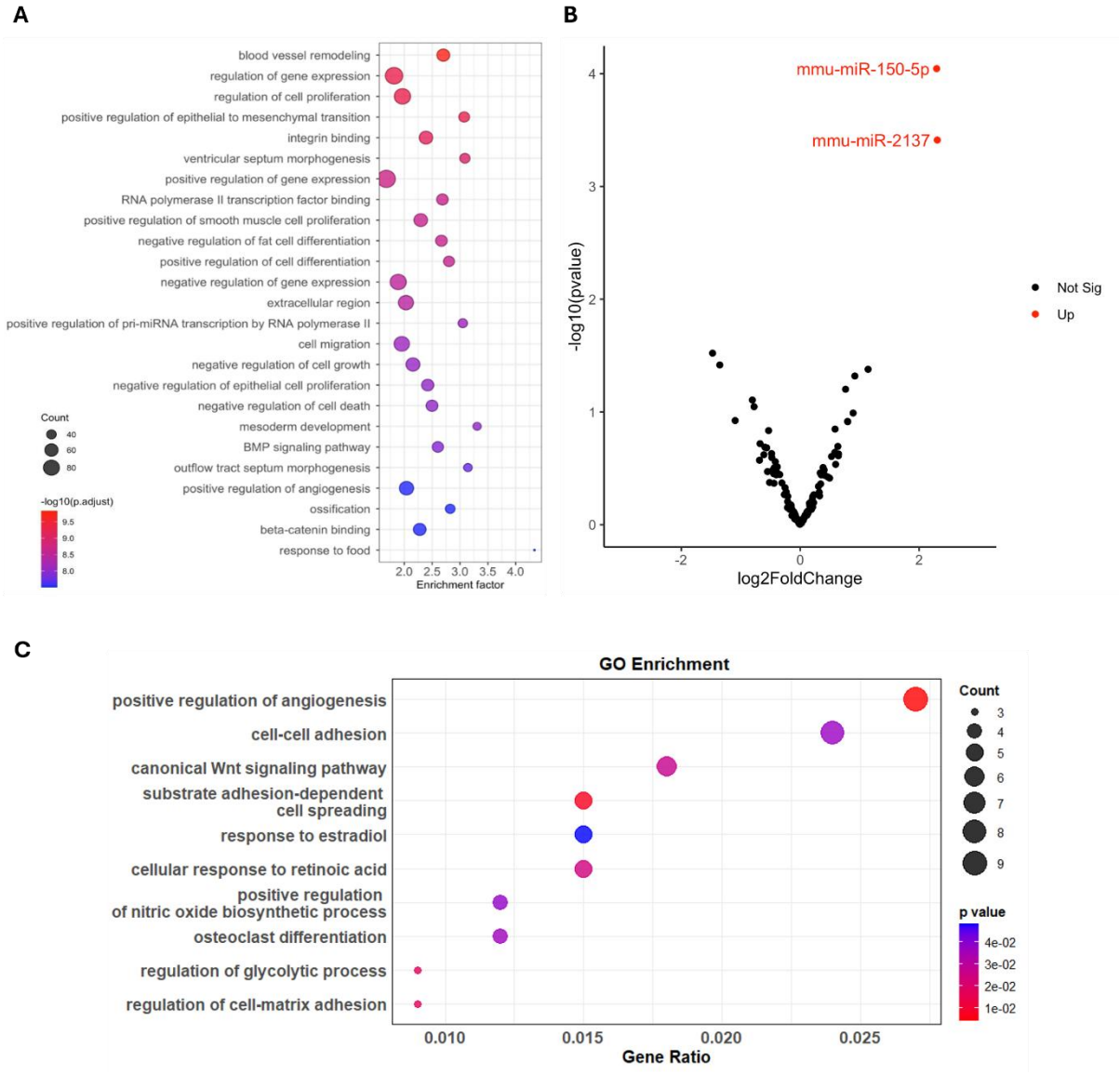

Figure 6.2. Mechanical stimulation of osteocytes results in the production of EVs significantly more enriched in miR-150-5p. (A) miEAA Enrichment of the 122 miRNAs detected in static (EV-S) and mechanically stimulated osteocyte-derived EVs (EV-F). **(B)** Volcano plot of miRNAs expressed in EV-S vs EV-F. Red dots represent the upregulated miRNAs (fold change ≥ 2; p-adjusted value ≤ 0.05). **(C)** GO enrichment analysis (Biological Process) of the target genes derived from Target Scan predictions of miR-150-5p.

6.3.2 miR-150-5p transfection promotes osteogenesis.

Mechanical stimulation of osteocytes was previously shown to promote osteogenesis through the release of EVs, indicating that EV-associated cargo contributes to this anabolic response [18]. In parallel, GO enrichment analysis of predicted miR-150-5p target genes identified significant associations with biological processes relevant to bone formation, including positive regulation of nitric oxide biosynthetic processes and canonical Wnt signalling. Together, these observations suggested that miR-150-5p may represent a key EV-associated mediator of osteogenic activity. Therefore, to evaluate the pro-osteogenic potential of miR-150-5p, mineral deposition was assessed in human osteoblast-like cells cultured in 2D following delivery of a miR-150-5p mimic at two concentrations (1 ng/µL and 5 ng/µL). A scrambled miRNA control was included at matched concentrations, alongside an osteogenic medium control (positive control), and mineralisation was assessed after 7 days of culture. Representative Alizarin Red stained images illustrate calcium deposition across experimental conditions (**Figure 6.3 A**). Quantitative analysis by CPC destaining revealed that treatment with scrambled miRNA at 1 ng/µL significantly increased mineralisation compared with the positive control (2.82-fold, $p < 0.0001$), indicating measurable effect of the RALA peptide-mediated delivery system itself at lower nucleic acid concentrations. Delivery of miR-150-5p at 1 ng/µL resulted in a further significant increase in mineral deposition relative to the positive control (3.33-fold, $p < 0.0001$) and promoted mineralisation to a greater extent compared to the scrambled miRNA control at the same concentration ($p<0.05$), suggesting a miRNA-specific pro-osteogenic effect. At the higher concentration, scrambled miRNA treatment did not increase mineralisation relative to the positive control and showed a significant reduction in mineral deposition compared with the lower dose ($p < 0.0001$). In contrast, miR-150-5p delivery at 5 ng/µL significantly increased mineralisation compared with the positive control (1.8-fold, $p<0.05$), although mineral deposition was significantly reduced relative to miR-150-5p treatment at 1 ng/µL ($p < 0.0001$) (**Figure 6.3 B**). Although the N:P ratio was maintained, increasing miRNA dose resulted in higher absolute RALA exposure, and cell-penetrating peptides have been shown to exhibit concentration-dependent membrane perturbation and cytotoxic effects at elevated peptide levels, which can blunt functional cellular responses [468]. Taken together, these findings demonstrate that miR-150-5p promotes osteogenic mineralisation *in vitro*,

with maximal anabolic effects observed at the lower concentration, supporting its role as a functionally relevant EV-associated mediator of osteocyte-driven osteogenesis.

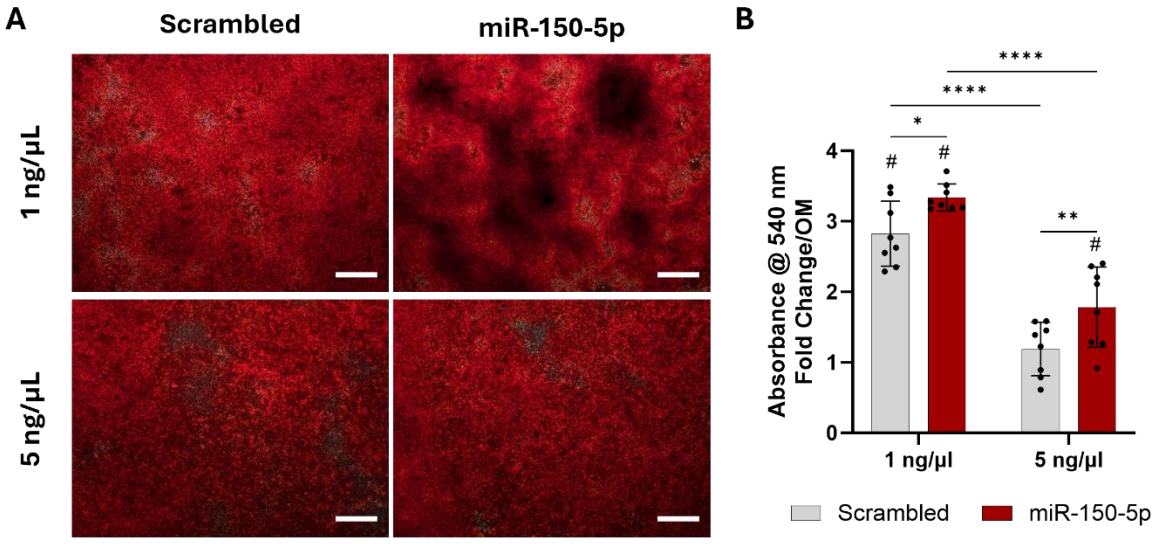

Figure 6.3. miR-150-5p enhances mineralisation to differing degrees depending on the miRNA dose. (A) Representative images of Alizarin red staining of SaOS-2 cells cultures following treatment with 1ng/µL and 5 ng/µL of scrambled control and miR-150-5p mimic. **(B)** Alizarin red semi-quantification via CPC destaining. Scale bar = 500 µm. Values are mean ± SD. Statistical analysis performed via Ordinary two-way ANOVA, *p<0.05, **p<0.01, ***p<0.001, **** p<0.0001, # p < 0.05 vs positive control.

6.3.3 miR-150-5p transfection promotes angiogenesis

Coupling between osteogenesis and angiogenesis is essential for successful bone healing. During the early stage of bone formation, angiogenic factors promote microvascular sprouting, which facilitates the recruitment of osteoblasts and their progenitors [469]. In the later stages, vascularization and mineralization are tightly coordinated to support the maturation of newly formed bone. Disruption of this coupling compromises bone regeneration, leading to abnormal bone formation and the development of skeletal disorders [470]. We previously demonstrated that osteocyte-derived EVs promote angiogenesis [19]. Consistent with these findings, GO analysis of predicted miR-150-5p target genes revealed a significant association with positive regulation of angiogenesis. Together with the identification of miR-150-5p as a mechanically regulated EV cargo, these observations led us to investigate whether miR-150-5p could directly mediate pro-angiogenic effects. To address this, miR-150-5p mimic was delivered at 1 ng/µL and 5 ng/µL to human endothelial cells cultured in the absence of angiogenic factors, and tube

formation was assessed. Cells in basal medium (negative control) or treated with matched concentration of scrambled miRNA were used as controls (**Figure 6.4 A**). Treatment with 1 ng/µL scrambled miRNA significantly enhanced tube formation compared to the negative control, as reflected by increases in the number of nodes, junctions, segments, and total segment length (1.92-, 1.88-, 2.56-, and 2.09-fold, respectively; all $p < 0.0001$ vs. negative control), indicating that the RALA peptide delivery system itself contributes to angiogenic responses at this concentration. At the same concentration, miR-150-5p further promoted tube formation compared with both control groups, resulting in 2.66-, 2.55-, 3.38-, and 2.76-fold increases across the analysed parameters ($p < 0.0001$ vs. negative control), with additional significance relative to the scrambled control ($p < 0.01$). A similar pattern was observed at 5 ng/µL, where both scrambled miRNA and miR-150-5p significantly enhanced tube formation compared with the negative control across all quantified parameters ($p < 0.0001$). Notably, treatment with the higher concentration of scrambled miRNA resulted in a greater angiogenic response than its lower dose, increasing the number of nodes, junctions, segments, and total segment length by 2.66-, 2.56-, 3.44-, and 2.87-fold, respectively ($p<0.01$). Given the non-targeting nature of the scrambled sequence, these dose-dependent effects are most likely driven by increased exposure to the RALA delivery system rather than miRNA-mediated mechanisms. Importantly, miR-150-5p at 5 ng/µL significantly exceeded the angiogenic response induced by scrambled miRNA, eliciting 3.58-, 3.42-, 4.76-, and 3.56-fold increases in nodes, junctions, segments, and total segment length, respectively ($p< 0.001$) (**Figure 6.4 B-E**), indicating a miRNA-specific effect. Together, these findings demonstrate that miR-150-5p exerts a robust pro-angiogenic effect, supporting its role as functionally relevant EV-associated mediator of osteocyte-driven angiogenesis.

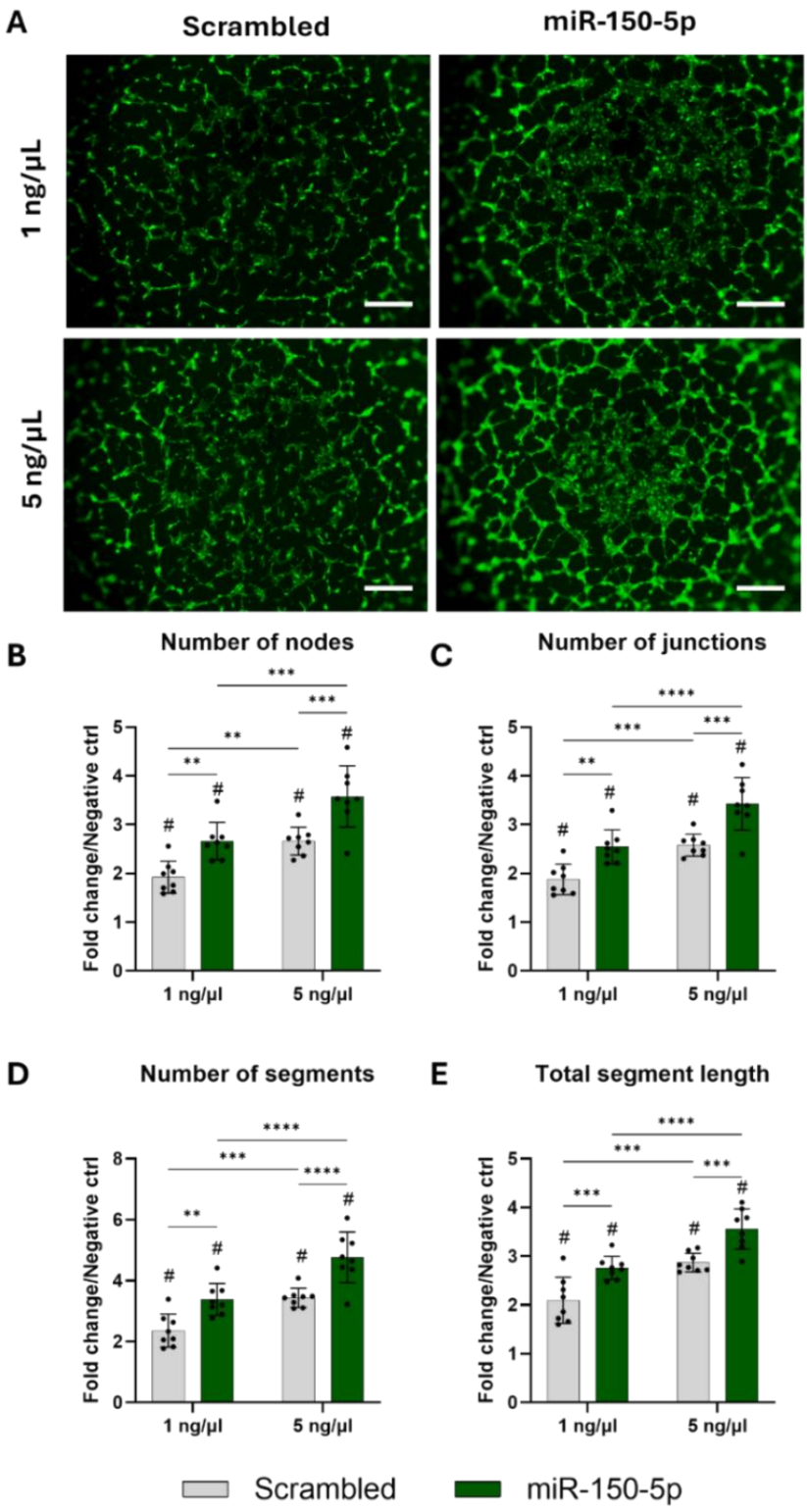

Figure 6.4. miR-150-5p enhances tube formation in a dose dependent manner. (A) Representative fluorescent images of tube formation at 8h following with 1ng/µL and 5 ng/µL of scrambled control and miR-150-5p **(B)** number of nodes, **(C)** number of junctions, **(D)** number of segments and **(E)** total segment length, each normalised to negative control. Scale bar = 500 µm. Values are mean ± SD. Statistical analysis performed via Ordinary Two -way ANOVA, *p<0.05, **p<0.01, ***p<0.001, **** p<0.0001, # p<0.05 vs negative control.

6.3.4 miR-150-5p inhibits osteoclast differentiation in a dose-dependent manner

Balanced bone regeneration requires not only enhanced osteogenesis and angiogenesis but also the suppression of excessive osteoclast-mediated bone resorption. We previously observed that osteocyte-derived EVs exert anti-catabolic effects and GO analysis of miR-150-5p target genes revealed enrichment of pathways associated with osteoclast differentiation. These findings suggested that miR-150-5p may contribute to the anti-catabolic effects of osteocyte-derived EVs. Therefore, we next examined the effect of miR-150-5p on osteoclast differentiation. Human monocytes were transfected with a miR-150-5p mimic at two concentrations (1 ng/µL and 5 ng/µL), and osteoclastogenesis was assessed. Cells treated with osteoclastogenic factors alone (+RANKL control) and cells transfected with matched concentrations of scrambled miRNA were included as controls (**Figure 6.5 A**). At the lower concentration (1 ng/µL), transfection with either scrambled miRNA or miR-150-5p significantly reduced osteoclast formation relative to the +RANKL control, resulting in 0.6-fold ($p = 0.001$) and 0.8-fold ($p<0.05$) decreases in osteoclast number, respectively. No significant difference in osteoclast number was observed between miR-150-5p and scrambled miRNA at this concentration. Assessment of osteoclast maturation, quantified by the number of nuclei per cell, revealed a similar reduction in both scrambled and miR-150-5p treated groups compared with the +RANKL control (0.77-fold, $p < 0.001$ and 0.8-fold, $p < 0.05$, respectively), with no significant difference between the two treatments. Total cell number was also comparable between scrambled and miR-150-5p conditions. However, scrambled miRNA transfection resulted in a modest reduction compared with the +RANKL control (0.65-fold, $p < 0.01$), without evidence of impaired monocyte adhesion. At the higher concentration (5 ng/µL), scrambled miRNA transfection produced effects similar to those observed at the lower dose, with reductions in osteoclast number (0.62-fold, $p < 0.05$), nuclei number (0.8-fold, $p < 0.0001$), and total cell number (0.5-fold, $p < 0.01$) relative to the +RANKL control. In contrast, miR-150-5p transfection at 5 ng/µL resulted in a markedly greater inhibition of osteoclastogenesis, reducing osteoclast number to 0.36-fold of the +RANKL control ($p < 0.0001$) and significantly below the scrambled control at the same concentration ($p < 0.05$). Osteoclasts formed under this condition also exhibited significantly fewer nuclei compared with both the +RANKL control (0.5-fold, $p < 0.0001$) and the scrambled miRNA condition ($p < 0.001$), indicating impaired

osteoclast maturation. Total cell number did not differ between scrambled and miR-150-5p treatments at this dose, although both were reduced relative to the +RANKL control (0.6- and 0.5-fold, respectively; $p < 0.0001$), with no evidence of altered monocyte adhesion (**Figure 6.5 B-D**). These findings suggest that miR-150-5p possess dose-dependent anti-catabolic properties, suggesting a role in mediating EVs anti-catabolic effects.

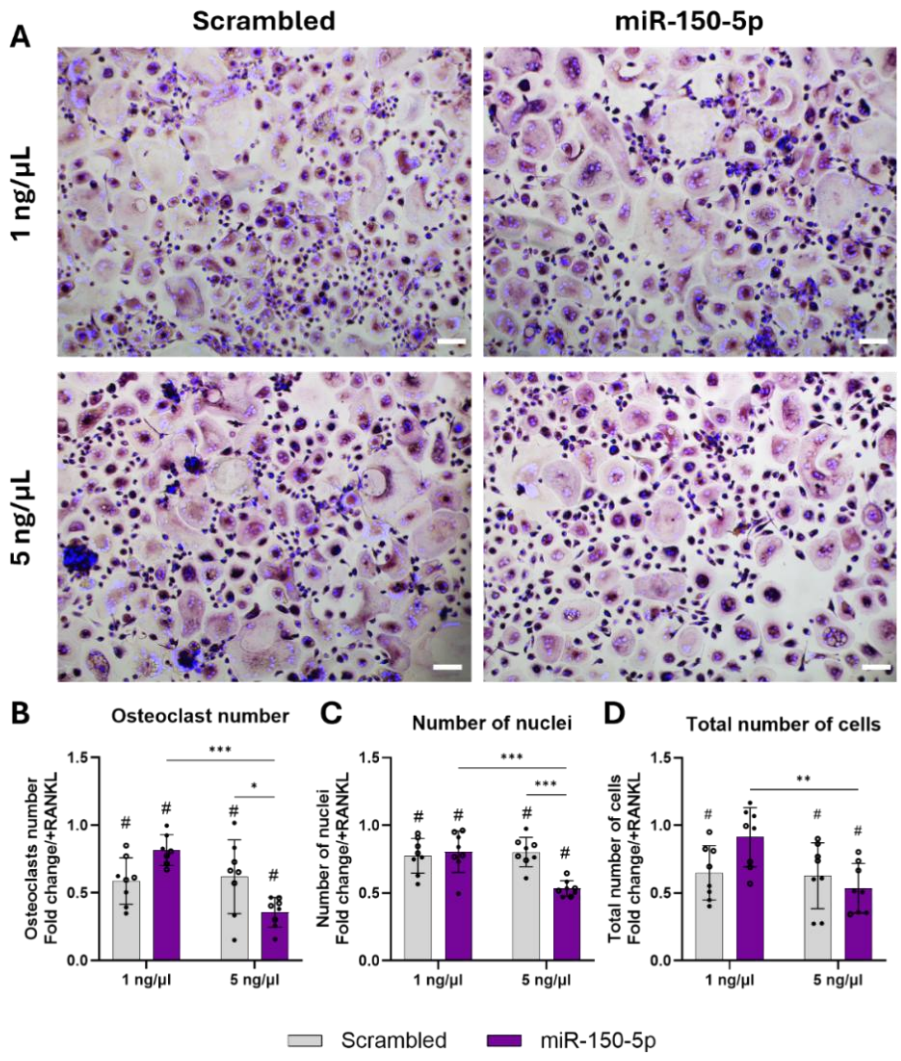

Figure 6.5. miR-150-5p inhibits osteoclastogenesis in a dose dependent manner. (A) Representative images of TRAP and DAPI staining of human $CD14^+$ monocytes transfected with 1 ng/µL and 5 ng/µL Scrambled control or miR-150-5p. Quantification of (B) Osteoclast number, (D) nuclei number and (D) total number of cells. Scale bar = 100 µm. Values are mean ± SD for 2 different human donors (● = Donor 1, ○ = Donor 2). Values are mean ± SD. Statistical analysis performed via Ordinary Two -way ANOVA, *p<0.05, **p<0.01, ***p<0.001, **** p<0.0001, # p<0.05 vs +RANKL.

6.3.5 Scaffold-mediated delivery of miR-150-5p promotes mineralisation

Having demonstrated the multi-targeted properties of miR-150-5p, we next investigated whether miR-150-5p could be delivered using the same approach as B-MVs in the previous chapter, and whether delivery of miR-150-5p alone using a clinically relevant platform could enhance osteogenesis and bone formation. To this end we functionalised a Coll-nHA scaffold with 5 ng/µL of RALA/miR-150-5p complexes and assessed hMSCs osteogenic differentiation and mineralisation after 21 days. Coll-nHA scaffolds functionalised with scrambled miRNA at the same concentration was used as control. Cell metabolic activity was assessed over time to determine whether delivery of miR-150-5p affected hMSC viability or metabolic function. Metabolic activity increased progressively across all time points for both scrambled miRNA treated and miR-150-5p treated cells, indicating sustained cell activity over the culture period. Quantitative analysis revealed an increase in metabolic activity over time relative to day 0 within each treatment group, consistent with cell proliferation. Importantly, no significant differences in metabolic activity were observed between scrambled miRNA and miR-150-5p treated cells at any assessed time point, indicating that delivery of miR-150-5p did not adversely affect cell metabolic activity or viability (**Figure 6.6 A**). Osteogenic and pro-regenerative gene expression was analysed after 7 days culture in osteogenic medium. For each marker assessed, both scrambled and miR-150-5p groups exhibited comparable expression levels, with no statistically significant differences detected between treatments (**Figure 6.6 B-F**), suggesting that miR-150-5p delivery did not alter early osteogenic marker expression relative to scrambled control under these conditions. At end point, total DNA content and ALP activity were comparable between groups (**Figure 6.6 G**), indicating similar cell numbers on control and miR-150-5p-activated scaffolds and confirming the earlier expression of ALP gene expression observed at day 7. Interestingly, miR-150-5p-activated scaffolds exhibited significantly higher calcium content normalised to DNA compared with scrambled control scaffolds ($p<0.05$) (**Figure 6.6 I**). Furthermore, histological analysis at 21 days demonstrated comparable collagen deposition between conditions, alongside increased mineral deposition in miR-150-5p-activated scaffolds, in agreement with the quantitative calcium measurements (**Figure 6.6 J**). Overall, despite no detectable effects on early osteogenic gene expression, miR-150-5p

significantly increased hMSC mineralisation after 21 days of culture, indicating a specific role in the later stages of osteogenic differentiation and matrix mineralisation.

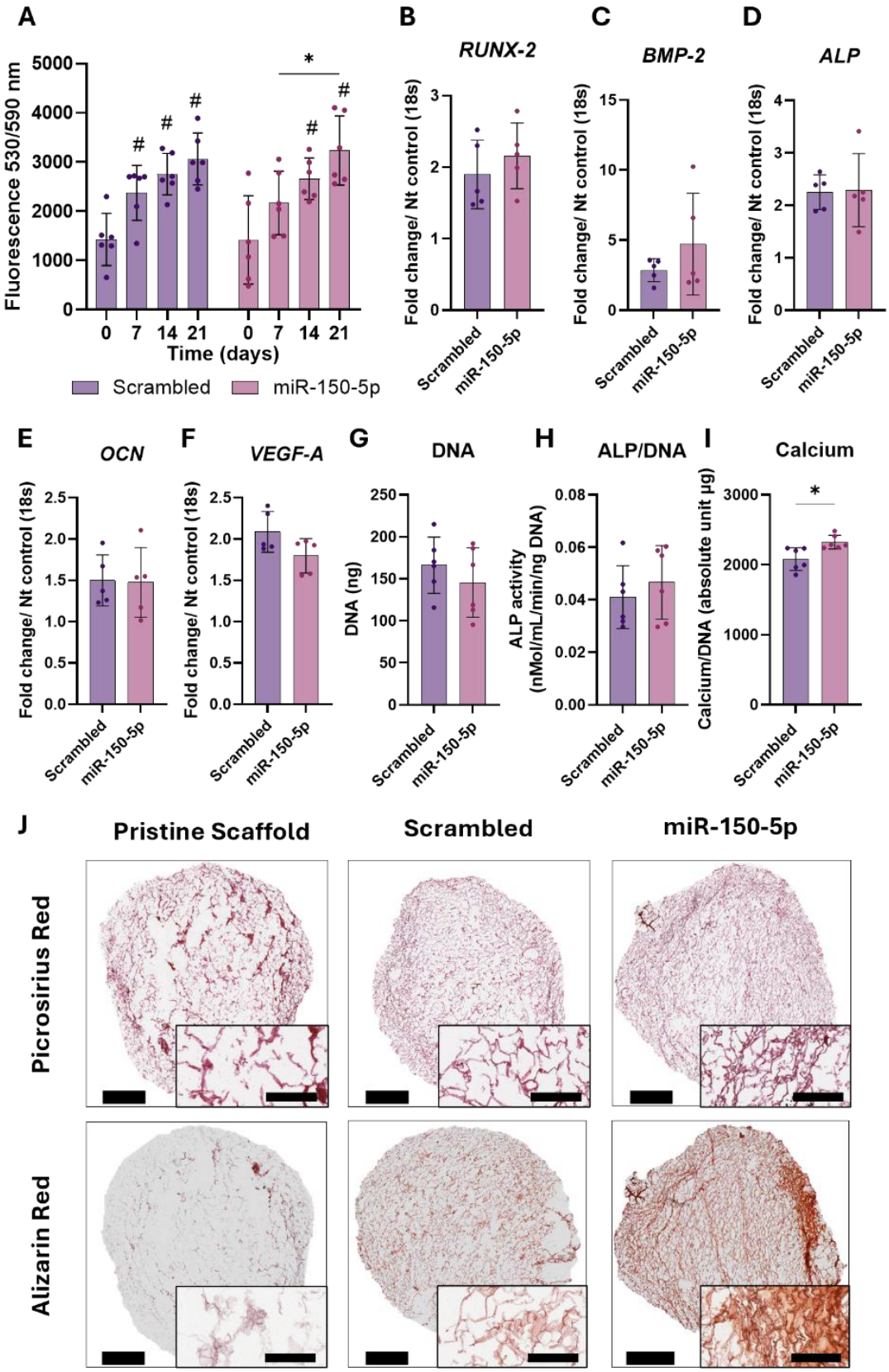

Figure 6.6. miR-150-5p-activated scaffold promotes hMSCs osteogenic differentiation. (A) Metabolic activity assessed by Alamar Blue assay over the culture period (n=6). **(B-F)** Gene expression analysis of osteogenic and pro-regenerative markers at day 7, including *RUNX-2* **(B)**, *BMP-2* **(C)**, *ALP* **(D)**, *OCN* **(E)**, and *VEGF-A* **(F) (n=4)**. **(G)** Total DNA content at day 21 (n=6). **(H)** Intracellular ALP activity normalized to DNA at day 21 (n=6). **(I)** Calcium content normalized to DNA at day 21 (n=6). **(J)** Representative histological images at day 21 with Picrosirius Red showing collagen deposition and Alizarin Red showing mineralization (n=4). Scale bar = 1 mm (200 µm-insert). For all analyses, n indicates the number of independent scaffolds, with each data point representing one scaffold. Statistical analysis was performed using ordinary two-way ANOVA for Alamar Blue data (#$p < 0.05$ vs. day 0) and unpaired or Welch's t-tests where appropriate, $p < 0.05$, *$p < 0.01$, **$p < 0.001$, ***$p < 0.0001$. Data are presented as mean ± SD.

6.4 Discussion

Successful bone regeneration depends on the coordinated integration of osteogenesis, vascularisation, and tightly regulated bone resorption to preserve skeletal integrity and enable repair. Mechanical loading is a central regulator of this process, driving adaptive bone remodelling through osteocyte-mediated sensing and transduction of mechanical cues into pro-regenerative signals. Increasing evidence indicates that EVs constitute a critical mediator of this osteocyte paracrine signalling network, enabling the targeted delivery of bioactive cargo, including microRNAs, that regulate osteoblast activity, vessel formation, and osteoclast differentiation [471]. Building on these concepts and the findings of the previous chapters, this chapter demonstrated that mechanical stimulation selectively tunes the miRNA cargo of osteocyte-derived EVs in a functionally relevant manner, identifying miR-150-5p as a mechanically regulated EV-associated miRNA with predicted roles in pathways central to bone regeneration. Functional validation revealed that miR-150-5p exhibits multi-targeted regenerative properties, simultaneously promoting mineralisation and angiogenesis while inhibiting osteoclast differentiation. Finally, we show that miR-150-5p can be delivered to hMSCs using a clinically relevant Coll-nHA scaffold, enhancing late-stage mineralisation. Collectively, these findings identify miR-150-5p as a mechanosensitive EV-associated miRNA with coordinated anabolic and anti-catabolic activity, offering mechanistic insight into EV-mediated regulation of bone regeneration and supporting this miRNA as a candidate for future regenerative strategies.

Mechanical stimulation selectively modulates the miRNA cargo of osteocyte-derived extracellular vesicles. Both miR-150-5p and miR-2137 were significantly enriched in EVs released by mechanically stimulated osteocytes compared with EVs from static cultures, indicating that mechanical cues influence EV miRNA composition. This observation is consistent with previous studies demonstrating that EV cargo is dynamically and selectively packaged in response to changes in the physiological state or stimulation of the parent cell, rather than passively reflecting intracellular RNA abundance [20, 415, 472]. Among the mechanically regulated EV-associated miRNAs, miR-150-5p emerged as a key candidate with strong enrichment in pathways central to bone regeneration. Bioinformatic analyses revealed that predicted miR-150-5p target genes are enriched within pathways regulating angiogenesis, canonical Wnt signalling, nitric oxide biosynthesis, and osteoclast

differentiation. This is biologically relevant because effective bone repair depends on tight osteogenic-angiogenic coupling. Specialised endothelium and vascular expansion actively support osteoprogenitor activity and bone formation, so enrichment of angiogenesis-associated terms fits a regenerative EVs programme [419, 420]. Likewise, canonical Wnt signalling is a central determinant of osteoblast-lineage commitment and bone mass regulation, making Wnt-related enrichment consistent with pro-osteogenic potential [473]. Finally, the presence of osteoclast differentiation-related GO enrichment suggests a multi-targeted effect: mechanically activated osteocyte EVs may carry miRNA signals that not only promote anabolic repair but also tune resorption. Overall, these finding support miR-150-5p as a mechanically regulated EV-associated miRNA with the potential to regulate bone remodelling in response to mechanical stimulation.

miR-150-5p exerts multi-targeted regenerative effects that mirror the regenerative properties of mechanically activated EVs [18, 19]. In this study, delivery of miR-150-5p enhanced osteoblast-mediated mineralisation, promoted endothelial tube formation, and inhibited osteoclast differentiation, collectively supporting its role as regulator of bone regeneration. However, the osteogenic role of miR-150-5p remains context dependent and controversial in the literature. Several studies support a pro-osteogenic function; for example, Dong *et al.* demonstrated that miR-150 promotes osteoblast differentiation and matrix mineralisation by targeting negative regulators of osteogenesis in murine pre-osteoblasts (MC3T3-E1) [474]. Consistent with this, Xu *et al.* showed that miR-150-5p delivered via hMSCs EVs, attached to magnetic nanoparticles, enhanced bone formation and ameliorated osteoporosis *in vivo* [460]. In contrast, other reports describe an inhibitory effect of miR-150-5p on osteogenic differentiation, depending on the cell type, differentiation stage, and delivery context [475, 476]. The enhancement of mineralisation observed here, with maximal effects at lower miR-150-5p concentrations, aligns with this mixed literature and suggests that miR-150-5p functions as a fine-tuning regulator rather than a unidirectional driver of osteogenesis. In addition, the pro-angiogenic properties of miR-150-5p are consistent with previous studies reporting that miR-150 secreted by monocytes induces endothelial tube formation *in vitro* and angiogenesis *in vivo*. Furthermore, down-regulation of miR-150 has been linked to an inhibition of angiogenesis seen in diabetes, cancer, and atherosclerosis [477]. Fang *et al.* further demonstrated that

miR-150-5p is significantly downregulated in plasma exosomes from patients with osteonecrosis of the femoral head and that delivery of miR-150-5p-modified MSCs exosomes promotes angiogenesis and may confer protective effects [478]. Notably, however, Wu *et al.* reported that exosomes derived from osteogenically differentiating bone marrow MSCs promote type H vessel formation through downregulation of miR-150-5p, highlighting that the role of miR-150-5p in angiogenesis may also be highly context specific and dependent on the cellular source and regenerative stage [459]. Finally, the anti-osteoclastogenic effects of miR-150-5p observed at higher doses are consistent with emerging evidence linking miR-150 to the regulation of bone remodelling. Genetic deletion of miR-150 in mice results in low bone mass accompanied by increased osteoclast numbers, suggesting that miR-150 normally contributes to restraining osteoclastogenesis *in vivo* [479]. Additional studies have shown that miR-150 can influence both osteoblast and osteoclast differentiation, supporting a broader role in coordinating formation-resorption coupling rather than acting exclusively on a single lineage [480]. Taken together, these findings indicate that miR-150-5p functions as a regulator of bone regeneration that integrates angiogenic promotion with modulation of remodelling balance. This multi-targeted activity provides a potential mechanistic explanation for how mechanically activated osteocyte-derived EVs can exert coordinated pro-regenerative effects across multiple cellular compartments during bone repair.

Scaffold-mediated delivery of miR-150-5p enhanced late-stage mineralisation, underscoring its translational potential for bone tissue engineering. At day 7, metabolic activity, DNA content, and the expression of key osteogenic and angiogenic markers, including *RUNX-2*, *BMP-2*, *ALP*, *OCN*, and *VEGF-A*, were comparable between miR-150-5p-functionalised and scrambled control scaffolds, indicating that scaffold mediated miRNA delivery supported cell viability and early osteoprogenitor commitment without significantly amplifying osteogenic transcriptional responses at this early stage. In contrast, miR-150-5p-functionalised scaffolds demonstrated significantly enhanced calcium deposition and increased Alizarin Red staining by day 21, indicating augmented matrix mineralisation at later stages of differentiation. This lack of direct correspondence between early osteogenic gene expression and later mineral deposition aligns with previous reports showing that scaffold-mediated miRNA delivery often produces delayed functional

outcomes. For example, scaffolds loaded with miR-26a have been shown to improve bone repair *in vivo* with superior mineralisation and vascularisation despite only modest early transcriptional activation, demonstrating the potential of miRNA-functionalised biomaterials in bone regeneration contexts [481]. The absence of a dedicated release kinetics study here reflects a broader challenge in RNA-based scaffold systems: achieving controlled, sustained release of miRNAs remains difficult due to rapid degradation, burst release, and the influence of scaffold porosity, crosslinking, and local enzymatic activity on cargo retention and diffusion. Reviews of RNA-based scaffolds for bone regeneration highlight these technical barriers and discuss how scaffold properties and vector design critically impact RNA delivery efficacy *in vivo* [482, 483]. Based on our results, the miR-150-5p dose within the Coll-nHA scaffold was sufficient to drive enhanced mineral deposition at later stages of osteogenesis but may not have maintained an intracellular concentration capable of amplifying early osteogenic gene programs compared to scrambled controls. This aligns with literature indicating that effective miRNA delivery from biomaterials often requires optimisation of dose, scaffold binding affinity, and release kinetics to synchronise RNA availability with key windows of osteoblast differentiation and matrix formation [484-486]. Taken together, these findings position miR-150-5p-activated scaffolds within the emerging class of nucleic acid-functionalised biomaterials capable of selectively enhancing functional bone matrix deposition while highlighting the need for future work focused on controlled release strategies and dose optimisation to fully harness scaffold-mediated miRNA therapeutic potential.

6.5 Conclusion

In summary, this chapter sought to identify and harness the specific EV-associated signalling components that mediate the pro-regenerative effects of mechanically activated osteocyte-derived EVs, with a particular focus on miRNA cargo. Using miRNA-sequencing, we demonstrate that osteocyte-derived EVs contain miRNAs enriched in biological processes central to bone regeneration and that mechanical stimulation selectively alters this cargo. Differential expression and functional enrichment analyses identified miR-150-5p as a mechanosensitive EV-associated miRNA whose predicted gene targets cluster within pathways linked to bone regeneration. Furthermore, we show that miR-150-5p exerts coordinated, multi-targeted effects that mirror the regenerative properties previously attributed to mechanically activated EVs. It has been demonstrated to enhance osteoblast mineral deposition, robustly promotes endothelial tube formation, and inhibits osteoclast differentiation. Finally, we demonstrate translational feasibility by incorporating miR-150-5p into a clinically relevant Coll-nHA scaffold, where scaffold-mediated delivery supports hMSCs viability and selectively enhances late-stage matrix mineralisation despite minimal changes in early osteogenic gene expression. Overall, this chapter advances our understanding of EV-mediated osteocyte mechanosignalling by identifying miR-150-5p as a mechanically regulated miRNA within osteocyte-derived EVs that exerts coordinated anabolic and anti-catabolic effects *in vitro*. In addition, it provides proof-of-concept that miR-150-5p can be delivered using a clinically relevant scaffold to enhance matrix mineralisation, supporting its potential as a cell-free therapeutic candidate for bone regeneration.

Chapter 7. Discussion

Bone regeneration and skeletal homeostasis require tightly regulated coordination of osteogenesis, angiogenesis, and bone resorption, processes that are strongly influenced by mechanical loading and are disrupted in conditions such as osteoporosis. This thesis explored bone-derived vesicles and their associated miRNAs as a novel multi-targeted approach for bone regeneration. In the first experimental chapter, we demonstrated that mesenchymal-lineage cells modulate osteoclast differentiation via paracrine signalling mechanisms that depend on both lineage commitment and mechanical environment, identifying EVs as central mediators of this anti-catabolic regulation and establishing osteocytes as the most effective parent cell source. In the second chapter, we examined the scalability of mechanically stimulated osteocyte EV production using nanovibration and showed that a 1 kHz, 30 nm vibration regimen was insufficient to activate osteocyte mechanotransduction or enhance EV regenerative potency. In the third chapter, we identified MVs isolated from mineralised bone as scalable, tissue-embedded vesicle populations with multi-targeted regenerative activity, capable of promoting osteogenesis and angiogenesis while inhibiting osteoclastogenesis, with bioactivity influenced by age, sex, and exercise. In the final chapter, we demonstrated that mechanical stimulation selectively alters the miRNA cargo of osteocyte-derived EVs and identified miR-150-5p as a mechanosensitive effector with coordinated anabolic, pro-angiogenic, and anti-catabolic activity that could be delivered using a clinically relevant scaffold to enhance late-stage mineralisation. Together, these findings establish a mechanosensitive vesicle-based signalling framework that integrates mechanical cues with multi-target regulation of bone regeneration and provides a foundation for the development of next-generation cell-free therapeutics.

7.1 Bone-derived vesicles and associated miRNAs as a therapeutic strategy for bone regeneration

The first study of this thesis demonstrates that bone cell regulation of osteoclastogenesis varies substantially along the mesenchymal lineage and is further shaped by mechanical cues. Rather than functioning as a single regulatory unit, MSCs, osteoblasts, and osteocytes exhibited distinct secretory programmes that translate into different anti-catabolic

properties, with osteocytes emerging as the most potent inhibitors of osteoclast differentiation. Mechanical cues further modulate these programmes in a lineage-specific manner, enhancing anti-osteoclastogenic signalling in osteoblasts and, most prominently, osteocytes, while not uniformly increasing inhibition in MSCs. These findings support a model in which mechanical loading reorganises paracrine output according to cell differentiation state and baseline secretory profile, aligning with the role of osteocytes as primary mechanosensors and orchestrators coordinating bone remodelling [287, 291, 487]. A further key advance is the identification of EVs as functional mediators of bone cell regulation of osteoclastogenesis. EVs from all mesenchymal cell types suppressed osteoclastogenesis, but their potency depended on parent cell identity and mechanical environment. Osteocyte-derived EVs exhibited the greatest inhibitory potency, particularly following mechanical stimulation, reinforcing the central role of osteocytes in regulating resorption during mechanoadaptation [488]. Importantly, EV activity was dose-dependent and, in some cases, biphasic: low doses inhibited osteoclast differentiation, whereas higher doses diminished this effect or promoted osteoclast formation. This observation supports the emerging view that EVs act as biologically active regulators with defined effective windows rather than inert supplements whose efficacy scales monotonically with dose [489, 490]. Moreover, the data might suggest that soluble factors and EVs act at distinct stages of osteoclast development, with soluble cues influencing early adhesion and EVs contributing more strongly to later maturation. Together, these findings define a hierarchical, context-dependent framework for vesicle-mediated regulation of osteoclastogenesis, governed by lineage stage and mechanical environment.

Building on our initial study which highlighted the mechanically activated osteocyte derived EVs as a potent inhibitor of osteoclastogenesis, the second study sought to overcome a practical barrier to clinical translation of EV therapy, that is low yield and limited standardisation of production. This thesis directly addressed this bottleneck by evaluating the Nanokick bioreactor as a scale-up platform for mechanically activated osteocyte-derived EVs production. Although the Nanokick bioreactor provides a time- and cost-efficient approach for generating large quantities of EVs, and previous work has demonstrated its capacity to enhance osteogenesis and suppress osteoclastogenesis [332, 342, 343], the specific nanovibration regimen tested (1 kHz, 30 nm displacement, 1 day)

was insufficient to trigger osteocyte mechanotransduction. Consequently, it didn't generate a pro-regenerative secretome or EVs with enhanced anti-catabolic activity. While negative, this finding is valuable because it demonstrates that not all mechanical regimens are interchangeable and mechanosensitive EVs optimisation requires stimulation parameters that fall within the cellular "responsive window" for the mechanosensory machinery engaged. Conceptually, these results reinforce two points. First, mechanical conditioning strategies must be defined with the same rigour as biochemical priming: frequency, amplitude, waveform, duration, and culture configuration can each determine whether a mechanotransduction programme is activated [325, 491]. Second, scale-up platforms cannot be judged solely on throughput, they must preserve or enhance functional potency [492]. Thus, while Nanokick may offer operational advantages, the regimen used here does not meet the mechanobiological requirements for generating enhanced osteocyte EV therapeutics, motivating future optimisation of vibration regimens or alternative scalable systems that better mimic physiologically relevant osteocyte stimuli.

To address scalability limitations of cell-derived EVs from a different angle, the third study of this thesis evaluated MVs isolated from bone tissue as an underexplored but highly translational vesicle population. MVs are naturally embedded within mineralised ECM, can persist within decellularised scaffolds, and are likely present in clinically used bone graft materials [203, 204, 366]. Here, we developed a robust MV isolation approach and demonstrated that bone-derived MVs possess a multi-targeted regenerative profile: they promoted mineralisation and angiogenesis while suppressing osteoclastogenesis, with functional outputs varying by tissue of origin. Molecular profiling further revealed distinct tissue-specific surface protein signatures and miRNA cargo profiles, providing a plausible molecular basis for functional differences and supporting the idea that MVs encode microenvironmental information [408]. Moreover, MVs can be delivered using a clinically relevant scaffold and enhance mineralisation. Another particularly interesting and potentially impactful finding is that MV potency is dynamically shaped by physiological context. Bone ageing is commonly associated with impaired mechanosensitivity and uncoupling of remodelling [430], yet bone-derived MVs from aged donors maintained anabolic and angiogenic properties and showed enhanced anti-osteoclastogenic activity. This observation raises the possibility that vesicles retained within aged bone matrix

accumulate or are selected to restrain resorption and preserve tissue integrity, and that such vesicles may contribute to the reported retained osteoinductive capacity of certain processed bone graft materials from older donors [432]. Exercise selectively enhanced anabolic outputs in a sex-dependent manner, consistent with known differences in skeletal mechanoadaptation [373]. Together, these findings position MVs as biologically responsive, tissue-informed vesicles that could complement or, in some contexts, substitute for cell-derived EVs in regenerative strategies.

This final study extends the vesicle-based framework by identifying miRNA cargo as a key mediator of the regenerative effects of mechanically conditioned osteocyte-derived EVs. The findings show that mechanical stimulation selectively alters EV miRNA composition, supporting active, mechanically regulated cargo loading rather than passive reflection of intracellular abundance [415, 472]. Within the mechanically regulated miRNAs, miR-150-5p emerged as a leading candidate linked to pathways central to bone regeneration, including angiogenesis, Wnt signalling, nitric oxide-related processes, and osteoclast differentiation. Functionally, miR-150-5p enhanced osteoblast mineralisation, promoted endothelial network formation, and inhibited osteoclast differentiation in a dose-dependent manner, indicating a role in fine-tuning remodelling balance rather than driving a single cellular response. This provides a conceptual bridge between whole-vesicle therapeutics and defined molecular effectors. Scaffold-mediated delivery further supported its translational relevance, as miR-150-5p incorporation enhanced late-stage mineralisation despite minimal early transcriptional changes, consistent with emerging RNA-based regenerative strategies and known delivery limitations [484]. Overall, these findings position EV-associated miRNAs, exemplified by miR-150-5p, as integral effectors of osteocyte mechanosignalling and promising components of future cell-free bone regeneration strategies.

Collectively, the findings of this thesis demonstrate that bone-derived vesicles and their associated microRNAs represent a mechanosensitive, multi-targeted regulatory system capable of coordinating osteogenesis, angiogenesis, and bone resorption in response to mechanical cues (**Figure 7.1**). By defining how vesicle bioactivity is shaped by parent cell origin, mechanical environment, and molecular cargo, this work establishes a coherent framework for exploiting vesicle-mediated paracrine signalling as a cell-free strategy for

bone regeneration. Importantly, the identification of both mechanically activated EVs and tissue-derived MVs, together with functionally relevant miRNA effectors, such as miR-150-5p, highlights a translational pathway through which vesicle-based therapies could be leveraged to restore remodelling balance and enhance bone repair in compromised skeletal environments, such as osteoporosis.

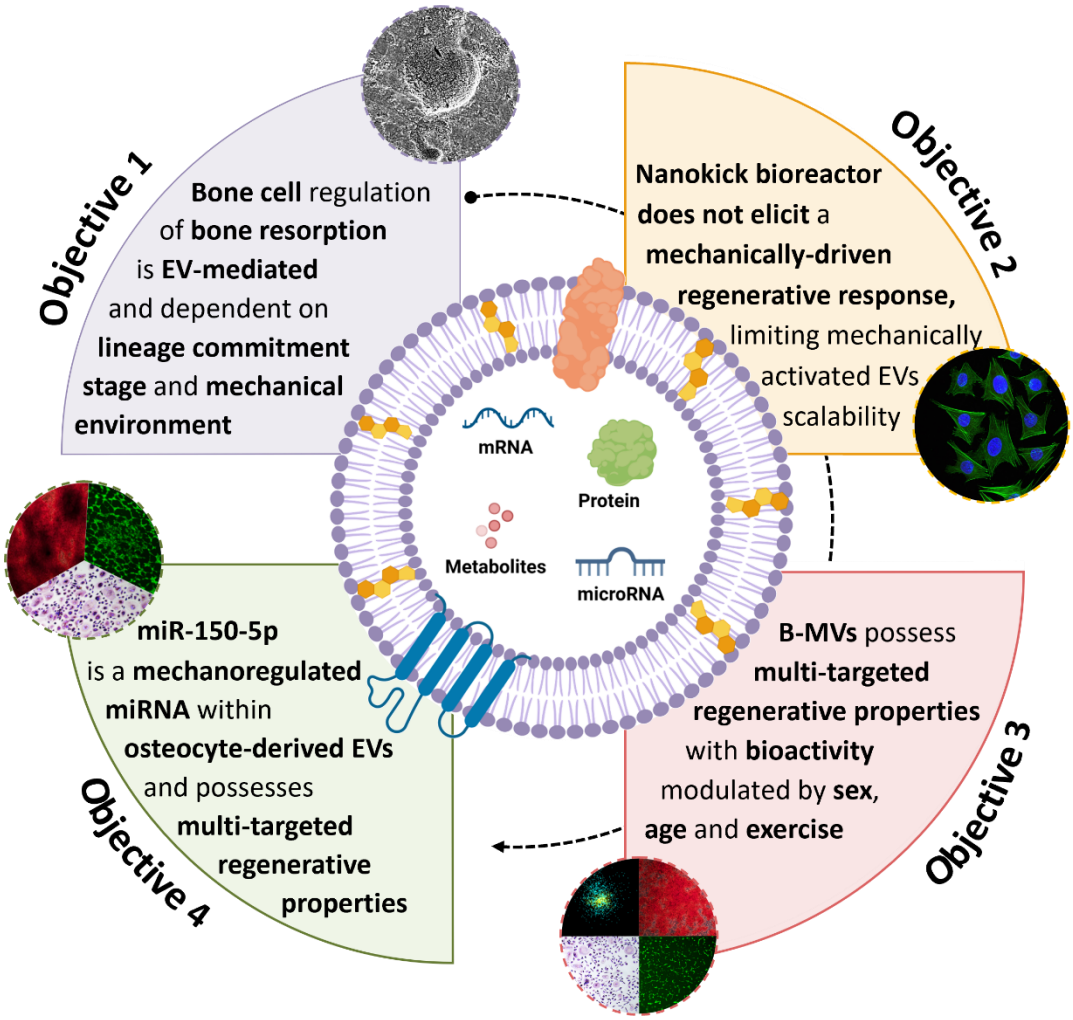

Figure 7.1. Summary of thesis achievements. This thesis demonstrates that bone cell regulation of osteoclastogenesis is mediated by EVs and is dependent on lineage commitment and the mechanical environment of the parent cell, identifying osteocyte-derived EVs as the population with greatest anti-catabolic potential. The Nanokick bioreactor was assessed as a scale-up platform for mechanically activated osteocyte-derived EVs, revealing that the tested nanovibration regimen was insufficient to induce a regenerative response. To overcome scalability limitations, bone tissue-derived MVs were isolated with high yield and shown to exhibit multi-target regenerative properties that are resilient to age yet modulated by sex and exercise. Finally, miR-150-5p was identified as a mechanoregulated miRNA within osteocyte-derived EVs and demonstrated it possesses multi-targeted regenerative effects by promoting osteogenesis and angiogenesis while inhibiting osteoclastogenesis.

7.2 Limitations and future work

While this thesis establishes a strong mechanistic and translational framework for mechanosensitive vesicle-mediated regulation of bone remodelling, several limitations should be acknowledged, as they shape interpretation of the findings and define clear priorities for future research.

A primary consideration relates to the cellular models used to generate osteocyte-derived EVs. Osteocyte-derived EVs were produced using the murine osteocyte-like cell line MLO-Y4 [296] and subsequently applied to human osteoclast precursors. Although the consistency of functional outcomes across species supports the conserved nature of vesicle-mediated signalling, species-specific differences in vesicle cargo composition may influence biological potency and limit direct extrapolation to human osteocyte biology. Moreover, while MLO-Y4 cells reproduce several hallmark osteocyte features, such as dendritic morphology and paracrine regulation of neighbouring bone cells, they do not fully recapitulate the mature osteocyte phenotype, including robust sclerostin expression and high DMP-1 levels [493]. As a result, the osteocyte secretome and vesicle cargo characterised here may not fully reflect that of mature osteocytes *in vivo*. Importantly, however, the strong anti-catabolic effects elicited by murine osteocyte-derived EVs on human cells indicate that osteocyte regulation of bone remodelling extends beyond sclerostin-dependent pathways and involves additional vesicle-associated signalling mechanisms, consistent with emerging views of osteocyte communication complexity [98]. Future studies employing more physiologically representative osteocyte models, despite their greater technical demands, will be essential to refine mechanistic insight and enhance translational relevance.

Methodological considerations related to mechanical conditioning further shape interpretation of the findings. Oscillatory fluid shear stress applied using parallel plate flow chambers enabled precise control over mechanical stimulation and provided a well-established proxy for osteocyte mechanotransduction within the lacunar-canalicular system [110]. However, the same shear profiles may not accurately reflect the dominant mechanical cues experienced by MSCs and osteoblasts *in vivo*, where matrix strain, compression, and substrate deformation are likely to play a more prominent role [494]. As

such, the mechanically induced responses observed in these cell populations may represent non-native or supra-physiological stimulation, potentially influencing their secretome composition and vesicle output.

In addition, the parallel plate system imposed practical constraints, including low conditioned medium yield, labour-intensive setup, and limited scalability, restricting the production of mechanically activated EVs for downstream characterisation and translational evaluation. In an effort to overcome these limitations, nanovibration-based stimulation was explored as a higher-throughput conditioning strategy. However, nanovibration at 1 kHz frequency and 30 nm displacement failed to elicit osteocyte mechanotransduction or enhance the regenerative potency of secreted EVs. Importantly, this outcome should be interpreted as regimen-specific rather than a definitive limitation of vibration-based approaches, as osteocyte responses to mechanical stimulation are highly sensitive to frequency, amplitude, duration, and loading context. Systematic exploration of alternative mechanical regimens, informed by osteocyte mechanobiology, will therefore be necessary to identify scalable conditioning strategies that preserve biological relevance.

A further limitation relates to donor variability and the number of biological replicates used in osteoclastogenesis assays. Some assays were conducted using cells from two independent donors, which may contribute to inter-donor variability, particularly in parameters influenced by osteoclast size or differentiation capacity. Although variation in absolute values was observed, consistent trends were maintained across donors. To optimise time and resources, experiments were prioritised based on their relevance to the central focus of the study. Notably, for the EV population identified as optimal (OCY-EVs), three independent donors were included to confirm the robustness and reproducibility of key findings. It should also be acknowledged that the collection of CM and mechanically activated EVs in sufficient quantities for functional characterisation is technically demanding and labour-intensive. Future studies incorporating a larger donor pool across all experimental stages would further strengthen the robustness and generalisability of these findings.

Additional limitations arise from the reductionist nature of the *in vitro* systems employed. While isolated 2D assays of osteoclastogenesis, osteogenesis, and angiogenesis enabled detailed mechanistic interrogation of vesicle-mediated effects, they do not capture the full

complexity of *in vivo* bone remodelling [495]. Key contributors such as immune cell populations, endocrine regulation, specialised vascular subtypes, and spatial gradients in oxygen tension and mechanical strain were not incorporated.

Vesicle characterisation further relied on targeted surface marker profiling and focused miRNA analysis. Although these approaches successfully identified distinct vesicle populations and highlighted miR-150-5p as a possible mechanosensitive effector, they do not provide comprehensive proteomic, lipidomic, or transcriptomic resolution. As a result, additional bioactive cargo components contributing to the observed multi-targeted effects may remain unidentified [412]. Moreover, EV collection was performed using differential ultracentrifugation, an approach that, while widely used, is increasingly recognised as insufficient for resolving discrete EV subpopulations and may result in co-isolation of heterogeneous vesicle sizes and non-vesicular contaminants. Emerging best-practice workflows frequently incorporate size-exclusion chromatography (SEC) following centrifugation to improve EV purity and enable more precise separation of small EV subsets [182, 496]. In addition, vesicle dosing was normalised primarily by mass concentration, which may not reflect particle number, or effective intracellular delivery, complicating cross-study comparison and therapeutic window definition, particularly in light of the dose-sensitive behaviour observed for osteocyte-derived EVs. Finally, although miR-150-5p was consistently enriched in mechanically activated EVs and correlated with downstream phenotypic responses, a direct causal role for this miRNA in mediating EV-driven effects was not formally demonstrated. Definitive mechanistic validation would require gain- and loss-of-function approaches, such as miR-150-5p knockdown or overexpression, or selective depletion of miR-150-5p from EV cargo prior to functional delivery, which remain important directions for future investigation.

With respect to MVs, several additional limitations warrant careful consideration. Although bone-derived MVs demonstrated robust multi-targeted regenerative activity and offer clear advantages in terms of scalability and physiological relevance, their precise definition and purity remain inherently challenging. Unlike cell-derived EVs, MVs are collected from mineralised tissues following enzymatic digestion, and the resulting vesicle preparations may represent a heterogeneous population. These isolates may contain a mixture of classical MVs, small EVs retained within the extracellular matrix, membrane

fragments, or vesicle-like mineral-complexes, making it difficult to definitively attribute observed biological effects to a single, well-defined vesicle subtype [497]. To address this heterogeneity, future work should implement orthogonal purification strategies, combining size- and density-based fractionation approaches, to better resolve distinct vesicle populations. In parallel, fraction-by-fraction functional assessment will be essential to map regenerative activity to specific purified fractions, thereby enabling more precise attribution of biological effects to defined MV subpopulations.

From a delivery perspective, scaffold-mediated incorporation of MVs and miRNAs demonstrated encouraging osteogenic outcomes, yet the absence of detailed vesicle and miRNA retention and release kinetics limited mechanistic interpretation of early versus late-stage effects. Rapid release or degradation of cargo may have constrained sustained bioactivity, highlighting the importance of future studies that integrate quantitative release profiling with functional outcomes. Optimisation of MVs and miRNAs dose, loading strategies, and release profiles will be critical to achieving controlled, sustained delivery aligned with key stages of osteogenic differentiation and matrix maturation.

Building on these findings, future work should prioritise validation of mechanically activated osteocyte EVs using human-relevant osteocyte models, alongside comprehensive multi-omic profiling to identify robust potency-associated cargo signatures. Establishing standardised, potency-linked dosing metrics will be essential to safely harness the dose-sensitive behaviour of osteocyte EVs and their miRNA cargo. Further optimisation of scalable mechanical conditioning platforms, informed by osteocyte mechanobiology, is required to reconcile yield with functional activation. In parallel, *in vivo* evaluation of both EV- and MV-based strategies in osteoporotic and critical-size defect models will be critical to confirm efficacy and safety in clinically relevant contexts. Finally, advances in biomaterial design that enable controlled, sustained delivery of vesicles or miRNAs will be key to translating these biologically sophisticated signalling systems into effective regenerative therapies.

7.3 Conclusion

In this thesis, we first established how cells across the mesenchymal lineage regulate bone resorption through paracrine signalling programmes that are shaped by both lineage commitment stage and mechanical environment. We then identified EVs as central mediators of this regulation and demonstrated that osteocyte-derived EVs exhibit the greatest anti-catabolic potency, particularly in response to mechanical stimulation. To address translational barriers related to EV yield, we next evaluated the Nanokick bioreactor as a scalable platform for producing mechanically activated osteocyte-derived EVs and showed that the nanovibration regimen tested was insufficient to activate osteocyte mechanotransduction or enhance EV regenerative properties. In parallel, and as an alternative scalability strategy, we investigated vesicles derived directly from bone tissue and demonstrated that bone-derived MVs possess distinct protein and miRNA signatures and multi-targeted regenerative activity. Importantly, their bioactivity was shown to be dynamically shaped by physiological factors, including age, sex, and exercise. Finally, we elucidated the molecular mechanism underlying the regenerative effects of mechanically activated osteocyte-derived EVs by identifying miR-150-5p as a mechanoregulated, EV-associated miRNA with coordinated anabolic, pro-angiogenic, and anti-catabolic activity. Together, these findings establish a mechanosensitive, vesicle-based framework that supports the development of scalable, multi-targeted, cell-free strategies for bone regeneration.

The key findings and achievements of this thesis are summarised below:

- Regulation of bone resorption by cells of the osteogenic lineage is mediated by EVs and depends on both lineage commitment stage and mechanical environment.
- Osteocyte-derived EVs exhibit maximal anti-catabolic potency, particularly following mechanical stimulation, identifying osteocytes as the optimal parent cell source for EV-based bone therapeutics.
- Nanovibration using the Nanokick bioreactor did not elicit osteocyte mechanotransduction or enhance EV regenerative activity under the conditions tested, demonstrating that scalable EV production requires biologically appropriate mechanical stimulation rather than throughput alone.

- Bone-derived MVs were collected in high yield and represent a scalable, physiologically relevant vesicle population with multi-targeted regenerative properties, capable of promoting osteogenesis and angiogenesis while suppressing osteoclastogenesis.
- Bone-derived MVs regenerative properties are dynamically shaped by physiological context, including donor age, sex, and long-term mechanical loading through exercise.
- Mechanical stimulation selectively alters the miRNA cargo of osteocyte-derived EVs, identifying miR-150-5p as a mechanoregulated effector with coordinated anabolic, pro-angiogenic, and anti-catabolic functions.
- miR-150-5p provides a mechanistic link between osteocyte mechanotransduction and vesicle-mediated bone regeneration, supporting its potential utility in future cell-free, miRNA-based regenerative therapies.

Supplementary figures

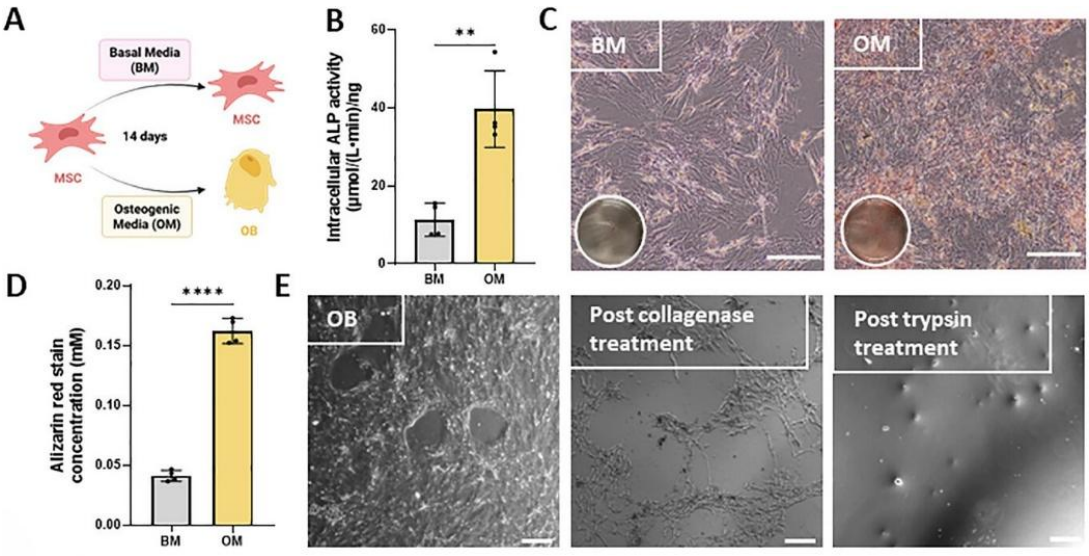

Figure S1. Evaluation of osteoblast differentiation. (A) Schematic representation of the experimental setup for osteoblast differentiation. **(B)** Intracellular ALP activity at day 14, normalised to DNA. **(C, D)** Alizarin red staining and quantification of cells cultured in either basal or osteogenic media at day 14. **(E)** Protocol for osteoblast detachment: differentiated OBs are first visualized on culture plastic (left), followed by enzymatic detachment using collagenase to release the cell layer (middle), and subsequent trypsin treatment to obtain a single-cell suspension suitable for reseeding (right). Scale bar = 200 µm. Data are presented as mean ± SD, n= 4. Adapted from [295].

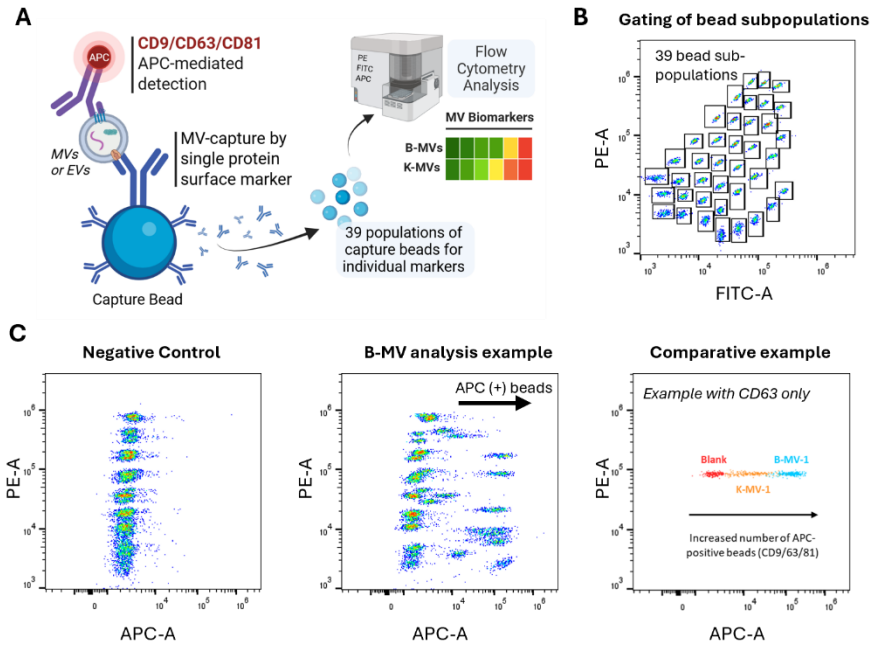

Figure S2. Multiplex bead-based flow cytometry (MACSPlex) analysis of vesicle surface protein markers. (A) Schematic Illustrating the workflow of the MACSPlex analysis. Created using Biorender.com **(B, C)** Example of microbead gating showcasing the presence of CD63 biomarker via APC detection.

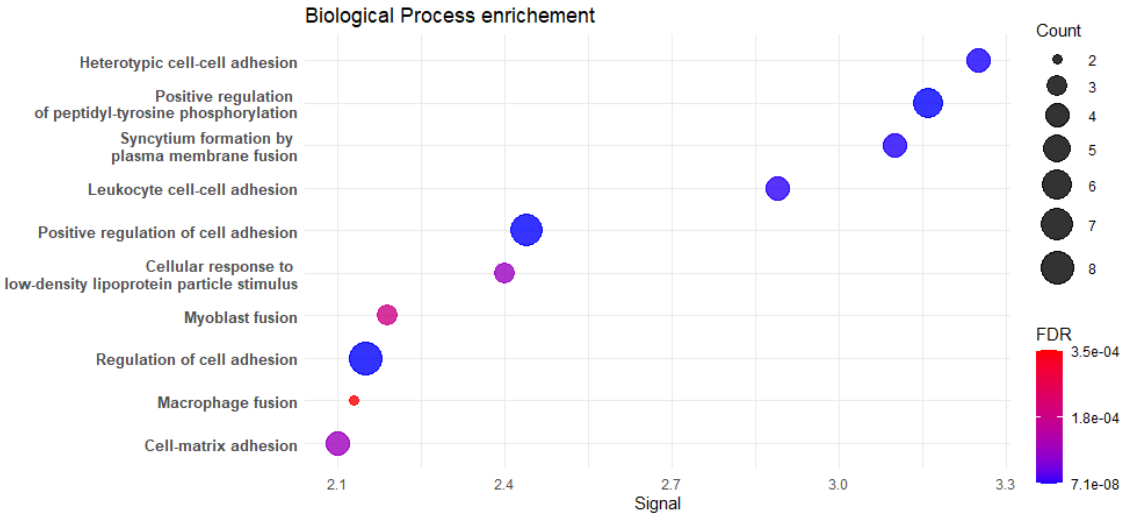

Figure S3. Shared markers between vesicle population are functionally associated with cell adhesion. Biological process enrichment of the 8 markers shared by B-MVs, K-MVs, OB-EVs and OCY-EVs.

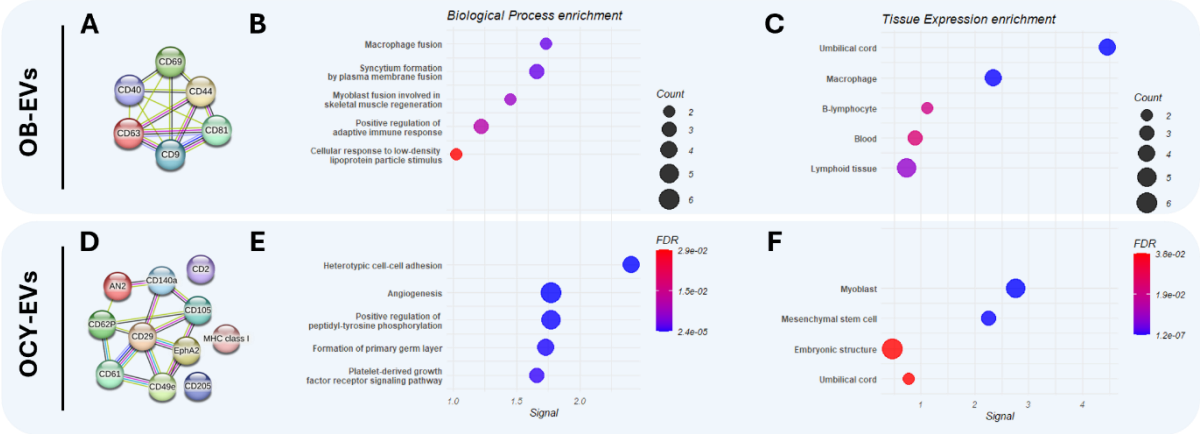

Figure S4. Surface marker clustering and biological process enrichment of cell-derived EVs. (A, D) PPI analysis displaying protein-protein interaction for OB-EVs and OCY-EVs respectively. **(E, H)** Biological process enrichment and **(F, I)** Tissue Expression enrichment of markers highly expressed in OB-EVs and OCY-EVs.

References

1. Clarke, B., *Normal bone anatomy and physiology.* Clin J Am Soc Nephrol, 2008. **3 Suppl 3**(Suppl 3): p. S131-9.
2. Seeman, E. and P.D. Delmas, *Bone quality--the material and structural basis of bone strength and fragility.* N Engl J Med, 2006. **354**(21): p. 2250-61.
3. FROST, H.M., *Dynamics of bone remodeling.* Bone biodynamics, 1964: p. 315-334.
4. Delgado-Calle, J. and T. Bellido, *The osteocyte as a signaling cell.* Physiol Rev, 2022. **102**(1): p. 379-410.
5. Salari, N., et al., *The global prevalence of osteoporosis in the world: a comprehensive systematic review and meta-analysis.* Journal of Orthopaedic Surgery and Research, 2021. **16**(1).
6. Kanis, J.A., et al., *SCOPE 2021: a new scorecard for osteoporosis in Europe.* Archives of osteoporosis, 2021. **16**(1): p. 82.
7. Fukumoto, S. and T. Matsumoto, *Recent advances in the management of osteoporosis.* F1000Research, 2017. **6**: p. 625.
8. Bandeira, L. and E.M. Lewiecki, *Anabolic therapy for osteoporosis: update on efficacy and safety.* Archives of endocrinology and metabolism, 2022. **66**(5): p. 707-716.
9. Bae, S., et al., *Position statement: exercise guidelines for osteoporosis management and fall prevention in osteoporosis patients.* Journal of bone metabolism, 2023. **30**(2): p. 149.
10. Wolff, J., *Das Gesetz der Transformation der Knochen.* DMW - Deutsche Medizinische Wochenschrift, 1893. **19**(47): p. 1222-1224.
11. Mellon, S.J. and K. Tanner, *Bone and its adaptation to mechanical loading: a review.* International Materials Reviews, 2012. **57**(5): p. 235-255.
12. Robling, A.G., A.B. Castillo, and C.H. Turner, *Biomechanical and molecular regulation of bone remodeling.* Annu. Rev. Biomed. Eng., 2006. **8**(1): p. 455-498.
13. Schaffler, M.B., et al., *Osteocytes: Master Orchestrators of Bone.* Calcified Tissue International, 2014. **94**(1): p. 5-24.
14. Papachroni, K.K., et al., *Mechanotransduction in osteoblast regulation and bone disease.* Trends in molecular medicine, 2009. **15**(5): p. 208-216.
15. Sun, Y., et al., *Mechanical Stimulation on Mesenchymal Stem Cells and Surrounding Microenvironments in Bone Regeneration: Regulations and Applications.* Front Cell Dev Biol, 2022. **10**: p. 808303.
16. Vig, S. and M.H. Fernandes, *Bone Cell Exosomes and Emerging Strategies in Bone Engineering.* Biomedicines, 2022. **10**(4).
17. Xiang, B., et al., *Microenvironmental Modulation for Therapeutic Efficacy of Extracellular Vesicles.* Adv Sci (Weinh), 2025. **12**(18): p. e2503027.
18. Eichholz, K.F., et al., *Human bone marrow stem/stromal cell osteogenesis is regulated via mechanically activated osteocyte-derived extracellular vesicles.* Stem Cells Translational Medicine, 2020. **9**(11): p. 1431-1447.
19. Shen, N., et al., *Mechanically activated mesenchymal-derived bone cells drive vessel formation via an extracellular vesicle mediated mechanism.* Journal of Tissue Engineering, 2023. **14**: p. 1-16.
20. Zhu, Y., et al., *Mechanically strained osteocyte-derived exosomes contained miR-3110-5p and miR-3058-3p and promoted osteoblastic differentiation.* Biomed Eng Online, 2024. **23**(1): p. 44.

21. Willis, G.R., S. Kourembanas, and S.A. Mitsialis, *Toward Exosome-Based Therapeutics: Isolation, Heterogeneity, and Fit-for-Purpose Potency.* Frontiers in Cardiovascular Medicine, 2017. **4**.
22. Jafari, D., et al., *Improvement, scaling-up, and downstream analysis of exosome production.* Critical Reviews in Biotechnology, 2020. **40**(8): p. 1098-1112.
23. Nordin, M. and V.H. Frankel, *Basic biomechanics of the musculoskeletal system*. 2001: Lippincott Williams & Wilkins.
24. Pravina, P., D. Sayaji, and M. Avinash, *Calcium and its role in human body.* International Journal of Research in Pharmaceutical and Biomedical Sciences, 2013. **4**(2): p. 659-668.
25. Bianco, P., *Bone and the hematopoietic niche: a tale of two stem cells.* Blood, 2011. **117**(20): p. 5281-5288.
26. Currey, J.D., *How Well Are Bones Designed to Resist Fracture?*.* Journal of Bone and Mineral Research, 2009. **18**(4): p. 591-598.
27. Rho, J.-Y., L. Kuhn-Spearing, and P. Zioupos, *Mechanical properties and the hierarchical structure of bone.* Medical Engineering & Physics, 1998. **20**(2): p. 92-102.
28. Ott, S.M., *Cortical or trabecular bone: what's the difference?* American journal of nephrology, 2018. **47**(6): p. 373-375.
29. Hart, N.H., et al., *Mechanical basis of bone strength: influence of bone material, bone structure and muscle action.* J Musculoskelet Neuronal Interact, 2017. **17**(3): p. 114-139.
30. Weiner, S. and W. Traub, *Bone structure: from ångstroms to microns.* The FASEB Journal, 1992. **6**(3): p. 879-885.
31. Dallas, S.L. and P.A. Veno, *Live Imaging of Bone Cell and Organ Cultures*, in *Bone Research Protocols*, M.H. Helfrich and S.H. Ralston, Editors. 2012, Humana Press: Totowa, NJ. p. 425-457.
32. Klein-Nulend, J., R. Bacabac, and A. Bakker, *Mechanical loading and how it affects bone cells: the role of the osteocyte cytoskeleton in maintaining our skeleton.* Eur Cell Mater, 2012. **24**(2): p. 279-291.
33. Li, C. and P. Fennessy, *The periosteum: a simple tissue with many faces, with special reference to the antler-lineage periostea.* Biol Direct, 2021. **16**(1): p. 17.
34. Fonseca, H., et al., *Bone Quality: The Determinants of Bone Strength and Fragility.* Sports Medicine, 2014. **44**(1): p. 37-53.
35. Burr, D.B., *The contribution of the organic matrix to bone's material properties.* Bone, 2002. **31**(1): p. 8-11.
36. Viguet-Carrin, S., P. Garnero, and P.D. Delmas, *The role of collagen in bone strength.* Osteoporosis International, 2006. **17**(3): p. 319-336.
37. Fratzl, P., et al., *Structure and mechanical quality of the collagen–mineral nano-composite in bone.* Journal of materials chemistry, 2004. **14**(14): p. 2115-2123.
38. Raggatt, L.J. and N.C. Partridge, *Cellular and Molecular Mechanisms of Bone Remodeling *.* Journal of Biological Chemistry, 2010. **285**(33): p. 25103-25108.
39. Eriksen, E.F., *Cellular mechanisms of bone remodeling.* Reviews in Endocrine and Metabolic Disorders, 2010. **11**(4): p. 219-227.
40. Fernández-Tresguerres-Hernández-Gil, I., et al., *Physiological bases of bone regeneration II. The remodeling process.* Med Oral Patol Oral Cir Bucal, 2006. **11**(2): p. E151-7.

41. Xiong, J. and C.A. O'Brien, *Osteocyte RANKL: new insights into the control of bone remodeling.* J Bone Miner Res, 2012. **27**(3): p. 499-505.
42. Blair, H.C., *How the osteoclast degrades bone.* Bioessays, 1998. **20**(10): p. 837-846.
43. Roodman, G.D., *Advances in Bone Biology: The Osteoclast*.* Endocrine Reviews, 1996. **17**(4): p. 308-332.
44. Delaisse, J.M., *The reversal phase of the bone-remodeling cycle: cellular prerequisites for coupling resorption and formation.* Bonekey Rep, 2014. **3**: p. 561.
45. Hadjidakis, D.J. and I.I. Androulakis, *Bone remodeling.* Annals of the New York academy of sciences, 2006. **1092**(1): p. 385-396.
46. Rowe, P., A. Koller, and S. Sharma, *Physiology, bone remodeling.* 2018.
47. Truesdell, S. and M. Saunders, *Bone remodeling platforms: Understanding the need for multicellular lab-on-a-chip systems and predictive agent-based models.* Mathematical Biosciences and Engineering, 2020. **17**: p. 1233-1252.
48. Friedenstein, A., R. Chailakhjan, and K. Lalykina, *The development of fibroblast colonies in monolayer cultures of guinea-pig bone marrow and spleen cells.* Cell Proliferation, 1970. **3**(4): p. 393-403.
49. Duchamp de Lageneste, O., et al., *Periosteum contains skeletal stem cells with high bone regenerative potential controlled by Periostin.* Nature Communications, 2018. **9**(1): p. 773.
50. Pittenger, M.F., et al., *Multilineage Potential of Adult Human Mesenchymal Stem Cells.* Science, 1999. **284**(5411): p. 143-147.
51. Kolf, C.M., E. Cho, and R.S. Tuan, *Mesenchymal stromal cells: Biology of adult mesenchymal stem cells: regulation of niche, self-renewal and differentiation.* Arthritis Research & Therapy, 2007. **9**(1): p. 204.
52. Chen, Q., et al., *Fate decision of mesenchymal stem cells: adipocytes or osteoblasts?* Cell Death & Differentiation, 2016. **23**(7): p. 1128-1139.
53. Jeon, E.-J., et al., *Bone morphogenetic protein-2 stimulates Runx2 acetylation.* Journal of Biological Chemistry, 2006. **281**(24): p. 16502-16511.
54. Yuan, Z., et al., *PPARγ and Wnt signaling in adipogenic and osteogenic differentiation of mesenchymal stem cells.* Current stem cell research & therapy, 2016. **11**(3): p. 216-225.
55. Mathieu, P.S. and E.G. Loboa, *Cytoskeletal and focal adhesion influences on mesenchymal stem cell shape, mechanical properties, and differentiation down osteogenic, adipogenic, and chondrogenic pathways.* Tissue Eng Part B Rev, 2012. **18**(6): p. 436-44.
56. Gao, F., et al., *Mesenchymal stem cells and immunomodulation: current status and future prospects.* Cell death & disease, 2016. **7**(1): p. e2062-e2062.
57. Tao, H., et al., *Proangiogenic Features of Mesenchymal Stem Cells and Their Therapeutic Applications.* Stem Cells International, 2016. **2016**(1): p. 1-11.
58. Osugi, M., et al., *Conditioned media from mesenchymal stem cells enhanced bone regeneration in rat calvarial bone defects.* Tissue engineering part A, 2012. **18**(13-14): p. 1479-1489.
59. Kim, M., et al., *Age-related alterations in mesenchymal stem cells related to shift in differentiation from osteogenic to adipogenic potential: Implication to age-associated bone diseases and defects.* Mechanisms of Ageing and Development, 2012. **133**(5): p. 215-225.

60. Mohamed, A.M., *An overview of bone cells and their regulating factors of differentiation.* Malays J Med Sci, 2008. **15**(1): p. 4-12.
61. Capulli, M., R. Paone, and N. Rucci, *Osteoblast and osteocyte: Games without frontiers.* Archives of Biochemistry and Biophysics, 2014. **561**: p. 3-12.
62. Nakashima, K., et al., *The novel zinc finger-containing transcription factor osterix is required for osteoblast differentiation and bone formation.* Cell, 2002. **108**(1): p. 17-29.
63. Zhao, Z., et al., *Gene Transfer of the Runx2 Transcription Factor Enhances Osteogenic Activity of Bone Marrow Stromal Cells in Vitro and in Vivo.* Molecular Therapy, 2005. **12**(2): p. 247-253.
64. Lian, J.B., et al., *Networks and hubs for the transcriptional control of osteoblastogenesis.* Reviews in Endocrine and Metabolic Disorders, 2006. **7**(1): p. 1-16.
65. Yellowley, C.E., et al., *Functional Gap Junctions Between Osteocytic and Osteoblastic Cells*.* Journal of Bone and Mineral Research, 2010. **15**(2): p. 209-217.
66. Florencio-Silva, R., et al., *Biology of Bone Tissue: Structure, Function, and Factors That Influence Bone Cells.* BioMed Research International, 2015. **2015**: p. 1-17.
67. Anderson, H.C., *Matrix vesicles and calcification.* Current rheumatology reports, 2003. **5**(3): p. 222-226.
68. Vimalraj, S., *Alkaline phosphatase: Structure, expression and its function in bone mineralization.* Gene, 2020. **754**: p. 144855.
69. Katsimbri, P., *The biology of normal bone remodelling.* Eur J Cancer Care (Engl), 2017. **26**(6).
70. Guo, J., et al., *Suppression of Wnt signaling by Dkk1 attenuates PTH-mediated stromal cell response and new bone formation.* Cell Metab, 2010. **11**(2): p. 161-71.
71. Marotti, G., et al., *Static and dynamic bone formation and the mechanism of collagen fiber orientation.* Bone, 1999. **25**: p. 156-156.
72. Atkins, G.J., et al., *RANKL expression is related to the differentiation state of human osteoblasts.* Journal of Bone and Mineral Research, 2003. **18**(6): p. 1088-1098.
73. Cawley, K.M., et al., *Local production of osteoprotegerin by osteoblasts suppresses bone resorption.* Cell reports, 2020. **32**(10).
74. Malone, J., et al., *Recruitment of osteoclast precursors by purified bone matrix constituents.* The Journal of cell biology, 1982. **92**(1): p. 227-230.
75. Li, X., et al., *Parathyroid hormone stimulates osteoblastic expression of MCP-1 to recruit and increase the fusion of pre/osteoclasts.* Journal of biological chemistry, 2007. **282**(45): p. 33098-33106.
76. Parfitt, A.M., *Osteonal and hemi-osteonal remodeling: The spatial and temporal framework for signal traffic in adult human bone.* Journal of cellular biochemistry, 1994. **55**(3): p. 273-286.
77. Manolagas, S.C. and A.M. Parfitt, *What old means to bone.* Trends in Endocrinology & Metabolism, 2010. **21**(6): p. 369-374.
78. Komori, T., *Cell death in chondrocytes, osteoblasts, and osteocytes.* International journal of molecular sciences, 2016. **17**(12): p. 2045.
79. Nagase, Y., et al., *Anti-apoptotic molecule Bcl-2 regulates the differentiation, activation, and survival of both osteoblasts and osteoclasts.* Journal of Biological Chemistry, 2009. **284**(52): p. 36659-36669.

80. Weinstein, R.S., et al., *Inhibition of osteoblastogenesis and promotion of apoptosis of osteoblasts and osteocytes by glucocorticoids. Potential mechanisms of their deleterious effects on bone.* The Journal of clinical investigation, 1998. **102**(2): p. 274-282.
81. Bonewald, L.F., *The amazing osteocyte.* Journal of Bone and Mineral Research, 2011. **26**(2): p. 229-238.
82. Teitelbaum, S.L. and F.P. Ross, *Genetic regulation of osteoclast development and function.* Nature Reviews Genetics, 2003. **4**(8): p. 638-649.
83. Collin-Osdoby, P., et al., *Receptor Activator of NF-κB and Osteoprotegerin Expression by Human Microvascular Endothelial Cells, Regulation by Inflammatory Cytokines, and Role in Human Osteoclastogenesis.* Journal of Biological Chemistry, 2001. **276**(23): p. 20659-20672.
84. Teitelbaum, S.L., *Bone Resorption by Osteoclasts.* Science, 2000. **289**(5484): p. 1504-1508.
85. Yoshida, H., et al., *The murine mutation osteopetrosis is in the coding region of the macrophage colony stimulating factor gene.* Nature, 1990. **345**(6274): p. 442-4.
86. Takayanagi, H., et al., *Induction and Activation of the Transcription Factor NFATc1 (NFAT2) Integrate RANKL Signaling in Terminal Differentiation of Osteoclasts.* Developmental Cell, 2002. **3**(6): p. 889-901.
87. Kim, J.H. and N. Kim, *Regulation of NFATc1 in Osteoclast Differentiation.* J Bone Metab, 2014. **21**(4): p. 233-41.
88. Kim, K., et al., *NFATc1 induces osteoclast fusion via up-regulation of Atp6v0d2 and the dendritic cell-specific transmembrane protein (DC-STAMP).* Molecular endocrinology, 2008. **22**(1): p. 176-185.
89. Hofbauer, L.C., et al., *The roles of osteoprotegerin and osteoprotegerin ligand in the paracrine regulation of bone resorption.* Journal of bone and mineral research, 2000. **15**(1): p. 2-12.
90. Zhu, L., et al., *Osteoclast-mediated bone resorption is controlled by a compensatory network of secreted and membrane-tethered metalloproteinases.* Sci Transl Med, 2020. **12**(529).
91. McHugh, K.P., et al., *Mice lacking β3 integrins are osteosclerotic because of dysfunctional osteoclasts.* The Journal of clinical investigation, 2000. **105**(4): p. 433-440.
92. Luxenburg, C., et al., *The Architecture of the Adhesive Apparatus of Cultured Osteoclasts: From Podosome Formation to Sealing Zone Assembly.* PLoS ONE, 2007. **2**(1): p. e179.
93. Rousselle, A.V. and D. Heymann, *Osteoclastic acidification pathways during bone resorption.* Bone, 2002. **30**(4): p. 533-40.
94. Yao, G., et al., *Characterization of vacuolar-ATPase and selective inhibition of vacuolar-H(+)-ATPase in osteoclasts.* Biochemical and Biophysical Research Communications, 2007. **357**(4): p. 821-827.
95. Nesbitt, S.A. and M.A. Horton, *Trafficking of Matrix Collagens Through Bone-Resorbing Osteoclasts.* Science, 1997. **276**(5310): p. 266-269.
96. Burr, D.B., T. Bellido, and K.E. White, *6 - Bone structure and function*, in *Rheumatology (Sixth Edition)*, M.C. Hochberg, et al., Editors. 2015, Mosby: Philadelphia. p. 42-55.
97. Frost, H. and C. Straatsma, *Bone remodelling dynamics*. 1964, LWW.

98. Dallas, S.L., M. Prideaux, and L.F. Bonewald, *The Osteocyte: An Endocrine Cell … and More.* Endocrine Reviews, 2013. **34**(5): p. 658-690.
99. Buenzli, P.R. and N.A. Sims, *Quantifying the osteocyte network in the human skeleton.* Bone, 2015. **75**: p. 144-50.
100. Kramer, I., et al., *Osteocyte Wnt/β-catenin signaling is required for normal bone homeostasis.* Molecular and cellular biology, 2010. **30**(12): p. 3071-3085.
101. Ivanova, M.M., et al., *Wnt signaling pathway inhibitors, sclerostin and DKK-1, correlate with pain and bone pathology in patients with Gaucher disease.* Front Endocrinol (Lausanne), 2022. **13**: p. 1029130.
102. Li, X., et al., *Targeted deletion of the sclerostin gene in mice results in increased bone formation and bone strength.* Journal of Bone and Mineral Research, 2008. **23**(6): p. 860-869.
103. Xiong, J., et al., *Osteocytes, not Osteoblasts or Lining Cells, are the Main Source of the RANKL Required for Osteoclast Formation in Remodeling Bone.* PLoS One, 2015. **10**(9): p. e0138189.
104. Wolff, J., *Das gestetz der transformation der knochem.* Verlag von August Hirschwald, 1892.
105. Fritton, S.P. and S. Weinbaum, *Fluid and Solute Transport in Bone: Flow-Induced Mechanotransduction.* Annu Rev Fluid Mech, 2009. **41**: p. 347-374.
106. LeBlanc, A., et al., *Bone mineral and lean tissue loss after long duration space flight.* J Musculoskelet Neuronal Interact, 2000. **1**(2): p. 157-60.
107. Modlesky, C.M., et al., *Trabecular bone microarchitecture is deteriorated in men with spinal cord injury.* Journal of Bone and Mineral Research, 2004. **19**(1): p. 48-55.
108. Huang, R.P., C.T. Rubin, and K.J. McLeod, *Changes in postural muscle dynamics as a function of age.* Journals of Gerontology Series A: Biomedical Sciences and Medical Sciences, 1999. **54**(8): p. B352-B357.
109. You, L., et al., *A model for strain amplification in the actin cytoskeleton of osteocytes due to fluid drag on pericellular matrix.* J Biomech, 2001. **34**(11): p. 1375-86.
110. Weinbaum, S., S.C. Cowin, and Y. Zeng, *A model for the excitation of osteocytes by mechanical loading-induced bone fluid shear stresses.* Journal of Biomechanics, 1994. **27**(3): p. 339-360.
111. van Tol, A.F., et al., *Network architecture strongly influences the fluid flow pattern through the lacunocanalicular network in human osteons.* Biomech Model Mechanobiol, 2020. **19**(3): p. 823-840.
112. Klein-Nulend, J., et al., *Sensitivity of osteocytes to biomechanical stress in vitro.* The FASEB Journal, 1995. **9**(5): p. 441-445.
113. Geoghegan, I.P., D.A. Hoey, and L.M. McNamara, *Integrins in Osteocyte Biology and Mechanotransduction.* Curr Osteoporos Rep, 2019. **17**(4): p. 195-206.
114. Cherian, P.P., et al., *Mechanical strain opens connexin 43 hemichannels in osteocytes: a novel mechanism for the release of prostaglandin.* Molecular biology of the cell, 2005. **16**(7): p. 3100-3106.
115. Malone, A.M., et al., *Primary cilia mediate mechanosensing in bone cells by a calcium-independent mechanism.* Proceedings of the National Academy of Sciences, 2007. **104**(33): p. 13325-13330.
116. Hoey, D.A., D.J. Kelly, and C.R. Jacobs, *A role for the primary cilium in paracrine signaling between mechanically stimulated osteocytes and mesenchymal stem cells.* Biochemical and Biophysical Research Communications, 2011. **412**(1): p. 182-187.

117. Sasaki, F., et al., *Mechanotransduction via the Piezo1-Akt pathway underlies Sost suppression in osteocytes.* Biochemical and biophysical research communications, 2020. **521**(3): p. 806-813.
118. Jing, D., et al., *In situ intracellular calcium oscillations in osteocytes in intact mouse long bones under dynamic mechanical loading.* The FASEB Journal, 2014. **28**(4): p. 1582.
119. Robinson, J.A., et al., *Wnt/β-catenin signaling is a normal physiological response to mechanical loading in bone.* Journal of Biological Chemistry, 2006. **281**(42): p. 31720-31728.
120. Plotkin, L.I., et al., *Mechanical stimulation prevents osteocyte apoptosis: requirement of integrins, Src kinases, and ERKs.* American Journal of Physiology-Cell Physiology, 2005. **289**(3): p. C633-C643.
121. Dupont, S., et al., *Role of YAP/TAZ in mechanotransduction.* Nature, 2011. **474**(7350): p. 179-183.
122. Panciera, T., et al., *Mechanobiology of YAP and TAZ in physiology and disease.* Nature Reviews Molecular Cell Biology, 2017. **18**(12): p. 758-770.
123. Piccolo, S., S. Dupont, and M. Cordenonsi, *The Biology of YAP/TAZ: Hippo Signaling and Beyond.* Physiological Reviews, 2014. **94**(4): p. 1287-1312.
124. Kim, K.M., et al., *Shear stress induced by an interstitial level of slow flow increases the osteogenic differentiation of mesenchymal stem cells through TAZ activation.* PLoS One, 2014. **9**(3): p. e92427.
125. Hong, J.-H., et al., *TAZ, a Transcriptional Modulator of Mesenchymal Stem Cell Differentiation.* Science, 2005. **309**(5737): p. 1074-1078.
126. Zarka, M., et al., *Mechanical loading activates the YAP/TAZ pathway and chemokine expression in the MLO-Y4 osteocyte-like cell line.* Laboratory Investigation, 2021. **101**: p. 1597-1604.
127. Nardone, G., et al., *YAP regulates cell mechanics by controlling focal adhesion assembly.* Nature Communications, 2017. **8**(1): p. 15321.
128. Pan, J.-X., et al., *YAP promotes osteogenesis and suppresses adipogenic differentiation by regulating β-catenin signaling.* Bone Research, 2018. **6**(1): p. 18.
129. Azzolin, L., et al., *YAP/TAZ Incorporation in the β-Catenin Destruction Complex Orchestrates the Wnt Response.* Cell, 2014. **158**(1): p. 157-170.
130. Zhao, X., et al., *Yap and Taz promote osteogenesis and prevent chondrogenesis in neural crest cells in vitro and in vivo.* Sci Signal, 2022. **15**(757): p. eabn9009.
131. Ajubi, N.E., et al., *Signal transduction pathways involved in fluid flow-induced PGE2 production by cultured osteocytes.* Am J Physiol, 1999. **276**(1): p. E171-8.
132. Klein-Nulend, J., et al., *Pulsating fluid flow increases nitric oxide (NO) synthesis by osteocytes but not periosteal fibroblasts--correlation with prostaglandin upregulation.* Biochem Biophys Res Commun, 1995. **217**(2): p. 640-8.
133. Sen, B., et al., *Mechanical strain inhibits adipogenesis in mesenchymal stem cells by stimulating a durable β-catenin signal.* Endocrinology, 2008. **149**(12): p. 6065-6075.
134. Yourek, G., et al., *Shear stress induces osteogenic differentiation of human mesenchymal stem cells.* Regenerative medicine, 2010. **5**(5): p. 713-724.
135. Rubin, J., et al., *Osteoclastogenesis is repressed by mechanical strain in an in vitro model.* Journal of orthopaedic research, 1999. **17**(5): p. 639-645.
136. Saunders, M.M., et al., *Mechanical stimulation effects on functional end effectors in osteoblastic MG-63 cells.* J Biomech, 2006. **39**(8): p. 1419-27.

137. Tang, L., Z. Lin, and Y.-m. Li, *Effects of different magnitudes of mechanical strain on Osteoblasts in vitro.* Biochemical and Biophysical Research Communications, 2006. **344**(1): p. 122-128.
138. Rubin, C.T. and L.E. Lanyon, *Regulation of bone formation by applied dynamic loads.* JBJS, 1984. **66**(3): p. 397-402.
139. Mosley, J., et al., *Strain magnitude related changes in whole bone architecture in growing rats.* Bone, 1997. **20**(3): p. 191-198.
140. Xie, L., et al., *Low-level mechanical vibrations can influence bone resorption and bone formation in the growing skeleton.* Bone, 2006. **39**(5): p. 1059-1066.
141. Globus, R.K., D.D. Bikle, and E. Morey-Holton, *The temporal response of bone to unloading.* Endocrinology, 1986. **118**(2): p. 733-742.
142. Stavenschi, E., M.-N. Labour, and D.A. Hoey, *Oscillatory fluid flow induces the osteogenic lineage commitment of mesenchymal stem cells: The effect of shear stress magnitude, frequency, and duration.* Journal of Biomechanics, 2017. **55**: p. 99-106.
143. Murray, D.W. and N. Rushton, *The effect of strain on bone cell prostaglandin E2 release: a new experimental method.* Calcif Tissue Int, 1990. **47**(1): p. 35-9.
144. McCoy, R.J. and F.J. O'Brien, *Influence of shear stress in perfusion bioreactor cultures for the development of three-dimensional bone tissue constructs: a review.* Tissue Engineering Part B: Reviews, 2010. **16**(6): p. 587-601.
145. Klibanski, A., et al., *Osteoporosis prevention, diagnosis, and therapy.* Journal of the American medical association, 2001. **285**(6): p. 785-795.
146. Cosman, F., et al., *Clinician's guide to prevention and treatment of osteoporosis.* Osteoporosis international, 2014. **25**(10): p. 2359-2381.
147. Watts, N., et al., *AACE Osteoporosis Task Force. American Association of Clinical Endocrinologists medical guidelines for clinical practice for the diagnosis and treatment of postmenopausal osteoporosis.* Endocr Pract, 2010. **16**(Suppl 3): p. 1-37.
148. Hannan, M.T., et al., *Risk factors for longitudinal bone loss in elderly men and women: the Framingham Osteoporosis Study.* Journal of Bone and Mineral Research, 2000. **15**(4): p. 710-720.
149. Ebeling, P.R., et al., *Secondary Osteoporosis.* Endocr Rev, 2022. **43**(2): p. 240-313.
150. Akbar, A., et al., *Evolving strategies for osteoporosis management in postmenopausal women: From tradition to innovation.* Medicine, 2025. **104**(7).
151. Hanley, D.A., et al., *Denosumab: mechanism of action and clinical outcomes.* International Journal of Clinical Practice, 2012. **66**(12): p. 1139-1146.
152. Anastasilakis, A.D., et al., *Long-term treatment of osteoporosis: safety and efficacy appraisal of denosumab.* Therapeutics and Clinical Risk Management, 2012: p. 295-306.
153. Estell, E.G. and C.J. Rosen, *Emerging insights into the comparative effectiveness of anabolic therapies for osteoporosis.* Nat Rev Endocrinol, 2021. **17**(1): p. 31-46.
154. TAM, C.S., et al., *Parathyroid hormone stimulates the bone apposition rate independently of its resorptive action: differential effects of intermittent and continuous administration.* Endocrinology, 1982. **110**(2): p. 506-512.
155. Saag, K.G., et al., *Romosozumab or alendronate for fracture prevention in women with osteoporosis.* New England Journal of Medicine, 2017. **377**(15): p. 1417-1427.

156. Thiruchelvam, N., et al., *Teriparatide induced delayed persistent hypercalcemia.* Case Rep Endocrinol, 2014. **2014**: p. 802473.
157. Chang, X., S. Xu, and H. Zhang, *Regulation of bone health through physical exercise: Mechanisms and types.* Frontiers in Endocrinology, 2022. **13**.
158. Khan, A.A., et al., *Osteoporotic Fractures: Diagnosis, Evaluation, and Significance From the International Working Group on DXA Best Practices.* Mayo Clinic Proceedings, 2024. **99**(7): p. 1127-1141.
159. Foundation, I.O. *A fracture every 3 seconds worldwide - That's osteoporosis!* 2019; Available from: https://www.osteoporosis.foundation/news/fracture-every-3-seconds-worldwidethats-osteoporosis-20191018-0900. .
160. Einhorn, T.A. and L.C. Gerstenfeld, *Fracture healing: mechanisms and interventions.* Nature Reviews Rheumatology, 2015. **11**(1): p. 45-54.
161. Claes, L., S. Recknagel, and A. Ignatius, *Fracture healing under healthy and inflammatory conditions.* Nature Reviews Rheumatology, 2012. **8**(3): p. 133-143.
162. Hak, D.J., *The biology of fracture healing in osteoporosis and in the presence of anti-osteoporotic drugs.* Injury, 2018. **49**(8): p. 1461-1465.
163. Orji, C., et al., *Fracture Non-Union in Osteoporotic Bones: Current Practice and Future Directions.* Cureus, 2024. **16**(9): p. e69778.
164. Prall, W.C., et al., *Mesenchymal stem cells from osteoporotic patients feature impaired signal transduction but sustained osteoinduction in response to BMP-2 stimulation.* Biochem Biophys Res Commun, 2013. **440**(4): p. 617-22.
165. Neidlinger-Wilke, C., et al., *Human osteoblasts from younger normal and osteoporotic donors show differences in proliferation and TGFβ-release in response to cyclic strain.* Journal of biomechanics, 1995. **28**(12): p. 1411-1418.
166. Cheung, W.H., et al., *Fracture healing in osteoporotic bone.* Injury, 2016. **47 Suppl 2**: p. S21-6.
167. Rolvien, T. and M. Amling, *Disuse Osteoporosis: Clinical and Mechanistic Insights.* Calcif Tissue Int, 2022. **110**(5): p. 592-604.
168. Von Rüden, C. and P. Augat, *Failure of fracture fixation in osteoporotic bone.* Injury, 2016. **47**: p. S3-S10.
169. Cornell, C.N., *Internal fracture fixation in patients with osteoporosis.* J Am Acad Orthop Surg, 2003. **11**(2): p. 109-19.
170. Baldwin, P., et al., *Autograft, Allograft, and Bone Graft Substitutes: Clinical Evidence and Indications for Use in the Setting of Orthopaedic Trauma Surgery.* J Orthop Trauma, 2019. **33**(4): p. 203-213.
171. Hegde, V., et al., *Effect of osteoporosis medications on fracture healing.* Osteoporos Int, 2016. **27**(3): p. 861-871.
172. Babu, S., N.A. Sandiford, and M. Vrahas, *Use of Teriparatide to improve fracture healing: What is the evidence?* World J Orthop, 2015. **6**(6): p. 457-61.
173. Busse, J.W., et al., *The effect of low-intensity pulsed ultrasound therapy on time to fracture healing: a meta-analysis.* Cmaj, 2002. **166**(4): p. 437-441.
174. Friedlaender, G.E., et al., *Osteogenic protein-1 (bone morphogenetic protein-7) in the treatment of tibial nonunions: a prospective, randomized clinical trial comparing rhOP-1 with fresh bone autograft.* JBJS, 2001. **83**(1): p. S151-S158.
175. Thurairajah, K., G.D. Briggs, and Z.J. Balogh, *Stem cell therapy for fracture non-union: the current evidence from human studies.* Journal of Orthopaedic Surgery, 2021. **29**(3): p. 23094990211036545.

176. Egermann, M., et al., *The potential of gene therapy for fracture healing in osteoporosis.* Osteoporosis International, 2005. **16**(2): p. S120-S128.
177. Koushik, T.M., C.M. Miller, and E. Antunes, *Bone Tissue Engineering Scaffolds: Function of Multi-Material Hierarchically Structured Scaffolds.* Advanced Healthcare Materials, 2023. **12**(9): p. 2202766.
178. Welsh, J.A., et al., *Minimal information for studies of extracellular vesicles (MISEV2023): From basic to advanced approaches.* Journal of Extracellular Vesicles, 2024. **13**(2).
179. D'Angelo, G., P.D. Stahl, and G. Raposo, *The cell biology of Extracellular Vesicles: A jigsaw puzzle with a myriad of pieces.* Current Opinion in Cell Biology, 2025. **94**: p. 102519.
180. Jiang, Y., et al., *Migrasomes, a new mode of intercellular communication.* Cell Communication and Signaling, 2023. **21**(1): p. 105.
181. Santavanond, J.P., et al., *Apoptotic bodies: mechanism of formation, isolation and functional relevance*, in *New Frontiers: extracellular vesicles*. 2021, Springer. p. 61-88.
182. Welsh, J.A., et al., *Minimal information for studies of extracellular vesicles (MISEV2023): From basic to advanced approaches.* Journal of extracellular vesicles, 2024. **13**(2): p. e12404.
183. Dixson, A.C., et al., *Context-specific regulation of extracellular vesicle biogenesis and cargo selection.* Nature Reviews Molecular Cell Biology, 2023. **24**(7): p. 454-476.
184. Hoshino, A., et al., *Tumour exosome integrins determine organotropic metastasis.* Nature, 2015. **527**(7578): p. 329-35.
185. Zhang, W., et al., *ICAM-1-mediated adhesion is a prerequisite for exosome-induced T cell suppression.* Dev Cell, 2022. **57**(3): p. 329-343.e7.
186. Kim, Y.K., et al., *Advantage of extracellular vesicles in hindering the CD47 signal for cancer immunotherapy.* Journal of Controlled Release, 2022. **351**: p. 727-738.
187. Lee, Y.J., K.J. Shin, and Y.C. Chae, *Regulation of cargo selection in exosome biogenesis and its biomedical applications in cancer.* Experimental & Molecular Medicine, 2024. **56**(4): p. 877-889.
188. Qin, Y., et al., *Bone marrow stromal/stem cell-derived extracellular vesicles regulate osteoblast activity and differentiation in vitro and promote bone regeneration in vivo.* Sci Rep, 2016. **6**: p. 21961.
189. Nakamura, Y., et al., *Mesenchymal-stem-cell-derived exosomes accelerate skeletal muscle regeneration.* FEBS letters, 2015. **589**(11): p. 1257-1265.
190. Pol, F., et al., *Extracellular vesicles in osteoimmunomodulation: Orchestrating immune-driven bone regeneration.* International Journal of Biological Macromolecules, 2026. **338**: p. 149614.
191. Furuta, T., et al., *Mesenchymal Stem Cell-Derived Exosomes Promote Fracture Healing in a Mouse Model.* Stem Cells Transl Med, 2016. **5**(12): p. 1620-1630.
192. Takeuchi, R., et al., *Exosomes from conditioned media of bone marrow-derived mesenchymal stem cells promote bone regeneration by enhancing angiogenesis.* PLoS One, 2019. **14**(11): p. e0225472.
193. Cui, Y., et al., *Exosomes derived from mineralizing osteoblasts promote ST2 cell osteogenic differentiation by alteration of microRNA expression.* FEBS letters, 2016. **590**(1): p. 185-192.

194. Davies, O.G., et al., *Osteoblast-Derived Vesicle Protein Content Is Temporally Regulated During Osteogenesis: Implications for Regenerative Therapies.* Front Bioeng Biotechnol, 2019. **7**: p. 92.
195. Uenaka, M., et al., *Osteoblast-derived vesicles induce a switch from bone-formation to bone-resorption in vivo.* Nature Communications, 2022. **13**(1): p. 1066.
196. Deng, L., et al., *Osteoblast-derived microvesicles: A novel mechanism for communication between osteoblasts and osteoclasts.* Bone, 2015. **79**: p. 37-42.
197. Wang, Q., et al., *Osteoblasts-derived exosomes regulate osteoclast differentiation through miR-503-3p/Hpse axis.* Acta Histochem, 2021. **123**(7): p. 151790.
198. Morrell, A.E., et al., *Mechanically induced Ca(2+) oscillations in osteocytes release extracellular vesicles and enhance bone formation.* Bone Res, 2018. **6**: p. 6.
199. Chen, Y., et al., *The roles of extracellular vesicles released by mechanically stimulated osteocytes in regulating osteoblast and osteoclast functions.* Mechanobiology in medicine, 2024. **2**(2): p. 100065.
200. Li, D., et al., *Osteoclast-derived exosomal miR-214-3p inhibits osteoblastic bone formation.* Nat Commun, 2016. **7**: p. 10872.
201. Chen, C., et al., *Biological characteristics of osteoclast exosomes and their role in the osteogenic differentiation of somatic cells prior to osteogenesis.* Journal of Biological Regulators and Homeostatic Agents, 2018. **32**(4): p. 815-823.
202. Anderson, H.C., *Molecular Biology of Matrix Vesicles.* Clinical Orthopaedics and Related Research®, 1995. **314**.
203. Anderson, H.C., *Vesicles associated with calcification in the matrix of epiphyseal cartilage.* J Cell Biol, 1969. **41**(1): p. 59-72.
204. Bonucci, E., *Fine structure and histochemistry of "calcifying globules" in epiphyseal cartilage.* Zeitschrift für Zellforschung und Mikroskopische Anatomie, 1970. **103**(2): p. 192-217.
205. Wu, L., et al., *Collagen-binding proteins in collagenase-released matrix vesicles from cartilage. Interaction between matrix vesicle proteins and different types of collagen.* Journal of Biological Chemistry, 1991. **266**(2): p. 1195-1203.
206. Kirsch, T. and M. Pfäffle, *Selective binding of anchorin CII (annexin V) to type II and X collagen and to chondrocalcin (C-propeptide of type II collagen) Implications for anchoring function between matrix vesicles and matrix proteins.* FEBS letters, 1992. **310**(2): p. 143-147.
207. Balcerzak, M., et al., *A comparative analysis of strategies for isolation of matrix vesicles.* Analytical biochemistry, 2007. **361**(2): p. 176-182.
208. Roberts, S., et al., *Functional Involvement of PHOSPHO1 in Matrix Vesicle–Mediated Skeletal Mineralization*.* Journal of Bone and Mineral Research, 2009. **22**(4): p. 617-627.
209. Bottini, M. and A.P. Ramos, *Mineralizing Vesicles : From Biochemical and Biophysical Properties to Their Roles in Physiology and Disease*. 2023, Chantilly, UNITED STATES: Elsevier Science & Technology.
210. Skelton, A.M., et al., *Osteoblast-Derived Matrix Vesicles Exhibit Exosomal Traits and a Unique Subset of microRNA: Their Caveolae-Dependent Endocytosis Results in Reduced Osteogenic Differentiation.* Int J Mol Sci, 2023. **24**(16).
211. Nahar, N.N., et al., *Matrix vesicles are carriers of bone morphogenetic proteins (BMPs), vascular endothelial growth factor (VEGF), and noncollagenous matrix proteins.* Journal of Bone and Mineral Metabolism, 2008. **26**(5): p. 514-519.

212. Xiao, Z., et al., *Analysis of the extracellular matrix vesicle proteome in mineralizing osteoblasts.* Journal of cellular physiology, 2007. **210**(2): p. 325-335.
213. Minamizaki, T., et al., *The matrix vesicle cargo miR-125b accumulates in the bone matrix, inhibiting bone resorption in mice.* Communications Biology, 2020. **3**(1).
214. Mizukami, Y., et al., *Matrix vesicles promote bone repair after a femoral bone defect in mice.* PLOS ONE, 2023. **18**(4): p. e0284258.
215. Su, G., et al., *Annexin A5 derived from matrix vesicles protects against osteoporotic bone loss via mineralization.* Bone Res, 2023. **11**(1): p. 60.
216. Chen, N.X., K.D. O'Neill, and S.M. Moe, *Matrix vesicles induce calcification of recipient vascular smooth muscle cells through multiple signaling pathways.* Kidney Int, 2018. **93**(2): p. 343-354.
217. Lee, C., et al., *Exosomes Mediate the Cytoprotective Action of Mesenchymal Stromal Cells on Hypoxia-Induced Pulmonary Hypertension.* Circulation, 2012. **126**(22): p. 2601-2611.
218. Haga, H., et al., *Extracellular vesicles from bone marrow-derived mesenchymal stem cells improve survival from lethal hepatic failure in mice.* Stem cells translational medicine, 2017. **6**(4): p. 1262-1272.
219. Eirin, A., et al., *Mesenchymal stem cell–derived extracellular vesicles attenuate kidney inflammation.* Kidney international, 2017. **92**(1): p. 114-124.
220. Kim, D.-k., et al., *Chromatographically isolated CD63+ CD81+ extracellular vesicles from mesenchymal stromal cells rescue cognitive impairments after TBI.* Proceedings of the National Academy of Sciences, 2016. **113**(1): p. 170-175.
221. Lai, R.C., et al., *Exosome secreted by MSC reduces myocardial ischemia/reperfusion injury.* Stem cell research, 2010. **4**(3): p. 214-222.
222. Cosenza, S., et al., *Mesenchymal stem cells derived exosomes and microparticles protect cartilage and bone from degradation in osteoarthritis.* Scientific reports, 2017. **7**(1): p. 16214.
223. Davies, O.G., *Extracellular vesicles: From bone development to regenerative orthopedics.* Molecular Therapy, 2023. **31**(5): p. 1251-1274.
224. Gimona, M., et al., *Manufacturing of human extracellular vesicle-based therapeutics for clinical use.* International journal of molecular sciences, 2017. **18**(6): p. 1190.
225. Liu, W., et al., *Hypoxic mesenchymal stem cell-derived exosomes promote bone fracture healing by the transfer of miR-126.* Acta biomaterialia, 2020. **103**: p. 196-212.
226. Zhang, Y., et al., *Exosomes from human umbilical cord mesenchymal stem cells enhance fracture healing through HIF-1α-mediated promotion of angiogenesis in a rat model of stabilized fracture.* Cell proliferation, 2019. **52**(2): p. e12570.
227. Lu, Z., et al., *Priming adipose stem cells with tumor necrosis factor-alpha preconditioning potentiates their exosome efficacy for bone regeneration.* Tissue Engineering Part A, 2017. **23**(21-22): p. 1212-1220.
228. Kang, M., et al., *Extracellular Vesicles From TNFα Preconditioned MSCs: Effects on Immunomodulation and Bone Regeneration.* Front Immunol, 2022. **13**: p. 878194.
229. Guo, S., et al., *Stimulating Extracellular Vesicles Production from Engineered Tissues by Mechanical Forces.* Nano Letters, 2021. **21**(6): p. 2497-2504.
230. Wu, D., et al., *Bone mesenchymal stem cells stimulation by magnetic nanoparticles and a static magnetic field: release of exosomal miR-1260a improves osteogenesis and angiogenesis.* Journal of nanobiotechnology, 2021. **19**(1): p. 209.

231. Huang, H., et al., *Static Topographical Cue Combined with Dynamic Fluid Stimulation Enhances the Macrophage Extracellular Vesicle Yield and Therapeutic Potential for Bone Defects.* ACS Nano, 2025. **19**(9): p. 8667-8691.
232. Zuo, R., et al., *BM-MSC-derived exosomes alleviate radiation-induced bone loss by restoring the function of recipient BM-MSCs and activating Wnt/β-catenin signaling.* Stem Cell Res Ther, 2019. **10**(1): p. 30.
233. Jin, Q., et al., *Extracellular vesicles derived from human dental pulp stem cells promote osteogenesis of adipose-derived stem cells via the MAPK pathway.* Journal of Tissue Engineering, 2020. **11**: p. 2041731420975569.
234. Faqeer, A., et al., *Cleaved SPP1-rich extracellular vesicles from osteoclasts promote bone regeneration via TGFβ1/SMAD3 signaling.* Biomaterials, 2023. **303**: p. 122367.
235. Ma, Y., et al., *Exosomal mRNAs for Angiogenic-Osteogenic Coupled Bone Repair.* Adv Sci (Weinh), 2023. **10**(33): p. e2302622.
236. Sagini, K., et al., *Extracellular Vesicles as Conveyors of Membrane-Derived Bioactive Lipids in Immune System.* Int J Mol Sci, 2018. **19**(4).
237. Qi, T., L. Li, and T. Weidong, *The Role of Sphingolipid Metabolism in Bone Remodeling.* Front Cell Dev Biol, 2021. **9**: p. 752540.
238. Fyfe, J., et al., *Role of lipid signalling in extracellular vesicles-mediated cell-to-cell communication.* Cytokine & Growth Factor Reviews, 2023. **73**: p. 20-26.
239. Xu, J., et al., *Human perivascular stem cell-derived extracellular vesicles mediate bone repair.* Elife, 2019. **8**: p. e48191.
240. Hoshino, A., et al., *Tumour exosome integrins determine organotropic metastasis.* Nature, 2015. **527**(7578): p. 329-335.
241. Kim, V.N., *MicroRNA biogenesis: coordinated cropping and dicing.* Nature Reviews Molecular Cell Biology, 2005. **6**(5): p. 376-385.
242. Binet, F., et al., *Exploring the molecular cargos associated with extracellular vesicles extracted from bone tissue to identify novel players in osteoblast function.* American Journal of Physiology-Cell Physiology, 2025. **329**(5): p. C1521-C1538.
243. Davis, C., et al., *MicroRNA-183-5p Increases with Age in Bone-Derived Extracellular Vesicles, Suppresses Bone Marrow Stromal (Stem) Cell Proliferation, and Induces Stem Cell Senescence.* Tissue Eng Part A, 2017. **23**(21-22): p. 1231-1240.
244. Kim, D.K., et al., *Mastocytosis-derived extracellular vesicles deliver miR-23a and miR-30a into pre-osteoblasts and prevent osteoblastogenesis and bone formation.* Nat Commun, 2021. **12**(1): p. 2527.
245. Chen, C., et al., *Mesenchymal stem cell transplantation in tight-skin mice identifies miR-151-5p as a therapeutic target for systemic sclerosis.* Cell Res, 2017. **27**(4): p. 559-577.
246. Goto, K., et al., *Harnessing miRNA-Containing Extracellular Vesicles from Mesenchymal Stromal Cell-Derived Extracellular Vesicles for Regeneration of Bone Defects: A Narrative Review of Mechanisms, Biomaterials, and Clinical Translation.* Cancers (Basel), 2025. **17**(15).
247. Lee, K.S., et al., *Extracellular vesicles from adipose tissue-derived stem cells alleviate osteoporosis through osteoprotegerin and miR-21-5p.* J Extracell Vesicles, 2021. **10**(12): p. e12152.
248. Kang, M., et al., *Bone regeneration is mediated by macrophage extracellular vesicles.* Bone, 2020. **141**: p. 115627.

249. Wang, Y., et al., *Extracellular vesicles: From large-scale production and engineering to clinical applications.* Journal of Tissue Engineering, 2025. **16**: p. 20417314251319474.
250. Strecanska, M., et al., *Automated Manufacturing Processes and Platforms for Large-scale Production of Clinical-grade Mesenchymal Stem/ Stromal Cells.* Stem Cell Rev Rep, 2025. **21**(2): p. 372-389.
251. Andriolo, G., et al., *Exosomes From Human Cardiac Progenitor Cells for Therapeutic Applications: Development of a GMP-Grade Manufacturing Method.* Frontiers in Physiology, 2018. **9**.
252. Paganini, C., et al., *Scalable Production and Isolation of Extracellular Vesicles: Available Sources and Lessons from Current Industrial Bioprocesses.* Biotechnology Journal, 2019. **14**(10): p. 1800528.
253. Haraszti, R.A., et al., *Exosomes produced from 3D cultures of MSCs by tangential flow filtration show higher yield and improved activity.* Molecular Therapy, 2018. **26**(12): p. 2838-2847.
254. Watson, D.C., et al., *Efficient production and enhanced tumor delivery of engineered extracellular vesicles.* Biomaterials, 2016. **105**: p. 195-205.
255. Gobin, J., et al., *Hollow-fiber bioreactor production of extracellular vesicles from human bone marrow mesenchymal stromal cells yields nanovesicles that mirrors the immuno-modulatory antigenic signature of the producer cell.* Stem Cell Res Ther, 2021. **12**(1): p. 127.
256. Artuyants, A., et al., *Production of Extracellular Vesicles Using a CELLine Adherent Bioreactor Flask.* Methods Mol Biol, 2022. **2436**: p. 183-192.
257. Fernandes-Platzgummer, A., et al., *Optimized operation of a controlled stirred tank reactor system for the production of mesenchymal stromal cells and their extracellular vesicles.* Biotechnology and Bioengineering, 2023. **120**(9): p. 2742-2755.
258. Hessvik, N.P., et al., *PIKfyve inhibition increases exosome release and induces secretory autophagy.* Cellular and Molecular Life Sciences, 2016. **73**(24): p. 4717-4737.
259. Wang, X., et al., *Hsp20-mediated activation of exosome biogenesis in cardiomyocytes improves cardiac function and angiogenesis in diabetic mice.* Diabetes, 2016. **65**(10): p. 3111-3128.
260. Schiller, L.T., et al., *Enhanced production of exosome-associated AAV by overexpression of the tetraspanin CD9.* Molecular therapy Methods & clinical development, 2018. **9**: p. 278-287.
261. Parolini, I., et al., *Microenvironmental pH is a key factor for exosome traffic in tumor cells.* Journal of Biological Chemistry, 2009. **284**(49): p. 34211-34222.
262. Garcia, N.A., et al., *Glucose starvation in cardiomyocytes enhances exosome secretion and promotes angiogenesis in endothelial cells.* PloS one, 2015. **10**(9): p. e0138849.
263. Hedlund, M., et al., *Thermal-and oxidative stress causes enhanced release of NKG2D ligand-bearing immunosuppressive exosomes in leukemia/lymphoma T and B cells.* PloS one, 2011. **6**(2): p. e16899.
264. Viola, M., et al., *Hypoxia and TNF-alpha modulate extracellular vesicle release from human induced pluripotent stem cell-derived cardiomyocytes.* J Extracell Vesicles, 2024. **13**(11): p. e70000.

265. Syromiatnikova, V., A. Prokopeva, and M. Gomzikova, *Methods of the Large-Scale Production of Extracellular Vesicles.* International Journal of Molecular Sciences, 2022. **23**(18): p. 10522.
266. Sil, S., et al., *Strategies for the use of Extracellular Vesicles for the Delivery of Therapeutics.* J Neuroimmune Pharmacol, 2020. **15**(3): p. 422-442.
267. Feng, X. and J.M. McDonald, *Disorders of bone remodeling.* Annu Rev Pathol, 2011. **6**: p. 121-45.
268. Zaidi, M., *Skeletal remodeling in health and disease.* Nat Med, 2007. **13**(7): p. 791-801.
269. Sobacchi, C., et al., *Osteopetrosis: genetics, treatment and new insights into osteoclast function.* Nat Rev Endocrinol, 2013. **9**(9): p. 522-36.
270. Patel, D. and S. Wairkar, *Bone regeneration in osteoporosis: opportunities and challenges.* Drug Deliv Transl Res, 2023. **13**(2): p. 419-432.
271. Boyle, W.J., W.S. Simonet, and D.L. Lacey, *Osteoclast differentiation and activation.* Nature, 2003. **423**(6937): p. 337-342.
272. Russell, G., et al., *Clinical disorders of bone resorption.* Novartis Found Symp, 2001. **232**: p. 251-67; discussion 267-71.
273. Chen, Y.-J., et al., *Osteoporosis treatment: current drugs and future developments.* Frontiers in Pharmacology, 2024. **15**.
274. Mbalaviele, G., et al., *Human Mesenchymal Stem Cells Promote Human Osteoclast Differentiation from CD34+ Bone Marrow Hematopoietic Progenitors*.* Endocrinology, 1999. **140**(8): p. 3736-3743.
275. Zhu, H., et al., *Tumor necrosis factor-alpha alters the modulatory effects of mesenchymal stem cells on osteoclast formation and function.* Stem Cells Dev, 2009. **18**(10): p. 1473-84.
276. Oshita, K., et al., *Human mesenchymal stem cells inhibit osteoclastogenesis through osteoprotegerin production.* Arthritis Rheum, 2011. **63**(6): p. 1658-67.
277. Abe, T., et al., *The effect of mesenchymal stem cells on osteoclast precursor cell differentiation.* J Oral Sci, 2019. **61**(1): p. 30-35.
278. Boyce, B.F. and L. Xing, *The RANKL/RANK/OPG pathway.* Current Osteoporosis Reports, 2007. **5**(3): p. 98-104.
279. Suda, T., et al., *Modulation of osteoclast differentiation and function by the new members of the tumor necrosis factor receptor and ligand families.* Endocr Rev, 1999. **20**(3): p. 345-57.
280. Marotti, G., *The structure of bone tissues and the cellular control of their deposition.* Ital J Anat Embryol, 1996. **101**(4): p. 25-79.
281. Riffault, M., et al., *Loss of Adenylyl Cyclase 6 in Leptin Receptor-Expressing Stromal Cells Attenuates Loading-Induced Endosteal Bone Formation.* JBMR Plus, 2020. **4**(11): p. e10408.
282. Wang, L., et al., *Mechanical sensing protein PIEZO1 regulates bone homeostasis via osteoblast-osteoclast crosstalk.* Nat Commun, 2020. **11**(1): p. 282.
283. Tatsumi, S., et al., *Targeted ablation of osteocytes induces osteoporosis with defective mechanotransduction.* Cell Metab, 2007. **5**(6): p. 464-75.
284. Wang, W., et al., *Mechanical Unloading Promotes Osteoclastic Differentiation and Bone Resorption by Modulating the MSC Secretome to Favor Inflammation.* Cell Transplantation, 2024. **33**.

285. You, L., et al., *Osteocytes as mechanosensors in the inhibition of bone resorption due to mechanical loading.* Bone, 2008. **42**(1): p. 172-179.
286. Hao, Z., et al., *Osteocytes regulate osteoblast differentiation and osteoclast activity through Interleukin-6 under mechanical loading.* RSC Adv., 2017. **7**(79): p. 50200-50209.
287. Klein-Nulend, J., et al., *Sensitivity of osteocytes to biomechanical stress in vitro.* The FASEB Journal, 1995. **9**(5): p. 441-445.
288. Allison, H. and L.M. McNamara, *Inhibition of osteoclastogenesis by mechanically stimulated osteoblasts is attenuated during estrogen deficiency.* Am J Physiol Cell Physiol, 2019. **317**(5): p. C969-c982.
289. Li, J., et al., *Osteoblasts Subjected to Mechanical Strain Inhibit Osteoclastic Differentiation and Bone Resorption in a Co-Culture System.* Annals of Biomedical Engineering, 2013. **41**(10): p. 2056-2066.
290. Tan, S.D., et al., *Osteocytes subjected to fluid flow inhibit osteoclast formation and bone resorption.* Bone, 2007. **41**(5): p. 745-751.
291. Kulkarni, R.N., et al., *Inhibition of Osteoclastogenesis by Mechanically Loaded Osteocytes: Involvement of MEPE.* Calcified Tissue International, 2010. **87**(5): p. 461-468.
292. Raposo, G. and P.D. Stahl, *Extracellular vesicles: a new communication paradigm?* Nature Reviews Molecular Cell Biology, 2019. **20**(9): p. 509-510.
293. van Niel, G., et al., *Challenges and directions in studying cell-cell communication by extracellular vesicles.* Nat Rev Mol Cell Biol, 2022. **23**(5): p. 369-382.
294. Stavenschi, E., et al., *Physiological cyclic hydrostatic pressure induces osteogenic lineage commitment of human bone marrow stem cells: a systematic study.* Stem Cell Research & Therapy, 2018. **9**(1).
295. Martins, C.S., et al., *Mechanical Cues and Lineage Commitment Govern the Angiogenic Potential of Mesenchymal Cell-Derived Extracellular Vesicles.* Adv Biol (Weinh), 2026. **10**(2): p. e00544.
296. Kato, Y., et al., *Establishment of an Osteocyte-like Cell Line, MLO-Y4.* Journal of Bone and Mineral Research, 1997. **12**(12): p. 2014-2023.
297. Rosser, J. and L.F. Bonewald, *Studying osteocyte function using the cell lines MLO-Y4 and MLO-A5.* Methods Mol Biol, 2012. **816**: p. 67-81.
298. Nahian, A. and A.M. AlEssa, *Histology, osteocytes.* 2020.
299. Qiu, Z.-Y., Y. Cui, and X.-M. Wang, *Chapter 1 - Natural Bone Tissue and Its Biomimetic*, in *Mineralized Collagen Bone Graft Substitutes*, X.-M. Wang, Z.-Y. Qiu, and H. Cui, Editors. 2019, Woodhead Publishing. p. 1-22.
300. Ji, X., et al., *Impact of mesenchymal stem cell size and adhesion modulation on in vivo distribution: insights from quantitative PET imaging.* Stem Cell Research & Therapy, 2024. **15**(1).
301. Stavenschi, E., M.N. Labour, and D.A. Hoey, *Oscillatory fluid flow induces the osteogenic lineage commitment of mesenchymal stem cells: The effect of shear stress magnitude, frequency, and duration.* J Biomech, 2017. **55**: p. 99-106.
302. Miyamoto, T., et al., *An adherent condition is required for formation of multinuclear osteoclasts in the presence of macrophage colony-stimulating factor and receptor activator of nuclear factor κB ligand.* Blood, 2000. **96**(13): p. 4335-4343.
303. Bellido, T., *Osteocyte-Driven Bone Remodeling.* Calcified Tissue International, 2014. **94**(1): p. 25-34.

304. Ogata, K., W. Katagiri, and H. Hibi, *Secretomes from mesenchymal stem cells participate in the regulation of osteoclastogenesis in vitro.* Clinical Oral Investigations, 2017. **21**(6): p. 1979-1988.
305. Heino, T.J., T.A. Hentunen, and H.K. Väänänen, *Osteocytes inhibit osteoclastic bone resorption through transforming growth factor-β: Enhancement by estrogen*.* Journal of Cellular Biochemistry, 2002. **85**(1): p. 185-197.
306. Gu, G., et al., *Death of osteocytes turns off the inhibition of osteoclasts and triggers local bone resorption.* Biochemical and Biophysical Research Communications, 2005. **335**(4): p. 1095-1101.
307. Kim, C.H., et al., *Oscillatory fluid flow-induced shear stress decreases osteoclastogenesis through RANKL and OPG signaling.* Bone, 2006. **39**(5): p. 1043-1047.
308. Liu, J., et al., *Pressure-Loaded MSCs During Early Osteodifferentiation Promote Osteoclastogenesis by Increase of RANKL/OPG Ratio.* Annals of Biomedical Engineering, 2009. **37**(4): p. 794-802.
309. Kaneuji, T., et al., *Mechanisms involved in regulation of osteoclastic differentiation by mechanical stress-loaded osteoblasts.* Biochem Biophys Res Commun, 2011. **408**(1): p. 103-9.
310. Zheng, L., et al., *Oscillating Fluid Flow Activated Osteocyte Lysate-Based Hydrogel for Regulating Osteoblast/Osteoclast Homeostasis to Enhance Bone Repair.* Advanced Science, 2023. **10**(15).
311. Cappariello, A., et al., *Osteoblast-Derived Extracellular Vesicles Are Biological Tools for the Delivery of Active Molecules to Bone.* Journal of Bone and Mineral Research, 2018. **33**(3): p. 517-533.
312. Nieuwoudt, M., et al., *Functionalization of Electrospun Polycaprolactone Scaffolds with Matrix-Binding Osteocyte-Derived Extracellular Vesicles Promotes Osteoblastic Differentiation and Mineralization.* Annals of Biomedical Engineering, 2021. **49**(12): p. 3621-3635.
313. Man, K., et al., *Development of a Bone-Mimetic 3D Printed Ti6Al4V Scaffold to Enhance Osteoblast-Derived Extracellular Vesicles' Therapeutic Efficacy for Bone Regeneration.* Front Bioeng Biotechnol, 2021. **9**: p. 757220.
314. Lee, K.S., et al., *Extracellular vesicles from adipose tissue-derived stem cells alleviate osteoporosis through osteoprotegerin and miR-21-5p.* Journal of Extracellular Vesicles, 2021. **10**(12).
315. Xiao, F., et al., *Exosomes derived from cyclic mechanical stretch-exposed bone marrow mesenchymal stem cells inhibit RANKL-induced osteoclastogenesis through the NF-κB signaling pathway.* Ann Transl Med, 2021. **9**(9): p. 798.
316. Burger, E.H., et al., *Function of osteocytes in bone--their role in mechanotransduction.* J Nutr, 1995. **125**(7 Suppl): p. 2020s-2023s.
317. Hagey, D.W., et al., *The cellular response to extracellular vesicles is dependent on their cell source and dose.* Sci Adv, 2023. **9**(35): p. eadh1168.
318. Garaeva, L., et al., *Delivery of functional exogenous proteins by plant-derived vesicles to human cells in vitro.* Scientific Reports, 2021. **11**(1): p. 6489.
319. Seyedrazizadeh, S.-Z., et al., *Extracellular vesicles derived from human ES-MSCs protect retinal ganglion cells and preserve retinal function in a rodent model of optic nerve injury.* Stem Cell Research & Therapy, 2020. **11**(1).

320. Wang, L., et al., *Mechanical regulation of bone remodeling.* Bone Research, 2022. **10**(1): p. 16.
321. Dallas, S.L., M. Prideaux, and L.F. Bonewald, *The osteocyte: an endocrine cell ... and more.* Endocr Rev, 2013. **34**(5): p. 658-90.
322. Klein-Nulend, J., et al., *Mechanosensation and transduction in osteocytes.* Bone, 2013. **54**(2): p. 182-190.
323. Rubin, C., S. Judex, and Y.-X. Qin, *Low-level mechanical signals and their potential as a non-pharmacological intervention for osteoporosis.* Age and Ageing, 2006. **35**(suppl_2): p. ii32-ii36.
324. Zhang, R., et al., *Seven Day Insertion Rest in Whole Body Vibration Improves Multi-Level Bone Quality in Tail Suspension Rats.* PLoS ONE, 2014. **9**(3): p. e92312.
325. Wu, X.T., et al., *The bio-response of osteocytes and its regulation on osteoblasts under vibration.* Cell Biology International, 2016. **40**(4): p. 397-406.
326. González-Torres, L.A., et al., *Influence of the frequency of the external mechanical stimulus on bone healing: a computational study.* Med Eng Phys, 2010. **32**(4): p. 363-71.
327. Chow, D.H.K., et al., *Low-magnitude high-frequency vibration (LMHFV) enhances bone remodeling in osteoporotic rat femoral fracture healing.* Journal of Orthopaedic Research, 2011. **29**(5): p. 746-752.
328. Leung, K.S., et al., *Low-magnitude high-frequency vibration accelerates callus formation, mineralization, and fracture healing in rats.* Journal of Orthopaedic Research, 2009. **27**(4): p. 458-465.
329. Wong, R.M.Y., et al., *Fibrinolysis as a target to enhance osteoporotic fracture healing by vibration therapy in a metaphyseal fracture model.* Bone & Joint Research, 2021. **10**(1): p. 41-50.
330. Haffner-Luntzer, M., et al., *Effects of low-magnitude high-frequency vibration on osteoblasts are dependent on estrogen receptor α signaling and cytoskeletal remodeling.* Biochemical and Biophysical Research Communications, 2018. **503**(4): p. 2678-2684.
331. Chow, S.K., et al., *Vibration treatment modulates macrophage polarisation and enhances early inflammatory response in oestrogen-deficient osteoporotic-fracture healing.* Eur Cell Mater, 2019. **38**: p. 228-245.
332. Kennedy, J.W., et al., *Nanovibrational stimulation inhibits osteoclastogenesis and enhances osteogenesis in co-cultures.* Scientific Reports, 2021. **11**(1).
333. Jawed, Y., et al., *Whole-Body Vibration Training Increases Stem/Progenitor Cell Circulation Levels and May Attenuate Inflammation.* Military Medicine, 2020. **185**(Supplement_1): p. 404-412.
334. Marín-Cascales, E., et al., *Whole-body vibration training and bone health in postmenopausal women: A systematic review and meta-analysis.* Medicine, 2018. **97**(34).
335. Sitjà-Rabert, M., et al., *Efficacy of whole body vibration exercise in older people: a systematic review.* Disabil Rehabil, 2012. **34**(11): p. 883-93.
336. DadeMatthews, O.O., et al., *Systematic review and meta-analyses on the effects of whole-body vibration on bone health.* Complement Ther Med, 2022. **65**: p. 102811.
337. Lv, L.L., et al., *Therapeutic application of extracellular vesicles in kidney disease: promises and challenges.* Journal of Cellular and Molecular Medicine, 2018. **22**(2): p. 728-737.

338. Whitford, W., J.W. Ludlow, and J.J.S. Cadwell, *Continuous Production of Exosomes.* Genetic Engineering & Biotechnology News, 2015. **35**(16): p. 34-34.
339. Cha, J.M., et al., *Efficient scalable production of therapeutic microvesicles derived from human mesenchymal stem cells.* Scientific Reports, 2018. **8**(1): p. 1171.
340. Liu, C., et al., *Profiling biomanufactured extracellular vesicles of human forebrain spheroids in a Vertical-Wheel Bioreactor.* Journal of Extracellular Biology, 2024. **3**(9).
341. Campsie, P., et al., *Design, construction and characterisation of a novel nanovibrational bioreactor and cultureware for osteogenesis.* Sci Rep, 2019. **9**(1): p. 12944.
342. Tsimbouri, P.M., et al., *Stimulation of 3D osteogenesis by mesenchymal stem cells using a nanovibrational bioreactor.* Nature Biomedical Engineering, 2017. **1**(9): p. 758-770.
343. Hodgkinson, T., et al., *The use of nanovibration to discover specific and potent bioactive metabolites that stimulate osteogenic differentiation in mesenchymal stem cells.* Science Advances, 2021. **7**(9): p. eabb7921.
344. Filipowska, J., et al., *The role of vasculature in bone development, regeneration and proper systemic functioning.* Angiogenesis, 2017. **20**(3): p. 291-302.
345. Maggio, M., et al., *Extracellular Vesicles-Mediated Crosstalk in Bone: miR-150-5p as a Mechanosensitive Inhibitor of Osteoclastogenesis.* bioRxiv, 2025: p. 2025.09.08.674886.
346. Lau, E., et al., *Effect of low-magnitude, high-frequency vibration on osteocytes in the regulation of osteoclasts.* Bone, 2010. **46**(6): p. 1508-1515.
347. Johnson-Love, O., et al., *Vibration-based cell engineering.* Nature Reviews Bioengineering, 2025. **3**(5): p. 408-429.
348. Pemberton, G.D., et al., *Nanoscale stimulation of osteoblastogenesis from mesenchymal stem cells: nanotopography and nanokicking.* Nanomedicine (Lond), 2015. **10**(4): p. 547-60.
349. Hodgkinson, T., et al., *The use of nanovibration to discover specific and potent bioactive metabolites that stimulate osteogenic differentiation in mesenchymal stem cells.* Science Advances. **7**(9): p. eabb7921.
350. Nikukar, H., et al., *Osteogenesis of mesenchymal stem cells by nanoscale mechanotransduction.* ACS Nano, 2013. **7**(3): p. 2758-67.
351. Orapiriyakul, W., et al., *Nanovibrational Stimulation of Mesenchymal Stem Cells Induces Therapeutic Reactive Oxygen Species and Inflammation for Three-Dimensional Bone Tissue Engineering.* ACS Nano, 2020. **14**(8): p. 10027-10044.
352. Sun, T., et al., *Effects of mechanical vibration on cell morphology, proliferation, apoptosis, and cytokine expression/secretion in osteocyte-like MLO-Y4 cells exposed to high glucose.* Cell Biol Int, 2020. **44**(1): p. 216-228.
353. Sakamoto, M., et al., *Vibration enhances osteoclastogenesis by inducing RANKL expression via NF-κB signaling in osteocytes.* Bone, 2019. **123**: p. 56-66.
354. Yan, J., et al., *The global burden of fractures and its underlying etiologies: results from and further analysis of the Global Burden of Disease Study 2021.* Archives of Osteoporosis, 2025. **20**(1): p. 111.
355. Oei, L., et al., *Diabetes, Diabetic Complications, and Fracture Risk.* Current Osteoporosis Reports, 2015. **13**(2): p. 106-115.
356. Bahney, C.S., et al., *Cellular biology of fracture healing.* Journal of Orthopaedic Research®, 2019. **37**(1): p. 35-50.

357. Yi, H., et al., *Preclinical and Clinical Amelioration of Bone Fractures with Mesenchymal Stromal Cells: a Systematic Review and Meta-Analysis.* Cell Transplantation, 2022. **31**: p. 09636897211051743.
358. Watson, L., S.J. Elliman, and C.M. Coleman, *From isolation to implantation: a concise review of mesenchymal stem cell therapy in bone fracture repair.* Stem Cell Res Ther, 2014. **5**(2): p. 51.
359. Wan, X., et al., *The Role of Extracellular Vesicles in Bone Regeneration and Associated Bone Diseases.* Curr Issues Mol Biol, 2024. **46**(9): p. 9269-9285.
360. Tsiapalis, D. and L. O'Driscoll, *Mesenchymal Stem Cell Derived Extracellular Vesicles for Tissue Engineering and Regenerative Medicine Applications.* Cells, 2020. **9**(4).
361. Colombo, F., et al., *Exploring the Spatial Limits of Extracellular Vesicles-Mediated Intercellular Communication.* J Extracell Vesicles, 2025. **14**(11): p. e70169.
362. Wuthier, R.E., *Lipid composition of isolated epiphyseal cartilage cells, membranes and matrix vesicles.* Biochim Biophys Acta, 1975. **409**(1): p. 128-43.
363. Anderson, H.C., *Mineralization by matrix vesicles.* Scan Electron Microsc, 1984(Pt 2): p. 953-64.
364. Boskey, A.L., *Noncollagenous matrix proteins and their role in mineralization.* Bone and Mineral, 1989. **6**(2): p. 111-123.
365. Boskey, A.L., *Mineral-Matrix Interactions in Bone and Cartilage.* Clinical Orthopaedics and Related Research®, 1992. **281**.
366. Huleihel, L., et al., *Matrix-bound nanovesicles within ECM bioscaffolds.* Science Advances, 2016. **2**(6): p. e1600502.
367. Turner, N.J., et al., *Matrix Bound Nanovesicles Have Tissue-Specific Characteristics That Suggest a Regulatory Role.* Tissue Engineering Part A, 2022. **28**(21-22): p. 879-892.
368. Zazzeroni, L., G. Faggioli, and G. Pasquinelli, *Mechanisms of Arterial Calcification: The Role of Matrix Vesicles.* European Journal of Vascular and Endovascular Surgery, 2018. **55**(3): p. 425-432.
369. Lin, Z., et al., *MicroRNA Contents in Matrix Vesicles Produced by Growth Plate Chondrocytes are Cell Maturation Dependent.* Sci Rep, 2018. **8**(1): p. 3609.
370. Nieves, J.W., *Sex-Differences in Skeletal Growth and Aging.* Curr Osteoporos Rep, 2017. **15**(2): p. 70-75.
371. Selle, M., et al., *Influence of age on stem cells depends on the sex of the bone marrow donor.* J Cell Mol Med, 2022. **26**(5): p. 1594-1605.
372. Weilner, S., et al., *Vesicular Galectin-3 levels decrease with donor age and contribute to the reduced osteo-inductive potential of human plasma derived extracellular vesicles.* Aging, 2016. **8**(1): p. 16-30.
373. Carriero, A., et al., *Age and Sex Differences in Load-Induced Tibial Cortical Bone Surface Strain Maps.* JBMR Plus, 2021. **5**(3): p. e10467.
374. Meakin, L.B., et al., *Age-related impairment of bones' adaptive response to loading in mice is associated with sex-related deficiencies in osteoblasts but no change in osteocytes.* Journal of Bone and Mineral Research, 2014. **29**(8): p. 1859-1871.
375. Galea, G.L., et al., *Bone gain following loading is site-specifically enhanced by prior and concurrent disuse in aged male mice.* Bone, 2020. **133**: p. 115255.
376. Metsalu, T. and J. Vilo, *ClustVis: a web tool for visualizing clustering of multivariate data using Principal Component Analysis and heatmap.* Nucleic Acids Research, 2015. **43**(W1): p. W566-W570.

377. Szklarczyk, D., et al., *The STRING database in 2025: protein networks with directionality of regulation.* Nucleic Acids Research, 2024. **53**(D1): p. D730-D737.
378. Khamina, K., et al., *A MicroRNA Next-Generation-Sequencing Discovery Assay (miND) for Genome-Scale Analysis and Absolute Quantitation of Circulating MicroRNA Biomarkers.* International Journal of Molecular Sciences, 2022. **23**(3): p. 1226.
379. Diendorfer, A., et al., *miND (miRNA NGS Discovery pipeline): a small RNA-seq analysis pipeline and report generator for microRNA biomarker discovery studies.* F1000Research, 2022. **11**: p. 233.
380. Maragkakis, M., et al., *DIANA-microT web server: elucidating microRNA functions through target prediction.* Nucleic acids research, 2009. **37**(suppl_2): p. W273-W276.
381. Miranda, K.C., et al., *A pattern-based method for the identification of MicroRNA binding sites and their corresponding heteroduplexes.* Cell, 2006. **126**(6): p. 1203-1217.
382. Lall, S., et al., *A genome-wide map of conserved microRNA targets in C. elegans.* Current biology, 2006. **16**(5): p. 460-471.
383. Friedman, R.C., et al., *Most mammalian mRNAs are conserved targets of microRNAs.* Genome research, 2009. **19**(1): p. 92-105.
384. Wong, N. and X. Wang, *miRDB: an online resource for microRNA target prediction and functional annotations.* Nucleic acids research, 2015. **43**(D1): p. D146-D152.
385. Cunniffe, G.M., et al., *Development and characterisation of a collagen nano-hydroxyapatite composite scaffold for bone tissue engineering.* J Mater Sci Mater Med, 2010. **21**(8): p. 2293-8.
386. Cunniffe, G.M., et al., *The synthesis and characterization of nanophase hydroxyapatite using a novel dispersant-aided precipitation method.* J Biomed Mater Res A, 2010. **95**(4): p. 1142-9.
387. Bonucci, E., *Fine structure of early cartilage calcification.* Journal of Ultrastructure Research, 1967. **20**(1): p. 33-50.
388. Bernard, G.W. and D.C. Pease, *An electron microscopic study of initial intramembranous osteogenesis.* Am J Anat, 1969. **125**(3): p. 271-90.
389. Dai, J. and A.B.M. Rabie, *VEGF: an Essential Mediator of Both Angiogenesis and Endochondral Ossification.* Journal of Dental Research, 2007. **86**(10): p. 937-950.
390. Hankenson, K.D., et al., *Angiogenesis in bone regeneration.* Injury, 2011. **42**(6): p. 556-561.
391. Du, J., et al., *BRD9-mediated chromatin remodeling suppresses osteoclastogenesis through negative feedback mechanism.* Nat Commun, 2023. **14**(1): p. 1413.
392. Zhang, Y., et al., *The chromatin remodeling factor Arid1a cooperates with Jun/Fos to promote osteoclastogenesis by epigenetically upregulating Siglec15 expression.* J Bone Miner Res, 2024. **39**(6): p. 775-790.
393. Chen, Y., et al., *Chromatin remodeling enzyme CHD7 is necessary for osteogenesis of human mesenchymal stem cells.* Biochemical and biophysical research communications, 2016. **478**(4): p. 1588-1593.
394. Takeuchi, T., et al., *Glucosamine suppresses osteoclast differentiation through the modulation of glycosylation including O-GlcNAcylation.* Biological and Pharmaceutical Bulletin, 2017. **40**(3): p. 352-356.

395. Sun, Y., et al., *Glycosylation of Dentin Matrix Protein 1 is critical for osteogenesis.* Sci Rep, 2015. **5**: p. 17518.
396. Pramojanee, S.N., et al., *Possible roles of insulin signaling in osteoblasts.* Endocr Res, 2014. **39**(4): p. 144-51.
397. Fulzele, K., et al., *Insulin receptor signaling in osteoblasts regulates postnatal bone acquisition and body composition.* Cell, 2010. **142**(2): p. 309-19.
398. Grosso, A., et al., *It Takes Two to Tango: Coupling of Angiogenesis and Osteogenesis for Bone Regeneration.* Front Bioeng Biotechnol, 2017. **5**: p. 68.
399. Cimatti, P., et al., *An Observational Prospective Clinical Study for the Evaluation of a Collagen-Hydroxyapatite Composite Scaffold in Hip Revision Surgery.* J Clin Med, 2022. **11**(21).
400. Giorgi, P., et al., *A New Bioinspired Collagen-Hydroxyapatite Bone Graft Substitute in Adult Scoliosis Surgery: Results at 3-Year Follow-Up.* Journal of Applied Biomaterials & Functional Materials, 2017. **15**(3): p. 262-270.
401. Iwatsu, J., et al., *Clinical outcome of porous hydroxyapatite/collagen graft on bone defects following curettage of bone tumors.* J Biomed Mater Res B Appl Biomater, 2022. **110**(10): p. 2211-2216.
402. Sims, N.A. and T.J. Martin, *Coupling the activities of bone formation and resorption: a multitude of signals within the basic multicellular unit.* Bonekey Rep, 2014. **3**: p. 481.
403. Ali, S.Y., S.W. Sajdera, and H.C. Anderson, *Isolation and Characterization of Calcifying Matrix Vesicles from Epiphyseal Cartilage.* Proceedings of the National Academy of Sciences, 1970. **67**(3): p. 1513-1520.
404. Siracusa, C., et al., *Understanding Vascular Calcification in Chronic Kidney Disease: Pathogenesis and Therapeutic Implications.* International Journal of Molecular Sciences, 2024. **25**(23): p. 13096.
405. Khan, S.R., et al., *Association of Randall plaque with collagen fibers and membrane vesicles.* J Urol, 2012. **187**(3): p. 1094-100.
406. Merino-González, C., et al., *Mesenchymal Stem Cell-Derived Extracellular Vesicles Promote Angiogenesis: Potencial Clinical Application.* Front Physiol, 2016. **7**: p. 24.
407. Li, S., et al., *Cell communication and relevant signaling pathways in osteogenesis–angiogenesis coupling.* Bone Research, 2025. **13**(1).
408. Yun, H.W., et al., *Matrix-bound nanovesicles recapitulate tissue-specific angiogenic properties of parent extracellular matrix with distinct miRNA profiles.* Biomater Adv, 2025. **175**: p. 214338.
409. Xie, H., et al., *Extracellular Vesicle-functionalized Decalcified Bone Matrix Scaffolds with Enhanced Pro-angiogenic and Pro-bone Regeneration Activities.* Scientific Reports, 2017. **7**(1): p. 45622.
410. Holkar, K., et al., *Biomaterials and extracellular vesicles in cell-free therapy for bone repair and regeneration: Future line of treatment in regenerative medicine.* Materialia, 2020. **12**: p. 100736.
411. Eichholz, K.F., et al., *Extracellular Vesicle Functionalized Melt Electrowritten Scaffolds for Bone Tissue Engineering.* Advanced NanoBiomed Research, 2021. **1**(10): p. 2100037.
412. Yáñez-Mó, M., et al., *Biological properties of extracellular vesicles and their physiological functions.* Journal of Extracellular Vesicles, 2015. **4**(1): p. 27066.

413. Takayanagi, H., *Osteoimmunology: shared mechanisms and crosstalk between the immune and bone systems.* Nature Reviews Immunology, 2007. **7**(4): p. 292-304.
414. Lorenzo, J., M. Horowitz, and Y. Choi, *Osteoimmunology: interactions of the bone and immune system.* Endocr Rev, 2008. **29**(4): p. 403-40.
415. Villarroya-Beltri, C., et al., *Sumoylated hnRNPA2B1 controls the sorting of miRNAs into exosomes through binding to specific motifs.* Nature Communications, 2013. **4**(1).
416. Groot, M. and H. Lee, *Sorting mechanisms for MicroRNAs into extracellular vesicles and their associated diseases.* Cells, 2020. **9**(4): p. 1044.
417. Lian, J.B., et al., *MicroRNA control of bone formation and homeostasis.* Nat Rev Endocrinol, 2012. **8**(4): p. 212-27.
418. Han, X. and Z. Fan, *MicroRNAs Regulation in Osteogenic Differentiation of Mesenchymal Stem Cells.* Frontiers in Dental Medicine, 2021. **2**.
419. Ramasamy, S.K., et al., *Endothelial Notch activity promotes angiogenesis and osteogenesis in bone.* Nature, 2014. **507**(7492): p. 376-380.
420. Kusumbe, A.P., S.K. Ramasamy, and R.H. Adams, *Coupling of angiogenesis and osteogenesis by a specific vessel subtype in bone.* Nature, 2014. **507**(7492): p. 323-328.
421. Ferron, M., et al., *Insulin signaling in osteoblasts integrates bone remodeling and energy metabolism.* Cell, 2010. **142**(2): p. 296-308.
422. Luo, Y., et al., *miR-30b-5p inhibits osteoblast differentiation through targeting BCL6.* Cell Cycle, 2022. **21**(6): p. 630-640.
423. Liu, G., et al., *Suppressing MicroRNA-30b by estrogen promotes osteogenesis in bone marrow mesenchymal stem cells.* Stem cells international, 2019. **2019**(1): p. 7547506.
424. Takayanagi, H., et al., *Induction and activation of the transcription factor NFATc1 (NFAT2) integrate RANKL signaling in terminal differentiation of osteoclasts.* Developmental cell, 2002. **3**(6): p. 889-901.
425. Grigoriadis, A.E., et al., *c-Fos: a key regulator of osteoclast-macrophage lineage determination and bone remodeling.* Science, 1994. **266**(5184): p. 443-8.
426. Zhao, Y., et al., *Role of chromatin modulator Dpy30 in osteoclast differentiation and function.* Bone, 2022. **159**: p. 116379.
427. Yang, S., et al., *Glycobiology in osteoclast differentiation and function.* Bone Res, 2023. **11**(1): p. 55.
428. Cai, X., et al., *The importance of N-glycosylation on β3 integrin ligand binding and conformational regulation.* Scientific Reports, 2017. **7**(1): p. 4656.
429. Chen, Y., J. Klein-Nulend, and N. Bravenboer, *Ageing-Related Changes in Ultrastructural Bone Matrix Composition and Osteocyte Mechanosensitivity.* Current Osteoporosis Reports, 2025. **23**(1): p. 35.
430. Boskey, A.L. and R. Coleman, *Aging and bone.* J Dent Res, 2010. **89**(12): p. 1333-48.
431. Smith, C.A., et al., *Human decellularized bone scaffolds from aged donors show improved osteoinductive capacity compared to young donor bone.* PLoS One, 2017. **12**(5): p. e0177416.
432. Traianedes, K., et al., *Donor age and gender effects on osteoinductivity of demineralized bone matrix.* J Biomed Mater Res B Appl Biomater, 2004. **70**(1): p. 21-9.

433. Delloye, C., et al., *Local complications of massive bone allografts: an appraisal of their prevalence in 128 patients.* Acta Orthop Belg, 2014. **80**(2): p. 196-204.
434. Nyssen-Behets, C., et al., *Aging effect on inductive capacity of human demineralized bone matrix.* Archives of Orthopaedic and Trauma Surgery, 1996. **115**(6): p. 303-306.
435. Schwartz, Z., et al., *Ability of commercial demineralized freeze-dried bone allograft to induce new bone formation is dependent on donor age but not gender.* J Periodontol, 1998. **69**(4): p. 470-8.
436. Henriksen, K., et al., *Osteoclasts prefer aged bone.* Osteoporosis International, 2007. **18**(6): p. 751-759.
437. Chung, P.L., et al., *Effect of age on regulation of human osteoclast differentiation.* J Cell Biochem, 2014. **115**(8): p. 1412-9.
438. Zhang, L., et al., *Consequences of Aging on Bone.* Aging Dis, 2023. **15**(6): p. 2417-2452.
439. Wallace, J.M., et al., *Exercise-induced changes in the cortical bone of growing mice are bone- and gender-specific.* Bone, 2007. **40**(4): p. 1120-1127.
440. Dimitriou, R., et al., *Bone regeneration: current concepts and future directions.* BMC Medicine, 2011. **9**(1): p. 66.
441. Duda, G.N., et al., *The decisive early phase of bone regeneration.* Nature Reviews Rheumatology, 2023. **19**(2): p. 78-95.
442. Ikebuchi, Y., et al., *Coupling of bone resorption and formation by RANKL reverse signalling.* Nature, 2018. **561**(7722): p. 195-200.
443. Erben, R.G., *Hypothesis: Coupling between Resorption and Formation in Cancellous bone Remodeling is a Mechanically Controlled Event.* Front Endocrinol (Lausanne), 2015. **6**: p. 82.
444. Robling, A.G. and C.H. Turner, *Mechanical Signaling for Bone Modeling and Remodeling.* Critical Reviews™ in Eukaryotic Gene Expression, 2009. **19**(4): p. 319-338.
445. Schaffler, M.B. and O.D. Kennedy, *Osteocyte Signaling in Bone.* Current Osteoporosis Reports, 2012. **10**(2): p. 118-125.
446. Neve, A., A. Corrado, and F.P. Cantatore, *Osteocytes: central conductors of bone biology in normal and pathological conditions.* Acta Physiol (Oxf), 2012. **204**(3): p. 317-30.
447. Liu, M., Y. Sun, and Q. Zhang, *Emerging Role of Extracellular Vesicles in Bone Remodeling.* J Dent Res, 2018. **97**(8): p. 859-868.
448. Bartel, D.P., *MicroRNAs: Genomics, Biogenesis, Mechanism, and Function.* Cell, 2004. **116**(2): p. 281-297.
449. Jing, D., et al., *The role of microRNAs in bone remodeling.* Int J Oral Sci, 2015. **7**(3): p. 131-43.
450. Pergoli, L., et al., *Extracellular vesicle-packaged miRNA release after short-term exposure to particulate matter is associated with increased coagulation.* Particle and Fibre Toxicology, 2017. **14**(1).
451. Xia, B., et al., *Mechanical stimulation of Schwann cells promote peripheral nerve regeneration via extracellular vesicle-mediated transfer of microRNA 23b-3p.* Theranostics, 2020. **10**(20): p. 8974-8995.
452. Kozomara, A., M. Birgaoanu, and S. Griffiths-Jones, *miRBase: from microRNA sequences to function.* Nucleic Acids Res, 2019. **47**(D1): p. D155-d162.

453. Sherman, B.T., et al., *DAVID: a web server for functional enrichment analysis and functional annotation of gene lists (2021 update).* Nucleic Acids Res, 2022. **50**(W1): p. W216-w221.
454. McCarthy, H.O., et al., *Development and characterization of self-assembling nanoparticles using a bio-inspired amphipathic peptide for gene delivery.* J Control Release, 2014. **189**: p. 141-9.
455. Bennett, R., et al., *RALA-mediated delivery of FKBPL nucleic acid therapeutics.* Nanomedicine (Lond), 2015. **10**(19): p. 2989-3001.
456. Cunniffe, G.M., et al., *Content-Dependent Osteogenic Response of Nanohydroxyapatite: An in Vitro and in Vivo Assessment within Collagen-Based Scaffolds.* ACS Applied Materials & Interfaces, 2016. **8**(36): p. 23477-23488.
457. Munir, J., J.K. Yoon, and S. Ryu, *Therapeutic miRNA-Enriched Extracellular Vesicles: Current Approaches and Future Prospects.* Cells, 2020. **9**(10): p. 2271.
458. Fang, S., et al. *MicroRNAs Regulate Bone Development and Regeneration*. International Journal of Molecular Sciences, 2015. **16**, 8227-8253 DOI: 10.3390/ijms16048227.
459. Wu, F., et al., *Exosomes derived from BMSCs in osteogenic differentiation promote type H blood vessel angiogenesis through miR-150-5p mediated metabolic reprogramming of endothelial cells.* Cellular and Molecular Life Sciences, 2024. **81**(1).
460. Xu, C., et al., *Extracellular vesicles derived from bone marrow mesenchymal stem cells loaded on magnetic nanoparticles delay the progression of diabetic osteoporosis via delivery of miR-150-5p.* Cell Biology and Toxicology, 2023. **39**(4): p. 1257-1274.
461. Komatsu, D.E., et al., *Modulation of Wnt signaling influences fracture repair.* Journal of Orthopaedic Research, 2010. **28**(7): p. 928-936.
462. Van'T Hof, R.J. and S.H. Ralston, *Nitric oxide and bone.* Immunology, 2001. **103**(3): p. 255-261.
463. Karner, C.M. and F. Long, *Glucose metabolism in bone.* Bone, 2018. **115**: p. 2-7.
464. Fiorino, C. and R.E. Harrison, *E-cadherin is important for cell differentiation during osteoclastogenesis.* Bone, 2016. **86**: p. 106-118.
465. McHugh, K.P., et al. *Role of Cell-matrix Interactions in Osteoclast Differentiation*. in *Osteoimmunology*. 2007. Boston, MA: Springer US.
466. Hu, L., et al., *Retinoic Acid Increases Proliferation of Human Osteoclast Progenitors and Inhibits RANKL-Stimulated Osteoclast Differentiation by Suppressing RANK.* PLoS ONE, 2010. **5**(10): p. e13305.
467. Saintier, D., et al., *Estradiol inhibits adhesion and promotes apoptosis in murine osteoclasts in vitro.* The Journal of Steroid Biochemistry and Molecular Biology, 2006. **99**(4): p. 165-173.
468. Saar, K., et al., *Cell-penetrating peptides: a comparative membrane toxicity study.* Analytical biochemistry, 2005. **345**(1): p. 55-65.
469. Gerber, H.-P. and N. Ferrara, *Angiogenesis and Bone Growth.* Trends in Cardiovascular Medicine, 2000. **10**(5): p. 223-228.
470. Kanczler, J. and R. Oreffo, *Osteogenesis and angiogenesis: the potential for engineering bone.* Eur Cell Mater, 2008. **15**(2): p. 100-114.

471. Ren, J., et al., *How Do Extracellular Vesicles Play a Key Role in the Maintenance of Bone Homeostasis and Regeneration? A Comprehensive Review of Literature.* Int J Nanomedicine, 2022. **17**: p. 5375-5389.
472. Valadi, H., et al., *Exosome-mediated transfer of mRNAs and microRNAs is a novel mechanism of genetic exchange between cells.* Nat Cell Biol, 2007. **9**(6): p. 654-9.
473. Baron, R. and M. Kneissel, *WNT signaling in bone homeostasis and disease: from human mutations to treatments.* Nat Med, 2013. **19**(2): p. 179-92.
474. Dong, C.L., et al., *The influence of MicroRNA-150 in Osteoblast Matrix Mineralization.* J Cell Biochem, 2015. **116**(12): p. 2970-9.
475. Qi, J.-L., et al., *mir-150-5p inhibits the osteogenic differentiation of bone marrow-derived mesenchymal stem cells by targeting irisin to regulate the p38/MAPK signaling pathway.* Journal of Orthopaedic Surgery and Research, 2024. **19**(1).
476. Wang, F., et al., *Adipose-derived stem cells with miR-150-5p inhibition laden in hydroxyapatite/tricalcium phosphate ceramic powders promote osteogenesis via regulating Notch3 and activating FAK/ERK and RhoA.* Acta Biomaterialia, 2023. **155**: p. 644-653.
477. Li, J., et al., *Microvesicle-mediated transfer of microRNA-150 from monocytes to endothelial cells promotes angiogenesis.* J Biol Chem, 2013. **288**(32): p. 23586-96.
478. Fang, S., et al., *MiR-150-5p-modified Bone Marrow Mesenchymal Stem Cells Derived Exosomes Ameliorate Osteonecrosis of Femoral Head by Promoting Endothelial Cell Angiogenesis*. 2020, Research Square Platform LLC.
479. Choi, S.W., et al., *Osteoporotic bone of miR-150-deficient mice: Possibly due to low serum OPG-mediated osteoclast activation.* Bone Rep, 2015. **3**: p. 5-10.
480. Moussa, F.M., et al., *The role of miR-150 regulates bone cell differentiation and function.* Bone, 2021. **145**: p. 115470.
481. Sadowska, J.M., et al., *Development of miR-26a-activated scaffold to promote healing of critical-sized bone defects through angiogenic and osteogenic mechanisms.* Biomaterials, 2023. **303**: p. 122398.
482. Leng, Q., L. Chen, and Y. Lv, *RNA-based scaffolds for bone regeneration: application and mechanisms of mRNA, miRNA and siRNA.* Theranostics, 2020. **10**(7): p. 3190-3205.
483. Curtin, C.M., I.M. Castaño, and F.J. O'Brien, *Scaffold-Based microRNA Therapies in Regenerative Medicine and Cancer.* Advanced Healthcare Materials, 2018. **7**(1): p. 1700695.
484. Wang, J., et al., *MicroRNA-loaded biomaterials for osteogenesis.* Front Bioeng Biotechnol, 2022. **10**: p. 952670.
485. Andrée, L., et al., *Designing biomaterials for the delivery of RNA therapeutics to stimulate bone healing.* Materials Today Bio, 2021. **10**: p. 100105.
486. Hu, S., et al., *Mechanisms of hydrogel-based microRNA delivery systems and its application strategies in targeting inflammatory diseases.* Journal of Tissue Engineering, 2024. **15**: p. 20417314241265897.
487. Brady, R.T., F.J. O'Brien, and D.A. Hoey, *Mechanically stimulated bone cells secrete paracrine factors that regulate osteoprogenitor recruitment, proliferation, and differentiation.* Biochem Biophys Res Commun, 2015. **459**(1): p. 118-23.
488. Santos, A., A.D. Bakker, and J. Klein-Nulend, *The role of osteocytes in bone mechanotransduction.* Osteoporosis International, 2009. **20**(6): p. 1027-1031.

489. Tabak, S., S. Schreiber-Avissar, and E. Beit-Yannai, *Extracellular vesicles have variable dose-dependent effects on cultured draining cells in the eye.* J Cell Mol Med, 2018. **22**(3): p. 1992-2000.
490. Hagey, D.W., et al., *The cellular response to extracellular vesicles is dependent on their cell source and dose.* Science advances, 2023. **9**(35): p. eadh1168.
491. Shikata, T., et al., *Effects of amplitude and frequency of mechanical vibration stimulation on cultured osteoblasts.* Journal of System Design and Dynamics, 2008. **2**(1): p. 382-388.
492. Ng, C.Y., et al., *Scalable Production of Extracellular Vesicles and Its Therapeutic Values: A Review.* International Journal of Molecular Sciences, 2022. **23**(14): p. 7986.
493. Shah, K.M., et al., *Osteocyte isolation and culture methods.* Bonekey Rep, 2016. **5**: p. 838.
494. Thompson, W.R., C.T. Rubin, and J. Rubin, *Mechanical regulation of signaling pathways in bone.* Gene, 2012. **503**(2): p. 179-193.
495. Kohli, N., et al., *Bone remodelling in vitro: Where are we headed?: -A review on the current understanding of physiological bone remodelling and inflammation and the strategies for testing biomaterials in vitro.* Bone, 2018. **110**: p. 38-46.
496. Monguió-Tortajada, M., et al., *Extracellular vesicle isolation methods: rising impact of size-exclusion chromatography.* Cellular and Molecular Life Sciences, 2019. **76**(12): p. 2369-2382.
497. Wuthier, R.E. and G.F. Lipscomb, *Matrix vesicles: structure, composition, formation and function in calcification.* Front Biosci (Landmark Ed), 2011. **16**(8): p. 2812-902.